



UNIVERSITÀ  
DEGLI STUDI  
FIRENZE

# DOTTORATO DI RICERCA IN SCIENZE CHIMICHE

CICLO XXXII

COORDINATORE Prof. PIERO BAGLIONI

Effects of inorganic nanoparticles and additives on the properties of lipid  
liquid crystalline mesophases

Settore Scientifico Disciplinare CHIM/02

**Dottorando**

Dott. Marco Mendozza

**Tutore**

Prof. Debora Berti

---

*(firma)*

---

*(firma)*

**Coordinatore**

Prof. Piero Baglioni

---

*(firma)*

Anni 2016/2019



# Abstract

The self-assembly of lipids into organized soft matter is ubiquitous in natural systems. The most prominent example is the lamellar structural unit of cell membranes, though the occurrence of several non-lamellar assemblies – such as cubic and hexagonal mesophases – is currently emerging as crucially connected to particular functions or pathological conditions. On the synthetic side, a wide range of lipid architectures can be built from amphiphilic lipids, and their structure can be controlled by varying the experimental conditions – such as temperature, pressure, pH, ionic strength and geometrical local constraints – in order to reproduce the same morphologies, found in living systems. These synthetic assemblies represent simplified mimics of the aforementioned biological interfaces. Furthermore, their biocompatibility – combined with the coexistence of hydrophobic and hydrophilic domains with morphology and spatial organization ruled by thermal equilibrium – lends itself to applications in the biomedical field, e.g. for the delivery of therapeutic or diagnostic active principles.

In this research work, the attention has been focused on the investigation of the effects of inorganic nanoparticles and molecular additives on the phase properties of lipid liquid-crystalline mesophases. In particular, the inclusion of gold (AuNPs) and iron oxide (SPIONs) nanoparticles coated with hydrophobic ligands in liquid crystalline mesophases has been explored to build up smart soft hybrid materials, where the biocompatibility of the lipid matrix (1-monoolein and phytantriol) mesophases is combined with the responsiveness to external stimuli, provided by the NPs. For cubic mesophases doped with hydrophobic AuNPs and SPIONs, the effects of NPs inclusion – both on the arrangement of the mesophase and on its rheological properties – have been investigated. For lipid cubic phases doped with SPIONs, we examined the magnetic properties and their dependence on the phase state and monitored *in-situ* the structural change caused by an oscillating magnetic field. To further modulate the phase behavior, and to tailor the size of hydrophobic and hydrophilic compartments, we studied the effects of additives with different polarities – i.e. sugar esters, oils (tetradecane) and other lipids (DOPG) – on the lattice parameters and stability of mesophases. To gain additional insight on the confinement of molecular and macromolecular active principles, we monitored the diffusion of hydrophilic

probes of different sizes through fluorescence correlation spectroscopy and the results have been interpreted in terms of motion dimensionality and size match between the probes and the hydrophilic channels. In addition, the enzymatic activity of a model enzyme – the alkaline phosphatase – has been investigated when the enzyme or the probe were included in the mesophase.

Finally, *in-vitro* tests on tumor cell lines provided information on biocompatibility and internalization, highlighting the potential of these hybrid systems as drug-delivery devices.

# List of Abbreviations

<b>AuNPs</b>	Gold Nanoparticles
<b>AuNRs</b>	Gold Nanorods
<b>CM</b>	Confocal Microscopy
<b>CPP</b>	Critical Packing Parameter
<b>Cryo-SEM</b>	Cryo-Scanning Electron Microscopy
<b>Cryo-TEM</b>	Cryo-Transmission Electron Microscopy
<b>DDs</b>	Drug-Delivery Systems
<b>DLS</b>	Dynamic Light Scattering
<b>DLPC</b>	1,2-dilauroyl-sn-glycero-3-phosphocholine
<b>DOPG</b>	1,2-dioleoyl-sn-glycero-3-phospho-(1'-rac-glycerol)
<b>DSPC</b>	1,2-distearoyl-sn-glycero-3-phosphocholine
<b>FCS</b>	Fluorescence Correlation Spectroscopy
<b>F127</b>	Pluronic F127
<b>IPMS</b>	Infinite Periodical Minimal Surface
<b>LCs</b>	Liquid Crystals
<b>LCDs</b>	Dispersed liquid crystals
<b>LF-AMF</b>	Low Frequency- Alternating Magnetic Field
<b>LLCs</b>	Lyotropic liquid crystals
<b>MO</b>	1-monoolein
<b>MRI</b>	Magnetic Resonance Imaging
<b>NIST</b>	National Institute of Standard and Technology
<b>NPs</b>	Nanoparticles
<b>PEGA</b>	poly- (ethylene glycol)-methyl ether acrylate
<b>PEO</b>	Polyethylene-oxide
<b>Phyt</b>	Phytantriol
<b>PPO</b>	Polypropylene-oxide
<b>QDs</b>	Quantum Dots
<b>SAXS</b>	Small Angle X-ray Scattering
<b>SPIONs</b>	Superparamagnetic Iron Oxide Nanoparticles
<b>SS</b>	Sucrose Stearate
<b>TD</b>	tetradecane



# Contents

<b>Abstract .....</b>	<b><i>i</i></b>
<b>List of Abbreviations.....</b>	<b><i>iii</i></b>
<b>Contents.....</b>	<b><i>v</i></b>
<b>Introduction .....</b>	<b><i>1</i></b>
<b>1.1 Lyotropic Liquid Crystals (LLCs) .....</b>	<b><i>2</i></b>
<b>1.2 Energetic terms describing the mesophases .....</b>	<b><i>4</i></b>
1.2.1 Frustration Packing energy.....	<i>4</i>
1.2.2 Free energy of elastic curvature.....	<i>5</i>
<b>1.3 Self-Assembly of cubic mesophases .....</b>	<b><i>6</i></b>
<b>1.4 Effects of Nanoparticles on cubic mesophases .....</b>	<b><i>8</i></b>
<b>1.5 Effects of additives on cubic mesophases .....</b>	<b><i>11</i></b>
1.5.1 Molecules assembled with lipids .....	<i>11</i>
1.5.2 Synthetic macromolecules interacting with lipid assemblies .....	<i>13</i>
<b>1.6 Confinement features of LLCs .....</b>	<b><i>15</i></b>
<b>Materials and Methods .....</b>	<b><i>19</i></b>
<b>2.1 Materials Preparation .....</b>	<b><i>19</i></b>
2.1.1 Synthesis of Superparamagnetic Iron Oxide Nanoparticles .....	<i>19</i>
2.1.2 Synthesis of Gold Nanoparticles .....	<i>19</i>
2.1.3 Preparation of bulk cubic phases .....	<i>20</i>
2.1.4 Preparation of dispersed liquid crystals.....	<i>20</i>
<b>2.2 Small-Angle X-Ray Scattering (SAXS).....</b>	<b><i>20</i></b>
<b>2.3 Dynamic Light Scattering (DLS) .....</b>	<b><i>24</i></b>
<b>2.4 Rheology .....</b>	<b><i>26</i></b>
<b>2.5 <i>In-vitro</i> test experiments .....</b>	<b><i>28</i></b>
2.5.1 Cell Culture.....	<i>28</i>
2.5.2 Cubosomes internalization assay .....	<i>28</i>
2.5.3 Incubation with Cubosomes and SPIONs-loaded Cubosomes.....	<i>28</i>
2.5.4 Cell viability assay.....	<i>29</i>
<b>2.6 Alternating Magnetic Field (AMF).....</b>	<b><i>29</i></b>
<b>2.7 Laser Scanning Confocal Microscopy (LSCM).....</b>	<b><i>30</i></b>

---

2.8 Fluorescence Correlation Spectroscopy (FCS) .....	31
<b>Results and Discussion .....</b>	<b>35</b>
<b>Part I .....</b>	<b>35</b>
3.1 Inclusion of NPs in Non-Lamellar lipid membrane (Paper I, II, III).....	35
3.2 Viscoelastic properties of Non-Lamellar lipid membrane (Paper II).....	42
3.3 Cubosomes and Magnetocubosomes dispersions (Paper I and IV).....	46
3.4 Magnetotropism of bulk and dispersed liquid crystals (Paper IV) .....	48
3.5 Interaction of dispersed LCs with cells (Paper IV) .....	53
<b>Part II .....</b>	<b>57</b>
3.6 Effects of additives on Non-Lamellar mesophases (Paper V and VI) ....	57
3.6.1 Sucrose Stearate on Phytantriol assemblies .....	57
3.6.2 DOPG and Tetradecane combined with MO assemblies .....	59
3.7 Release and diffusive properties of mesophases (Paper V and VI) .....	63
3.7.1 Effects on the enzymatic kinetic reaction .....	63
3.7.2 Relationship between structure and diffusive properties .....	72
<b>Conclusions and Future perspective .....</b>	<b>80</b>
<b>Bibliography .....</b>	<b>85</b>
<b>Appendices: List of Papers .....</b>	<b>95</b>
<b>Paper I .....</b>	<b>97</b>
<b>Paper II .....</b>	<b>127</b>
<b>Paper III .....</b>	<b>167</b>
<b>Paper IV .....</b>	<b>201</b>
<b>Paper V .....</b>	<b>233</b>
<b>Paper VI .....</b>	<b>259</b>

# 1

## Introduction

Amphiphilic molecules play a central part in our daily life. Their role as proteins, components of lipid membranes and polymers in living systems, and their use as surfactants, emulsifiers, stabilizers in the industry, are indicative of their ubiquitous presence. From a technological point of view, their application is related to the ability to self-assemble in supramolecular structures, guided by hydrophobic, electrostatic and hydrogen bonds interactions. In aqueous environment, self-assembly results in the segregation of hydrophobic portions – allowing the interaction of polar heads with the medium – thereby minimizing the unfavorable interaction between water and hydrophobic blocks.

The coexistence of both hydrophobic and hydrophilic domains allows application in the biomedical field for drug-delivery, for spatial and temporal control of the release of encapsulated active molecules.

This PhD thesis will discuss the phase behavior of lipid-based liquid crystals, ubiquitous in natural systems, modified with molecular additives or inorganic nanoparticles to build-up stimuli-responsive nanodevices, with end-use in the biomedical field as drug-delivery vehicles (DDs).

In **Chapter 1**, I will provide a general introduction on lyotropic mesophases, with a short theoretical description of the curvature associated to the amphiphilic film. I will then address the interaction of these mesophases with nanoparticles and additives, to monitor their effects on the diffusive properties of molecules confined within the liquid crystals. **Chapter 2** will examine the main techniques used for this research work, as well as the theoretical descriptions and the experimental conditions. **Chapter 3** will summarize the main results of the project, and it will consist of two parts: *part I* will deal with the phase behavior and the physico-chemical properties of lyotropic liquid crystals, doped with Superparamagnetic Iron Oxide Nanoparticles (SPIONs) or gold nanoparticles (AuNPs); *part II* will present the application of lyotropic lipid liquid crystals as DDS, i.e., the structural change induced by sugar esters (Sucrose Stearate (SS)), lipids and oils (DOPG and tetradecane). Finally, **chapter 4** will report the conclusive remarks and introduce possible future developments.

The last part of this thesis consists of the papers – published, submitted or in preparation – connected to this research work.

## 1.1 Lyotropic Liquid Crystals (LLCs)

According to the IUPAC Gold Book<sup>[1]</sup> definition, a liquid crystal is “a substance in the liquid-crystalline state”, which corresponds to a mesomorphic state having long-range orientational order, and either partial position order or complete positional disorder (isotropic system i.e., liquid, gas and amorphous solid). The adjective "lyotropic" indicates that a liquid crystal forms by dissolving an amphiphile in a suitable solvent, under appropriate conditions of concentration, temperature, and pressure.<sup>[2]</sup> In addition to these main factors, there are many other "global" elements which temper the structure of the mesophases – such as pH, ionic strength and geometrical (local) constrains – which impart lateral stresses upon an amphiphile to encourage the adoption of one or more mesophases.<sup>[3–5]</sup>

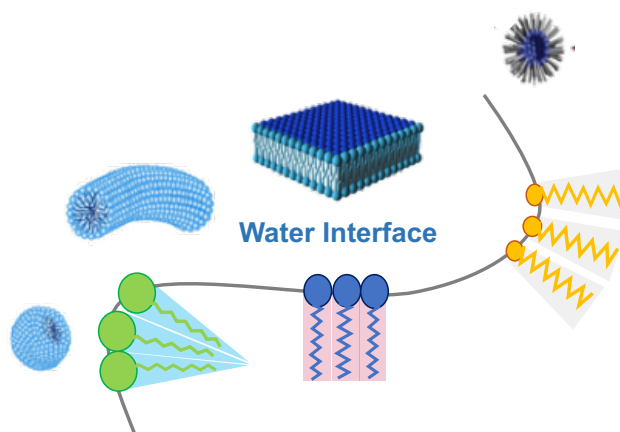


**Figure 1** Amphiphiles at water interface and their organization based on the geometry. Increasing the hindrance of hydrocarbon chains with respect to the headgroup, a variation in the spontaneous curvature can be obtained.

Regarding the latter term – based on a purely geometrical consideration of the amphiphiles through their Critical Packing Parameter (CPP) – the observed phase behavior can be partially explained in terms of direct or inverted structures  $CPP = \frac{v_0}{a_0 l_c}$  where  $v_0$  is the volume of hydrophobic part,  $a_0$  the cross-section of polar head group and  $l_c$  the length of the hydrophobic chain. However, it is

conventionally recognized that positive curvature ( $CPP < 1$ ) corresponds to the monolayer bending towards the hydrocarbon chain region and away from the water region, while negative curvature ( $CPP > 1$ ) corresponds to the bending in the opposite way.<sup>[6,7]</sup> Considering the CPP, by increasing the steric hindrance of the hydrophobic chain, a change of the spontaneous curvature can be experimentally observed at the water-amphiphile interface. Fig. 1 shows the typical structures assumed by surfactants in water: spherical micelles, rod-like structures, lamellar phases and inverted structures are the simplest nano-objects detectable. In the literature, at least six possible inverted structures are reported possessing a high level of symmetry (Figure 2).

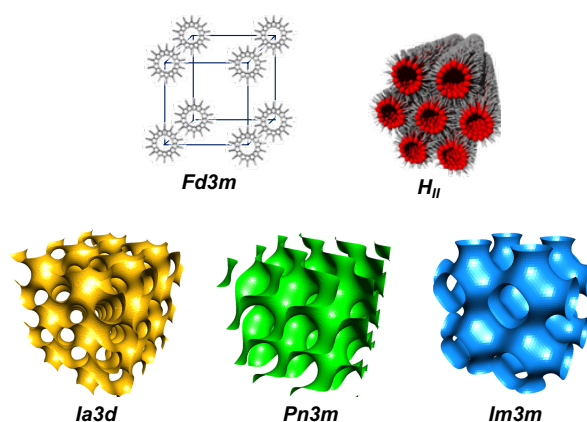


**Figure 2** Graphical representation of inverted mesophases.  $Fd3m$  corresponds to inverted micelles positioned at the edges of a cubic arrangement;  $H_{II}$  is an inverted hexagonal mesophases with water channels confined by the leaflet of lipid membrane;  $Ia3d$ ,  $Pn3m$  and  $Im3m$  correspond to the inverted bicontinuous cubic phases, respectively: gyroid, diamond and primitive cubic phase. The figure shows the IPMS representation which can be indicated also as  $Q_{II}^G$ ,  $Q_{II}^D$  and  $Q_{II}^P$ .

These are inverted structures, corresponding to inverted micelles packed in a cubic lattice (identified with  $Fd3m$  spatial group), inverted hexagonal mesophases ( $H_{II}$ ) and bicontinuous cubic mesophases ( $Q_{II}$ ). Moreover, in disordered systems, the most common assemblies are the inverted micelles, where a cubic lattice cannot be recognized due to the high volume of dispersant oil.  $Q_{II}$  is the most commonly studied lipid phase and consists of a lipid bilayer arranged on an infinite periodic minimal surface (IPMS).<sup>[8,9]</sup> Three bicontinuous cubic phases – i.e., the Schwarz diamond ( $Q_{II}^D$ ), primitive ( $Q_{II}^P$ ), and the Schoen gyroid ( $Q_{II}^G$ ) cubic phases – have been observed experimentally. In each case, the

lipid bilayer subdivides the space into two interpenetrating and interconnected water networks.<sup>[10]</sup> These mesophases are often identified with spatial groups – Pn3m, Im3m and Ia3d respectively – describing the high level of symmetry of lipid architectures. The following equations describe the complex spatial organization of the non-lamellar lipid membrane:<sup>[11]</sup>

$$f(x, y, z) = \cos\left(\frac{2\pi x}{d}\right) + \cos\left(\frac{2\pi y}{d}\right) + \cos\left(\frac{2\pi z}{d}\right) \quad (1.1) \quad \mathbf{Im3m}$$

$$f(x, y, z) = \cos\left(\frac{\pi x}{d}\right) \cos\left(\frac{\pi y}{d}\right) \cos\left(\frac{\pi z}{d}\right) + \sin\left(\frac{\pi x}{d}\right) \sin\left(\frac{\pi y}{d}\right) \sin\left(\frac{\pi z}{d}\right) \quad (1.2) \quad \mathbf{Pn3m}$$

$$f(x, y, z) = \sin\left(\frac{2\pi x}{d}\right) \cos\left(\frac{2\pi y}{d}\right) + \sin\left(\frac{2\pi y}{d}\right) \cos\left(\frac{2\pi z}{d}\right) + \sin\left(\frac{2\pi z}{d}\right) \cos\left(\frac{2\pi x}{d}\right) \quad (1.3) \quad \mathbf{Ia3d}$$

## 1.2 Energetic terms describing the mesophases

The CPP model is useful to understand most of the features of phase behavior. However, it is more complicated to make predictions, as many global factors influence the parameter.<sup>[4]</sup> Moreover, the CPP does not consider the regions of the phase diagram where there is a coexistence of different structures.

There are at least three additional energetic terms that should be taken into account to explain the phase behavior of amphiphiles: the geometrical constraint of the lipids (frustration packing energy), the curvature (free energy of elastic curvature) and the interaction with solvent (water-surfactant interaction energy). However, on an experimental level, the latter term is negligible compared to the first two terms.

### 1.2.1 Frustration Packing energy

When the lateral stress in the hydrophobic chains outweighs the one in the headgroup region, the amphiphilic monolayer curves towards the polar region, promoting the formation of an inverted monolayer. However, the formation of a bilayer from the inverted monolayer implies both a non-uniform interfacial curvature and a uniformly filled hydrophobic part; this is the origin of the frustration packing energy, related to the molecular geometry of the amphiphile. In other words, lipid molecules have to stretch or compress away from their relaxed state to fill the “voids” of the membrane. This contribution can be roughly calculated with a harmonic oscillator model,<sup>[5,12]</sup> or alternatively with molecular dynamic simulation.<sup>[13]</sup>

In this thesis, this energetic term will be recalled to interpret the main phase transitions observed for MO/SPIONs and MO/additives. The packing energy value is higher for the hexagonal phase than for the cubic mesophases, while the elastic curvature shows an opposite trend.<sup>[5,8]</sup> However, the addition of nanoparticles and additives – depending on their hydrophobic/hydrophilic nature – modifies the main terms describing the bilayer, allowing the modulation of both parameters to control the structure.

### **1.2.2 Free energy of elastic curvature**

Concerning the elastic curvature ( $g_c$ ), it is defined by the equation (1.4) below, in agreement with the theory proposed by Helfrich<sup>[14]</sup> reducing the system to an infinitely thin elastic surface:

$$g_c = 2\kappa(H - H_0)^2 + \kappa_G K \quad (1.4)$$

where  $H_0$  is the spontaneous mean curvature of the relaxed surface determined by the lateral stress,  $\kappa$  the bending modulus,  $\kappa_G$  the Gaussian modulus,  $H$  the mean curvature calculated as the average of the two-principal curvatures ( $c_1$  and  $c_2$ ), and  $K$  the Gaussian curvature given by the product of  $c_1$  and  $c_2$ . The membrane elasticity may be interpreted as the energy needed to deform the membrane provoking a deviation from  $H_0$ . The bending and Gaussian moduli are typically different for each lipid film and should be determined experimentally. However, this description is useful to calculate the elastic energy of a monolayer. Helfrich's equation (1.4) is mathematically the same for a bilayer, although the associated parameters change as reported below:

$$H_0^b = 0 \quad (1.5)$$

$$\kappa^b = 2\kappa \quad (1.6)$$

$$\kappa_G^b = 2(\kappa_G - 4\kappa H_0 l) \quad (1.7)$$

where the bilayer is taken to be symmetric, and  $l$  is the monolayer thickness. From these equations one can deduce that the bending modulus is always positive both for monolayers and bilayers, while the situation for the Gaussian modulus is more complicated. Its value is predicted to be negative for monolayer inverted systems and smaller than the bending modulus in absolute value, while

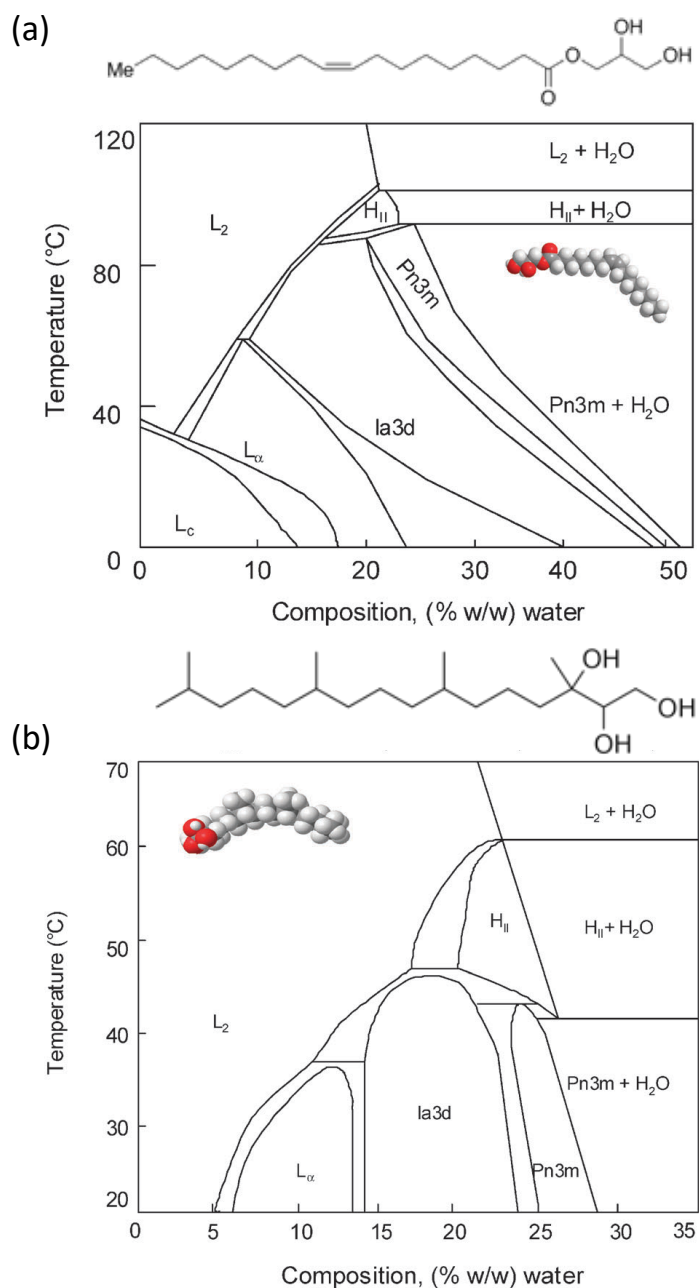
the Gaussian modulus seems to be positive and probably larger in magnitude than the other term.

The bending moduli decrease with a temperature increase both for monolayers and bilayers. Less is known about the Gaussian modulus as, especially for the bilayer term, all the parameters expressed in equation (1.7) depend on temperature.

## 1.3 Self-Assembly of cubic mesophases

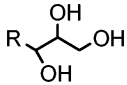
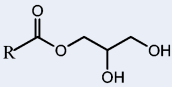
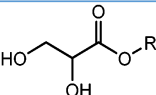
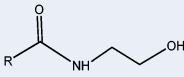
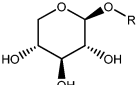
1-monoolein (MO) is a glycerol monoester, a biocompatible and biodegradable lipid, acknowledged by the Food and Drug Administration as "*generally recognized as safe*" and used in the food industry as an emulsifier.<sup>[15]</sup> MO can assemble into lyotropic liquid crystals, showing a very rich polymorphism (see Figure 3a) as a function of water content and temperature. Increasing the water amount at room temperature, different mesophases – *i.e.*, Lamellar crystalline phase ( $L_C$ ) and Lamellar fluid phase ( $L_\alpha$ ) – can be detected; above 25%wt, MO exhibits gyroid ( $Q^G_{II}$ ) and diamond ( $Q^D_{II}$ ) bicontinuous cubic mesophases. Above room temperature, the inverted hexagonal mesophase ( $H_{II}$ ) can be observed around 80 °C, and inverted micelles ( $L_2$ ) around 100 °C. These structures exhibit a typical diffraction pattern detected through small-angle scattering techniques (see Chapter 2), allowing us to determine the investigated structure univocally. The cubic diamond region is of interest, because it is thermodynamically stable in excess water. Increasing the water amount, no structural change can be observed, and the system stays at the maximum hydration level. The polyalcohol ohytantriol (Phyt)<sup>[16]</sup> presents a similar structural organization and rich phase behavior in water as the MO/H<sub>2</sub>O system, as shown in Fig.3b. Slight differences in the phase diagrams can be explained in terms of bilayer curvature (see par. 1.2 in this Chapter). Indeed, at the maximum hydration level, Phyt/water shows a smaller lattice parameter and, consequently, smaller water nanochannels than the MO/water mesophase. Additionally, the phase transition temperature from cubic to hexagonal is around 50 °C: this is an effect of the more negative curvature of the Phyt bilayer compared to MO.

The coexistence of both hydrophobic and hydrophilic domains of the mesophases makes these materials attractive for the biomedical field and in particular for the uptake and release of bioactive molecules with spatial and temporal control.



**Figure 3** Molecular Structure and Phase Diagram of 1-monoolein as function of temperature and water composition. Reproduced from reference<sup>[4]</sup> with permission from The Royal Society of Chemistry.

The ability to assemble in cubic mesophases is not a prerogative of 1-monoolein or phytantriol. Molecules like glycerate, monoethanolamide and glycolipids can assemble in non-lamellar mesophases. Table 1 reports few cases studied in literature; more examples are extensively reported in this review<sup>[4]</sup>.

Table 1: Headgroup, structure, tails and phase sequences increasing the temperature of the main molecules able to assemble in Non-Lamellar mesophases			
Headgroup	Structure	Tails	Phase Sequence (excess H <sub>2</sub> O)
<i>Alcohol</i>		Phytanyl	Q <sup>D</sup> <sub>II</sub> →H <sub>II</sub> →L <sub>2</sub>
<i>Monoacylglyceride</i>		C14:c9 (MM) C18:c9 (MO) Phyt	L <sub>α</sub> →Q <sup>D</sup> <sub>II</sub> →L <sub>2</sub> Q <sup>D</sup> <sub>II</sub> →H <sub>II</sub> →L <sub>2</sub> H <sub>II</sub> →L <sub>2</sub>
<i>Glycerate</i>		C18:c9 Phyt	Q <sup>D</sup> <sub>II</sub> →H <sub>II</sub> →L <sub>2</sub> H <sub>II</sub> →L <sub>2</sub>
<i>Monoethanolamide</i>		C18: c9 C18: c9, c12 C18: c9, c12, c15 Phyt	Q <sup>D</sup> <sub>II</sub> →L <sub>2</sub> Q <sup>G</sup> <sub>II</sub> →Q <sup>D</sup> <sub>II</sub> →L <sub>2</sub> Q <sup>G</sup> <sub>II</sub> →Q <sup>D</sup> <sub>II</sub> →L <sub>2</sub> Q <sup>D</sup> <sub>II</sub> →H <sub>II</sub> →L <sub>2</sub>
<i>Glycolipid: β-Xyloside</i>		*C <sub>14+3</sub> *C <sub>16+4</sub> *C <sub>18+4</sub>	L <sub>α</sub> L <sub>c</sub> →Q <sub>II</sub> →H <sub>II</sub> Q <sub>II</sub> →H <sub>II</sub>

\*C<sub>f+g</sub> denote isoprenoid chains where f is the number of carbon atoms of the main chains, while g is related to the number of methyl branches.

## 1.4 Effects of Nanoparticles on cubic mesophases

We will consider hybrid systems from nanoparticles and non-lamellar lipid membranes, designed with the final purpose of combining the physico-chemical properties of nanoscale inorganic materials and the features of lipid architectures. In the literature, the quantum confinement properties of nanoparticles<sup>[17–19]</sup> are extensively described: i.e. plasmonic properties of gold and silver nanoparticles, or enhanced fluorescent properties of quantum dots, or magnetic responsivity of iron oxide nanoparticles, making such systems attractive platforms to build up new functional responsive materials not available on the macro-scale. These features are attractive for biomedical

applications as drug-delivery systems (DDs),<sup>[20]</sup> imaging<sup>[17]</sup> and magnetic resonance imaging (MRI).<sup>[21,22]</sup>

The hydrophobic or hydrophilic nature of NPs – depending on the capping agents – is a crucial factor to determine their localization in a lipid assembly. As previously described, non-lamellar lipid assemblies exhibit both hydrophobic and hydrophilic domains, able to host NPs of different nature. The inclusion of NPs in the lipid architecture will affect the physico-chemical and structural properties of the scaffold, modifying for instance its fluidity, bending properties, local thickness, the phase behavior and the viscoelastic properties.

For instance, the inclusion of hydrophobic superparamagnetic iron oxide NPs (SPIONs) in a liposome bilayer affects the average thickness of the membrane, the orientation of the phospholipid chains and the lipid melting temperature.<sup>[23,24]</sup> The inclusion of nanoparticles can also modify the final structure of the bilayer; for instance, a Cryo-TEM investigation by Chen *et al.*<sup>[25]</sup> on liposomes containing hydrophobic SPIONs, has highlighted the formation of liposomal aggregates, with SPIONs clusters acting as bridging agents. These local perturbations highlight the fact that some structural rearrangement of a planar lipid membrane can be possible preserving the overall lipid mesophase architecture. However, as reported by Briscoe *et al.*<sup>[26]</sup>, the inclusion of NPs in significant amounts might promote – in certain conditions – a transition from lamellar to hexagonal mesophases.

The inclusion of NPs into non-lamellar lipid assemblies mostly affects the mesophase structure in terms of lattice parameter, and therefore both the water amount and the size of aqueous nanochannels. If the NPs size is similar or smaller than the lattice parameter, the NPs remain entrapped between the leaflets of the membrane. Venugopal *et al.*<sup>[27]</sup> described the effects of encapsulating SiNPs of 8 nm diameter into a monolinolein mesophase. In this case, the NPs were too large to be encapsulated in the nanochannels (3.0-3.8 nm in diameter). Moreover, the addition of NPs determines an overall dehydration of the lipid scaffold causing – at high concentrations – the transition to a gyroid cubic structure (Ia3d). The authors interpret this behavior considering that, since the energy cost to include the NPs in the nanochannels is too high (above 100  $k_B T$ ), the NPs minimize their interfacial energy, aggregating along the grain boundaries of the mesophase, similarly to what reported for the lamellar bilayer.<sup>[28]</sup>

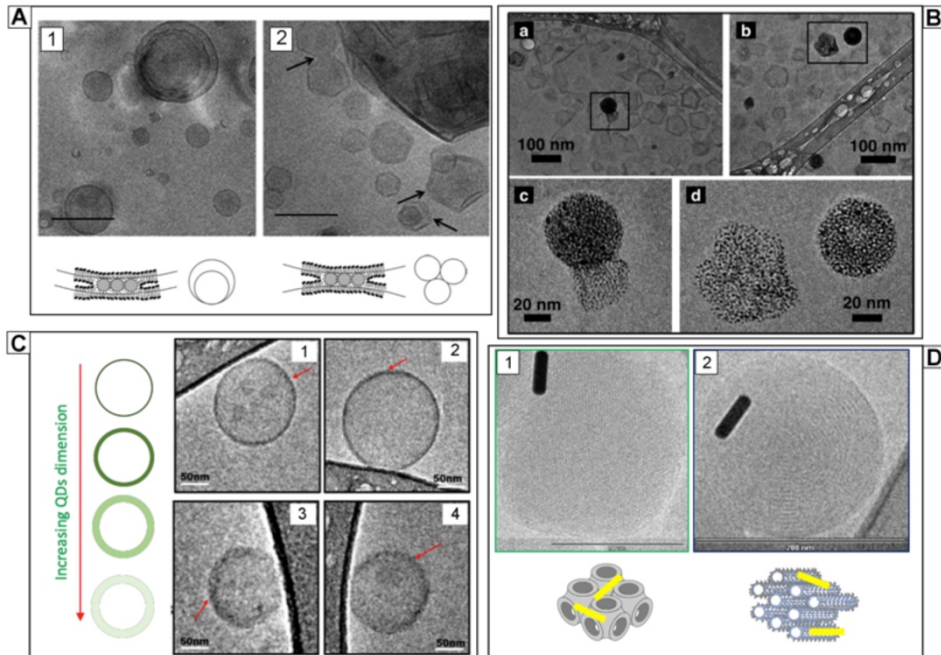


**Figure 4** Cryo-Microscopies of Lamellar and Non-Lamellar Lipid membranes assembled with hydrophobic NPs. Panel (A): Cryo-TEM images highlighting the structural changes induced by hydrophobic SPIONs interacting with liposomes: on the left, TEM image showing liposomes arranged in a multiwalled configuration with SPIONs bridging; on the right, TEM image of liposomes' aggregates bridged by SPIONs clusters embedded in the bilayer. Adapted with permission from Ref.<sup>[25]</sup>, copyright (2010) American Chemical Society. Panel (B): DPPC liposomes decorated with dodecanethiol-capped AuNPs shown at different magnifications. Adapted with permission from Ref.<sup>[29]</sup>, copyright (2017) American Chemical Society. Panel (C): TEM images of POPC/POPE liposomes assembled with Quantum Dots (QDs) of different sizes embedded in the bilayer. The size increase of QDs (from 1 to 4 progressively) increases the perturbation of the lipid membrane: this appears sharp when small QDs are included (1 and 2), while with the larger ones the membrane becomes fuzzier (3 and 4). Reproduced from Ref.<sup>[30]</sup> with permission from The Royal Society of Chemistry. Panel (D): Cryo-SEM of non-lamellar mesophases interacting with Au NRs. On the left: phytantriol cubic mesophase, on the right phytantriol hexagonal mesophase, both assembled with Au NRs. Adapted with permission from Ref.<sup>[31]</sup>, copyright (2012) American Chemical Society. Reprinted from reference<sup>[32]</sup>. Reproduced by permission of The Royal Society of Chemistry.

The same authors also investigated the structural features of monolinolein mesophases loaded with hydrophilic SPIONs. Upon application of

a static magnetic field, a reorganization of the lipid domains along the direction of the field<sup>[33,34]</sup> was found, highlighting how the responsiveness of SPIONs to magnetic fields can be exploited to modify the whole lipid mesophase. This effect has been applied, for instance, to control the release of drugs confined in the lipid mesophases<sup>[33]</sup> or for applications in optical memory storage.<sup>[35]</sup>

Conversely, hydrophobic NPs localize spontaneously in the hydrophobic domains of the non-lamellar mesophases, led by the affinity of NPs for the lipid chains;<sup>[36,37]</sup> in this case, the size is of paramount importance to avoid the disruption of the lipid scaffold.

In the literature, very few examples address the inclusion of non-spherical NPs in non-lamellar lipid assemblies; Boyd et al.<sup>[38]</sup> reported on hydrophobic NRs included in phytantriol, selachyl alcohol and monoolein lipid mesophases, aiming to build up photo-responsive hybrid materials. The authors investigated the effect of NRs on the cubic mesophases, evidencing a slight reduction in the phase transition temperature and the lattice parameter. Interestingly, similarly to spherical hydrophobic NPs, gold NRs shift the cubic-to-hexagonal boundaries to lower temperatures.<sup>[31]</sup> For hexosomes of selachyl alcohol interacting with AuNRs, the lattice parameter or water volume fraction<sup>[39,40]</sup> does not change with respect to the neat mesophase. The authors suggest that NRs are positioned along the axis of hexosomes but – due to their large sizes – they are in proximity of the lipid bilayer, without being efficiently included inside it. Nevertheless, irradiation of the hybrid structure with NIR laser promoted the phase transition from cubic to hexagonal phase, similarly to what observed for the application of AMF on monoolein-SPIONs hybrids.

## **1.5 Effects of additives on cubic mesophases**

The structure and the physico-chemical features of lyotropic liquid crystals can be finely tuned, doping the lipid membrane with additives of different nature. The addition of molecules – similar or bigger in size – to the building blocks of hierarchical assemblies will be treated in the next subparagraphs, describing how they affect the phase behavior, as well as the advantages and disadvantages of their technological applications.

### **1.5.1 Molecules assembled with lipids**

The addition of molecular compounds to the mesophases affects the structural properties and their related physico-chemical features (see paragraph

1.6). Thus, the inclusion of different kinds of molecules can be a useful approach to tune the mesophases and to choose the best conditions for each technological purpose. The addition of different chemical compounds than lipids promote – above a “critical” concentration – a phase transition. Moreover, the addition of molecules with responsivity to the pH, UV-Vis light, magnetic field and ionic strength, imparts the same responsivity, promoting a structural change. Even in this case, the packing and curvature energy can explain the complex phase behavior of lipid/additives mixed systems.

A more accurate description of the effects promoted by molecular additives on the curvature – and consequently on the structural parameter of the mesophase – can be obtained by distinguishing the additives in hydrophobic and amphiphilic. Hydrophobic molecules generally interact mainly with the hydrophobic chains of lipids, increasing the volume of the hydrophobic portion; thus, the curvature increases, becoming more negative and promoting a transition from cubic to inverted hexagonal phases. However, this is true for relatively low concentrations of oils,<sup>[8,41–43]</sup> above a certain fraction of hydrophobic additive, the oil-lipid mixture assembles into bicontinuous cubic micelles (Fd3m symmetry) or inverted micelles.<sup>[44,45]</sup> In other words, the water nanochannels of the mesophases become progressively smaller until the dispersant oil separates the water domains through a surfactant monolayer. However, there are literature reports on these effects also in the case of fatty acids<sup>[46–49]</sup> or vitamin E,<sup>[50]</sup> thus, hydrophobic additives are not necessarily oils. For instance, oleic acid is a surfactant with a small headgroup. Thus, its behavior will be similar to that displayed by oils, and for this reason it can be classified as a hydrophobic additive. It is of relevance to evaluate also the effects of active hydrophobic molecules on the structure of the cubic mesophases as reported by Drummond *et al.*<sup>[51]</sup> or also the enzymes modifying the lipid organization.<sup>[52]</sup>

Amphiphiles interact with the lipid membrane locating themselves spontaneously at the interface; however, the final effects are a combination of the chemical composition of the surfactant film and of the hindrance of hydrophobic chains. Mezzenga *et al.*<sup>[53]</sup> have reported the effect of a sugar ester, sucrose stearate, on the structure of the mesophases. Considering a larger volume of headgroup with respect to the hydrophobic chains, and the propensity to form hydrogen bonds with water, the diamond cubic structures is swollen into a primitive cubic mesophases where the diameter of the nanochannels is larger. However, other amphiphiles are reported in literature,

e.g. caproic acid combined with 1,2-dilauroyl-sn-glycero-3-phosphocholine (DLPC) or 1,2-distearoyl-sn-glycero-3-phosphocholine (DSPC),<sup>[54]</sup> 1,2-dioleoyl-sn-glycero-3-phospho-(1'-rac-glycerol) (DOPG),<sup>[55,56]</sup> which can promote a transition in mesophases presenting a less negative curvature, until the lamellar phases.

As a general rule, the inclusion of hydrophobic compounds stabilizes the mesophases (hexagonal mesophases and inverted micelles) that would present a higher frustration packing energy in the absence of the doping agent, promoting a more negative curvature of the bilayer. Conversely, the inclusion of amphiphiles promotes the transition to a swelled cubic phase and eventually to lamellar stacks. These considerations can be useful to classify the behavior of stimuli-responsive additives included into the bilayer; indeed, photochromic molecules,<sup>[57–62]</sup> oleic acid and charged lipids can be used to build up liquid crystals sensitive to light (by changing the molecular conformations) or to pH<sup>[63–68]</sup> or ionic strength<sup>[69]</sup> (by changing the ratio of the hydrophobic and hydrophilic molecular volumes). In this way, by means of external stimuli, an additive can impart its hydrophobic or amphiphilic behavior promoting structural changes.

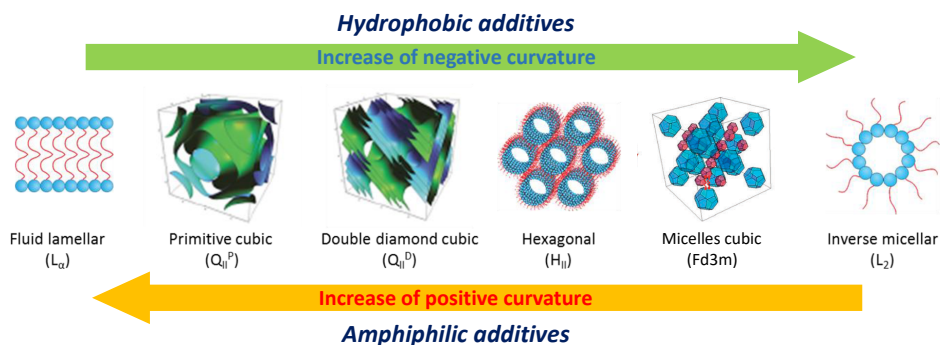


**Figure 5:** Increasing the concentration of hydrophobic additives embedded into the mesophases, transitions to liquid crystals with higher negative curvature are promoted. However, increasing the concentration of amphiphilic compounds, the positive curvature systems are promoted until the lamellar phase. Readapted with permission from reference<sup>[54]</sup>.

### 1.5.2 Synthetic macromolecules interacting with lipid assemblies

One of the breakthroughs in the field of lipid LCs concerns their interaction with amphiphilic block copolymers. In particular, with the appropriate energy input, some copolymers promote the dispersion of lyotropic liquid crystals in a colloidal system (LCDs) whilst retaining an internal liquid crystalline structure of the

particles.<sup>[70]</sup> Based on the internal structure, the colloidal particles are termed cubosomes (colloids showing a cubic structure) or hexosomes (showing a hexagonal array). Their final hydrodynamic diameter depends on the chemical nature of the polymers and on the energy applied to disperse the system; generally, cubosomes are around 200-250 nm<sup>[70,71]</sup> even if dispersed systems on microscale are reported.<sup>[72]</sup> The most frequently used dispersants are Pluronic®, a commercial group of triblock copolymers composed by poly-ethylene oxide – poly-propylene oxide (PPO) – poly-ethylene oxide (PEO-PPO-PEO) blocks. While the PEO blocks represents the hydrophilic parts, interacting with the water environment, PPO is the hydrophobic block and interacts with the lipid bilayer.<sup>[71,73–76]</sup>

The most important criteria to select a stabilizing agent for cubosomes are related to the minimum amount of polymer needed to stabilize a given amount of mesophase, the promotion of stability for an extended period of time and a limited effect on the structure of the internal phase.<sup>[77]</sup> One of the essential parameters of the PEO domain is the length of the unit. Generally, short PEO block fail to achieve dispersion of LC particles, while for more extended PEO units, the LCDs formulation shows both Im3m and Pn3m structures. Moreover, the triblock copolymers should have a cloud point >100 °C, in order to avoid phase separation produced by the dehydration of PEO units. In summary, for the Pluronic series an EO% over 50% and a molecular weight greater or equal to 6500 are necessary to stabilize the dispersion.

Several reports concern the use of Tween 80, whose hydrophilic part is a polysorbate moiety, while the hydrophobic region is a C18 unsaturated chain. The stabilization with Tween 80 affects the internal structure, promoting a transition to primitive mesophase for the Phyt assemblies,<sup>[78]</sup> while for MO – due probably to the similarity of the hydrophobic chains – the diamond cubic structure is still preserved.

Aiming to build up multifunctional LCDs as DDs, the design of functional stabilizers providing both colloidal stabilization and the ability to control the internal nanostructure can be useful to vary the physico-chemical properties of the dispersion and their interactions with cell membranes. Zhai et al.<sup>[79]</sup> have synthesized a brush copolymer, composed by a hydrophobic C12 chain and an hydrophilic poly-(ethylene glycol)-methyl ether acrylate (PEGA) with a multiple 9 units of PEO brushes with various molecular weight.

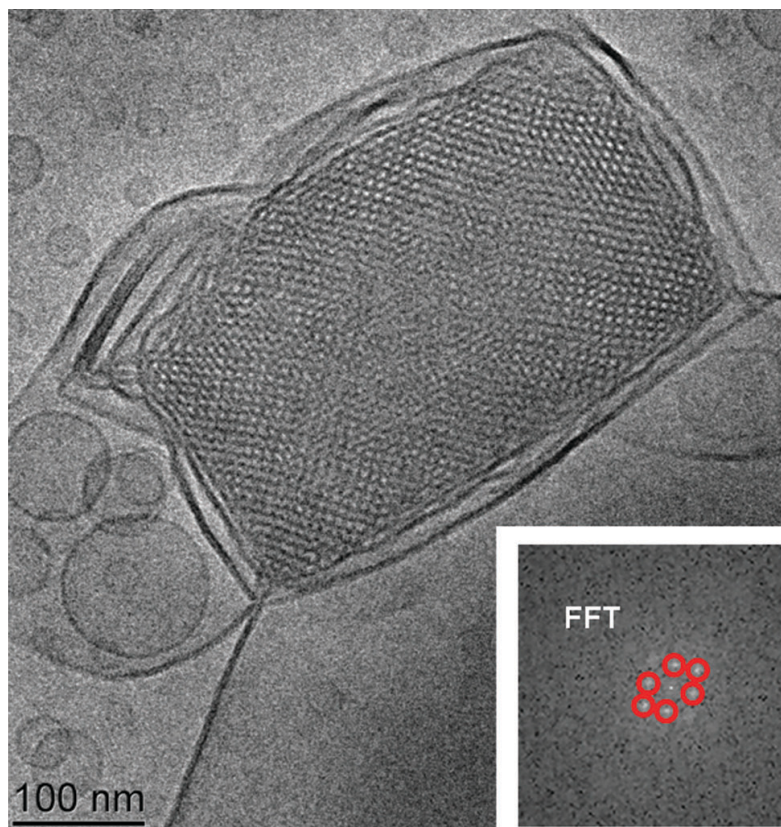


**Figure 6** Cryo TEM image of cubosomes stabilized by Pluronic F127. Reprinted from reference<sup>[80]</sup> published by The Royal Society of Chemistry.

## 1.6 Confinement features of LLCs

To apply these materials in the biotechnological field as drug-delivery systems, a precise knowledge of the molecular transport properties in cubic liquid crystals has been the subject of several reports.<sup>[53,81,82]</sup> Many factors determine the final diffusive properties of guest molecules, *e.g.*, the chemical nature of active therapeutics, their size compared to the diameter of channels, or even the symmetry of liquid crystals.<sup>[83]</sup> Thus, a diffusion model applicable to real applications – *i.e.*, in vivo experiments<sup>[84,85]</sup> – would be needed in order to predict the release of different bioactive molecules. To describe the diffusive properties one should consider that water features dramatically change when confined in nanoscale domains; the freezing point temperature<sup>[86,87]</sup> is one example, but the most important – to apply LLCs as DDs – are the slow down motions. Since water

molecules are located in different local environments, where they engage in different types of interactions; the bound water is considerably slowed down compared to bulk water, some others water molecules show more bulk-like properties due to mainly interactions with other water molecules (the so called “pseudo-bound” exhibiting a faster motion).<sup>[88,89]</sup> Indeed, the slow diffusion component has been ascribed to the water molecules bound to the hydrophilic headgroups. The interaction with lipids causes a structural ordering of the closest water molecules, which is particularly evident at temperatures below the gel-to-liquid phase transition of the lipid bilayers. Thus, based on the proximity of the water to the membrane, it can be classified as pseudo-bound water.<sup>[90]</sup>

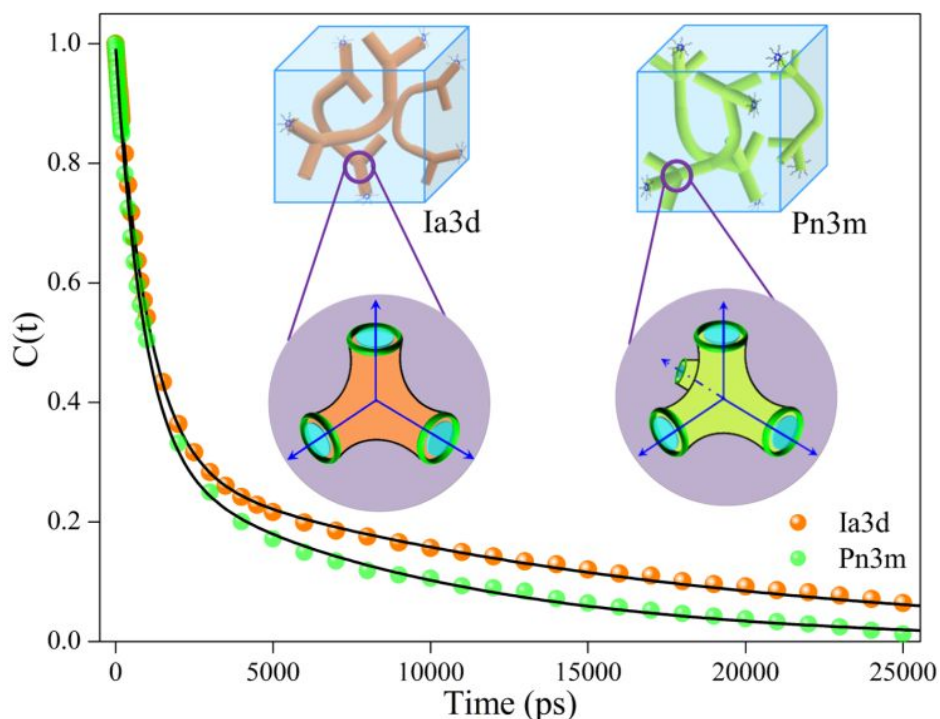


**Figure 7** Correlation function of fluorophore released from bicontinuous cubic phase. Slightly differences are detectable between Ia3d and Pn3m structure. Reprinted with permission from reference <sup>[88]</sup>.

The curvature affects the diffusive properties of water embedded in liquid crystals: the hydration dynamics of Ia3d nanochannels is significantly slower than in the Pn3m phase. Probably, as the curvature becomes more negative, the energy of elastic curvature becomes higher, and consequently a

higher hydrophobic packing stress in the Ia3d phases restricts the flexibility of the lipid headgroups. This effect produces lower mobility of water, which is hampered to diffuse in Ia3d more than the Pn3m phase.<sup>[88]</sup> However, when the inhomogeneities are not relevant, the diffusion is determined by the size of the diffusion domain with no difference between Ia3d, Pn3m, and Im3m. When the confinement seems to be significant, the presence and extent of bottlenecks become the first term describing the diffusive profiles<sup>[11]</sup>.



## 2

# Materials and Methods

This section will describe sample preparation and will introduce the experimental techniques used to characterize soft matter assemblies in the presence of inorganic nanoparticles and molecular additives. Each paragraph presents a concise instrumental description and a short theoretical background of the method, together with an introduction to data analysis to obtain the structural parameters describing the systems.

## 2.1 Materials Preparation

### 2.1.1 Synthesis of Superparamagnetic Iron Oxide Nanoparticles

Iron oxide nanoparticles were synthesized according to the protocol reported by Wang et al.<sup>[91,92]</sup> Briefly, 0.71 g  $\text{Fe}(\text{acac})_3$  (2 mmol) were dissolved in 20 mL of phenyl ether with 2 mL of oleic acid (6 mmol) and 2 mL of oleylamine (4 mmol) under nitrogen atmosphere and vigorous stirring. 1,2-hexadecanediol (2.58g, 10 mmol) was added into the solution. The solution was heated to 210 °C, refluxed for 2 h and then cooled to RT. Ethanol was added to the solution and the precipitate collected, washed with ethanol and re-dispersed in 20 mL of hexane in the presence of 75 mM each of oleic acid and oleylamine. A stable dispersion of the magnetic SPIONs with a hydrophobic coating of oleic acid and oleylamine in hexane was obtained.

### 2.1.2 Synthesis of Gold Nanoparticles

Hydrophobic gold nanoparticles were synthesized according to the protocol reported by Brust et al.<sup>[93]</sup> Briefly, an aqueous solution of  $\text{HAuCl}_4$  (30 mL, 30 mM) was mixed with a solution of tetraoctylammonium bromide (TOAB) in toluene (80 mL, 50 mM). The two-phase mixture was vigorously stirred until all the gold-(III) compound was transferred into the organic layer. Then, dodecanethiol (170 mg) was added to the organic phase. A freshly prepared aqueous solution of sodium borohydride (25 mL, 0.4 M) was slowly added with vigorous stirring. After 3 h stirring, the organic phase was separated, evaporated

to 10 mL in a rotavapor and mixed with 400 mL ethanol to remove excess thiol. The mixture was kept for 24 h at 18 °C and the dark brown precipitate was filtered off and washed with ethanol. The crude product was dissolved in 10 mL toluene and again precipitated with 400 mL ethanol. Then, the twice washed precipitated was dispersed in 20 mL hexane.

### 2.1.3 Preparation of bulk cubic phases

Bulk cubic phases with or without SPIONs and AuNPs were prepared according to the following procedure: 30 mg of MO (or Phyt) were weighted in 2 mL glass vessels in the absence (for neat cubic mesophases) or in the presence (for NPs-loaded cubic mesophases) of appropriate volumes of SPIONs and AuNPs dispersions in hexane. About 1 mL of hexane was used to solubilize the mixtures, then the solvent was removed under a gentle nitrogen flux. The dry films were left under vacuum overnight, then hydrated with 50  $\mu$ L Milli-Q water and centrifuged ten times, 5 min each time, at 9000 rpm, alternating a run with the cap facing upward with another with the cap facing downward.

Samples containing an amphiphilic additive (Chapter 3 paragraph 3.6) were prepared following the same procedure described earlier, adding the proper amount of additive before drying with nitrogen flux. In the case of hydrophilic compounds (paragraph 3.7), a previously prepared aqueous solution of the additive was used to hydrate the lipid film instead of pure water.

### 2.1.4 Preparation of dispersed liquid crystals

For the preparation of cubosomes, first an MO or MO-NPs film was obtained, as described in 2.1.3. Briefly, 8 mg of Pluronic F-127 were added to the dry films and the mixture was heated in a water bath at 70 °C for 5' to melt the polymer and then vortexed for 5'. Five cycles of heating/vortexing were carried out and then 500  $\mu$ L of preheated H<sub>2</sub>O at 70 °C were added. The dispersion was then sonicated in a bath-sonicator at (59 kHz and 100%) of power for 6 h, to homogenize the system.

## 2.2 Small-Angle X-Ray Scattering (SAXS)

For many years, small-angle scattering techniques have been widely used to study polymers, surfactants, nanostructures and liquid crystals. Both static and dynamic information could be obtained – *i.e.*, the structure of liquid

crystals and the size and shape of the nanoparticles – as well as the structural changes induced upon an external stimulus for in-situ detection of the investigated systems.

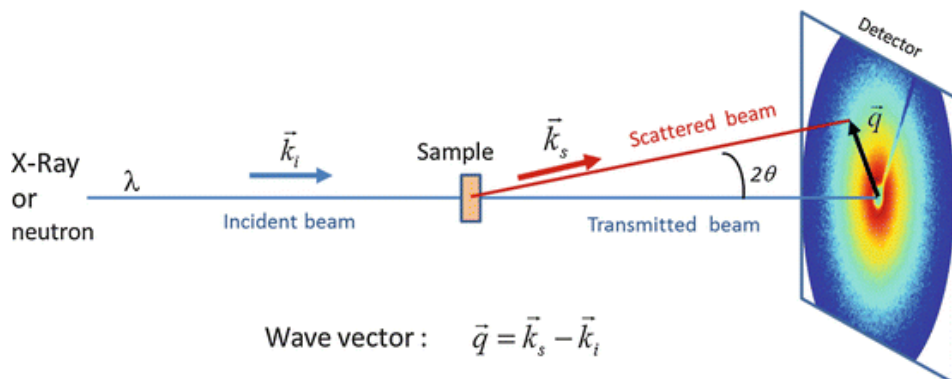


**Figure 8** Geometry of a small-angle X-ray scattering experiment. The incident beam hits the sample and the pattern of scattered X-rays (assuming elastic scattering) is revealed with a 2D detector. The modulus of the wave vector  $q$  is defined as  $4\pi\sin(\vartheta)/\lambda$ , with  $2\vartheta$  being the angle between the incident and scattered beams.

The small-angle X-ray scattering techniques were originally developed to obtain information on the mesoscale of proteins, polymers, types of cement, and amphiphilic assembled structures. Based on an X-ray beam focused on the sample, the recorded elastic scattering contribution in a small angle range (0.1–4°), allows extracting information about size, shape, distribution, and orientation of the investigated samples. The methods are accurate, generally non-destructive and – despite this is not being true for every instrument – the investigation in a small angle range (generally to the LSF) is possible.

In-house SAXS measurements were carried out on an S3-MICRO SWAXS instrument (HECUS GmbH, Graz, Austria) consisting of a GeniX microfocus X-ray sealed Cu K $\alpha$  source (Xenocs, Grenoble, France);  $\lambda = 0.1542$  nm; maximum power 50 W. The instrument is equipped with two one-dimensional (1D) position-sensitive detectors (HECUS 1D-PSD-50 M system). Each detector is 50 mm long (spatial resolution 54  $\mu\text{m}/\text{channel}$ , 1024 channels) and covers the SAXS  $q$ -range ( $0.009 < q < 0.6 \text{ \AA}^{-1}$ ) and the WAXS  $q$ -range ( $1.2 < q < 1.9 \text{ \AA}^{-1}$ ). The temperature was controlled using a Peltier TCCS-3 Hecus system.

Small-angle X-ray scattering was used in this work to characterize the structure of lyotropic liquid crystals under different constraints. First, all the

nanoparticles synthesized during this PhD project (both SPIONs and AuNPs) were characterized by extracting their size and polydispersity. To this end, raw SAXS data were first reduced by subtracting the contribution of the solvent and the cell, to obtain a plot of the scattered intensity  $I(q)$  as a function of the scattering vector modulus  $q$ . Such curves were then analyzed using the software Igor Pro (Wavemetrics Inc.) and the set of mathematical models provided by NIST.<sup>[94,95]</sup>

The experimental curves obtained for nanoparticles dispersions were modelled using a function representing the scattering of spherical objects with uniform scattering length density (SLD); real samples of nanoparticles always present a certain size polydispersity, which can be interpreted through a Schulz distribution (Eq. 2.1):

$$f(R) = (z + 1)^{z+1} x^z \frac{\exp [-(z + 1)x]}{R_{avg} \Gamma(z + 1)} \quad (2.1)$$

where  $R_{avg}$  is the mean radius,  $x=R/R_{avg}$ ,  $z$  is related to the polydispersity  $p=\sigma/R_{avg}$  by  $z=1/(p^2-1)$ ;  $\sigma^2$  is the variance of distribution. The scattering intensity  $I(q)$  is modeled as described by Eq. 2.2:

$$I(q) = \left(\frac{4\pi}{3}\right)^2 N_0 \Delta\rho^2 \int_0^\infty f(R) R^6 F^2(qR) dR \quad (2.2)$$

where  $N_0$  is the total number of particles per unit volume, and  $\Delta\rho$  is the difference in scattering length density,  $F(qR)$  the scattering amplitude for a sphere reported in Eq.2.3:

$$F(qR) = \frac{3[\sin(qR) - qR\cos(qR)]}{(qR)^3} \quad (2.3)$$

No interparticle interference effects are included in this calculation.

Moreover, the SAXS technique was used to investigate the structure of lyotropic liquid crystals and phase transition induced by nanoparticles. Eq. 2.4 was used to calculate the lattice parameter ( $d$ ) of lyotropic liquid crystals:

$$|q| = \left(\frac{2\pi}{d}\right) \sqrt{h^2 + k^2 + l^2} \quad (2.4)$$

where (hkl) are Miller indexes related to the considered structures. In a Pn3m structure these are (110), (111), (200), (211), (220)...; in an Im3m structure they are (110), (200), (211), (310), (321)... while in H<sub>II</sub> mesophases are (100), (111), (200)...

From the preliminary information obtained by SAXS curves (*i.e.*, the type of structure and the lattice parameter), it is possible to estimate the size of the water nanochannels as well as the volume fraction of water hydrating the lipid membrane. Eq. (2.5)<sup>[53]</sup> was used to calculate water channel radii  $r_w$  in Pn3m and Im3m cubic phases while Eq. (2.6)<sup>[96]</sup> was used to calculate the water volume fraction  $\varphi_w$ :

$$r_w = \sqrt{\left(-\frac{A_0}{2\pi\chi}\right)d - l_c} \quad (2.5)$$

$$\varphi_w = 1 - 2A_0\left(\frac{l_c}{d}\right) - \frac{4}{3}\pi\chi\left(\frac{l_c}{d}\right)^3 \quad (2.6)$$

where  $A_0$  and  $\chi$  are topological parameters, respectively the ratio of the area of the minimal surface in a unit cell to (unit cell volume)<sup>2/3</sup> and the Euler–Poincare characteristic. For the diamond cubic mesophase (Pn3m) these are  $A_0=1.919$  and  $\chi=-2$ , while for Im3m mesophases they are  $A_0=2.432$  and  $\chi=-4$ . Equations (2.7)<sup>[96]</sup> and (2.8)<sup>[97]</sup> describe the water channel radii ( $r_w$ ) and water volume fraction ( $\varphi_w$ ) for an hexagonal phase H<sub>II</sub> respectively:

$$r_w = \frac{0.5256d - l_c}{0.994} \quad (2.7)$$

$$\varphi_w = \frac{2\pi r_w^2}{\sqrt{3}d^2} \quad (2.8)$$

The chain length  $l_c$  was assumed constant in the 25-50 °C range with a value of about 9 Å<sup>[50]</sup> in Phyt systems and around 1.6 nm<sup>[98]</sup> in the case of MO.

The effects of temperature were evaluated to report the thermotropism of LCs doped with inorganic nanoparticles and additives. All the experiments were performed after the samples had reached the thermodynamic equilibrium (after one day). SAXS measurements executed at the large-scale facilities (LSF) (SAXS beamline in Elettra, Trieste, Italy and ID02 instrument in ESRF, Grenoble,

France), were performed to study the *in-situ* structural changes induced by AMF on the hybrid systems composed by responsive nanoparticles. In particular, the colloidal dispersion of cubosomes and magnetocubosomes (cubosomes doped with SPIONs) were investigated on LSF due to the slight difference between the Scattering Length Density (SLD) of lipid and water.

## 2.3 Dynamic Light Scattering (DLS)

DLS measurements were carried out on a Brookhaven Instruments apparatus (BI 9000AT correlator and BI 200 SM goniometer). An EMI 9863B/350 photomultiplier detected the signal. The light source was the second harmonic of a diode Nd:YAG laser,  $\lambda = 532$  nm (Torus, mpc3000, LaserQuantum, UK), linearly polarized in the vertical direction.

Dynamic light scattering (DLS) is one of the most popular methods used to determine the size of particles. When light hits particles, the coherent and monochromatic radiation beam scatters in all the directions with a time-dependent scattering intensity fluctuation. These fluctuations are the consequence of the Brownian motion of colloids in solution. The dynamic information of the system results from the autocorrelation function recorded during the experiment. The equation describing the autocorrelation function  $g^2(q,t)$  is expressed as follows Eq. (2.9):

$$g^2(q, t) = \frac{\langle I(t)I(t + \tau) \rangle}{\langle I(t) \rangle^2} \quad (2.9)$$

where  $\tau$  is the delay time, and  $I$  is the scattering intensity acquired at an angle  $\theta$  (here,  $90^\circ$ ). At short delay times, the correlation is maximum due to the particles which have not changed their position from the original: the two signals at  $\tau_0$  and  $\tau_1$  are not much different. As the time delay becomes progressively longer, the correlation starts to decay to zero exponentially. It means that, after a long delay time, the relative position of the particles is entirely different compared to the beginning. However, more exponential functions should be taken into account if the colloidal objects present size polydispersity. The decay profile recorded during the experiments can be easily fitted with numerical methods, in order to extract the diffusion coefficient of the particles in solution and, through the

Stokes-Einstein equation (assuming a spherical shape),<sup>[99]</sup> the hydrodynamic diameter of nanoparticles (Eq. 2.10).

$$D_H = \frac{k_B T}{3\pi\eta D} \quad (2.10)$$

where T is the temperature (K),  $k_B$  the Boltzman constant, D the diffusion coefficient extract from DLS measurements and  $\eta$  the solvent viscosity.

First, from the  $g^2(q,t)$  correlation functions, through the Sigert equation (Eq.2.11), it is possible to calculate the  $g^1(q,t)$ :

$$g^2(q, \tau) = 1 + \beta [g^1(q, t)]^2 \quad (2.11)$$

where the  $\beta$  parameter is a correction factor which depends on the geometry and alignment of the laser beam in the experimental setup. At this point, different mathematical approaches can be employed to determine size and polydispersity. The most straightforward approach considers a simple exponential decay of correlation functions which is appropriate in the case of monodisperse systems. When the polydispersity is relatively high, a general approach consists into expanding the autocorrelation functions in terms of the distribution moments of the decay through the cumulant analysis, stopped to the second order (Eq.2.12):

$$g^1(\tau) = e^{-\Gamma_1 \tau - \frac{1}{2!} \Gamma_2 \tau^2} \quad (2.12)$$

For highly polydisperse systems, a weighted distribution of the decay rates has to be taken into account, leading to the following equation for the autocorrelation function (Eq.2.13):

$$g^1(\tau) = \int_0^\infty W(\Gamma) e^{-\Gamma \tau} d\Gamma \quad (2.13)$$

where  $W(\Gamma)$  is the intensity-weighted distribution of the scattering objects. The Laplace inversion of the autocorrelation function allows to determine the intensity-weighted distribution of the scattering objects (CONTIN algorithm).

Finally – to avoid the multiple scattering phenomena – a dilution of the sample (especially if this is milk-like at the beginning) is necessary. Moreover, if nanoparticles interact with each other, the diffusion coefficient will be affected in different ways depending on the nature (attractive or repulsive) of the interactions, and the real hydrodynamic diameter related to the single colloidal system can be hardly extracted.

In this project, DLS was used to determine the average particle dimension in a colloidal dispersion of cubosomes or magnetocubosomes. Their dimensions were also estimated as a function of the temperature, scanning between 25-50 °C increasing of 5 °C each step. The hydrodynamic diameters ( $D_H$ ) of colloids analyzed during this PhD were calculated from the diffusion coefficients through the Stokes-Einstein equation (Eq. 2.10)

## 2.4 Rheology

Rheology studies the flow and deformation of matter. Theoretical aspects of rheology focus on the relation of the flow and deformation behavior of a material within its internal structure. By studying the relationship between stress (force) and strain (deformation) or strain rate (flow) in a material, it is possible to learn about the internal structure of the material. Elastic, viscous, or plastic behavior can be detected and measured by performing rheological measurements.<sup>[100]</sup>

\*\*\*Rheometers can carry out both transient and dynamic experiments but this thesis will focus on the dynamic ones. In this type of experiments, an oscillating stress (or strain) is applied, and the corresponding oscillating strain (or stress) is observed. Dynamic methods are used to learn about the viscoelastic properties of the material, by measuring the amplitude and phase shift of the strain after a stress was applied. The amplitude of the applied stress in the region of interest is usually very small. The region of interest is where the proportionality between the stress and the strain is constant, which is called the “linear viscoelastic region” (LVR). Usually, the rheological properties of a viscoelastic material are independent on strain up to a critical strain level (Amplitude Sweep Test). Beyond this critical strain level, the material’s behavior is non-linear, and the storage modulus declines. So, measuring the strain amplitude dependence on the storage and loss moduli ( $G'$ ,  $G''$ ) is a good first step taken in characterizing viscoelastic behavior: a strain sweep will establish the

extent of the material's linearity. The structure is intact below the critical value and the material behaves solid-like with  $G' > G''$ , indicating that the material is highly structured. Increasing the strain above the critical strain disrupts the network structure. The product of critical strain and complex modulus  $G^*$  is a good indication of the materials yield stress, and correlates well with the yield stress determined from the viscosity maximum obtained in a stress ramp.

After the fluid's LVR has been defined by a strain sweep, its structure can be further characterized using a frequency sweep at a strain below the critical strain. This provides more information about the effect of colloidal forces, the interactions among particles or droplets. In a frequency sweep, measurements are made over a range of oscillation frequencies at a constant oscillation amplitude and temperature. Below the critical strain, the elastic modulus  $G'$  is often nearly independent on frequency, as would be expected from a structured or solid-like material. The more frequency dependent the elastic modulus is, the more fluid-like is the material.

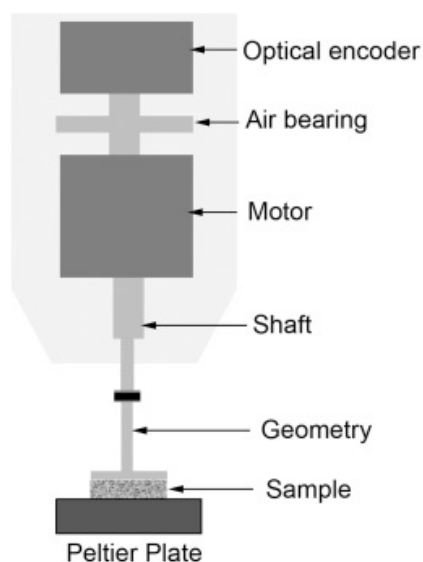


**Figure 9** Schematic diagram of a stress-controlled rheometer main unit.  
Reprinted with permission from reference<sup>[101]</sup>.

A schematic diagram of a rheometer is reported in Fig.9. All rheology tests were performed using a Physica-Paar UDS 200 rheometer, equipped with a plate-plate geometry measuring system (diameter of the upper plate 20 mm, measuring gap: 200  $\mu$ m). The temperature was controlled with a Peltier device. All the oscillatory measurements were performed within the linear viscoelastic range (1

Hz about the amplitude sweep curves). For all the measurements, once the samples were deposited on the surface of the measuring plate, a delay time of 10 min was set in order to ensure the complete equilibration of the sample; in that way no loading effect was observed for all the investigated samples. In order to minimize the evaporation of water, silicone oil was applied to the rim of the samples when temperature was varied in 25–50 °C. The instrumental setups for the rheology tests are the following:

- Frequency sweep test: frequency range 100–0.001 Hz; amplitude 0.1% strain;
- Amplitude sweep test: strain % from 0.001% to 10%; frequency 1 Hz.

## 2.5 *In-vitro* test experiments

### 2.5.1 Cell Culture

Colorectal adenocarcinoma cancer cells HT29 were purchased from European Collection of Cell Culture (ECACC). Cells were routinely cultured in Dulbecco's Modified Eagle's Medium (DMEM) – high glucose (4500mg/L) supplemented with 2 mM glutamine, with penicillin (100 U/mL) and streptomycin (100 µg/mL), and with 10% fetal bovine serum (FBS, Euroclone). Cells were incubated at 37 °C in a humidified atmosphere of 5% CO<sub>2</sub>- 95% air.

### 2.5.2 Cubosomes internalization assay

1x10<sup>4</sup> colorectal adenocarcinoma cells HT29 were plated and 24 hours later were treated with culture medium in presence or absence of different concentrations (0.6 µg/mL, 6 µg/mL, and 60 µg/mL) of octadecyl-rhodamine conjugated cubosomes loaded with 190 µL SPIONs. Cells were incubated 2, 20 and 40 minutes at 37°C in humidified 5% CO<sub>2</sub> atmosphere and then were washed with PBS 1x and imaged with a Leica AM 6000 microscope equipped with a DFC350FX camera and 40x 0.60NA air objective. All images were equally adjusted for display purposes using Fiji-Image J smart LUT.<sup>[102]</sup>

### 2.5.3 Incubation with Cubosomes and SPIONs-loaded Cubosomes

2x10<sup>5</sup> cells for each condition were incubated in suspension with different concentration (0.6 µg/mL, 6 µg/mL, and 60 µg/mL) of cubosomes, magnetocubosomes (NPs-cubo) and magnetohexosomes (NPs-hexo), for 40 minutes at 37 °C and 5% CO<sub>2</sub> to allow the internalization of the colloids. In order to evaluate their toxicity, the same volume of each suspension (corresponding to 2X10<sup>4</sup> cells of control) has been seeded in MW96 in triplicates

for 48 hours and cell viability has been assayed. Otherwise, in order to evaluate the effect of the AMF, cells were exposed to the alternate magnetic field for 30 minutes after the internalization.

### 2.5.4 Cell viability assay

5mM MTT (3-(4,5-Dimethylthiazol-2-yl)-2,5-diphenyltetrazolium bromide (Sigma) was added to cells and incubated for 1h at 37 °C. Cells were suspended in 200  $\mu$ L of dimethyl sulfoxide: the measuring wavelength of measuring was 595 nm.

## 2.6 Alternating Magnetic Field (AMF)

The magnetic properties of the NPs and bulk phases in absence or in presence of SPIONs were measured using a Quantum Design MPMS SQUID magnetometer. The field was always applied parallel to the pellet plane. The Zero Field Cooled/Field Cooled (ZFC/FC) procedure was performed applying a 5 mT probe field. The magnetization versus temperature measurements were performed in zero-field-cooled (ZFC) condition with a 10 mT probe field.

A sinusoidal field was generated in the gap of a broken toroidal magnet carrying a solenoid through which an alternating electric current (AC) from a tone generator was led. Samples to be treated with LF-AMF (6 kHz) were placed in the middle of the gap within 1 cm quartz cells. Details about the intensity of the magnetic field at different positions are given in Figure 10.

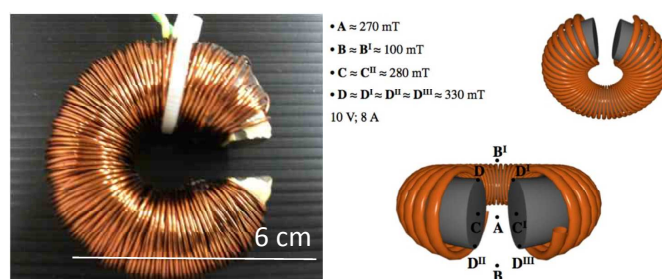


**Figure 10** Broken toroidal solenoid to generate low frequency Alternating Magnetic Field (LF-AMF). Magnetic field values at different positions of the broken toroidal magnet used to apply the LF-AMF. Magnetic field values were measured by means of a GM-07 Gaussmeter (HIRST Magnetic Instruments Ltd, UK).

## 2.7 Laser Scanning Confocal Microscopy (LSCM)

Laser scanning confocal microscopy (LSCM) has become an invaluable tool for a wide range of investigations in the biological and medical science, for imaging thin optical sections in living and fixed specimens ranging in thickness up to 100  $\mu\text{m}$ . LSCM is a technique able to catch image with high-resolution and depth selectivity; the key feature is its ability to acquire in-focus images from a selected depth, allowing a 3D reconstruction of topologically complex objects. In a conventional light microscope, object-to-image transformation takes place simultaneously and parallel for all object points. By contrast, the specimen in LSCM is irradiated in a point-wise fashion – *i.e.*, serially – and the physical interaction between the laser light and the irradiated specimen detail (*e.g.*, fluorescence) is measured point by point. It is necessary to guide the laser beam – a process known as scanning – to obtain information about the entire specimen. To obtain images of microscopic resolution from an LSCM, a computer and dedicated software are essential. A schematic presentation of an LSCM is shown in Figure 11.

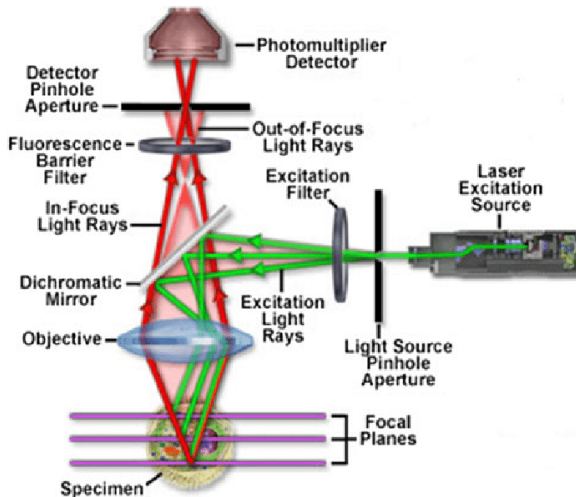


**Figure 11** Confocal microscopy geometry. Source Olympus Microscopy Resource Centre.

Coherent light emitted by the laser system (excitation source) passes through a pinhole aperture which is situated in a conjugate plane (confocal) with a scanning point on the specimen and a second pinhole aperture positioned in front of the detector (a photomultiplier tube). As the laser is reflected by the

dichromatic mirror and scanned across the specimen in a defined focal plane, secondary fluorescence emitted from points on the specimen (in the same focal plane) passes back through the dichromatic mirror and is focused as the confocal point at the detector pinhole aperture. Only a small fraction of the out-of-focus fluorescence is delivered through the pinhole aperture. Most of the extraneous light is not detected by the photomultiplier and does not contribute to the resulting image. The objective refocused in a confocal microscope shifts the excitation and emission points on the specimen to a new plane that becomes confocal with the pinhole apertures of the light source and detector. With LSCM it is possible to exclusively image a thin optical slice out of thick specimen (typically, up to 1  $\mu\text{m}$ ), a method known as optical sectioning. Under suitable conditions, the thickness (Z dimension) of such a slice may be less than 500 nm. Therefore, a LSCM can be used to advantage, especially where thick specimens (such as biological cells in tissue) have to be examined by fluorescence. The possibility of optical sectioning eliminates the drawback attached to the observation of such specimens by a single plane (or slice) of a thick specimen in good contrast, and optical sectioning allows a significant number of slices to be cut and recorded at different planes of controlled increments. The result is a 3D data set, which provides information about the spatial structure of the object. The quality and accuracy of this information depend on the slice thickness and the spacing between slices.

The experiments were carried out with a Leica TCS SP2 (Leica Microsystems GmbH, Wetzlar, Germany) equipped with a 63x water immersion objective instrument by using argon-ion (488 nm), DPSS (561 nm) and HeNe (633 nm) lasers.

## **2.8 Fluorescence Correlation Spectroscopy (FCS)**

Fluorescence Correlation Spectroscopy (FCS) is a technique which collects the fluctuation of the emission intensity of fluorophore probes in a confocal volume. The time-dependent fluctuation pattern allows to extract the correlation function of fluorescent probes. The experimental setup is shown in Figure 12.

A high numerical aperture microscope objective (typically water or oil immersion) is used to focus the laser beam to a different limited spot into the

sample. The same objective collects the fluorescent light. After passing through the dichroic mirror and an emission filter, the emitted light impacts onto a confocal pinhole, blocking the fluorescent light not originating from the focal region. Thus, a small observation volume  $V$  (below  $1 \mu\text{m}^3$ ) is created. The detection is performed by a fast and sensitive detector, typically a single photon counting avalanche photodiode (APD).<sup>[103]</sup>

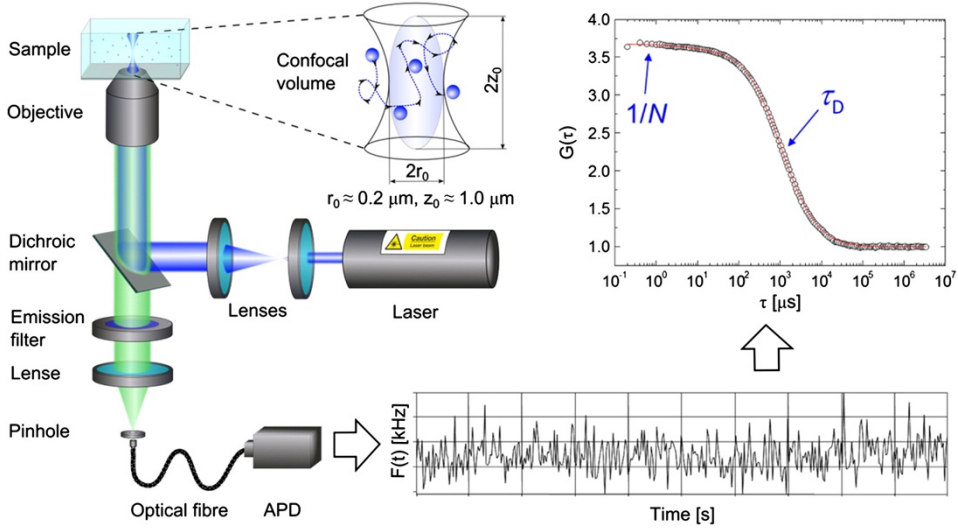


**Figure 12** Schematic representation of a typical confocal FCS setup and its principles of operation. Reprinted with permission from reference<sup>[104]</sup>.

The temporal fluctuations in the detected fluorescence intensity, caused by the diffusion of the fluorescent species inside and outside the observation volume, are recorded and analyzed through their autocorrelation function (Eq.2.13):

$$G(\tau) = \frac{\langle \delta F(t) \delta F(t + \tau) \rangle}{\langle F(t) \rangle^2} \quad (2.13)$$

where the intensity temporal fluctuations are evaluated by comparison of the signal obtained at the time  $t$  with the signal at time  $t+\tau$ . The case of a 3D ( $z=3$ ) normal diffusion ( $\alpha=1$ ) with a 3D Gaussian volume shape, can be described by the ACF expression as:

$$G(\tau) = \frac{1}{N} \left(1 + \frac{\tau}{\tau_D}\right)^{-1} \left(1 + \frac{\tau}{s^2 \tau_D}\right)^{-\frac{1}{2}} \quad (2.14)$$

where  $s$  is the aspect ratio of the detection volume and is connected to the experimental setup, and  $N$  and  $\tau_D$  contain information on the sample.  $N$  is the average number of particles in the effective detection volume  $\tau_D = u_0^2/4D$ , with  $D$  the diffusion coefficient of the probe. The potentially accurate evaluation of these parameters – with nM concentration range of the fluorophore – makes FCS an almost single-molecule technique with spatially resolved diffusion/concentration measurements. Moreover, physical or chemical process producing fluorescence fluctuations inside the observation volume, due to a change in fluorescence quantum efficiency can be investigated through FCS, to obtain information on the kinetics of these processes and the corresponding rate constants. Finally, FCS allows the specific investigation of selected phenomena within complex environments, thus making it interesting for the study of a host of processes related to biologically relevant systems. FCS measurements were conducted with an ISS instrument (ISS, Inc., 1602 Newton Drive Champaign, IL, USA), equipped with two APD with 500-530 nm and 607-683 nm BP.

## 2.9 UV-Vis Spectroscopy

UV-Vis measurements were performed on UV-Cary 3500 Agilent Technologies, which allows data collection in the range 190-1100 nm wavelength with different available bandwidths that can be selected between 0.1 and 5.0 nm at 0.01 nm intervals: the light spot on the sample is 1.5 mm. The instrument presents a Xenon flash lamp, double out-of-plane Littrow monochromator for fast data collection. There are eight cuvette position with eight detectors collecting the light signal which arrive on the sample at 1.5 cm from the bottom of the cuvette. It presents a magnetic stirrer able to mix the solution in cuvette with the appropriate stir bar.

To perform these measurements, we built-up a home-made modified plastic flask where a plastic ring was tied to the top of cuvette leaving the mesophase infusing into the buffer until the reaction was complete. Moreover, in order to homogenize the reaction solution, the buffer was stirred with cuvette stirrer bars during all the time of the experiments.



# 3

## Results and Discussion

### Part I

#### 3.1 Inclusion of NPs in Non-Lamellar lipid membrane (Paper I, II, III)

The inclusion of nanoparticles in lipid mesophases allows building up new functional materials, characterized by modified physico-chemical properties with respect to the neat lipid assemblies, both in terms of structure and responsivity upon external stimuli. Hydrophobic Fe<sub>3</sub>O<sub>4</sub> nanoparticles were synthesized in hexane, with oleic acid and oleylamine as capping agents; the analysis of the dispersion through SAXS and ICP-AES confirmed the size around 3-4 nm, and a concentration of 6.22 mg/mL Fe<sub>3</sub>O<sub>4</sub>. The diffraction patterns collected through the SAXS, with increasing NPs concentration loaded in MO mesophases, allowed to determine the structural effects of SPIONs on MO phase diagram (as reported in Papers I and II attached). If the temperature is kept fixed at 25 °C, the diamond cubic structure of the lipid mesophase is preserved while increasing the concentration of nanoparticles, until a threshold limit value over which a phase transition from cubic to hexagonal arrangement can be detected (Figure 13). However, even for lower nanoparticles concentration than the threshold value, the Bragg peaks of MO Pn3m cubic phase assembled with SPIONs are shifted to higher q vectors, which is attributable to a shrinking of the water channels promoted by the hindrance of the nanoparticles included in the bilayer. MO/SPIONs phase behavior can be rationalized taking into account the frustration packing energy and free energy of elastic curvature of the lipid bilayer. Since the diamond cubic structure presents a lower frustration packing than the hexagonal phase (which are the two structures involved during this process) and a higher elastic curvature energy, at 25 °C the detectable structure is the diamond cubic phase. When nanoparticles localize into the bilayer – due

to the hindrance of spherical shape between two leaflets – the frustration packing energy increases proportionally to the concentration of SPIONs. In my hypothesis, this increased energy of the Pn3m mesophase is higher than  $H_{II}$ ; indeed, the packing energy of  $H_{II}$  with nanoparticles embedded in the hydrophobic region should decrease this term, promoting a transition to a mesophase with higher negative curvature.

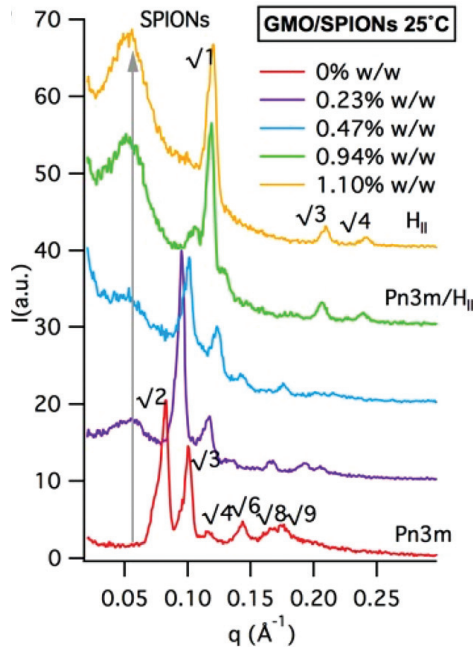


**Figure 13** Small angle X-ray scattering patterns of cubic mesophases doped with increasing amounts of SPIONs at 25 °C, up to the maximum hydration level. Reprinted from reference<sup>[39]</sup>.

If the concentration of SPIONs loaded in the LCs is kept fixed, the effect of temperature increase on MO/SPIONs assemblies is similar as previously discussed, *i.e.*, a cubic-hexagonal phase transition in the range 25-50 °C. Actually, as we can see from Figure 14, there is a coexistence region where both Pn3m and  $H_{II}$  phase can be detected. However, by increasing the concentration of SPIONs, the phase transition temperature decreases. This effect could be of relevance in biomedical field applications, for instance in, drug-delivery, in order to tune the cubic to hexagonal transition temperature with respect to the body one. Moreover, as it can be calculated by the equation reported in the Chapter 2 (Eq.2.6 related to the topology of the interface), the water volume fraction in each mesophase can be estimated, since the structure and the hydrophobic

chain length are known. Since cubic structures loaded with SPIONs are less hydrated than the pure MO/water systems, the water released during the cubic to hexagonal phase transition is around 50%, with respect to the MO/water systems where the volume fraction decrease is 25%: MO/water systems loaded with SPIONs can, therefore, behave like a sponge, releasing a high amount of water upon phase transition.

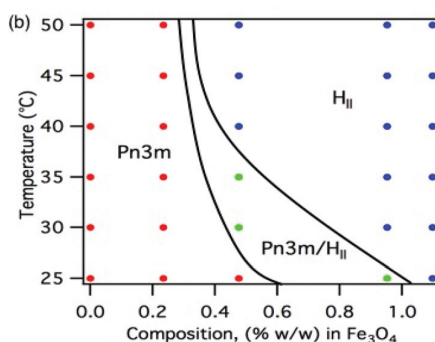


**Figure 14** Phase diagram mapped through small angle X-ray scattering of MO/SPIONs assemblies as function of temperature into the range 25-50 °C and SPIONs %w/w. Reprinted from reference<sup>[39]</sup>.

Focusing on MO/SPIONs system, a Pn3m-H<sub>II</sub> transition is shown by increasing the temperature as reported in Figure 15.

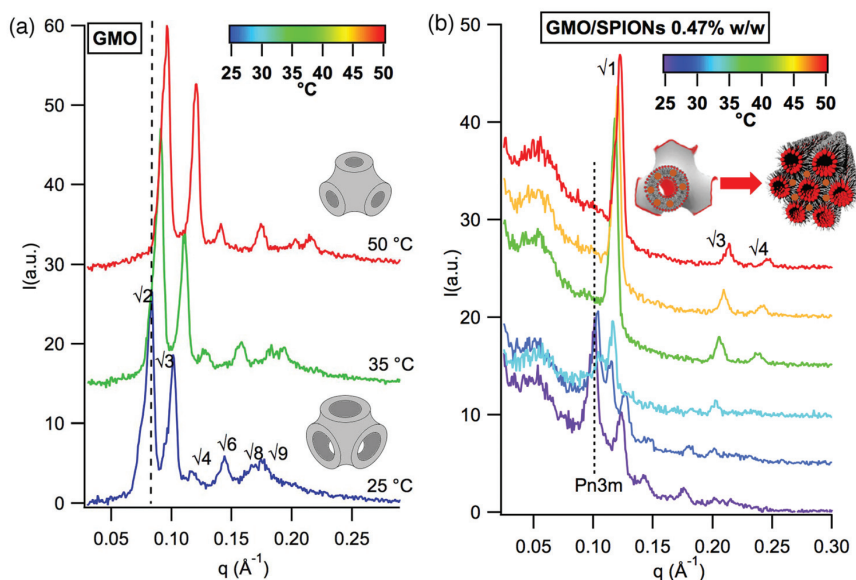


**Figure 15** SAXS curves of MO/Water mesophase (a) and MO/SPIONs/water mesophase (b) into the range 25-50 °C. Reprinted from reference<sup>[39]</sup>.

To provide an overall theoretical rationalization for the Pn3m-H<sub>II</sub> phase transition induced by SPIONs insertion, together with temperature variation, a combination of both energies of elastic curvature and frustration packing should be considered (par.1.3 Chapter1). Whereas the free energy describing the arrangement of the bilayer can be expressed as a linear combination of free energy of elastic curvature and frustration packing energy, the energy variation involved in the phase transition can be expressed as follows:

$$\Delta g_t = g_{H_{II}} - g_{Pn3m} = (g_c + g_p)_{H_{II}} - (g_c + g_p)_{Pn3m} = \Delta g_c + \Delta g_p \quad (3.1)$$

However, the free energy variation describing a spontaneous process should be negative. For this reason:

$$\Delta g_t = \Delta g_c + \Delta g_p < 0 \quad (3.2)$$

Considering the Eqs. 1.4to 1.7, and taking into account that an H<sub>II</sub> phase has Gaussian curvature K=0 that the mean curvature is H=0 for Pn3m at the mid-plane, the free energy of elastic curvature for the hexagonal and for the cubic phase can be written as follows:

$$g_c(H_{II}) = 4\kappa H^2 \quad (3.3)$$

$$g_c(Pn3m) = 2(\kappa_G - 2H_0\kappa l_c)K \quad (3.4)$$

Combining Eqs. 3.3 and 3.4, the variation of elastic curvature can be written:

$$\Delta g_c = g_c(H_{II}) - g_c(Pn3m) = 4\kappa H^2 - 2(\kappa_G - 2H_0\kappa l_c)K \quad (3.5)$$

Finally, combining Eqs. 3.2 and 3.5 the free energy of elastic curvature becomes:

$$\frac{\Delta g_p}{\kappa} + 4H^2 < 2K \left( \frac{\kappa_G}{\kappa} - 2H_0 l_c \right) \quad (3.6)$$

One should consider that  $\kappa, \kappa_G$  and  $H_0$  decrease if the temperature increases:  $\kappa$  and  $\kappa_G$  are related to the membrane elasticity, while  $H_0$  depends on the molecular geometry. Therefore, ultimately, the prevalence of a H<sub>II</sub> or a Pn3m phase depends on the balance between these two contributions:  $H_0$  and  $\kappa_G/\kappa$ . In

the neat MO binary system, the Pn3m-H<sub>II</sub> transition takes place around 90 °C. In the presence of SPIONs, as already discussed, an overall increase of the spontaneous curvature occurs – also at room temperature – determining an overall decrease of  $\Delta g_p$ , thus decreasing the minimum value of free energy of elastic curvature necessary to observe the phase transition. Thus, the presence of the SPIONs affects the thermotropic behavior of the MO liquid crystalline phase, influencing both the free energy of elastic curvature and the free energy of packing frustration. Overall, these energetic considerations are useful to highlight the potential of MO/NPs systems. Thermotropism can be finely tuned through SPIONs content in lipid structure, considering that magnetic nanoparticles affect both packing frustration and elastic curvature's free energies.

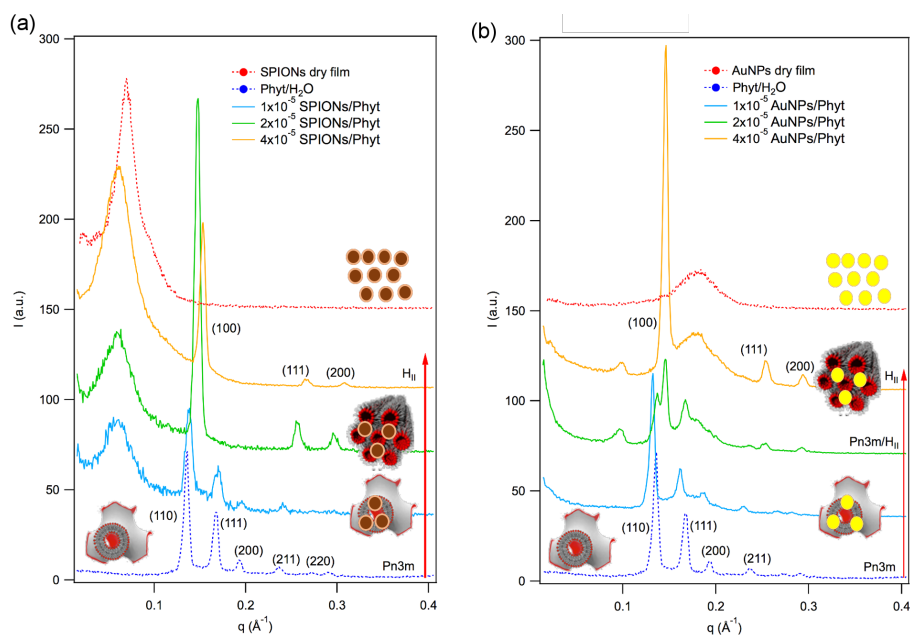


**Figure 16** SAXS of Phyt/H<sub>2</sub>O mesophases as the concentration ( $1 \times 10^{-5}$ ,  $2 \times 10^{-5}$ ,  $4 \times 10^{-5}$  NPs per Phyt molecule) of (a) SPIONs and (b) AuNPs increases, compared to the SAXS profile of Phyt/H<sub>2</sub>O in the absence of NPs (blue dashed line) and with the spectra measured for a dry film of (a) SPIONs and (b) AuNPs (dashed red lines). Reprinted from reference [40].

At this point, it appears necessary to understand whether the Pn3m-H<sub>II</sub> transition observed for the combination MO/SPIONs is a more general phenomenon or if it is related to the chemical composition of nanoparticles. As

reported in paper II, phytantriol is a polymorphic amphiphile similarly to MO, and it is able to self-assemble in cubic mesophase: the study of the phase behavior of cubic mesophases loaded with hydrophobic nanoparticles was thus extended to phytantriol as the building block of the cubic mesophase in water, and gold nanoparticles capped with a thiol were used as hydrophobic nanoparticles (diameter of AuNPs: 3.0 nm).

As shown in Figure 16, comparing phytantriol/water cubic phase assembled with gold and iron oxide nanoparticles, the increased NPs amount promotes the same transition. Since the dimensions are quite similar and the number of NPs encapsulated in the lipid membrane are the same, the slight differences between the two systems can be ascribed to the difference in the volume fraction of nanoparticles added to the cubic mesophase. The addition of increasing amounts of both SPIONs and AuNPs results in a precise modification of the mesostructure. Even small amounts of NPs ( $1 \times 10^{-5}$  NPs/Phyt) cause the appearance of an additional peak in the SAXS profile: broad and centered at  $0.18 \text{ \AA}^{-1}$  for AuNPs, more intense and centered at  $0.06 \text{ \AA}^{-1}$  for SPIONs. These peaks are present for all Phyt/NPs SAXS profiles (see Fig. 16a, 16b), without any significant shift of the maximum, irrespectively of the amounts of NPs. To gain more insight into this effect, we recorded SAXS profiles of dry NP films. The dry AuNPs film exhibits a broad peak, centered at  $0.18 \text{ \AA}^{-1}$ , which perfectly matches the  $q$ -value of the extra-peak in the mixed mesophase. The SAXS profile of dry SPIONs is characterized by an intense peak (centered at  $0.07 \text{ \AA}^{-1}$ ), which is slightly shifted to higher scattering vectors if compared to the extra peak in the corresponding mixed mesophase. The peaks observed for the dry films can be interpreted as arising from interparticle correlations, thereby ascribing the extra-peaks in the composite samples to a partial clusterization of NPs along the grain boundaries of the polycrystalline mesophases, as previously shown for similar systems in other studies.<sup>[28,35,105,106]</sup> The difference in the correlation length of SPIONs and AuNPs in the dry film might be related either to the core differences or to the slightly different hydrophobic coating of NPs, which might lead to a different arrangement of the alkyl chains between neighboring NPs. The shift of the correlation peak from  $0.07 \text{ \AA}^{-1}$  (dry film) to  $0.06 \text{ \AA}^{-1}$  (NPs inside Phyt) observed for SPIONs – corresponding to a variation in the NP-NP correlation distance from 8.90 to 10.5 nm – hints at the coexistence of SPIONs at the grain boundaries with particles effectively embedded in the mesophase. The same effect is more evident for AuNPs than SPIONs, where an

additional correlation peak at  $0.097 \text{ \AA}^{-1}$  is detected, which can be unambiguously attributed to AuNPs embedded inside the lipid architecture. Interestingly, the estimated correlation distance (6.5 nm) closely matches the nanometric organization of the mesophase. Figure 17 displays the profiles of the binary Phyt/ $\text{H}_2\text{O}$  system in excess water, which shows the characteristic  $\text{Pn3m-H}_{II}$  transition at  $50 \text{ }^\circ\text{C}$ , in full agreement with previous work on the effects of SPIONs on MO/water phase behavior.<sup>[39]</sup>

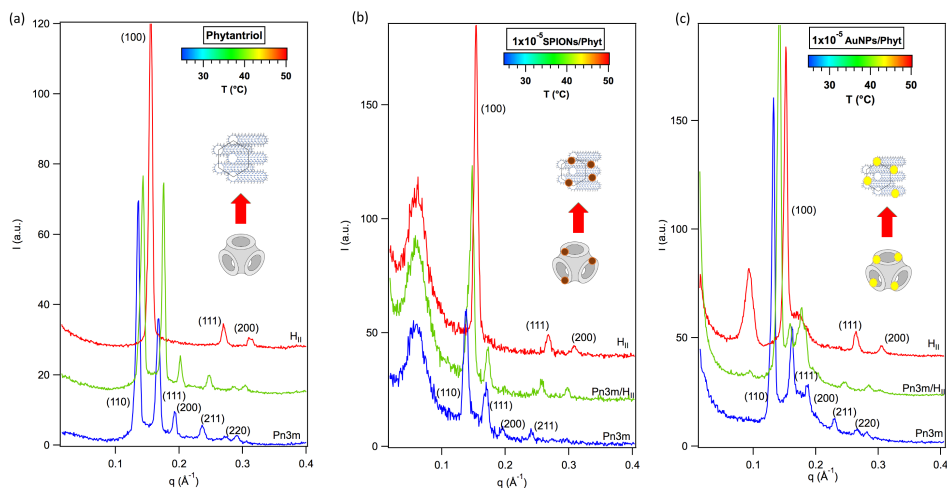


**Figure 17** SAXS profiles of Phyt/ $\text{H}_2\text{O}$  mesophases in the absence (a) and in the presence of (b, c)  $1 \times 10^{-5}$  NPs ((b) SPIONs and (c) AuNPs) per Phyt molecule at  $25 \text{ }^\circ\text{C}$  (blue curves),  $35 \text{ }^\circ\text{C}$  (green curves) and  $50 \text{ }^\circ\text{C}$  (red curves); the Miller indexes assignments ( $hkl$ ) of the  $\text{Pn3m}$  and hexagonal phase are also reported. Reprinted from reference <sup>[40]</sup>.

Upon loading phyt/water mesophases with the same number of SPIONs and AuNPs (Fig. 17b and 17c, respectively), the  $\text{Pn3m}$  phase persists at room temperature (blue curves). A temperature increase to  $35 \text{ }^\circ\text{C}$  partially promotes the phase transition to the hexagonal phase, both for SPIONs (more pronounced) and for AuNPs (Fig. 17b, c green curves). Therefore, the  $\text{Pn3m-H}_{II}$  transition can be induced both by increasing the amounts of NPs and – at a fixed amount of NPs – by raising the temperature to a value which is considerably lower than the transition temperature of the binary phase. The correlation peak, observed for higher NPs concentrations (see Fig. 16), also appears increasing the temperature in the sample with the lower amount of nanoparticles (Fig. 17c). This effect might be related to a reorganization of the NPs that, at higher temperature, are characterized by higher mobility inside the mesophase. Nevertheless, these

results further prove that this behavior is not explicitly related to a defined lipid molecule or NP kind, but to a general phenomenon. Besides, in this description the nature of the NPs core does not show a significant impact.

### 3.2 Viscoelastic properties of non-lamellar lipid membranes (Paper II)

Rheological experiments allowed investigating the viscoelastic properties of the hybrid materials described, from a structural point of view, in paragraph 3.1.

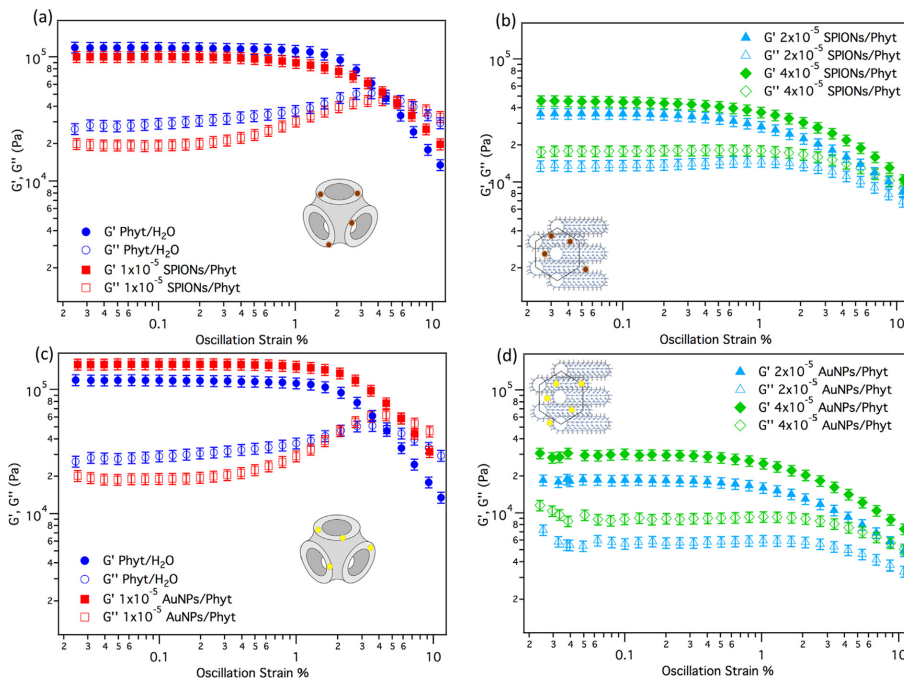


**Figure 18** Amplitude sweep analysis performed at 1 Hz and 25 °C for: (a,c) Phyt/H<sub>2</sub>O Pn3m mesophases with 1x10<sup>-5</sup> NPs/Phyt molecule (red markers) or without (blue markers) SPIONs (a) and AuNPs (c); (b,d) rheological tests performed on H<sub>II</sub> mesophases with 2x10<sup>-5</sup> NPs/Phyt molecules (light blue markers) and 4x10<sup>-5</sup> NPs/Phyt molecules SPIONs (b) and AuNPs (d). Reprinted from reference [40].

Figure 18 shows the amplitude sweep measurements. The storage modulus  $G'$  and the loss modulus  $G''$  of the different liquid crystalline mesophases are displayed as a function of the applied strain. The curves

measured for the hybrid Pn3m mesophases doped with low amounts of nanoparticles (red markers, SPIONs in Fig. 18a, AuNPs in Fig. 18c) are compared to those measured for Phyt/H<sub>2</sub>O in the absence of NPs (blue markers).

Figures 18b,d show the profiles measured for hybrid H<sub>II</sub> mesophases doped with increasing amounts of NPs. Different structural arrangements of liquid crystalline mesophases present a markedly diverse rheological response.<sup>[107,108]</sup> Accordingly, the inclusion of NPs (both SPIONs and AuNPs) in the Phyt/H<sub>2</sub>O cubic mesophase – which induces a cubic-to-hexagonal phase transition – is associated with a striking variation in the rheological behavior. As a matter of fact, for the pure Phyt assembly and with Phyt/NPs loading, the amplitude sweep curve (Fig. 18a, c) is characterized by the typical behavior of a 3D isotropic network, with no preferential directionality: after an initial increase for low strain values, it reaches a maximum – above which a strain increase causes the disruption of the network – resulting in the decrease of both  $G'$  and  $G''$ . The 1D-directional nature of the hexagonal phase, whose domains can align along the shear direction,<sup>[109]</sup> determines a monotonic decrease of both moduli with the increasing strain (Fig. 18b,d).

In summary, the arrangement of the lipid scaffold appears as the main factor affecting the rheological behavior, as inferred from amplitude sweep measurements. Within the same structural arrangement (Pn3m or H<sub>II</sub>), increasing the NPs number density does not have significant effects. Furthermore, the dependence of the storage and loss moduli of the material on the frequency of the applied shear perturbation was investigated in the linear viscoelastic regime (strain 0.1%, see Materials and Methods for details). Figure 19 reports the main results of frequency sweep tests. The results highlight a different dependence of both  $G'$  and  $G''$  on the frequency of the applied strain for Pn3m (Fig. 19a,c) and H<sub>II</sub> (Fig. 19b,d) mesophases. As a first observation, the transition from Pn3m to H<sub>II</sub> induces a decrease of  $G'$ , highlighting the lower rigidity of the hexagonal phase,<sup>[44,108]</sup> ascribable to the transition from a 3D-to-1D geometry. The Pn3m mesophases (Fig. 19a,c) behave as a viscoelastic fluid: for  $\omega > \omega_c$  (with  $\omega_c$  crossover frequency between  $G'$  and  $G''$  curves),  $G'$  is higher than  $G''$ , which indicates a predominantly elastic behavior, while the viscous character is dominant for  $\omega < \omega_c$ . Concerning the H<sub>II</sub> mesophase (Fig. 19b, d), the material shows a non-newtonian behavior, with  $G'$  higher than  $G''$  in the whole range of investigated frequencies. Increasing the number of NPs does not significantly affect the viscoelastic properties. Conversely, the inclusion of

nanoparticles in a Pn3m mesophase significantly modifies the rheological response. Although the trend described for the binary phase is preserved for systems doped with SPIONs (Fig. 19a, red markers) and AuNPs (Fig. 19c, red markers), the crossover frequency between  $G'$  and  $G''$  is shifted to lower  $\omega$  values. This effect is more evident for SPIONs than for AuNPs, where the  $\omega_c$  value is outside the available frequency range of the available rheometer.

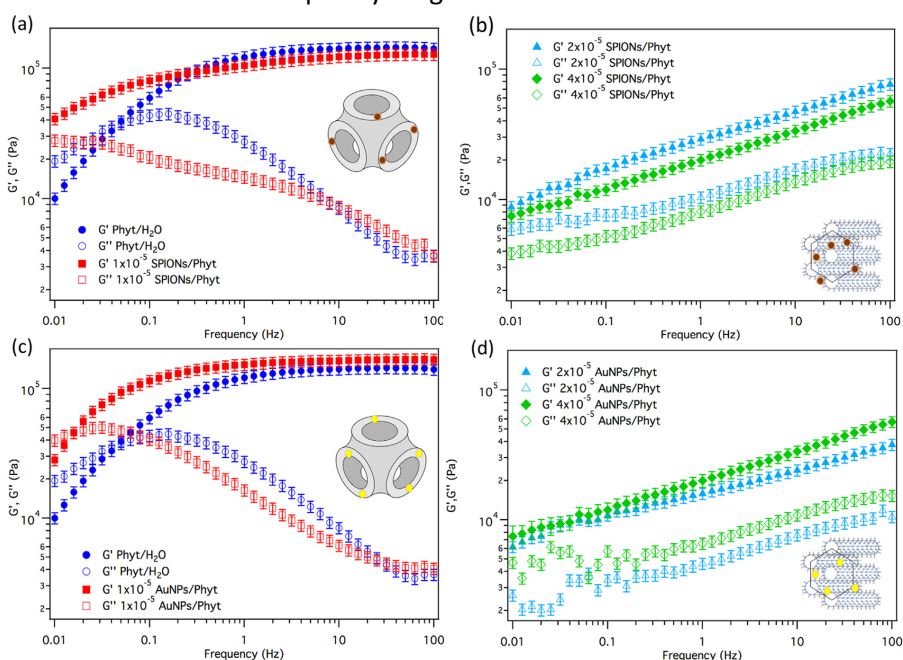


**Figure 19** Frequency sweep curves measured at 25 °C for: (a,c) Phyt/H<sub>2</sub>O Pn3m mesophases in the absence (blue markers) and in presence (red markers) of  $1 \times 10^{-5}$  NPs/Phyt molecule (a) SPIONs and (c) AuNPs; (b,d) Phyt/H<sub>2</sub>O H<sub>II</sub> mesophases in presence of  $2 \times 10^{-5}$  NPs/Phyt molecule (light blue markers) and  $4 \times 10^{-5}$  NPs/Phyt molecule (green markers) SPIONs (b) and AuNPs (d). Reprinted from reference [40].

The  $\omega_c$  marks the transition from the rubbery plateau to the viscous regime and corresponds to the longest relaxation time ( $\tau_{max}$ ) of the system, *i.e.*, the longest characteristic time required to relax back to the equilibrium configuration. According to the model proposed by Mezzenga et al.,<sup>[107,108]</sup> the physical meaning of  $\tau_{max}$  can be attributed to the diffusion time of the lipid molecules at the water-lipid interface. The  $\tau_{max}$  value markedly increases in presence of  $1 \times 10^{-5}$  NPs/Phyt, passing from 1 s to 10 s for AuNPs, and to >10 s for

SPIONs, accounting for a slower response of the material to the applied stress, which is a clear sign of an enhanced solid-like behavior.

The frequency sweep curves were transformed in continuum relaxation spectra through the following equation:

$$G'(\omega) = G_0 + \int_0^{\infty} H(\tau) \frac{(\omega\tau)^2}{1 + (\omega\tau)^2} \frac{d\tau}{\tau} \quad (3.7)$$

$$G''(\omega) = G_0 + \int_0^{\infty} H(\tau) \frac{\omega\tau}{1 + (\omega\tau)^2} \frac{d\tau}{\tau} \quad (3.8)$$

The results are shown in Figure 20. For the neat binary system, from a physical point of view, the main relaxation term describing the system is the diffusion time of lipid molecules to the water lipid interface. However, systems loaded by NPs present a broadened relaxation mode distribution, and the spectrum complexity increases indeed – for both kind of NPs – the main relaxation mode splits into a multimodal distribution, suggesting a non-trivial effect on the rheological properties of the lipid bilayer. This feature can be interpreted in terms of coexistence of lipids freely diffusing at the lipid/water interface, with a slower relaxation time ascribable to a hampered lipid diffusion at the NPs' surface.

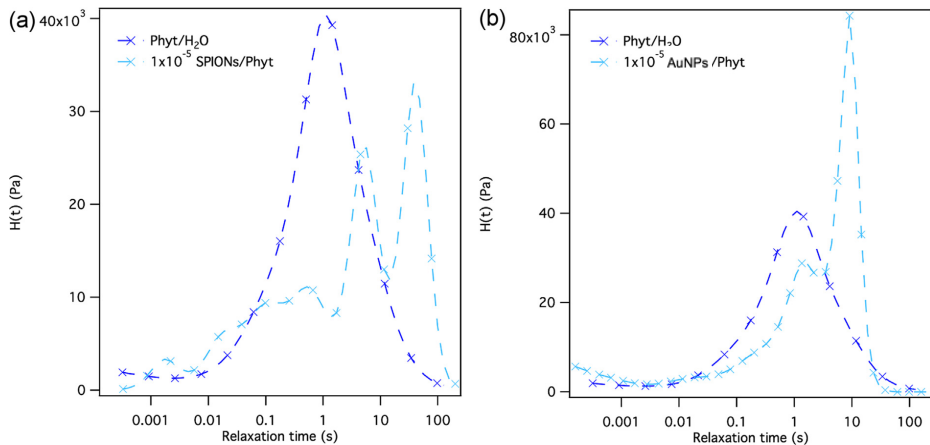


**Figure 20** Viscoelastic relaxation spectra of Pn3m mesophases: Phyt/H<sub>2</sub>O (blue markers and line in both plots), Phyt/SPIONs (cyan markers and line in (a)), and Phyt/AuNPs (cyan markers and line in (b)). Reprinted from reference [40].

Although the NPs diameters are comparable and the phase behavior similar, the addition of SPIONs leads to a higher relaxation time value compared to AuNPs, as the comparison between Fig. 20a and b highlights. This significant effect can be related to the stiffening of the material originated at the nanoscale level, where dipolar interactions between SPIONs inside the bilayer may additionally hamper the free diffusion of lipids.

### 3.3 Cubosomes and magnetocubosomes dispersions (Paper I and IV)

Pluronic F-127 is the most used block copolymer able to stabilize lipid-based dispersed LCs. The PEO blocks interact with the water environment, while the PPO block interacts with the lipid bilayer. According to dynamic light scattering analysis, the measured average dimension of cubosomes was around 200-250 nm, in agreement with the literature.<sup>[70]</sup> However, since lipid bilayers interact with F127, the structure of mesophases is slightly different from the bulk mesophase. Indeed, investigation through SAXS allows to detect a primitive cubic phase (Im3m) with higher hydration level and larger nanochannels (See Paper I and IV).

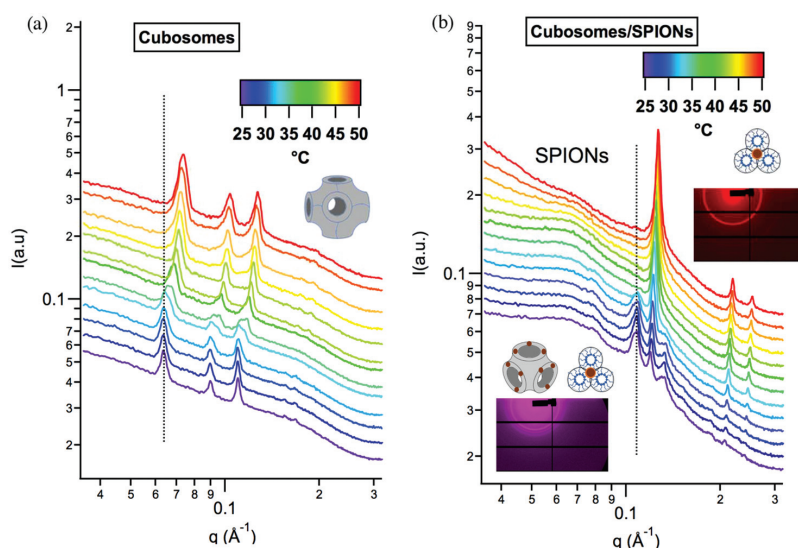


**Figure 21** SAXS data of cubosomes (a) and magnetocubosomes (b) into the range 25-50 °C; data collected at the SAXS beamline at Elettra Synchrotron Radiation Source Trieste, Italy. Reprinted from reference<sup>[39]</sup>.

The structure is preserved, into the range 25-50 °C. The addition of SPIONs into the cubosomes affects the structure of dispersed liquid crystals dramatically: the diamond mesophase coexists with the  $H_{II}$  structure according to the new curvature adopted by the lipid membrane including SPIONs. In analogy to SAXS data showed in the previous paragraph on bulk cubic mesophases, SPIONs leads to a more negative curvature of the lipid membrane according to the increase (in absolute value) of the curvature  $Im3m$ - $Pn3m$ - $Ia3d$ - $H_{II}$ . It was estimated that the minimum amount of nanoparticles required to cause a phase transition is in the range 0.26-0.3 mM SPIONs as showed in Paper IV (supporting information) at the end of this thesis. Moreover, a single cubosome should be a monocrystal structure (according to the Cryo-TEM images reported in literature<sup>[80,110,111]</sup>), since no grain-boundaries are present. For that reasons, nanoparticles are included into the bilayer and clusterization is possible into the membrane<sup>[112]</sup>.

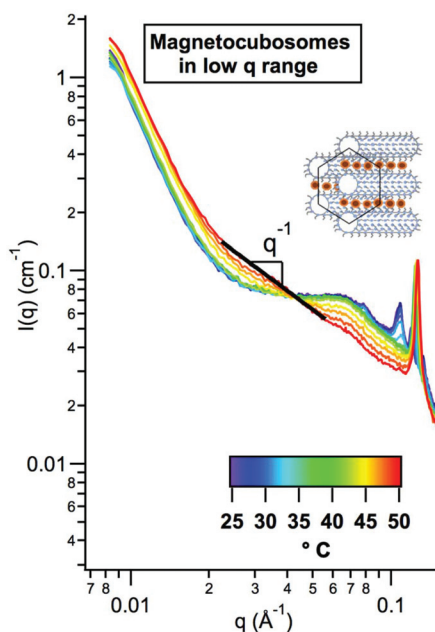


**Figure 22** Low- $q$  region of dispersed liquid crystals doped by SPIONs as a function of the temperature. Reprinted from reference<sup>[39]</sup>.

However, a quantitative analysis of the number of nanoparticles included into the membrane is tricky since no Cryo-TEM images are available to estimate that. Moreover, such task is complicated by the possibility of

nanoparticles to clusterize externally to the membrane, remaining dispersed in solution along with cubosomes. As a matter of fact, comparing the results of bulk and dispersed LCs, the effect of NPs is remarkable, since the higher surface/volume ratio of colloids (Figure 21).

The structural change – in analogy with bulk liquid crystals – shows a transition to  $H_{II}$  mesophases. The variation of the lattice parameter as a function of the temperature shows a steep decrease of  $d$  around 35 °C, near to the body temperature. NPs adapt their spatial distribution to the structure of the lipid scaffold: NPs included in the membranes change their relative position following the scaffold transition. This effect is detectable modification through SAXS profile.

The low- $q$  region describing the NPs correlation progressively changes in scalar law (as observed in a log/log plot of  $I(q)$  vs.  $q$ ) with increasing temperature, as highlighted in Figure 22. The scattering intensity for low- $q$  vector values shows a change of the scalar law beyond the Guiner region. A  $q^{-1}$  trend is related to elongated structures: since NPs have a spherical shape, compatible with the trend showed by the violet curve (25 °C), elongated structures are possible if SPIONs assemble in a pearl-necklace like structure. This hypothesis is in agreement with the one about frustration packing energy decrease as the NPs concentration increases (See paragraph 3.1). Indeed, NPs included in  $H_{II}$  structure, are probably located along the interstitial region of the cylindrical array. At this point, SPIONs reorganization promotes a modification on the magnetic properties of cubic mesophases, as reported in Paragraph 3.4.

### 3.4 Magnetotropism of bulk and dispersed liquid crystals (Paper IV)

The magnetic features of bulk mesophases, assembled with SPIONs, has been investigated by measuring the variation of magnetization ( $M$ ) as a function of temperature. In particular, the data of  $Pn3m$  and  $H_{II}$  mesophases at 25 °C, are compared and reported in Fig.23.

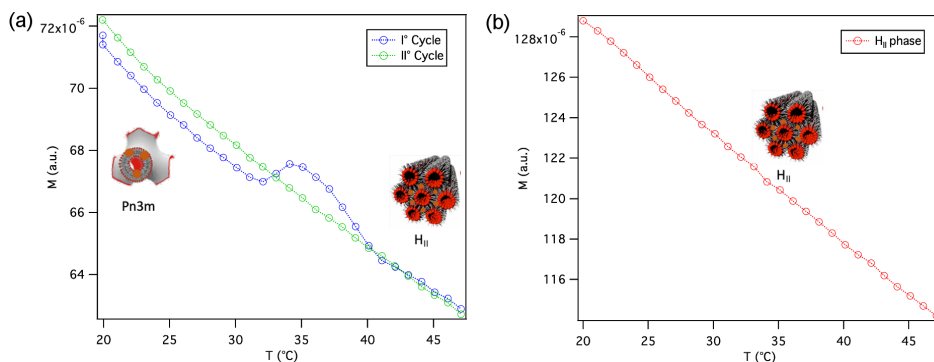


**Figure 23** The magnetization of cubic (a) and hexagonal (b) mesophases doped with SPIONs was investigated in the range 20–47 °C. In (a) blue markers and line show the magnetization of Pn3m structure before the phase transition, whilst red and green line and markers show the same experiment performed on the sample after the phase transition. In (b) the curve describing the magnetic behavior of hexagonal mesophases is reported, where no phase transition can be detected.

The magnetization of uncoated SPIONs has been recorded at 10 Oe and the results show a linear decay in the range 20–47 °C, typical of superparamagnetic nanoparticles in agreement to the Curie Law. Figure 23 shows the M vs. T profile for 0.26 mM SPIONs (green and blue line and markers) and 0.39 mM SPIONs (red line and markers). First, a brief introduction on the large number of interactions involved should be taken into account to discuss these results. A change in magnetization can be detected with the nanoparticles' spatial correlation variation: Van der Waals or electrostatic interactions, steric repulsion, magnetic attraction/repulsion and the relative orientation of magnetic dipoles,<sup>[113]</sup> are the main forces involved to describe the system. Considering hydrophobic nanoparticles entrapped in a highly viscous material, the Brownian relaxation process is negligible with respect to the Néel's one. Moreover, the electrostatic and steric repulsion are negligible, due to the nature of synthesized nanoparticles. Thus – according to the SAXS data of MO LCs – where the phase behavior is affected by SPIONs, we can hypothesize a reorganization of SPIONs locked in the bilayer, which follows the new wrapping adopted by the membrane.

In the Pn3m cubic structure assembled with SPIONs (Figure 23a), the magnetization follows a typical linear decay until 32 °C, over which a non-monotonic variation of magnetic properties is detected from 35 °C on. Increasing the temperature, the system shows a decrease with a linear trend up to 40 °C. The temperature values are in agreement with T behavior of SAXS profiles,

where (Figure 15b) SPIONs-loaded LCs promote a transition to an  $H_{II}$  array. Thus, following the structural change of the lipid scaffold, NPs significantly deviate from the linear decay of uncoated SPIONs, due to their reorganization. Probably, at 32 °C the thermal energy produces a decrease of the bilayer viscosity, which allows the SPIONs diffusion into the membrane and a detectable deviation of  $M$  vs.  $T$ . Moreover, with the chosen experimental setup (see Paper V), samples' dehydration can be neglected in the time range of the experiments. After the first thermal cycle, the same experiment was repeated (green markers and line, Figure 23a), but no magnetic transition could be observed, thus highlighting the existence of hysteresis. However, it should be noted that the green markers and lines in Figure 23a follow the same scalar law of the system after the transition in the 40-45 °C range. It is reasonable to assume that, since – as demonstrated in previous work<sup>[40]</sup> – a prolonged recovery of the original Pn3m structure (around 3-4 h) occurs. Therefore, in the second cycle the hexagonal structure is preserved. To demonstrate that the magnetic variation is related to the Pn3m- $H_{II}$  transition, MO with 0.39 mM SPIONs was analyzed (see Figure 23b). The red curve displays a typical linear decay with no magnetization deviation. This suggests that the bump observed in Figure 23a can be associated to the lipid phase transition which drives the supraorganization of SPIONs.

In order to test the responsiveness of SPIONs/lipids assembly, the following experiment was performed at the Synchrotron Radiation Source Elettra (Trieste, Italy): an oscillating magnetic field was generated with a broken toroidal solenoid, and the structural changes induced by the magnetic field were investigated by means of SAXS (are shown in Figure 24).

It is well known that SPIONs are responsive to an alternating magnetic field: their magnetic relaxation causes local heating and this has been used to trigger the release from carriers such as liposomes<sup>[25,114,115]</sup> or magnetocubosomes<sup>[116,117]</sup> of model drugs confined in the hydrophilic domains. The structural effects of the AMF, monitored “live”, have been here investigated on MO cubic bulk phase in the presence or in the absence of SPIONs (Fig. 24). With a dedicated experimental setup (Paper I and IV) – as shown in Fig. 24a – the AMF applied to GMO cubic phase (without SPIONs) does not induce structural changes. However, a mild Joule Effect of the coil, producing an overall minor shift ( $\sim 4.4 \times 10^{-5} \text{ \AA}^{-1}$ ) of the Bragg reflections, is observed, consistent with a temperature increase of 0.6 °C.

Conversely, when SPIONs-loaded Pn3m MO mesophases are exposed to the same magnetic field (Fig. 24b), an extra peak appears, whose position agrees with the first reflection of the  $H_{II}$  phase. After 10 minutes' application, the intensity of the peak increases, even if no complete transition is observed. Considering a non-complete phase transition and a negligible temperature, measured on the reference sample, we can safely ascribe this extra peak as due to a phase transition induced by the local heating effect of SPIONs.

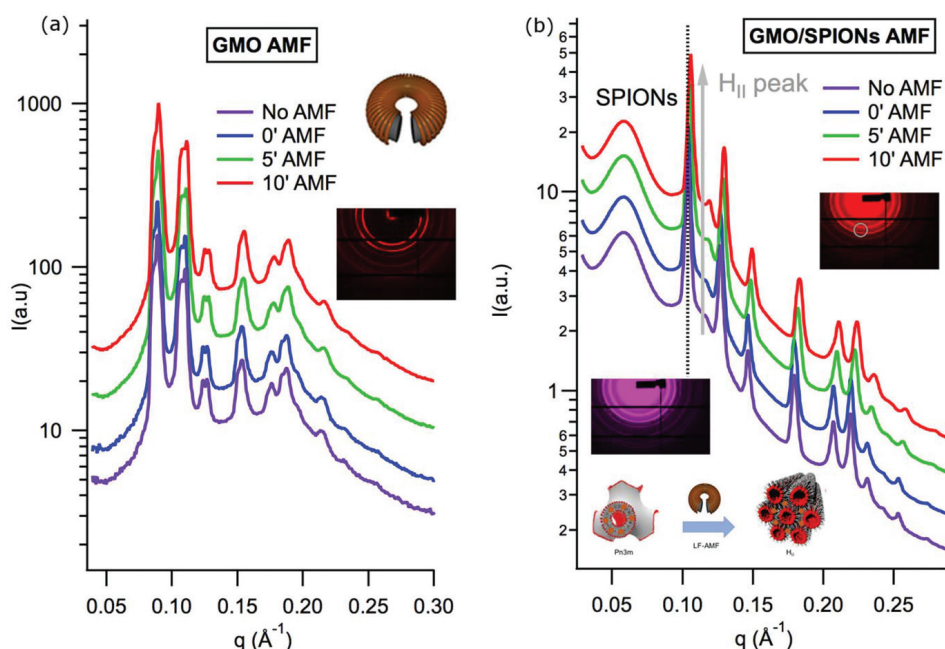


**Figure 24** SAXS curves of (a) GMO bulk cubic phase and (b) GMO bulk cubic phase with 0.47% SPIONs monitored during 10 minutes of LF-AMF application at RT. (a) A very mild shift of cubic phase Bragg peaks upon 10 minutes AMF application, corresponding to a temperature increase of 0.6 °C; (b) the appearance of an extra-peak at low  $q$  occur attributable to a  $H_{II}$  phase proves the occurrence of a Pn3m/ $H_{II}$  phase transition. Reprinted from reference<sup>[39]</sup>.

This phase transition is preserved in the magneto-colloidal dispersion. The experiments were performed on the ID02 beamline (ESRF, Grenoble, France). In particular, a fan was used during the experiments to cool down the temperature of the coil, so that the Joule effect of the magnetic field generator

(see paper V for details) could be neglected. In this way, the hyperthermia shown by SPIONs exposed to AMF, is the main term to consider during the investigation. Figure 25 shows the results of in-situ SAXS experiments of cubosomes and magnetocubosomes exposed to the oscillating magnetic field. As we can see in Figure 25a, during the application of AMF no relevant shift for the Bragg reflections of cubosomes can be observed. Moreover, the intensity of the peaks – as in the case of cubosomes references (Figure 21a) – does not change whilst increasing the temperature, thus suggesting that the temperature reached by the coil is below 37 °C. The increase of the temperature is around 2°C, which can be justified in terms of a weak coil Joule Effect. The experiments on magnetocubosomes (Figure 25b) – performed in the same conditions as cubosomes – show a different behavior.

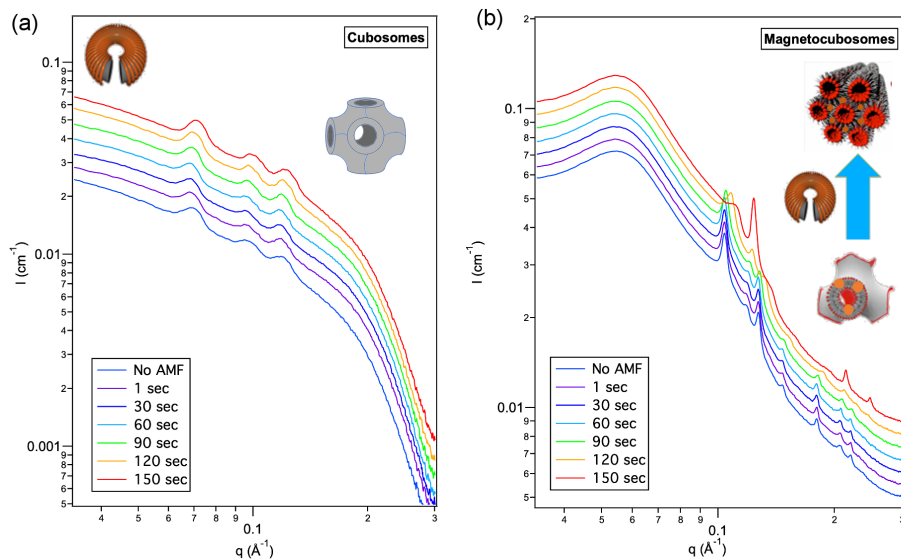


**Figure 25** In situ SAXS experiments of cubosomes (a) and cubosomes assembled with 0.26 mM SPIONs (b) under the alternating magnetic field of 4.22 kHz. Curves were recorded every 30 seconds to control the hyperthermic effect of nanoparticles. In (b) it is showed the transition to a hexagonal array of the dispersion after 150 sec upon AMF (red curve).

After 90 seconds of AMF applications, the first Bragg reflection starts to shift to higher q values, together with an increase of the intensity of the first Bragg hexagonal reflection. This latter peak becomes progressively higher at 120 secs, and a decrease in the Pn3m reflexes is seen. Finally, a complete transition is reached at 150 secs, and the diamond cubic structure almost disappears. The evaluation of the lattice parameter allows us to estimate the temperature

reached by the sample exposed to AMF after 150 secs, which is around 39 °C. That value is not enough to induce a phase transition (heating the magnetocubosomes sample; the transition is observed at 41-43 °C).

For this reason, we can conclude that with the experimental setup of that measurements, no coil Joule effect is detectable – or it is negligible – and it does not affect the results, suggesting that the leading term involved in the re-arrangement of the bilayers is the hyperthermia of nanoparticles. Comparing the induced transition in bulk and dispersed LCs, the time needed by bulk Pn3m structure is around 10-15 minutes, while for cubosomes, after 3 minutes, a complete transition is detectable. This is ascribable to the higher surface/volume ratio of dispersed LCs, which gives rise to more “defects” in the structure where the transition starts.

### 3.5 Interaction of dispersed LCs with cells (Paper IV)

Some reports in the literature address the interaction of cubosomes with cell membranes, and their ability to delivery chemotherapeutics for cellular death.<sup>[51,98,118–123]</sup> In order to prove that cubosomes doped with SPIONs are suitable candidates in drug-delivery, in-vitro test experiments were performed on tumor cells. To the best of my knowledge, this was the first investigation about the effects of LCDs combined with SPIONs on cells.

HT29 adenocarcinoma colorectal cells were used to test the internalization of cubosomes. In order to determine the time of internalization,  $1 \times 10^4$  HT29 cells were incubated in suspension with octadecyl-rhodamine B conjugated cubosomes (0.01% mol with respect to the MO amount) at 0.6  $\mu\text{g}/\text{mL}$ , 6  $\mu\text{g}/\text{mL}$ , and 60  $\mu\text{g}/\text{mL}$  at 37°C. The negligible amount of Octadecyl-Rhodamine B does not modify the structure of cubosomes thus, the possible effects are ascribable to the cytotoxicity of the lipids and not related to the structure. The internalization was evaluated through confocal microscopy, detecting the fluorescence intensity of the internalized probe after different interaction times: 2, 20 and 40 minutes. The maximum internalization was reached after 40 minutes at the concentration of 60  $\mu\text{g}/\text{mL}$ , see Figure 26. The advantage of cubosomes, with respect to "free" hydrophobic drugs, can be related to the low bioavailability in biological fluids of non-conjugated

therapeutics. In fact, the enormous hydrophobic domain allows to efficiently transport significant amounts of drugs (compared to the solubility of the active molecules in bio-fluids) in a relatively short interaction time.

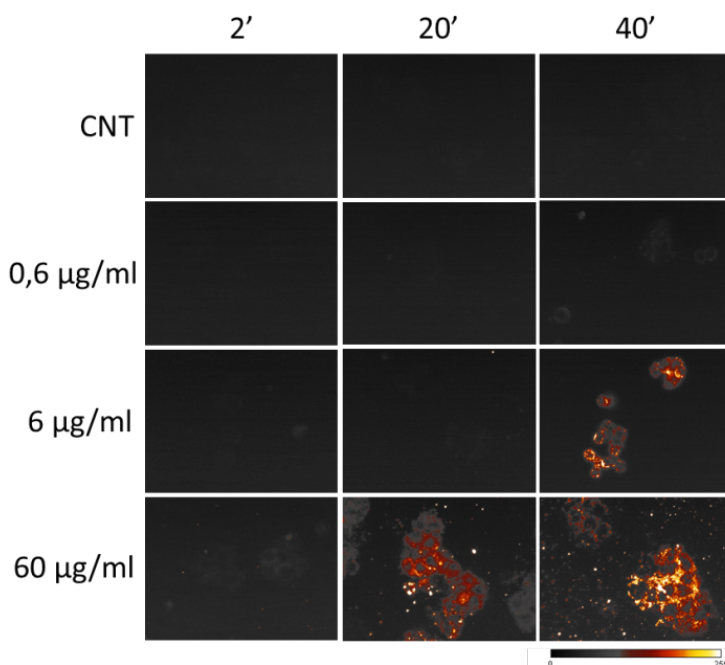


**Figure 26** Confocal images of Octadecyl-Rhodamine B conjugated cubosomes internalization in HT29 cells at 2, 20 and 40 minutes at different concentrations (0.6 µg/ml, 6 µg/ml, and 60 µg/ml).

Moreover, it is known from the literature that cubosomes stabilized with Pluronic F127 have the right size to present a typical enhanced permeability and retention effect (EPR),<sup>[124–126]</sup> due to the PEO blocks of the copolymer, allowing localization of dispersed liquid crystals in tumor tissues.

The toxicity of cubosomes, magnetocubosomes (0.26 mM SPIONs) and magneto-hexosomes (0.39 mM SPIONs) was evaluated by incubating  $2 \times 10^5$  HT29 in suspension with 0.6 µg/mL, 6 µg/mL and 60 µg/mL of cubosomes, NPs-cubosomes and NPs-hexosomes for 40 minutes at 37°C. After incubation, the same volume of each suspension (corresponding to  $2 \times 10^4$  cells of control) was seeded in a cell plate for 48 hours. Cell viability was evaluated by the MTT assay (Figure 27). Results suggest that these colloids can be internalized and that they are not toxic for cells at such experimental conditions. Since the exposure of NPs-cubosomes and NPs-hexosomes to an alternate magnetic field (AMF) should

cause an increase of their temperature, HT29 cells were treated at the higher dose (60  $\mu\text{g/ml}$ ) of cubosomes, NPs-cubosomes and NPs-hexosomes for 40 minutes and then they were exposed for 60 minutes to the AMF.

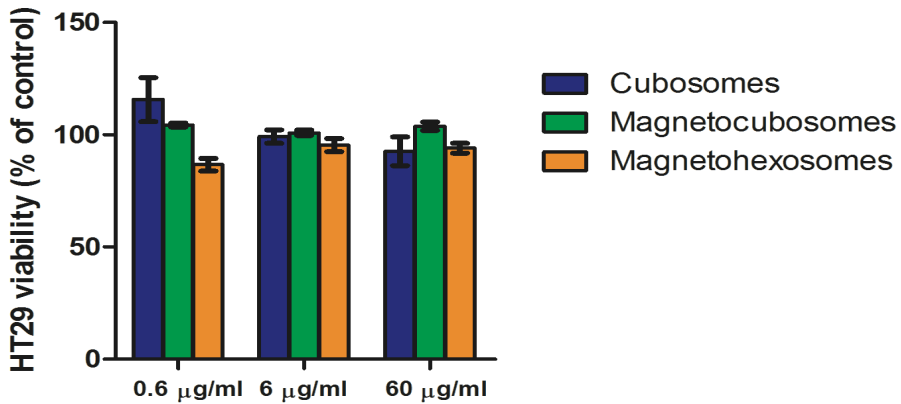


**Figure 27** Cell viability of HT29 treated with different concentration (0.6  $\mu\text{g/ml}$ , 6  $\mu\text{g/ml}$ , and 60  $\mu\text{g/ml}$ ) of cubosomes, magnetocubosomes and magnetohexosomes.

The viability of HT29 cells, plated in MW96 as previously described (based on control sample without AMF), was assayed after 48 hours in order to evaluate if AMF could cause the death of treated cells. The graph (Figure 28) does not show toxic effect in samples under AMF compared to samples without AMF.

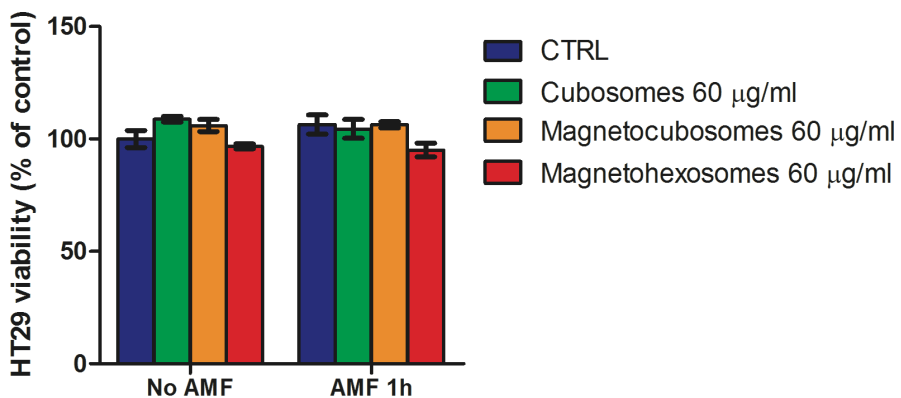


**Figure 28** Cell viability of HT29 treated with cubosomes, magnetocubosomes and magnetohexosomes at 60  $\mu\text{g/ml}$  under the alternate magnetic field.

These results demonstrate the complete biocompatibility of cubosomes, NPs-cubosomes and NPs-hexosomes for their use on human cells in presence of AMF. The absence of an hyperthermic effect, related to the supraparticles organization of SPIONs embedded into the bilayer, during the interaction with cells, could be related to different processes. First, the heat generated by SPIONs upon AMF could be enough to reorganize the lipids, but to the phase transition  $Pn3m-H_{II}$  requires energy, thus the latent heat associated to the transition decrease the efficiency of hyperthermia process. Moreover, fully in line with the literature,<sup>[127–131]</sup> cubosomes fuse with lipid membrane and, consequently, the interaction provokes a disruption of the cubosomes' structure and the pearl-necklace organization of SPIONs. The result is a less efficient hyperthermia behavior, not detectable with the experimental condition of the present measurements.

## Part II

### 3.6 Effects of additives on non-lamellar mesophases (Paper V and VI)

#### 3.6.1 Sucrose stearate on phytantriol assemblies

In order to determine the impact of sucrose stearate (SS) on the arrangement of Phyt mesophases in excess water, we characterized the structure of Phyt/water binary systems, including increasing amounts of SS at different temperatures. Fig. 29 shows representative Small Angle X-ray Scattering (SAXS) curves of Phyt cubic mesophases assembled with increasing concentrations of SS, namely 5% (Fig. 29a), 10% (29b) and 15% (29c) measured at 25, 30, 35, 40, 45, 50 °C.

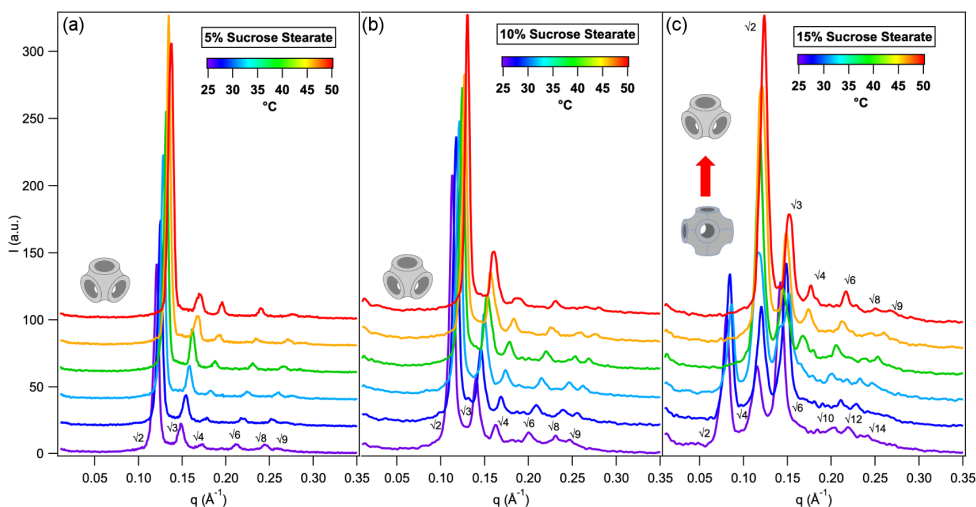


**Figure 29** SAXS curves of phytantriol assemblies with increasing concentration of sucrose stearate (SS); (a) 5%, (b) 10%, (c) 15% SS, investigated into the range 25–50 °C.

In excess water, phytantriol is characterized by a well-known phase diagram<sup>[16]</sup> reported in Figure 3b. The lattice parameters concerning the binary system Phyt/H<sub>2</sub>O, reported in Table 2, highlight a known trend with increasing temperature: an overall shrinkage of the lattice parameter, that is related to the conformation of the amphiphile chains spreading away each other, increasing the hydrophobic molecular portion. In terms of curvature of the lipid membrane,

increasing the temperature, the spontaneous curvature of the leaflets becomes more negative, leading to an overall shrinking of the lipid mesophase.<sup>[5]</sup>

**Table 2:** Lattice parameter  $d$  (Å), diameter of water channels  $d_w$  (nm) and water volume fraction  $\phi_w$  of Phyt mesophases doped with increasing concentrations (5% w/w, 10% w/w, 15% w/w,) of SS, measured and calculated at different temperatures in the range  $T=25-50$  °C.

T (°C)	No SS			5% SS			10% SS			15% SS		
	$d$ (Å) <sup>#</sup>	$d_w$ (nm)	$\phi_w$	$d$ (Å)	$d_w$ (nm)	$\phi_w$	$d$ (Å)	$d_w$ (nm)	$\phi_w$	$d$ (Å)	$d_w$ (nm)	$\phi_w$
25	66*±1	2.3	0.21	72*±1	2.8	0.27	75*±1	3.0	0.30	105*±2	3.6	0.39
30	65*±1	2.2	0.20	70*±1	2.6	0.25	72*±2	2.8	0.27	103*±1	3.4	0.38
35	64*±1	2.2	0.19	67*±1	2.4	0.22	71*±2	2.7	0.26	99*±2	3.2	0.35
40	63*±1	2.0	0.18	66*±1	2.3	0.21	69*±1	2.6	0.24	74*±2	2.9	0.29
45	48 <sup>§</sup> ±2	1.9	0.16	66*±2	2.3	0.21	67*±2	2.4	0.22	71*±1	2.7	0.26
50	40 <sup>§</sup> ±1	1.2	0.094	64*±2	2.2	0.19	66*±1	2.3	0.21	70*±1	2.6	0.25

\*Pn3m structure; § H<sub>II</sub> structure; † Im3m structure;

#Phyt/water lattice parameters are reported here by reference<sup>[16]</sup>

The addition of the lowest and intermediate concentrations of SS to the lipid scaffold (5% and 10% w/w SS) does not modify the Pn3m structure in the whole temperature range investigated (25-50 °C). However, at each temperature, the lattice parameters of the liquid-crystalline phase are progressively increased by the addition of sucrose stearate. Sugar esters localize at the water-lipid interface, where they attract a higher amount of water molecules into the nanochannels and determine an increase of the curvature of the membrane, overall promoting a swelling of the lipid mesophase. This effect is more pronounced for the sample containing 15% w/w SS: in this case, at 25 °C the mesophase exhibit an Im3m spatial arrangement, characterized by a lower curvature of the lipid membrane compared to the Pn3m. Interestingly, as the addition of increasing amounts of SS and the temperature increase lead to opposite effects (the former tends to decrease the localized curvature, while the latter tends to increase it), at higher temperature (from 40 °C), the Phyt/SS/H<sub>2</sub>O sample with 15% w/w SS undergoes a transition from Im3m to Pn3m (which is the thermodynamically stable structure for a Phyt/H<sub>2</sub>O mesophase in the absence of additives at low temperature). Thus, the effects of high additive amount and high temperature are perfectly counterbalanced, and the lattice parameter is similar to that observed for Phyt/H<sub>2</sub>O binary system at 25 °C (see Table 2).

The values of the diameters of water nanochannels and the water volume fraction, calculated through the equation reported in Chapter 2 paragraph 2.2, reflect the trend of the lattice parameters of the mesophase: for instance, at 25 °C the diameter of water nanochannels is 2.2 nm for neat Phyt/H<sub>2</sub>O system, and it progressively increases to 2.8 nm for 5% w/w SS, to 3.0 nm for 10% w/w SS and, finally, to 3.6 nm for 15% w/w SS. On the other hand, for each mesophase, the temperature increase yields a progressive shrinkage of the water channels, determining a progressive water release from the mesophase.

### 3.6.2 DOPG and tetradecane combined with MO assemblies

As discussed in the previous paragraphs, the MO assemblies can be modified both with inorganic nanoparticles and with additives. This section will present the inclusion of DOPG and tetradecane (TD) additive on the MO mesophases to control the dimension of the channels. The swelling or shrinking effects will be of relevance in order to study the diffusive properties of an hydrophilic fluorophore embedded into the structure (see paragraph 3.7.2).

We evaluated the effect of the inclusion of increasing amounts of tetradecane on the MO cubic mesophases in excess water at 25 °C, and the results are shown in Figure 30. Notably, all the curves with an increased concentration of TD show a shift to higher scattering vectors, suggesting a decrease of a parameter in the direct space, *i.e.*, the channels' size. For relatively low amounts of tetradecane, the diamond cubic structure is preserved. However, above 10% w/w TD, a phase transition from cubic to hexagonal array is observed, analogously to the inclusion of hydrophobic inorganic nanoparticles showed in paragraph 3.1. This behavior can be fully explained in terms of frustration packing energy, since the inclusion of a hydrophobic additive produces a decrease of this energetic term, favoring the hexagonal array. However, higher amounts of TD in the MO mesophases induce a phase transition corresponding to the Fd3m structure, consisting of a micelles arranged in a cubic lattice. The higher the amount of the oil, the higher the lattice disorder, since the typical Bragg reflexes of Fd3m structure disappear (Figure 30), showing a broad scattering curve positioned around  $0.092 \text{ \AA}^{-1}$ . This value corresponds to a typical dimension around 6.8 nm, which describes the average distance between micelles dispersed in the oil environment. The existence of inverted micelles can be justified considering the significant amount of oil molecules functioning as

dispersant medium, while the MO surfactant separates water from oil in a nanoscopic spherical micelles.

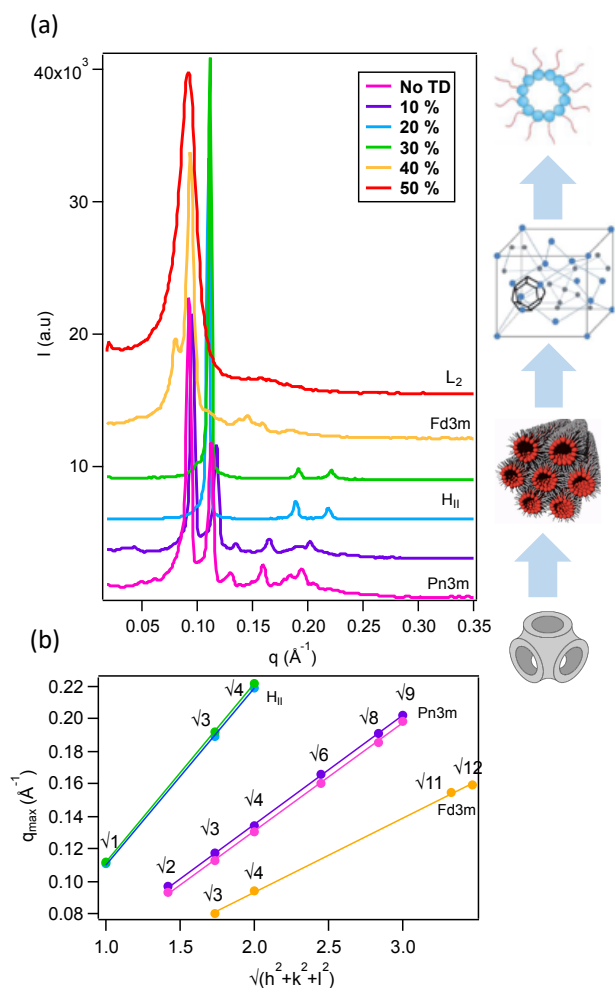


**Figure 30** (a) SAXS curves recorded at 25 °C at the maximum hydration level in MO assemblies doped with increasing amounts of tetradecane additive: 0 % TD (purple curve), 10% w/w (violet curve), 20% w/w (cyan curve), 30% w/w (green curve), 40% (orange curve) and 50% w/w (red curve). (b) Linear fit of the Miller indexes for each phase, used to calculate the lattice parameter of mesophases; the sample containing 50% TD it is not shown since it is an inverted micellar structure.

In summary, the inclusion of TD, in agreement with some works reported in literature,<sup>[44,45]</sup> due to its hydrophobic nature, produces the shrinking of the

water nanochannels, promoting the transition to structures with an increased (in absolute value) membrane curvature.

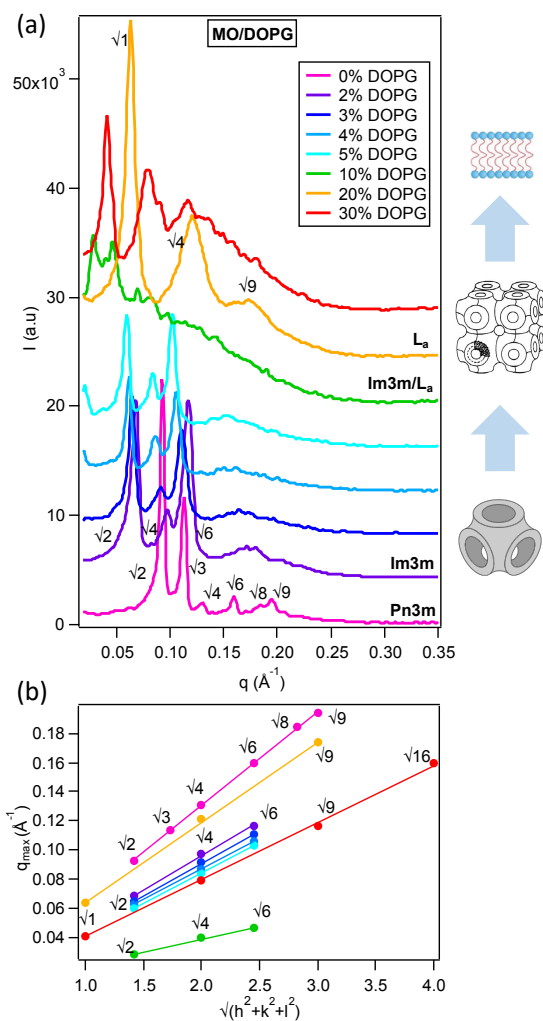


**Figure 31** (a) SAXS curves recorded at 25 °C at the maximum hydration level in MO assemblies doped with increasing amounts of DOPG additive: 0% w/w (purple curve), 2% w/w (violet curve), 3% w/w (blue curve), 4% w/w (cyan curve), 5% w/w (light cyan curve), 10% w/w (green curve), 20% w/w (orange curve) and 30% w/w (red curve). (b) Linear Fit of the Miller indexes for each phase, used to calculate the lattice parameter of mesophases.

In order to evaluate the effects of DOPG lipid on the MO bilayer, an increasing amount of the additive was mixed with MO, and the structural changes we investigated. While the TD molecules interact mainly with the

hydrophobic chains of the bilayer, DOPG locates spontaneously to the interface: its bulky polar headgroup causes an uptake of water into the channels, analogously to the SS behavior described in the previous paragraph 3.6.1. The effect of the inclusion of DOPG on the lipid bilayer is shown in Figure 31, where – increasing the concentration of the amphiphilic additive – a shift to lower scattering vectors is recorded. Oppositely to the TD effect, DOPG swells the lipid bilayer; indeed, the relatively low DOPG amount (2-5% w/w) produces a swelling effect on the Pn3m structure, promoting a transition from diamond to primitive cubic assemblies. In agreement with the literature, the lamellar phases are observed starting from 10% w/w DOPG, where both lamellar and Im3m mesophases can be observed. The SAXS profiles, relative to the samples with 10% DOPG, show an intensity increase in the low q-region: since water excess hydrates the dry lipid film, the broad contribution to the scattering intensity describes a partial dispersion of MO/DOPG lipids in liposomes. Moreover, for the samples with more than 10% DOPG, the lamellar Bragg reflex can be detected, overlapped to the liposome's contribution, indicating the coexistence of liposomes and bulk multilayers. The high amount of DOPG (around 30%) in MO assemblies produces a lamellar profile but, in this case, a different scattering profile is observed; the curve seems to show more lamellar phases coexisting with each other. Analogously to the TD effects, a higher amount of amphiphilic additive produces an increase of the disorder of mesophases.

Some considerations should be made, concerning the MO/DOPG and MO/TD systems. All concentrations in this paragraph are expressed as % w/w; from Figure 31, a relatively low DOPG concentration produces a dramatical effect on the bilayer morphology compared to the TD additive. The molecular weight ratio between TD and DOPG is around 1:4; thus, the small DOPG concentration corresponds to an exiguous number of molecules assembled with MO. Therefore, DOPG imposes its curvature more than TD; tetradecane does not assemble at the water-lipid interface, due to its no-surfactant nature.

After an initial evaluation of TD and DOPG effects, a mixture of MO with both the additives allows to explore the ternary phase diagram, taking into account that the system presents four components, considering water added in excess.

All the results are reported in the ternary phase diagram and shown in Figure 32. The  $L_{\alpha}$  region is the most extended for the investigated concentration of the additives. The Im3m structure is observed in a small region of the phase

diagram, analogously for the Pn3m. Thus, it seems that the bicontinuous mesophases are stable in case of an insignificant perturbation of the bilayer. It is evident that the possibility to control both the thickness and the water channel size of bicontinuous phases is limited by the thermodynamical stability of the structures, and these features of the mesophases cannot be modified in an infinite range of possibilities in any case.

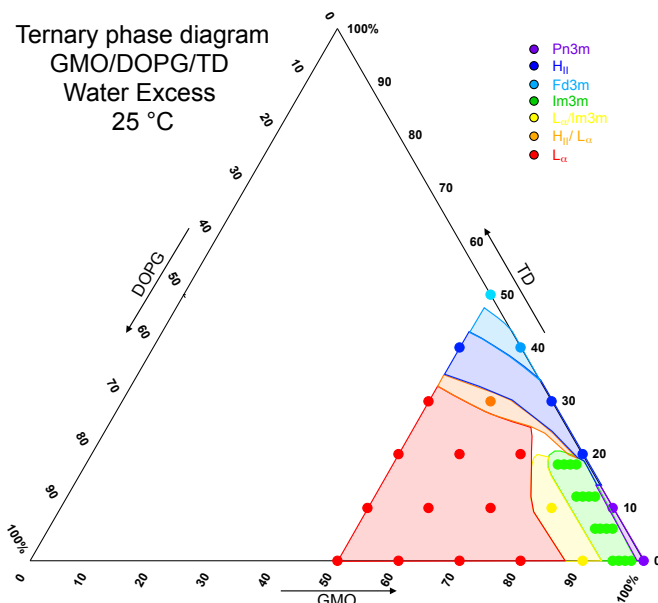


**Figure 32** Ternary phase diagram of MO/DOPG/TD system showing the Pn3m structure (violet region), Im3m (green region), Lamellar (red region), H<sub>II</sub> (blue region), Fd3m (cyan region). The orange and yellow regions describe the coexistence of lamellar/H<sub>II</sub> and lamellar/Im3m structure. The white region reported here, was out of the aim of the project.

## 3.7 Release and diffusive properties of mesophases (Paper V and VI)

### 3.7.1 Effects on the enzymatic kinetic reaction

From the data displayed in paragraph 3.6.1, it appears that – by playing with the additive amount – it is possible to finely tune the structural parameters of a Phyt mesophase finely. The aim of this study is to include two model drugs of different

size in the aqueous channels of the lipid mesophases: a small molecule (*p*-nitrophenyl phosphate), which is the substrate for an enzymatic reaction, and the alkaline phosphatase (AP) enzyme, to verify how they are released from the lipid structure.

The AP converts the uncoloured substrate *p*-nitrophenyl phosphate to *p*-nitrophenol (yellow-green product) in TRIS buffer at pH 7.5; the progressive formation of the product was followed through UV-vis spectroscopy. The molar extinction coefficients calculated from the Lambert-Beer plots of both the reaction substrate and product are  $\epsilon=10186 \text{ L mol}^{-1}\text{cm}^{-1}$  and  $\epsilon=16349 \text{ L mol}^{-1}\text{cm}^{-1}$  at 310 and 400 nm for *p*-nitrophenyl phosphate and *p*-nitrophenol, respectively. To characterize the reaction in aqueous solution, in the absence of the mesophase, we monitored the reaction kinetics at different substrate concentrations ( $1 \times 10^{-5}$ ,  $2 \times 10^{-5}$ ,  $4 \times 10^{-5}$ ,  $5 \times 10^{-5}$ ,  $6 \times 10^{-5}$  M) in the presence of 0.2 U/mL AP enzyme. The kinetics of formation of the enzymatic product were followed with a UV-Vis spectrophotometer at 400 nm. The complete kinetics are reported in Figure 33b, while the variation of the absorbance during the initial step of the reaction (from  $t = 0$  to  $t = 30$  s) is reported in Figure 33c.

Aiming to calculate the Michaelis-Menten constant and the maximum velocity of reaction, we calculated the linear Lineweaver-Burk plot (Equation 3.9):

$$\frac{1}{v} = \frac{K_M + [S]_0}{V_{max}[S]_0} = \frac{K_M}{V_{max}} \frac{1}{[S]_0} + \frac{1}{V_{max}} \quad (3.9)$$

where  $v$  is the velocity of reaction during the initial step,  $[S]_0$  the substrate concentration,  $K_M$  the Michaelis-Menten constant and  $V_{max}$  is the maximum velocity of reaction. The plot is reported in Figure 33d. From these results, the calculated Michaelis-Menten constant  $K_M$  and the  $V_{max}$  values are  $K_M=0.034 \text{ mM}$  and  $V_{max} = 7.9 \times 10^{-2} \text{ } \mu\text{mol of product/min}$ , respectively, which are slightly different from the values reported in literature.<sup>[132]</sup> However, they are fully explained taking into account the specific experimental conditions here adopted, *i.e.*, 25 °C instead of 37 °C, pH 7.5 instead of strong alkaline pH, the high concentration of products with respect to the enzyme and the very low concentration of metal ion ( $\text{Zn}^{2+}$  or  $\text{Mg}^{2+}$ ).

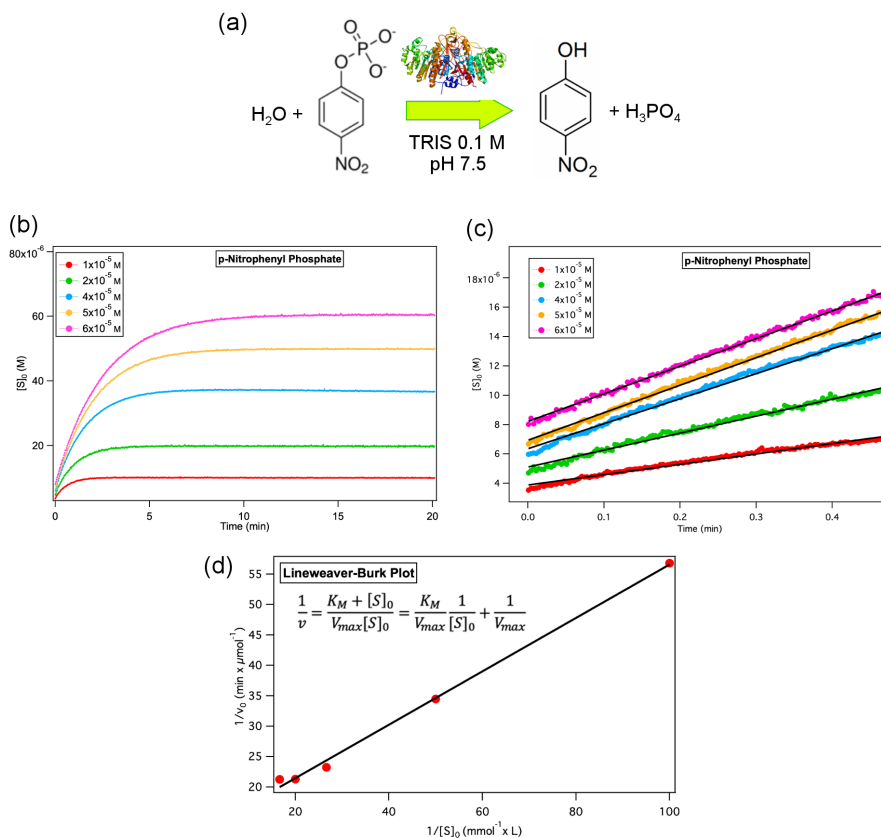


**Figure 33** a) Scheme of the conversion of *p*-nitrophenyl phosphate into the green-yellow product *p*-nitrophenol catalyzed by the enzyme Alkaline Phosphatase (AP) in TRIS buffer at pH 7.5 of; (b) Enzymatic reaction varying the concentration of substrate:  $1 \times 10^{-5}$  M (red),  $2 \times 10^{-5}$  M (green),  $4 \times 10^{-5}$  M (cyan),  $5 \times 10^{-5}$  M (yellow) and  $6 \times 10^{-5}$  M (purple) with their linear fit (black bold lines). The fixed amount of enzyme was 0.2 U/mL, and the reaction was followed with a UV-Vis Spectrophotometer at  $\lambda = 400$  nm during the initial step. (c) Linear fit (black solid line) performed during the initial step of enzymatic reaction per each concentration of substrate. (d) Lineweaver-Burk plot to extract the Michaelis-Menten constant and the maximum velocity of the reaction. The error bars on each point are smaller than the dimension of markers.

At this point, the impact of the confined *p*-nitrophenyl phosphate in the aqueous channels of different sizes was investigated, and the results are reported in Figure 34. The Phyt or Phyt/SS sample was hydrated with a proper amount of *p*-nitrophenyl phosphate solution; the hydrated mesophase was immersed in 2.5 mL of TRIS buffer solution with 0.2 U/mL AP enzyme in a UV-Vis

cuvette, and the reaction was followed for 6 days. The concentration of the substrate in the mesophase was chosen to reach a theoretical value of absorbance  $A=1$ . Figure 34b shows the conversion of substrate into the product by the AP enzyme dispersed in the surrounding TRIS buffer solution, while Figures 34c-d show the substrate and the product absorbance profile during the first 4 hours of enzymatic reaction. To observe product formation, two different pathways for substrate/enzyme contact are possible: (i) the enzyme diffuses inside the nanochannels and converts the substrate, the product leaves the nanochannels; (ii) the substrate diffuses from the nanochannels to the external medium and is then converted. The typical sizes of the enzyme (around 5 nm diameter) and the substrate (around 0.8 nm) are significantly different and should be compared to the sizes of the nanochannels.

From the data displayed in Figures 34c and 34d, it appears that over the first 5 minutes a steep increase of *p*-nitrophenol absorbance is observed for all systems (in the absence or the presence of increasing amounts of SS). This initial effect can be probably attributed to a part of the substrate localized at the interface of the lipid mesophase and the surrounding medium which freely diffuses in the buffer. There, AP readily converts it to *p*-nitrophenol. Conversely, for longer times, the increase in both *p*-nitrophenyl phosphate and *p*-nitrophenol absorbance over time is slower, consistent with the conversion of the substrate confined in the aqueous channels.

Therefore, we can expect that the substrate is locked but its diffusion towards the surrounding medium (driven by a chemical potential imbalance) can be differently hampered as a function of the size of the nanochannels characterizing the mesophases with different SS amounts. As we can see in Fig. 34c, the kinetic profile at each concentration of SS shows that the reaction proceeds slowly for the pure Phyt systems, and the rate of conversion gradually increases with the addition of sucrose stearate to the cubic phase. This is fully in line with the SAXS results. Several reports in the literature show that the diffusion rate of molecular probes depends on the channel size.<sup>[11,53,133]</sup> Therefore, in the second reaction regime the diffusion of the substrate from the nanochannels is the rate determining step.

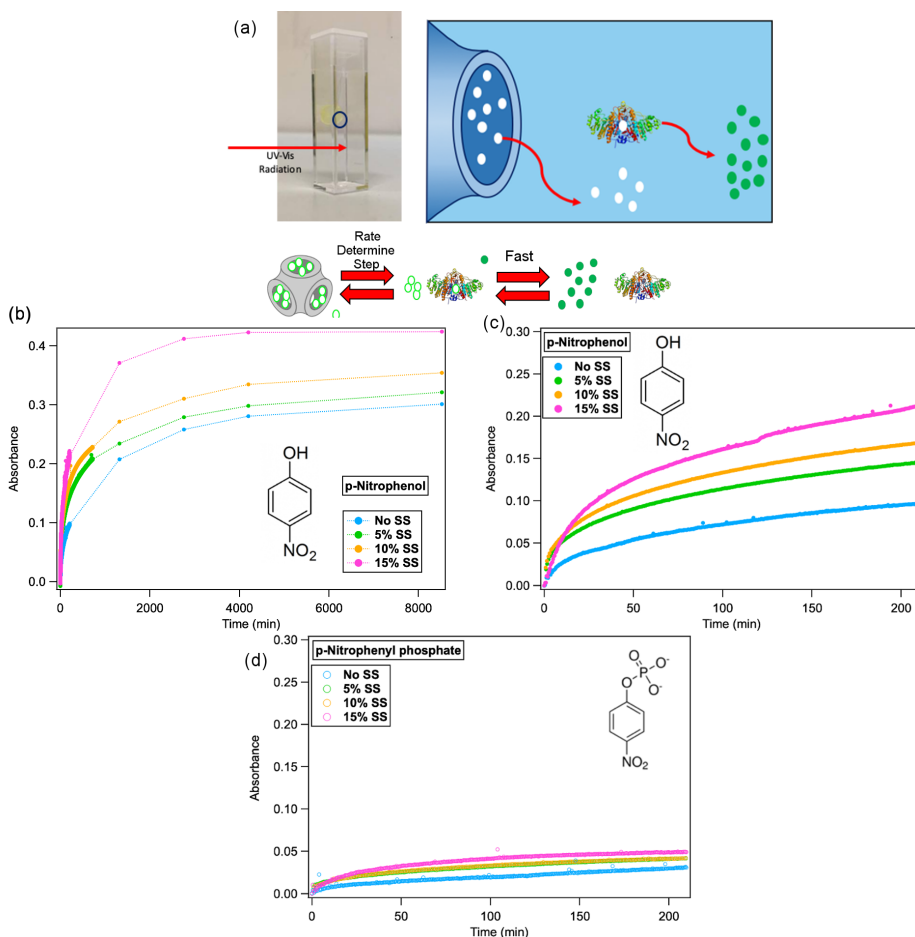


**Figure 34** (a) Sketch of the substrate (white dots with light green line) released in solution from cubic phase, converted by the enzyme Alkaline Phosphatase in TRIS buffer solution and the conversion into the final product of reaction p-nitrophenol (green dots). Panel (b) reports the complete kinetic profiles after 6 days of substrate release by mesophases and conversion by AP enzyme, recording the signal at 400 nm: No SS (cyan markers), 5% SS (green markers), 10% SS (orange markers) and 15% (purple markers). Panel (c) reports the increase of reaction product during the first 4 h for the cubic mesophases: No SS (cyan markers), 5% SS (green markers), 10% SS (orange markers) and 15% (purple markers). (d) Substrate release profiles detected through UV-Vis spectrophotometer at 310 nm during the first 4 h: No SS (empty cyan markers), 5% SS (empty green markers), 10% SS (empty orange markers) and 15% (empty purple markers).

Finally, if the whole reaction kinetics is considered, it is highlighted that, despite the amount of p-nitrophenyl phosphate released and converted by the enzyme being higher for the primitive cubic structure even after six days of

reaction, the absorbance is significantly different than the expected theoretical value, considering a complete release of the substrate. The origin of this inconsistency could be related to two possible reasons. First, due to the domains of liquid crystals not interconnected to each other and separated by grain boundaries, a complete release of the substrate could be not observed.<sup>[33]</sup> Secondly, the Alkaline Phosphatase enzymatic function is inhibited by the presence of high concentrations of the enzymatic products *p*-nitrophenol. This latter hypothesis is in agreement with the release profile of the substrate followed for long times at 310 nm: as a matter of fact, it appears that the substrate concentration in solution keeps increasing (due to its continuous release from the cubic phase), without being mirrored by the same trend of the product (monitored at 400 nm). However, for relatively short times, it appears that the rate-determining step of the reaction kinetics can be attributed to the release of the substrate to the reaction environment, while its conversion is a relatively fast process.

The diffusion is controlled, with a good approximation, by the size of water channel, which is dependent on the SS amount: the Phyt/SS/H<sub>2</sub>O mixed mesophases can be therefore of interest in the biomedical field as DDs vehicles to release continuously active molecules in a structurally controlled manner. As an example, while the binary mixture Phyt/water presents an initial velocity of product formation around  $3.78 \times 10^{-4}$  mmol/min, and the maximum absorbance is reached after 3 days, in the case of the ternary matrix the release can be accelerated up to 2 days with the higher amount of SS tested, where the initial velocity is enhanced to  $8.56 \times 10^{-4}$  mmol/min. More in general, the initial velocity of substrate conversion, when it is confined into the mesophases, is decreased by 2 orders of magnitude compared to the substrate freely diffusing in buffer solution (see Table 3).

An interesting application of cubic mesophases is their use for the delivery of macromolecules, such as proteins,<sup>[81,134,135]</sup> or also as biosensing and biocatalytic fuel cells.<sup>[133,136–139]</sup> In particular, due to the peculiar structure of these liquid-crystalline mesophases, it is possible to identify the existence of cages and necks, allowing hosting and retaining proteins to better control their release/diffusion. On the other hand, the mesophases affect the enzymatic activity,<sup>[133]</sup> the confinement of horseradish peroxidase dramatically affects its activity, both in its decreased ability to transform the substrate and in terms of deviation from the Michaelis-Menten behaviour. Moreover, the confinement in

the water channels slows down the diffusion of the protein molecules in the structure and their crystallization.<sup>[140]</sup> For that reason, the enzymatic kinetics are more complicated due to the poorly understood main factors which promote this phenomenon.<sup>[86]</sup>

**Table 3:** Rate of reactions expressed in mmol/min of converted substrate and channels size (nm). Data obtained from the release of substrate converted by the AP enzyme in buffer solution.

<b>Samples</b>	<b>Rate (mmol/min)</b>	<b>Channels Size (nm)</b>
<b>Solution</b>	$1.180 \times 10^{-2} (\pm 6 \times 10^{-5})$	/
<b>Phyt</b>	$3.78 \times 10^{-4} (\pm 3 \times 10^{-6})$	2.3
<b>Phyt/5% SS</b>	$5.3 \times 10^{-4} (\pm 1 \times 10^{-5})$	2.8
<b>Phyt/10% SS</b>	$5.5 \times 10^{-4} (\pm 1 \times 10^{-5})$	3.0
<b>Phyt/15% SS</b>	$8.56 \times 10^{-4} (\pm 3 \times 10^{-6})$	3.6

The inclusion of the AP enzyme in the Phyt/H<sub>2</sub>O mesophase was investigated in the absence and in the presence of SS, to monitor the effect of the confinement on the enzymatic reaction. As previously mentioned,<sup>[141]</sup> the dimension of the enzyme is around 5 nm. Considering a partial distribution of the enzyme between the leaflet facing the water environment and the nanochannels of the cubic mesophases, the encapsulation of the protein could be reached. However, we can probably expect that, in the absence of a chemical potential driving its diffusion from the mesophase to the surrounding medium, the enzyme will be more conveniently localized in the cages of the structure, rather than in the nanochannels.

To monitor the effect of enzymatic confinement on the AP enzymatic reaction, we adopted the following experimental set-up. The enzymatic reaction was followed for neat Phyt/H<sub>2</sub>O and swelled (Phyt/H<sub>2</sub>O/SS) cubic phases in a buffer solution containing  $6 \times 10^{-5}$  M of substrate. First, the enzymatic reaction was monitored at 400 nm for 90 minutes, during which the mesophase and the buffer were put in contact. In this way, it is possible to monitor the release of some non-encapsulated enzyme (localized on the cubic phase surface) and/or of the enzyme localized quite close to the cubic phase/aqueous environment interface. The reaction kinetics is reported in Figure 35b. As a second step, the cubic phase was placed in another cuvette with a fresh substrate at the same

concentration. In this way, it was possible to monitor the enzymatic catalysis due to the AP encapsulated within the cubic phase (Figure 35c).

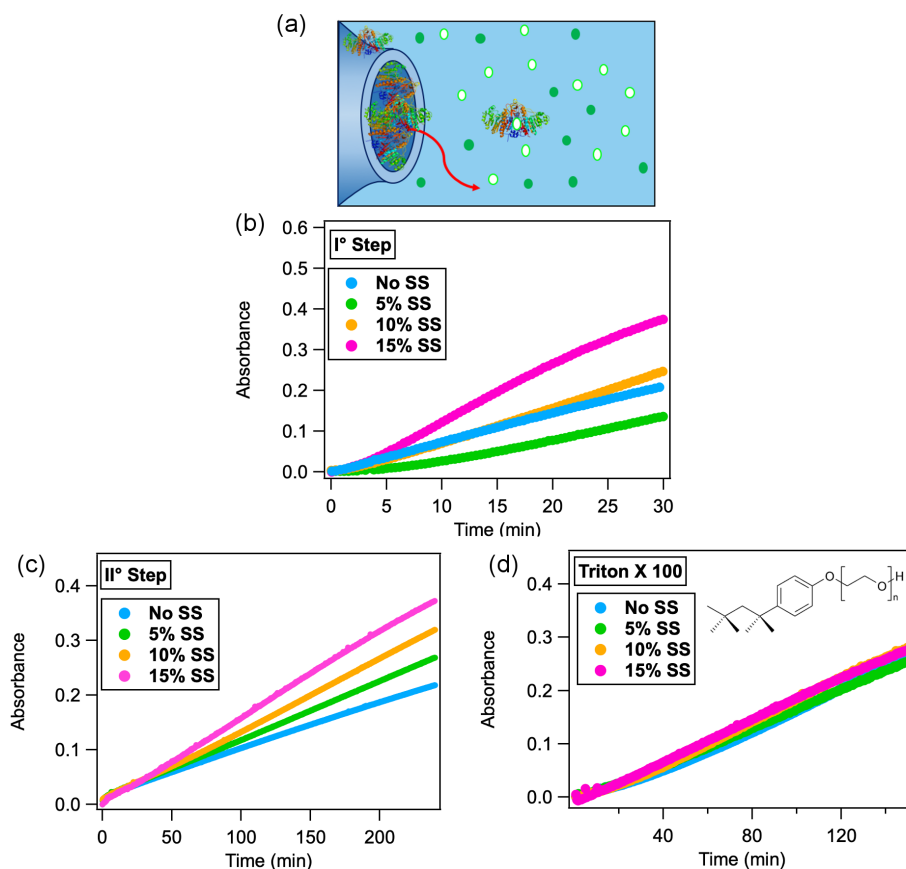


**Figure 35** Enzymatic kinetics of *p*-nitrophenyl phosphate in TRIS buffer during the release of AP enzyme encapsulated in cubic phase, schematized in (a). (b) Phyt (cyan markers), Phyt/ 5% w/w SS (green markers), Phyt/10% w/w SS (orange markers) and Phyt/15% w/w SS (purple markers) reaction profiles during the first 30 minutes (b) of enzyme released in the buffer solution with substrate: (c) kinetic profiles in a fresh buffer and substrate solution after the step described in (b). (d) Kinetic profiles pertaining to the cubic phase with or without SS: during the matching second step of experiment reported in (c), with the addition of Triton-X-100 which destroys the mesophase.

Analogously to the substrate confined in the channels, the encapsulated AP enzyme should be discussed in terms of possible pathways for the enzymatic reaction to proceed. When the enzyme is confined in the liquid crystalline

mesophase, the release of the encapsulated protein to the aqueous environment is a first possible mechanism to guarantee the close interaction of the enzyme with the substrate. Oppositely, a second possible mechanism is the penetration of the substrate inside the nanochannels of the liquid crystal, where it meets the enzyme, and it is subsequently released in the aqueous environment, as the reaction product.

Considering the first experiment (the cubic phase with the encapsulated enzyme directly immersed in a substrate solution), different enzymatic reaction kinetics for the enzyme encapsulated in liquid crystalline mesophases, with or without the sucrose stearate, were investigated. In particular, for all mesophases containing sucrose stearate, two trends can be identified in the kinetics of the enzymatic reaction. In order to rationalize this behaviour, it can be considered that – as previously pointed out – part of the enzyme could be localized at the liquid crystalline phase/water interface and it is fast released. At this point, the AP in solution is available to convert the substrate molecules, while the remaining AP resides inside the liquid crystalline structure and catalyses the substrate conversion more slowly. In line with this hypothesis, samples with varying SS amounts exhibit a lag time<sup>[142]</sup> between the first and second enzymatic kinetic trend. This is progressively decreased by enhancing the SS concentration: about 10 minutes for 5% w/w SS, 7-8 minutes in the case of 10% w/w SS and 5 minutes with 15% w/w SS (Figure 32b). Considering the swelling of the mesophase induced by the addition of SS, one can relate this variable effect to a variable amount of the enzyme trapped in the mesophases due to the higher water fraction characterizing the mesophase. Indeed, for the binary system, *i.e.*, Phyt/H<sub>2</sub>O in the absence of SS, the trend of the kinetic curve is monotonous (Figure 32b), suggesting that in this case the encapsulation of the enzyme in the liquid crystalline phase is strongly hampered, due to the small size of the nanochannels.

Concerning the second part of the curves for SS samples, the enzymatic reaction proceeds with a faster rate for the systems with higher SS percentage, suggesting that the size of the nanochannels has a prominent role, which might be related either to the release of the enzyme from the mesophase or to the penetration rate of the substrate into the aqueous channels of the mesophase. However, it should be noted that Phyt-15%wt SS shows an Im3m structure and, in agreement with the literature,<sup>[142]</sup> the topology, with the channel size, plays a fundamental role on the enzymatic activity.

After the first step, a control experiment was performed to verify that: (i) a significant amount of the enzyme is present inside the mesophases, after the first 90 minutes; (ii) the amount of the enzyme present in the different mesophases is comparable, in order to be able to compare the different mesophases in similar experimental conditions. The control experiment is displayed in Figure 35d: briefly, after a first step of the experiment (with similar results as those shown in Figure 35b), the "control" mesophases were destroyed by immersion in a 24 mg/mL solution of Triton X 100: the non-ionic surfactant, in relatively high concentration,<sup>[143,144]</sup> can dissolve the lipid assembly to yield mixed micelles, with a simultaneous quantitative release of AP originally contained in the mesophases. In Figure 35d, the absorbance of p-nitrophenol over time is reported for the different samples: the kinetic curves are almost overlapping, confirming both that a significant amount of enzyme is present inside the mesophases after the first step of the experiment, and that this amount is comparable for all liquid crystalline mesophases. Figure 35c reports the second step of the experiment, after the initial 90 minutes of mesophase immersion. All the curves display a monotonous trend, and the conversion rate appears strictly dependent on the size of the nanochannels of the mesophase.

The ensemble of experimental data does not allow distinguishing which pathways is occurring, *i.e.* whether the substrate diffuses into the mesophase or the enzyme is released. A simple size argument would rule out AP diffusion from the mesophase to the external medium as the prevailing mechanism, but we are not currently able to rule out the simultaneous substrate diffusion in the mesophase.

Besides the mechanism of enzyme-substrate interaction, it is interesting to notice that the enzymatic reaction is in the case of enzyme confinement in the lipid mesophase, strongly slowed down with respect to the case of substrate confinement and no confinement case. In addition, as already discussed, the reaction rate and mechanism depend on the topology of the lipid mesophase, in particular on the size of the aqueous channels, which is finely tuneable by controlling the additive concentration.

### 3.7.2 Relationship between structure and diffusive properties

Based on the results showed in paragraph 3.6.2, the introduction of molecules with different features allows us to extend the LCs structure range compared to the neat MO systems. As highlighted before, the inclusion of DOPG

and TD to MO assemblies shows a complex phase behavior depending on the relative concentration of the additives and their ability to impose their curvature in MO bilayer. However, even if their contribution can be perfectly counterbalanced (since they have opposite effects), it is reasonable to think that the *in-meso* diffusive properties of molecular probes confined into the channels are dependent on the variation of the water channels size. Indeed, the inclusion of DOPG and TD in MO systems allows for swelling or shrinking the nanochannels, producing a different lattice parameter for the same structure; for this reason, the diffusive properties of fluorophore through FCS experiments can be tested to verify a relationship between structure and diffusive properties. The molecular probes involved in this investigation are Rhodamine 110 and Rhodamine B Dextran, two hydrophilic fluorophores spontaneously encapsulated in the hydrophilic domains of liquid crystals. The molecular structure and FCS curves of the probes freely diffusing in water at 25 °C, are reported in Figure 36. The mathematical model to extract information on the diffusion coefficients of the probes is reported in Eq. 3.10:

$$G(\tau) = \frac{1}{\langle c \rangle \pi^2 w_0^2 z_0} \left( 1 + \frac{4D\tau}{w_0^2} \right)^{-1} \left( 1 + \frac{4D\tau}{z_0^2} \right)^{-\frac{1}{2}} \quad (3.10)$$

where  $\langle c \rangle$  is the average concentration of the probe in the confocal volume,  $w_0$  and  $z_0$  are respectively the lateral and axial parameters defining the detection volume (approximated as a 3D-ellipsoidal Gaussian shape), and  $D$  the diffusion coefficient of the probe. This model provides information on one fluorescent probe diffusing in a 3D space. While Rhodamine 110 shows an excellent fit result with the equation 3.10, the Rhodamine B Dextran, due probably to the synthesis procedure and work-up, does not show a single component: this is also confirmed by a separation of a concentrated fluorophore solution with a Vivaspin® provided with a membrane cut-off 5000  $M_w$ . The best-fitting result can be obtained with a 3D model of two different components, and the mathematical equation reported in Eq. 3.11:

$$G(\tau) = \frac{1}{\langle c \rangle \pi^2 w_0^2 z_0} \left[ f_1 \left( 1 + \frac{4D_1\tau}{w_0^2} \right)^{-1} \left( 1 + \frac{4D_1\tau}{z_0^2} \right)^{-\frac{1}{2}} + f_2 \left( 1 + \frac{4D_2\tau}{w_0^2} \right)^{-1} \left( 1 + \frac{4D_2\tau}{z_0^2} \right)^{-\frac{1}{2}} \right] \quad (3.11)$$

where  $f_1$  and  $f_2$  are the fractions parameters describing the abundance of a fluorescent component with respect to the other.

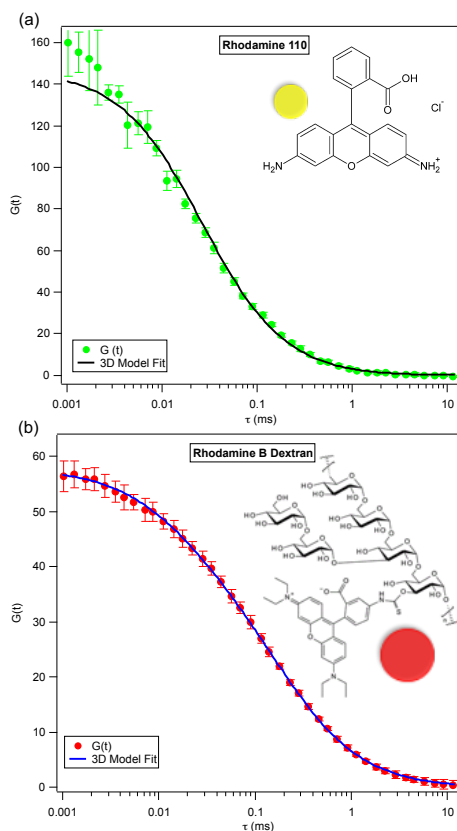


**Figure 36** FCS curves of (a) Rhodamine 110 and (b) Rhodamine B Dextran in water at 25 °C and their fit curves obtained by a 3D model with (a) single component and (b) two component.

The diffusion coefficient of the Rhodamine 110 probe is  $430 \mu\text{m}^2/\text{s}$ ,<sup>[145]</sup> while there are two diffusion coefficients for Rhodamine B-Dextran:  $420 \mu\text{m}^2/\text{s}$ <sup>[145]</sup> for the free Rhodamine B and  $41 \mu\text{m}^2/\text{s}$  for the Rhodamine B conjugated to the polysaccharide. In order make the discussion clearer, the

diffusion coefficient of Rhodamine B Dextran will be expressed as an average value based on the relative abundance of the two species:  $D_{\text{RBDex}}=166 \mu\text{m}^2/\text{s}^{[146]}$ .

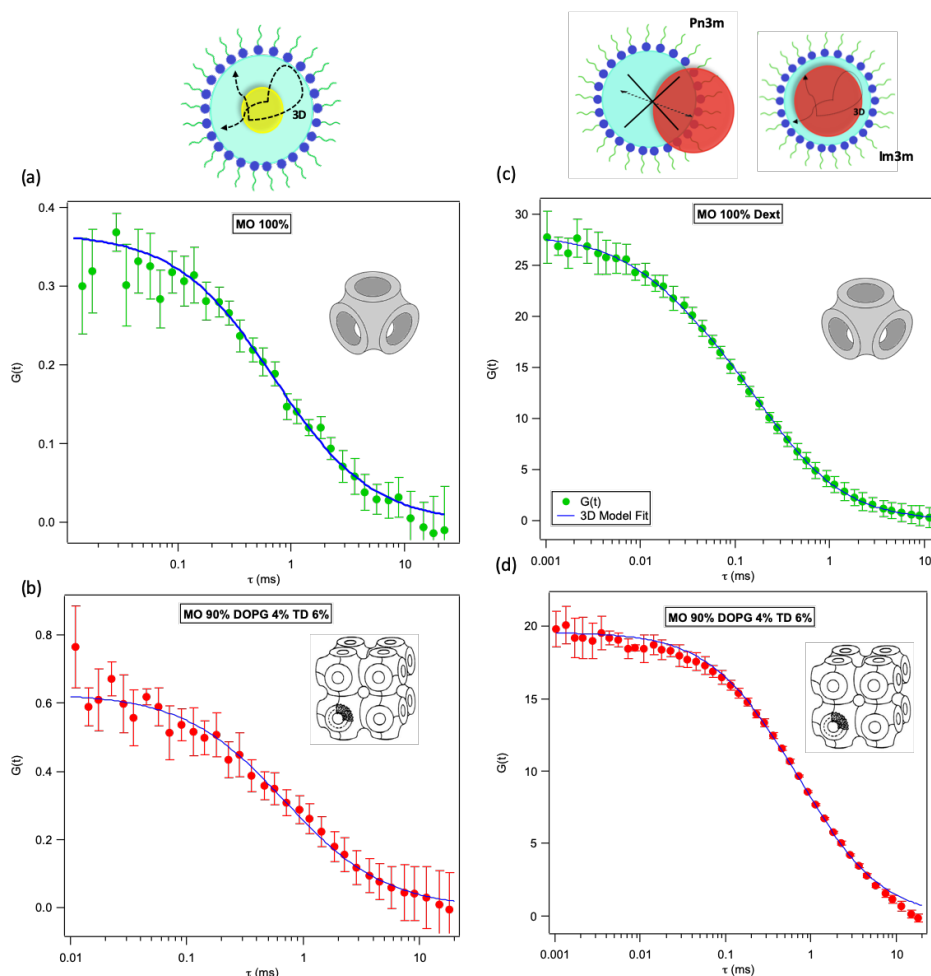


**Figure 37** FCS curves of Rhodamine 110 (a-b) and Rhodamine B Dextran (c-d) in Pn3m structure (a-c) and Im3m (b-d) structures. On top, a representative sketch of the probe Rhodamine 110 (yellow dot) in a water nanochannels of both Pn3m and Im3m mesophases, while the Rhodamine B Dextran (represented as red dot double in size of yellow dot), matches the dimension of Im3m nanochannels but while it locates spontaneously out of the channels in a Pn3m mesophases.

In agreement with the literature,<sup>[146]</sup> the sizes of the probes are around 1 nm and 2.6 nm for Rhodamine 110 e Rhodamine B Dextran, respectively. The encapsulation in the liquid crystalline matrix can be evaluated in terms of probe size compared to the lattice parameters. Using the same treatment reported in

Eqs 3.10 and 3.11, the fitting models were used to treat the FCS results for Pn3m (100% MO composition) and Im3m (90% MO, 4% DOPG and 6% TD) liquid crystals. In these cases, the 3D motion of the probes is allowed by the 3D tortuosity of cubic mesophases nanochannels, since the data can be interpreted using the same model as for “free” fluorophores. These results suggest that, in the case of Rhodamine 110, a confinement effect can be seen in both samples; indeed, the diffusion coefficient, compared to one for freely diffusing probes in water, is at least one order of magnitude lower. This phenomenon is related to the confinement in nanochannels, as previously highlighted in paragraph 1.7 of Chapter 1. The Rhodamine B Dextran shows a different behavior: while the average diffusion coefficient is around  $30 \mu\text{m}^2/\text{s}$  in Im3m mesophases, showing a confinement effect, in the case of Pn3m it is quite close to the  $166 \mu\text{m}^2/\text{s}$  value. Thus, considering the size of the diamond cubic structure comparable to the probe size, the hindered fluorophore cannot be entrapped, producing a “free” diffusion of the probe detectable through FCS.

Then, to connect structure with diffusive properties, the FCS experiments were performed on lamellar and hexagonal mesophases, comparing samples showing the same phase behavior but characterized by a different lattice parameter. In these cases, the equation describing the diffusion of the probes is slightly different from the 3D model reported in Eqs 3.10-3.11: the spatial probes diffusion is allowed in a 2D direction in case of a lamellar structure (a thick layer of water separates two bilayers, and the probes move parallel or perpendicular to the lipid membrane), and 1D direction of hexagonal mesophases where the movement of the probes is only possible along the direction of the cylindrical structure. The equations are reported in Eq. 3.12 and 3.13, for 2 components for a 2D and 1D diffusion respectively.<sup>[147]</sup> However, it should be taken into account that in case of Rhodamine 110,  $f_1=1$  and  $f_2=0$  in both of these equations.

$$G(t) = \frac{1}{N} \left[ f_1 \left( 1 + \frac{4D_1\tau}{w_0^2} \right)^{-1} + f_2 \left( 1 + \frac{4D_2\tau}{w_0^2} \right)^{-1} \right] \quad (3.12)$$

$$G(t) = \frac{1}{N} \left[ f_1 \left( 1 + \frac{4D_1\tau}{z_0^2} \right)^{-1/2} + f_2 \left( 1 + \frac{4D_2\tau}{z_0^2} \right)^{-1/2} \right] \quad (3.13)$$

The lamellar samples compared in that analysis present a lattice parameter of 115 Å (80% MO and 20% DOPG) and 216 Å (50% MO, 20% DOPG and 30% TD). Thus, a swelled lamellar phase can be reached in that conditions, since the water amount added to the dry lipid film is the same in both case. The FCS experiments performed with the fluorophores are showed in Figure 38.

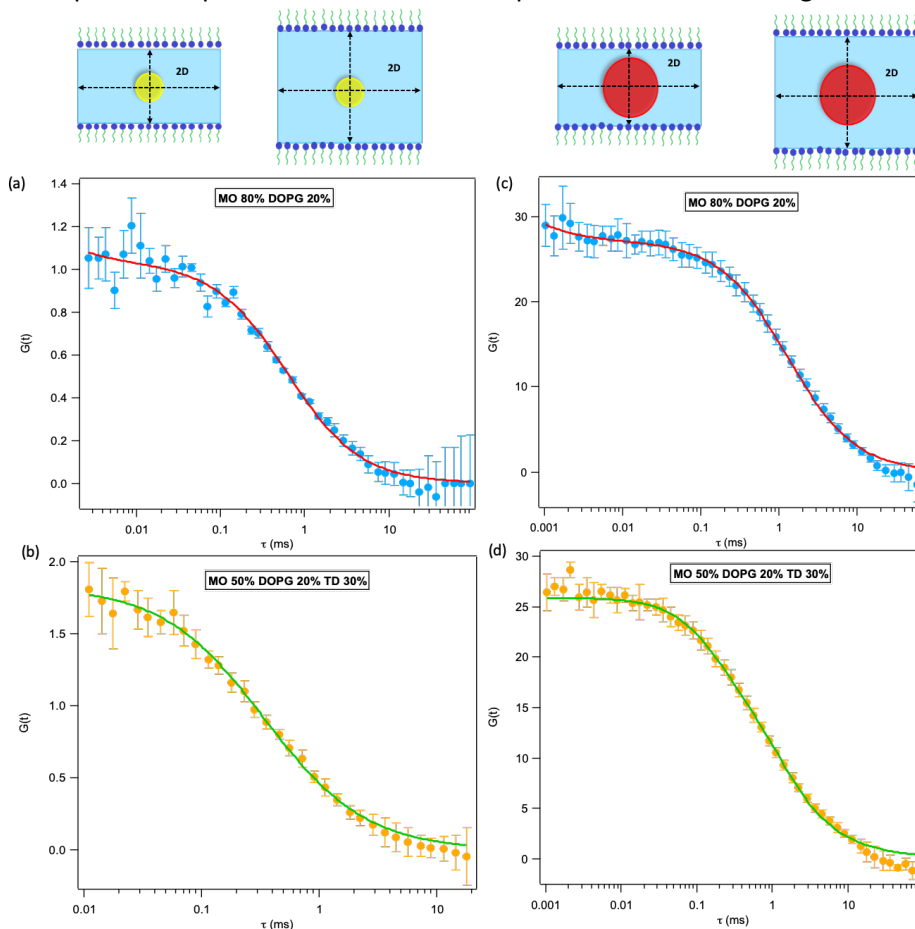


**Figure 38** FCS curves of Rhodamine 110 (a-b) and Rhodamine B Dextran (c-d) in lamellar structure with different lattice parameters; (a-c) are relative to the sample MO 80% and DOPG 20% with a lattice parameter 115 Å, while (b-d) represent the FCS curves relative to the sample swelled (MO 50%, DOPG 20% and TD 30%) with a lattice parameter 216 Å. On top, a representative sketch of the probe Rhodamine 110 (yellow dot) and Rhodamine B Dextran (represented as red dot double in size of yellow dot), located in water.

From the fitting results obtained with equation 3.12, the Rhodamine 110 diffusion coefficients for both lamellar samples are smaller than for the probes

in aqueous solution, thus in agreement with the results for cubic mesophases. It is reasonable to ascribe the results to a confinement of the fluorophore between two lipid bilayers separated by a thin layer of water. In particular, the results highlight that the swelled samples present a less restricted diffusion for Rhodamine 110: indeed, the diffusion coefficients are  $13 \mu\text{m}^2/\text{s}$  and  $24 \mu\text{m}^2/\text{s}$  for MO 80%-DOPG 20% and MO 50%-DOPG 20%-TD 30% respectively. The analysis of Rhodamine B Dextran curves shows a peculiar behavior: the size of the probe is similar to the water layer separating two adjoining bilayers; thus the probe is locked between the bilayers, as confirmed by the very low diffusion coefficient (the average value is around  $1 \mu\text{m}^2/\text{s}$  and  $1.2 \mu\text{m}^2/\text{s}$  for the un-swelled and swelled sample respectively). In these conditions, the Rhodamine label shows restricted diffusion.

Figure 39 shows the best fitting result modeling the FCS curves as the Eq. 3.13. About the hexagonal mesophases, the probe's motion is permitted along with the directionality imposed by the cylinders assembled in an  $H_{II}$  array. Thus, accordingly to the 1D model, the diffusion coefficient was extracted. In that experiment, comparing the hexagonal sample composed by a mixture of MO (70%) and TD (30%) with the swelled sample containing 60% MO, 10% DOPG and 30% TD, a swelling of the system by around 2 nm is observed (from 57 Å to 76 Å of lattice parameter). Rhodamine 110 shows a smaller diffusion coefficient in both samples, showing a more pronounced confinement of the fluorophore than the other mesophases. This is consistent with the dimension of the hydrophilic domains, where the probes are encapsulated, since the water nanochannels in the  $H_{II}$  structure are smaller than in the cubic phase. Moreover, the Rhodamine B Dextran size is larger than that of the water channels; thus, the encapsulation is not possible within the sample 70% MO 30% TD, while the probe is almost locked in case of swelled  $H_{II}$ . In order to summarize the results, all the diffusion coefficients are reported in Table 4 as a function of water nanochannels size or thickness of the water layer.

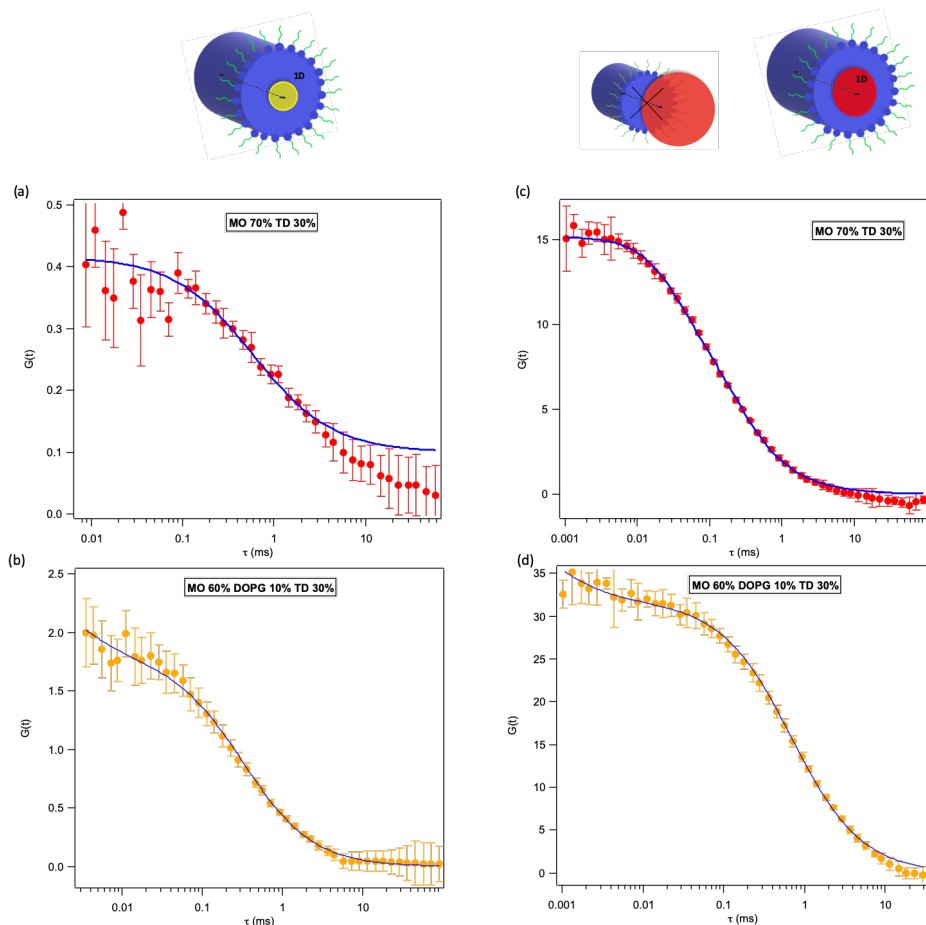


**Figure 39** FCS curves of Rhodamine 110 (a-b) and Rhodamine B Dextran (c-d) in hexagonal structure with different lattice parameters; (a-c) are relative to the sample MO 70% and TD 30% with a lattice parameter 57 Å, while (b-d) represent the FCS curves relative to the sample swelled (MO 60% DOPG 10% TD 30%) with a lattice parameter 76 Å. On top, a representative sketch of the probe Rhodamine 110 (yellow dot) and Rhodamine B Dextran (represented as red dot double in size of yellow one), located in water channels.

**Table 4:** Comparison of the diffusion coefficients derived by FCS curve for swelled and de-swelled cubic, hexagonal and lamellar phases. Rhodamine 110 and Rhodamine B Dextran were used for the experiments.

Samples	Rhodamine 110		Rhodamine B Dextran	
	$D_{\text{No-Swelled}}$	$D_{\text{Swelled}}$	$D_{\text{No-Swelled}}$	$D_{\text{Swelled}}$
Cubic	11±1	12±1	140±18	17±1
Lamellar	13±1	24±2	15±5	10±3
Hexagonal	14±2	5±1	158±15	8±2

# 4

## Conclusions and future perspective

In this PhD thesis, non-lamellar lipid mesophases with different additives (inorganic nanoparticles or hydrophobic and/or hydrophilic small molecules) have been studied, both in bulk and as nanosized particle dispersion. The final aim was to develop functional self-assembled materials with controlled structural and physicochemical features, appealing for biomedical applications.

Concerning bulk mesophases (MO/water or Phyt/water), we highlighted that the insertion of hydrophobic inorganic nanoparticles deeply modifies the phase behavior. In particular, as the concentration of nanoparticles in the lipid scaffold and/or the temperature increase, a Pn3m-H<sub>II</sub> phase transition is promoted. This structural effect can be fully rationalized according to simple energetic considerations, taking into account how the mesophase geometry, the coating and size of NPs affect the frustration packing and elastic energy of the lipid bilayer.<sup>[39]</sup> In addition, it should be pointed out that the Pn3m-to-H<sub>II</sub> phase transition causes a shrinking of the mesophase, and is therefore associated with a burst release of water and of the hydrophilic molecules originally confined in the water channels: this effect is of particular relevance, in view of the application of these systems as drug delivery vehicles, highlighting the possibility to exploit this phase transition to promote the release of hydrophilic active principles from the mesophase. In this respect, we have also shown that hydrophobic magnetic nanoparticles endow the MO cubic mesophases with responsiveness to external oscillating magnetic fields, promoting the Pn3m-to-H<sub>II</sub> phase transition which allows a spatio-temporal control of the release of small molecules confined in the lipid bilayers or in the water channels.<sup>[117]</sup> Besides the structural effects, the significant impact of hydrophobic NPs (both of gold and of magnetite, in the liquid crystalline mesophases) on the rheological properties of Phyt/water mesophase was shown. In particular, the presence of NPs enhances the solid-like behavior of the material. Interestingly, this effect is significantly

more pronounced for SPIONs with respect to AuNPs, evidencing possible long-range dipolar interactions between magnetic nanoparticles that may constitute an additional structuring factor for the material, decreasing its deformability upon stress deformation.<sup>[40]</sup>

To better explore the potential of these hybrid materials, the magnetic features of lipid liquid crystals combined with SPIONs were investigated, evaluating the magnetization of SPIONs as a function of temperature. The results suggest that during the Pn3m-H<sub>II</sub> phase transition the structural modification of the lipid scaffold induces a rearrangement of the SPIONs, which modify their interaction, ultimately determining an increase of the magnetization. Consistently with this hypothesis, a spontaneous reorganization of the NPs into a pearl-necklace supraparticle structure upon Pn3m to H<sub>II</sub> phase transition was observed.<sup>[39]</sup>

Liquid crystalline cubic phases of MO/water loaded with SPIONs were also dispersed into nanometric particles preserving the cubic internal structure, called magnetocubosomes, which are the most interesting systems for applicative purposes in the biomedical field, in particular, as responsive vectors for drug delivery. In this view, the Pn3m-H<sub>II</sub> transition induced upon an oscillating magnetic field – due to local heating operated by the NPs – is preserved both in bulk and dispersed liquid crystals. In addition, *in-vitro* test experiments proved the biocompatibility of magnetocubosomes on HT29 cell lines. It was highlighted how SPIONs inclusion affects the magnetic properties of lyotropic liquid crystals and how the responsivity of the hybrid biocompatible material can be exploited in the biomedical field.

Concerning the effect of additives small molecules for a systematic investigation on the effect of different amounts of sucrose stearate (SS) or a combination of DOPG and TD, on Phyt and MO mesophases, was performed to explore the phase diagram.

Structural data on phytantriol assemblies doped with increasing amounts of SS highlighted a good correlation between the amount of additive loaded in the lipid mesophase and the structural parameters of the lipid mesophase. This suggests the possibility to achieve an excellent control over the arrangement and the diameter of the water nanochannels of the cubic mesophases. The mesophases with different structural features were tested in terms of effects on the kinetics of the enzymatic reaction catalyzed by Alkaline Phosphatase, converting the substrate *p*-nitrophenyl phosphate into *p*-

nitrophenol, upon confinement of either the substrate or the enzyme in the mesophases doped with different amounts of additives. Two factors were shown to control the kinetics of the enzymatic reaction: the size of the confined molecule (substrate or enzyme) in comparison with the size of the water channels, and the entity of mesophase swelling (dictated by the amount of added SS).

Finally, MO mesophases doped with variable amounts of DOPG and TD showed a very complex phase diagram, with different arrangements of the lipid scaffold and different swelling degree of the mesophases. Upon confinement of hydrophilic fluorescent probes of different sizes (taken as model hydrophilic drugs) in the water channels of the lipid scaffolds, a correlation was found between the diffusing behavior of the model drugs with the structural features of the mesophase, both in terms of dimensionality of the mesophase and in terms of confinement efficiency (related to the swelling degree). Overall, the provided data confirm that these systems can efficiently retain active principles of different sizes in the water channels, with a tunable retention efficiency controlling the inclusion of additives: these systems can therefore be interesting as a vector for therapeutics with different molecular characteristics and sizes.

During the past years, non-lamellar mesophases and their structural change promoted by nanoparticles and additives have been rationalized and explained with theoretical prediction and experimental results. Several studies have shown a controlled tunability of the physico-chemical properties of mesophases, and this is of paramount to apply cubic structures in technological fields. Due to their simple preparation methods and the possibility to study their structural properties easily, bulk mesophases are more studied than dispersed liquid crystals. Dispersed liquid crystals are useful in the biomedical field to control the release of therapeutics. There are some examples in literature about cubosomes interacting with cells, containing hydrophobic drugs or big hydrophilic molecules, but there are not enough studies on the inclusion of small hydrophilic drugs tested in-vitro. Despite the effort to control the release of hydrophilic drugs through an ON-OFF mechanism, these are not efficiently retained due to a spontaneous leakage in solution. Possibly, this effect can be overcome by increasing our understanding on the stabilizer agents of cubosomes. In fact, a lack of experimental results is related to the small number of polymers tested and reported in the literature that could stabilize the colloidal liquid crystals. A thermoresponsive block co-polymer able to preserve the

cubosome structure and to generate a shell retaining drugs in the lipid scaffold, could be structurally modulated by local heating generated by AMF. In that way, a second generation of cubosome formulations can be designed to improve our control on the release of hydrophilic payloads.



---

# Bibliography

- [1] In *IUPAC Compend. Chem. Terminol.*, IUPAC, Research Triangle Park, NC, **2008**, p. 6854.
- [2] In *IUPAC Compend. Chem. Terminol.*, IUPAC, Research Triangle Park, NC, **2008**, p. 6896.
- [3] J. Zhai, C. Fong, N. Tran, C. J. Drummond, *ACS Nano* **2019**, *13*, 6178–6206.
- [4] C. Fong, T. Le, C. J. Drummond, *Chem. Soc. Rev.* **2012**, *41*, 1297.
- [5] G. C. Shearman, O. Ces, R. H. Templer, J. M. Seddon, *J. Phys. Condens. Matter* **2006**, *18*, S1105–S1124.
- [6] L. van 't Hag, S. L. Gras, C. E. Conn, C. J. Drummond, *Chem. Soc. Rev.* **2017**, *46*, 2705–2731.
- [7] S. Assenza, R. Mezzenga, *Nat. Rev. Phys.* **2019**, *1*, 551–566.
- [8] R. H. Templer, J. M. Seddon, P. M. Duesing, R. Winter, J. Erbes, *J. Phys. Chem. B* **1998**, *102*, 7262–7271.
- [9] H. Vacklin, B. J. Khoo, K. H. Madan, J. M. Seddon, R. H. Templer, *Langmuir* **2000**, *16*, 4741–4748.
- [10] M. Fuhrmans, V. Knecht, S. J. Marrink, *J. Am. Chem. Soc.* **2009**, *131*, 9166–9167.
- [11] S. Assenza, R. Mezzenga, *J. Chem. Phys.* **2018**, *148*, DOI 10.1063/1.5019224.
- [12] R. H. Templer, *Curr. Opin. Colloid Interface Sci.* **1998**, *3*, 255–263.
- [13] P. M. Duesing, R. H. Templer, J. M. Seddon, *Langmuir* **1997**, *13*, 351–359.
- [14] W. Helfrich, *Zeitschrift fur Naturforsch. - Sect. C J. Biosci.* **1973**, *28*, 693–703.
- [15] C. V. Kulkarni, W. Wachter, G. Iglesias-Salto, S. Engelskirchen, S. Ahualli, *Phys. Chem. Chem. Phys.* **2011**, *13*, 3004–3021.
- [16] J. Barauskas, T. Landh, *Langmuir* **2003**, *19*, 9562–9565.
- [17] X. Michalet, *Science (80- )*. **2005**, *307*, 538–544.
- [18] E. Lee, H. Jeon, M. Lee, J. Ryu, C. Kang, S. Kim, J. Jung, Y. Kwon, *Sci. Rep.* **2019**, *9*, 2494.
- [19] C. C. Fleischer, C. K. Payne, *Acc. Chem. Res.* **2014**, *47*, 2651–2659.
- [20] P. M. Castillo, A. Jimenez-Ruiz, J. M. Carnerero, R. Prado-Gotor, *ChemPhysChem* **2018**, *19*, 2810–2828.

- [21] K. Yang, Y. Liu, Y. Liu, Q. Zhang, C. Kong, C. Yi, Z. Zhou, Z. Wang, G. Zhang, Y. Zhang, et al., *J. Am. Chem. Soc.* **2018**, *140*, 4666–4677.
- [22] Y. C. Park, J. B. Smith, T. Pham, R. D. Whitaker, C. A. Sucato, J. A. Hamilton, E. Bartolak-Suki, J. Y. Wong, *Colloids Surfaces B Biointerfaces* **2014**, *119*, 106–114.
- [23] A. Salvatore, C. Montis, D. Berti, P. Baglioni, *ACS Nano* **2016**, *10*, 7749–7760.
- [24] O. Bixner, E. Reimhult, *J. Colloid Interface Sci.* **2016**, *466*, 62–71.
- [25] Y. Chen, A. Bose, G. D. Bothun, *ACS Nano* **2010**, *4*, 3215–3221.
- [26] J. M. Bulpett, T. Snow, B. Quignon, C. M. Beddoes, T.-Y. D. Tang, S. Mann, O. Shebanova, C. L. Pizzey, N. J. Terrill, S. A. Davis, et al., *Soft Matter* **2015**, *11*, 8789–800.
- [27] E. Venugopal, S. K. Bhat, J. J. Vallooran, R. Mezzenga, *Langmuir* **2011**, *27*, 9792–9800.
- [28] J. B. Marlow, M. J. Pottage, T. M. McCoy, L. De Campo, A. Sokolova, T. D. M. Bell, R. F. Tabor, *Phys. Chem. Chem. Phys.* **2018**, *20*, 16592–16603.
- [29] M. R. Preiss, A. Hart, C. Kitchens, G. D. Bothun, *J. Phys. Chem. B* **2017**, *121*, 5040–5047.
- [30] M. Wlodek, M. Kolasinska-Sojka, M. Szuwarzynski, S. Kereiche, L. Kovacik, L. Zhou, L. Islas, P. Warszynski, W. H. Briscoe, *Nanoscale* **2018**, *10*, 17965–17974.
- [31] W. K. Fong, T. L. Hanley, B. Thierry, N. Kirby, L. J. Waddington, B. J. Boyd, *Langmuir* **2012**, *28*, 14450–14460.
- [32] M. Mendoza, L. Caselli, A. Salvatore, C. Montis, D. Berti, *Soft Matter* **2019**, DOI 10.1039/C9SM01601E.
- [33] J. J. Vallooran, R. Negrini, R. Mezzenga, *Langmuir* **2013**, *29*, 999–1004.
- [34] J. J. Vallooran, S. Handschin, S. Bolisetty, R. Mezzenga, *Langmuir* **2012**, *28*, 5589–5595.
- [35] J. J. Vallooran, S. Bolisetty, R. Mezzenga, *Adv. Mater.* **2011**, *23*, 3932–3937.
- [36] S. Nappini, S. Fogli, B. Castroflorio, M. Bonini, F. Baldelli Bombelli, P. Baglioni, *J. Mater. Chem. B* **2016**, *4*, 716–725.
- [37] H. Sub Wi, K. Lee, H. Kyu Pak, *J. Phys. Condens. Matter* **2008**, *20*, 494211.
- [38] W. K. Fong, T. L. Hanley, B. Thierry, A. Tilley, N. Kirby, L. J. Waddington, B. J. Boyd, *Phys. Chem. Chem. Phys.* **2014**, *16*,

- 24936–24953.
- [39] M. Mendoza, C. Montis, L. Caselli, M. Wolf, P. Baglioni, D. Berti, *Nanoscale* **2018**, *10*, 3480–3488.
- [40] M. Mendoza, L. Caselli, C. Montis, S. Orazzini, E. Carretti, P. Baglioni, D. Berti, *J. Colloid Interface Sci.* **2019**, *541*, 329–338.
- [41] M. Rappolt, F. Cacho-Nerin, C. Morello, A. Yaghmur, *Soft Matter* **2013**, *9*, 6291.
- [42] M. Mionić Ebersold, M. Petrović, W.-K. Fong, D. Bonvin, H. Hofmann, I. Milošević, *Nanomaterials* **2018**, *8*, 91.
- [43] S. Guillot, S. Salentinig, A. Chemelli, L. Sagalowicz, M. E. Leser, O. Glatter, *Langmuir* **2010**, *26*, 6222–6229.
- [44] M. Pouzot, R. Mezzenga, M. Leser, L. Sagalowicz, S. Guillote, O. Glatter, *Langmuir* **2007**, *23*, 9618–9628.
- [45] A. Yaghmur, L. de Campo, S. Salentinig, L. Sagalowicz, M. E. Leser, O. Glatter, *Langmuir* **2006**, *22*, 517–521.
- [46] N. Tran, A. M. Hawley, J. Zhai, B. W. Muir, C. Fong, C. J. Drummond, X. Mulet, *Langmuir* **2016**, *32*, 4509–4520.
- [47] N. Tran, X. Mulet, A. M. Hawley, C. Fong, J. Zhai, T. C. Le, J. Ratcliffe, C. J. Drummond, *Langmuir* **2018**, *34*, 2764–2773.
- [48] A. Yaghmur, S. Al-Hosayni, H. Amenitsch, S. Salentinig, *Langmuir* **2017**, *33*, 14045–14057.
- [49] X. Shao, G. Bor, S. Al-Hosayni, S. Salentinig, A. Yaghmur, *Phys. Chem. Chem. Phys.* **2018**, *20*, 23928–23941.
- [50] Y. Da Dong, I. Larson, T. Hanley, B. J. Boyd, *Langmuir* **2006**, *22*, 9512–9518.
- [51] J. Zhai, R. B. Luwor, N. Ahmed, R. Escalona, F. H. Tan, C. Fong, J. Ratcliffe, J. A. Scoble, C. J. Drummond, N. Tran, *ACS Appl. Mater. Interfaces* **2018**, *10*, 25174–25185.
- [52] W. Fong, A. Sanchez-Ferrer, M. Rappolt, B. J. Boyd, R. Mezzenga, *Langmuir* **2019**, acs.langmuir.9b02288.
- [53] R. Negrini, R. Mezzenga, *Langmuir* **2012**, *28*, 16455–16462.
- [54] J. Zhai, N. Tran, S. Sarkar, C. Fong, X. Mulet, C. J. Drummond, *Langmuir* **2017**, *33*, 2571–2580.
- [55] A. I. I. Tyler, H. M. G. Barriga, E. S. Parsons, N. L. C. McCarthy, O. Ces, R. V. Law, J. M. Seddon, N. J. Brooks, *Soft Matter* **2015**, *11*, 3279–3286.
- [56] H. M. G. Barriga, A. I. I. Tyler, N. L. C. McCarthy, E. S. Parsons, O. Ces, R. V. Law, J. M. Seddon, N. J. Brooks, *Soft Matter* **2015**, *11*,

- 600–607.
- [57] S. Jia, A. Tan, A. Hawley, B. Graham, B. J. Boyd, *J. Colloid Interface Sci.* **2019**, *548*, 151–159.
- [58] K. J. Tangso, W. K. Fong, T. Darwish, N. Kirby, B. J. Boyd, T. L. Hanley, *J. Phys. Chem. B* **2013**, *117*, 10203–10210.
- [59] W. Fong, R. Negrini, J. J. Vallooran, R. Mezzenga, B. J. Boyd, *J. Colloid Interface Sci.* **2016**, *484*, 320–339.
- [60] W.-K. Fong, N. Malic, R. A. Evans, A. Hawley, B. J. Boyd, T. L. Hanley, *Biointerphases* **2012**, *7*, 3.
- [61] S. Jia, W.-K. Fong, B. Graham, B. J. Boyd, *Chem. Mater.* **2018**, *30*, 2873–2887.
- [62] J. D. Du, W.-K. Fong, S. Salentinig, S. M. Caliph, A. Hawley, B. J. Boyd, *Phys. Chem. Chem. Phys.* **2015**, *17*, 14021–14027.
- [63] R. Negrini, W.-K. Fong, B. J. Boyd, R. Mezzenga, *Chem. Commun.* **2015**, *51*, 6671–6674.
- [64] S. Salentinig, L. Sagalowicz, O. Glatter, *Langmuir* **2010**, *26*, 11670–11679.
- [65] M. Gontsarik, M. Mohammadtaheri, A. Yaghmur, S. Salentinig, *Biomater. Sci.* **2018**, *6*, 803–812.
- [66] R. Prajapati, M. Gontsarik, A. Yaghmur, S. Salentinig, *Langmuir* **2019**, *35*, 7954–7961.
- [67] M. Gontsarik, A. Yaghmur, Q. Ren, K. Maniura-Weber, S. Salentinig, *ACS Appl. Mater. Interfaces* **2019**, *11*, 2821–2829.
- [68] Y. Li, A. Angelova, F. Hu, V. M. Garamus, C. Peng, N. Li, J. Liu, D. Liu, A. Zou, *Langmuir* **2019**, *acs.langmuir.9b02257*.
- [69] T. Oka, M. Hasan, M. Z. Islam, M. Moniruzzaman, M. Yamazaki, *Langmuir* **2017**, *33*, 12487–12496.
- [70] C. Neto, D. Berti, G. D. Aloisi, P. Baglioni, K. Larsson, *Prog. Coll. Polym. Sci.* **2000**, *115*, 295–299.
- [71] J. Gustafsson, H. Ljusberg-Wahren, M. Almgren, K. Larsson, *Langmuir* **1997**, *13*, 6964–6971.
- [72] J. Barauskas, M. Johnsson, F. Joabsson, F. Tiberg, *Langmuir* **2005**, *21*, 2569–2577.
- [73] F. Caboi, G. S. Amico, P. Pitzalis, M. Monduzzi, T. Nylander, K. Larsson, *Chem. Phys. Lipids* **2001**, *109*, 47–62.
- [74] K. Larsson, *Curr. Opin. Colloid Interface Sci.* **2000**, *5*, 64–69.
- [75] J. Gustafsson, H. Ljusberg-Wahren, M. Almgren, K. Larsson, *Langmuir* **1997**, *13*, 6964–6971.

- [76] J. Gustafsson, H. Ljusberg-Wahren, M. Almgren, K. Larsson, *Langmuir* **1996**, *12*, 4611–4613.
- [77] J. Y. T. Chong, X. Mulet, L. J. Waddington, B. J. Boyd, C. J. Drummond, *Soft Matter* **2011**, *7*, 4768.
- [78] N. R. Yepuri, A. J. Clulow, R. N. Prentice, E. P. Gilbert, A. Hawley, S. B. Rizwan, B. J. Boyd, T. A. Darwish, *J. Colloid Interface Sci.* **2019**, *534*, 399–407.
- [79] J. Zhai, R. Suryadinata, B. Luan, N. Tran, T. M. Hinton, J. Ratcliffe, X. Hao, C. J. Drummond, *Faraday Discuss.* **2016**, *191*, 545–563.
- [80] B. Angelov, A. Angelova, M. Drechsler, V. M. Garamus, R. Mutafchieva, S. Lesieur, *Soft Matter* **2015**, *11*, 3686–3692.
- [81] R. Ghanbari, S. Assenza, A. Saha, R. Mezzenga, *Langmuir* **2017**, *33*, 3491–3498.
- [82] R. Negrini, R. Mezzenga, *Langmuir* **2011**, *27*, 5296–5303.
- [83] S. Phan, W.-K. Fong, N. Kirby, T. Hanley, B. J. Boyd, *Int. J. Pharm.* **2011**, *421*, 176–182.
- [84] Z. A. Almsherqi, S. D. Kohlwein, Y. Deng, *J. Cell Biol.* **2006**, *173*, 839–844.
- [85] E. L. Snapp, R. S. Hegde, M. Francolini, F. Lombardo, S. Colombo, E. Pedrazzini, N. Borgese, J. Lippincott-Schwartz, *J. Cell Biol.* **2003**, *163*, 257–269.
- [86] J. J. Vallooran, S. Assenza, R. Mezzenga, *Angew. Chemie - Int. Ed.* **2019**, *58*, 7289–7293.
- [87] L. Salvati Manni, S. Assenza, M. Duss, J. J. Vallooran, F. Juranyi, S. Jurt, O. Zerbe, E. M. Landau, R. Mezzenga, *Nat. Nanotechnol.* **2019**, *14*, 609–615.
- [88] K. Das, B. Roy, S. Satpathi, P. Hazra, *J. Phys. Chem. B* **2019**, *123*, 4118–4128.
- [89] J. Swenson, F. Kargl, P. Berntsen, C. Svanberg, *J. Chem. Phys.* **2008**, *129*, 045101.
- [90] A. Miskowiec, Z. N. Buck, F. Y. Hansen, H. Kaiser, H. Taub, M. Tyagi, S. O. Diallo, E. Mamontov, K. W. Herwig, *J. Chem. Phys.* **2017**, *146*, 125102.
- [91] L. Wang, J. Luo, Q. Fan, M. Suzuki, I. S. Suzuki, M. H. Engelhard, Y. Lin, N. Kim, J. Q. Wang, C. J. Zhong, *J. Phys. Chem. B* **2005**, *109*, 21593–21601.
- [92] S. Sun, H. Zeng, D. B. Robinson, S. Raoux, P. M. Rice, S. X. Wang, G. Li, *J. Am. Chem. Soc.* **2004**, *126*, 273–279.
-

- [93] M. Brust, M. Walker, D. Bethell, D. J. Schiffrin, R. Whyman, *J. Chem. Soc. Chem. Commun.* **1994**, 801–802.
- [94] D. Begriff, A. Hand, D. Zerlegung, D. Fraktionierung, A. Grund, D. Fraktionierbarkeit, S. Kurven, S.- Dinger, I. Authenticated, D. Date, **1940**, *70*, 155–193.
- [95] M. Kotlarchyk, S.-H. Chen, *J. Chem. Phys.* **1983**, *79*, 2461.
- [96] C. W. Reese, Z. I. Strango, Z. R. Dell, S. Tristram-Nagle, P. E. Harper, *Phys. Chem. Chem. Phys.* **2015**, *17*, 9194–204.
- [97] D. Marsh, *Handbook of Lipid Bilayers*, **2013**.
- [98] C. Caltagirone, A. M. Falchi, S. Lampis, V. Lippolis, V. Meli, M. Monduzzi, L. Prodi, J. Schmidt, M. Sgarzi, Y. Talmon, et al., *Langmuir* **2014**, *30*, 6228–6236.
- [99] P. A. Hassan, S. Rana, G. Verma, *Langmuir* **2015**, *31*, 3–12.
- [100] James F. Steffe, *Rheological Methods in Food Process Engineering*, Elsevier, **1996**.
- [101] P. Fernanda, in *Struct. Anal. Edible Fats*, Elsevier, **2018**, pp. 313–385.
- [102] J. Schindelin, I. Arganda-Carreras, E. Frise, V. Kaynig, M. Longair, T. Pietzsch, S. Preibisch, C. Rueden, S. Saalfeld, B. Schmid, et al., *Nat. Methods* **2012**, *9*, 676–682.
- [103] Y. Tian, M. M. Martinez, D. Pappas, *Appl. Spectrosc.* **2011**, *65*, 115–124.
- [104] K. Koynov, H.-J. Butt, *Curr. Opin. Colloid Interface Sci.* **2012**, *17*, 377–387.
- [105] S. Aleandri, C. Speciale, R. Mezzenga, E. M. Landau, *Langmuir* **2015**, *31*, 6981–6987.
- [106] J. B. Marlow, T. M. McCoy, C. Q. Ho, L. de Campo, R. Knott, T. D. M. Bell, R. F. Tabor, *Phys. Chem. Chem. Phys.* **2019**, *21*, 25649–25657.
- [107] R. Mezzenga, C. Meyer, C. Servais, A. I. Romoscanu, L. Sagalowicz, R. C. Hayward, *Langmuir* **2005**, *21*, 3322–3333.
- [108] C. Speciale, R. Ghanbari, R. Mezzenga, *Langmuir* **2018**, *34*, 5052–5059.
- [109] G. Schmidt, P. Lindner, I. Laue-langevin, *Colloid Polym. Sci.* **1996**, *88*, 85–88.
- [110] W. K. Fong, T. L. Hanley, B. Thierry, A. Tilley, N. Kirby, L. J. Waddington, B. J. Boyd, *Phys. Chem. Chem. Phys.* **2014**, *16*, 24936–24953.

- [111] R. Mezzenga, J. M. Seddon, C. J. Drummond, B. J. Boyd, G. E. Schröder-Turk, L. Sagalowicz, *Adv. Mater.* **2019**, *1900818*, 1–19.
- [112] C. Bonnaud, C. A. Monnier, D. Demurtas, C. Jud, D. Vanhecke, X. Montet, R. Hovius, M. Lattuada, B. Rothen-Rutishauser, A. Petri-Fink, *ACS Nano* **2014**, *8*, 3451–3460.
- [113] J. Faraudo, J. S. Andreu, C. Calero, J. Camacho, *Adv. Funct. Mater.* **2016**, *26*, 3837–3858.
- [114] M. Bonini, D. Berti, P. Baglioni, *Curr. Opin. Colloid Interface Sci.* **2013**, *18*, 459–467.
- [115] M. S. Martina, J. P. Fortin, C. Ménager, O. Clément, G. Barratt, C. Grabielle-Madelmont, F. Gazeau, V. Cabuil, S. Lesieur, *J. Am. Chem. Soc.* **2005**, *127*, 10676–10685.
- [116] M. Szlezak, D. Nieciecka, A. Joniec, M. Pękała, E. Gorecka, M. Emo, M. J. Stébé, P. Krysiński, R. Bilewicz, *ACS Appl. Mater. Interfaces* **2017**, *9*, 2796–2805.
- [117] C. Montis, B. Castroflorio, M. Mendozza, A. Salvatore, D. Berti, P. Baglioni, *J. Colloid Interface Sci.* **2015**, *449*, 317–326.
- [118] S. Biffi, L. Andolfi, C. Caltagirone, C. Garrovo, A. M. Falchi, V. Lippolis, A. Lorenzon, P. Macor, V. Meli, M. Monduzzi, et al., *Nanotechnology* **2017**, *28*, 055102.
- [119] S. Murgia, S. Bonacchi, A. M. Falchi, S. Lampis, V. Lippolis, V. Meli, M. Monduzzi, L. Prodi, J. Schmidt, Y. Talmon, et al., *Langmuir* **2013**, *29*, 6673–6679.
- [120] S. Murgia, A. M. Falchi, V. Meli, K. Schillén, V. Lippolis, M. Monduzzi, A. Rosa, J. Schmidt, Y. Talmon, R. Bizzarri, et al., *Colloids Surfaces B Biointerfaces* **2015**, *129*, 87–94.
- [121] S. Saesoo, S. Sathornsumetee, P. Anekwiang, C. Treetidnipa, P. Thuwajit, S. Bunthot, W. Maneepprakorn, L. Maurizi, H. Hofmann, R. U. Rungsardthong, et al., *Colloids Surfaces B Biointerfaces* **2018**, *161*, 497–507.
- [122] P. Astolfi, E. Giorgini, V. Gambini, B. Rossi, L. Vaccari, F. Vita, O. Francescangeli, C. Marchini, M. Pisani, *Langmuir* **2017**, *33*, 12369–12378.
- [123] M. Gontsarik, M. T. Buhmann, A. Yagmur, Q. Ren, K. Maniura-Weber, S. Salentinig, *J. Phys. Chem. Lett.* **2016**, *7*, 3482–3486.
- [124] H. Meng, M. Xue, T. Xia, Z. Ji, D. Y. Tarn, J. I. Zink, A. E. Nel, *ACS Nano* **2011**, *5*, 4131–4144.
- [125] E. Blanco, H. Shen, M. Ferrari, *Nat. Biotechnol.* **2015**, *33*, 941–951.
-

- [126] Q. He, Z. Zhang, F. Gao, Y. Li, J. Shi, *Small* **2011**, *7*, 271–280.
- [127] B. P. Dyett, H. Yu, J. Strachan, C. J. Drummond, C. E. Conn, *Nat. Commun.* **2019**, *10*, 4492.
- [128] Y. Da Dong, I. Larson, T. J. Barnes, C. A. Prestidge, B. J. Boyd, *ACS Appl. Mater. Interfaces* **2011**, *3*, 1771–1780.
- [129] D. P. Chang, J. Barauskas, A. P. Dabkowska, M. Wadsäter, F. Tiberg, T. Nylander, *Adv. Colloid Interface Sci.* **2015**, *222*, 135–147.
- [130] D. P. Chang, M. Jankunec, J. Barauskas, F. Tiberg, T. Nylander, *ACS Appl. Mater. Interfaces* **2012**, *4*, 2643–2651.
- [131] P. Vandoolaeghe, J. Barauskas, M. Johnsson, F. Tiberg, T. Nylander, *Langmuir* **2009**, *25*, 3999–4008.
- [132] R. L. Dean, *Biochem. Mol. Biol. Educ.* **2002**, *30*, 401–407.
- [133] W. Sun, J. J. Vallooran, A. Zabara, R. Mezzenga, *Nanoscale* **2014**, *6*, 6853–6859.
- [134] L. Van’T Hag, L. De Campo, C. J. Garvey, G. C. Feast, A. E. Leung, N. R. Yepuri, R. Knott, T. L. Greaves, N. Tran, S. L. Gras, et al., *J. Phys. Chem. Lett.* **2016**, *7*, 2862–2866.
- [135] C. Speziale, A. F. Zabara, C. J. Drummond, R. Mezzenga, *ACS Nano* **2017**, *11*, 11687–11693.
- [136] W. Sun, J. J. Vallooran, W.-K. Fong, R. Mezzenga, *J. Phys. Chem. Lett.* **2016**, *7*, 1507–1512.
- [137] E. Nazaruk, R. Bilewicz, G. Lindblom, B. Lindholm-Sethson, *Anal. Bioanal. Chem.* **2008**, *391*, 1569–1578.
- [138] D. Li, M. Caffrey, *Proc. Natl. Acad. Sci.* **2011**, *108*, 8639–8644.
- [139] J. J. Vallooran, S. Handschin, S. M. Pillai, B. N. Vetter, S. Rusch, H.-P. Beck, R. Mezzenga, *Adv. Funct. Mater.* **2016**, *26*, 181–190.
- [140] L. Van’T Hag, L. De Campo, N. Tran, A. Sokolova, R. Trenker, M. E. Call, M. J. Call, C. J. Garvey, A. E. Leung, T. A. Darwish, et al., *Langmuir* **2019**, DOI 10.1021/acs.langmuir.9b00647.
- [141] M. de Backer, S. McSweeney, H. B. Rasmussen, B. W. Riise, P. Lindley, E. Hough, *J. Mol. Biol.* **2002**, *318*, 1265–1274.
- [142] W. Sun, J. J. Vallooran, R. Mezzenga, *Langmuir* **2015**, *31*, 4558–4565.
- [143] A. C. Caritá, B. Mattei, C. C. Domingues, E. De Paula, K. A. Riske, *Langmuir* **2017**, *33*, 7312–7321.
- [144] A. Pizzirusso, A. De Nicola, G. J. A. Sevink, A. Correa, M. Cascella, T. Kawakatsu, M. Rocco, Y. Zhao, M. Celino, G. Milano, *Phys. Chem. Chem. Phys.* **2017**, *19*, 29780–29794.

- [145] P.-O. Gendron, F. Avaltroni, K. J. Wilkinson, *J. Fluoresc.* **2008**, *18*, 1093–1101.
- [146] T. Peulen, K. J. Wilkinson, *Environ. Sci. Technol.* **2011**, *45*, 3367–3373.
- [147] C. Montis, P. Baglioni, D. Berti, *Soft Matter* **2014**, *10*, 39–43.

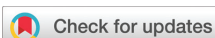


# Appendices: List of Papers



# Paper I





Cite this: *Nanoscale*, 2018, **10**, 3480

## On the thermotropic and magnetotropic phase behavior of lipid liquid crystals containing magnetic nanoparticles†

Marco Mendoza, <sup>a</sup> Costanza Montis, <sup>a</sup> Lucrezia Caselli, <sup>a</sup> Marcell Wolf,<sup>b</sup> Piero Baglioni<sup>a</sup> and Debora Berti <sup>\*,a</sup>

The inclusion of superparamagnetic iron oxide nanoparticles (SPIONs) in lipid mesophases is a promising strategy for drug-delivery applications, combining the innate biocompatibility of lipid architectures with SPIONs' response to external magnetic fields. Moreover, the organization of SPIONs within the lipid scaffold can lead to locally enhanced SPIONs concentration and improved magnetic response, which is key to overcome the current limitations of hyperthermic treatments. Here we present a Small-Angle X-ray Scattering (SAXS) structural investigation of the thermotropic and magnetotropic behavior of glyceryl monooleate (GMO)/water mesophases, loaded with hydrophobic SPIONs. We prove that even very low amounts of SPIONs deeply alter the phase behavior and thermotropic properties of the mesophases, promoting a cubic to hexagonal phase transition, which is similarly induced upon application of an Alternating Magnetic Field (AMF). Moreover, in the hexagonal phase SPIONs spontaneously self-assemble within the lipid scaffold into a linear supraparticle. This phase behavior is interpreted in the framework of the Helfrich's theory, which shows that SPIONs affect the mesophase both from a viscoelastic and from a structural standpoint. Finally, the dispersion of these cubic phases into stable magnetic colloidal particles, which retain their liquid crystalline internal structure, is addressed as a promising route towards magneto-responsive drug-delivery systems (DDS).

Received 14th November 2017,

Accepted 26th January 2018

DOI: 10.1039/c7nr08478a

rsc.li/nanoscale

## Introduction

Lipid self-assembly into lamellar and non-lamellar architectures is ubiquitous in natural systems,<sup>1</sup> the most prominent example being the lamellar structural unit of cell membranes. Synthetic lipid assemblies have been used to model and understand membrane-related processes in simplified architectures<sup>2,3</sup> and to engineer compartmentalized systems that can have numerous applications, especially in the biomedical field. Based on their molecular architecture and on experimental conditions, lipids show a rich polymorphism, with structures where both hydrophobic and hydrophilic domains occur. The volume fractions and the morphology of these domains depend on the phase structure and phase transitions

can be promoted by tuning control parameters, such as temperature, pressure and water content.

Several features of lipid assemblies lend themselves to the development of nanostructured vehicles for the encapsulation and release of drugs<sup>4–6</sup> or nucleic acids.<sup>7,8</sup> Structural change in lipid mesophase is caused by some external stimuli like temperature, pH<sup>9</sup> and magnetic field<sup>10,11</sup> or, in other case, adding additives that modify lipid assembly.<sup>12,13</sup>

Glyceryl monooleate (GMO) has been extensively studied for its biocompatibility, biodegradability and variegated phase structure, which depends on water content and temperature. At room temperature, the GMO/H<sub>2</sub>O mixture displays a lamellar phase L<sub>c</sub> for low water amounts and a bicontinuous cubic phase gyroid (*Ia3d*) and diamond (*Pn3m*) at relatively higher water contents. These mesophases have a high degree of symmetry and periodical water nanochannels,<sup>14</sup> whose geometry can be described using infinite periodical minimal surfaces (IPMS) or, in other words, a triply periodically surface with zero mean curvature. The three possible IPMSs described by Schoen and Schwartz are the gyroid (G), diamond (D) and primitive (P), with spatial groups *Ia3d*, *Pn3m* and *Im3m*, respectively, all of them observed for GMO cubic phases, depending on the experimental conditions. While the phase

<sup>a</sup>Department of chemistry and CSGI, University of Florence, Via della Lastruccia 3, Sesto Fiorentino, 50019 Florence, Italy. E-mail: debora.berti@unifi.it

<sup>b</sup>Institute of Inorganic Chemistry, Graz University of Technology, Stremayrgasse 9/IV, 8010 Graz, Austria

† Electronic supplementary information (ESI) available: Detailed Materials and methods section, additional SAXS data, derivation of principal equation and DLS analysis. See DOI: 10.1039/c7nr08478a

diagram of GMO/H<sub>2</sub>O binary system is well-established, the structural effects of additives on GMO-based systems have been the subject of more recent studies addressing the relevant phenomena connected with the topological variations of GMO mesophases designed for drug delivery, *e.g.*, in drug loading-release processes<sup>15</sup> or protein crystallization.<sup>16,17</sup>

Concerning this topic, the inclusion of magnetic nanoparticles (SPIONs) in lipid mesophases is of particular interest, giving the possibility to endow the lipid matrix with responsiveness to magnetic fields. Recently, it has been shown that hydrophilic SPIONs embedded in monolinolein liquid crystals control the structural organization of the lipid mesophase when exposed to an external static magnetic field.<sup>18–20</sup>

A prominent relevance, particularly for biomedical applications, is SPIONs responsiveness to alternating magnetic fields (AMF). In this respect, the inclusion of SPIONs into lipid scaffolds is interesting from at least two different standpoints. First, as a possible way to overcome the necessity of high SPIONs concentration in tissues, to abide by the so-called Brezovich criterion, *i.e.*, the exposure safety limit to magnetic fields for the application of SPIONs in hyperthermia-based medical treatments.<sup>21–23</sup> Secondly, as a promising strategy for the development of biocompatible smart lipid-based drug delivery systems (DDS) responsive to static and alternating magnetic fields.

The responsivity of SPIONs to alternating magnetic fields (AMF) has been extensively addressed for applications in hyperthermia-based therapies. SPIONs concentrated into tumor tissues, *e.g.* thanks to a DDS or to simple enhanced permeability and retention (EPR) effect, act as local heaters, if subjected to AMF, due to Brownian and Néel relaxations, eventually causing the ablation of cells or tissues that need to be removed. To reach a sustainable efficiency, the local concentration of SPIONs in the target tissues should reach a level which is virtually unachievable.<sup>21</sup> This limitation has been tackled either by modifying the morphology of NPs<sup>22</sup> or by employing clusters of NPs,<sup>24</sup> rather than separated NPs. The spontaneous organization of SPIONs in lipid scaffolds of different architectures represents a strategy to achieve a locally enhanced SPIONs' concentration, maintaining a fine control on the particle arrangement and, thus, on their overall magnetic response.

The inclusion of SPIONs in lipid assemblies, particularly liposomes to form magnetoliposomes,<sup>25–27</sup> has been reported in the literature. When embedded in DPPC (dipalmitoyl-phosphatidylcholine) liposomes, SPIONs act as local heaters upon application of a low-frequency alternating magnetic field (LF-AMF) and induce a gel-to-liquid-crystalline transition of the bilayer, with enhanced permeability and consequent release of molecules entrapped in the lumen.

In a previous work,<sup>10</sup> whose findings were also confirmed by Szlezak *et al.*,<sup>4</sup> we demonstrated that a GMO cubic phase doped with hydrophobic SPIONs displays a similar AMF-responsivity, showing burst release of a model hydrophilic drug contained in the water channels of the mesophase when

exposed to a LF-AMF. At variance from the gel to liquid crystalline phase transition occurring in DPPC magnetoliposomes, the structural variations on the cubic lipid scaffold implied in the controlled release of hydrophilic drugs from water channels are not yet clear.

A fundamental comprehension of the effect of SPIONs on phase behavior of lipid mesophases is key to fully explore the potential of these hybrid devices, both for hyperthermia and for controlled release applications.

In this contribution, we investigate the structural effects of the inclusion of hydrophobic SPIONs towards the polymorphic behavior of GMO assemblies in water excess. The phase behavior of GMO/H<sub>2</sub>O/SPIONs is investigated as a function of the SPIONs percentage with respect to GMO and as a function of temperature. The arrangement of the SPIONs in lipid scaffolds of different geometries is investigated as well. The structure of GMO/H<sub>2</sub>O/SPIONs hybrid architectures in different conditions (SPIONs amount and temperature) is interpreted according to simple thermodynamic considerations in the framework of Helfrich's theory, to understand the effect of SPIONs on the structural and viscoelastic features of the lipid assemblies and devise a simple predictive model for SPIONs–lipids interaction. Finally, to explore the applicative potential of these hybrid architectures, we investigate the thermotropic behavior of dispersed GMO/water/SPIONs assemblies (magnetocubosomes), and we perform an on-line investigation on the structural responsiveness of bulk GMO/water/SPIONs assemblies to LF-AMF, monitoring the magnetotropic response of the system.

## Results and discussion

### SPIONs inclusion in GMO mesophases

Hydrophobic Fe<sub>3</sub>O<sub>4</sub> magnetic nanoparticles (SPIONs) passivated with oleic acid and oleylamine were synthesized according to a well-established protocol<sup>28,29</sup> (see ESI for details†). The SAXS curves of the as-prepared dispersions (2.19 mg mL<sup>-1</sup> Fe<sub>3</sub>O<sub>4</sub> from ICP-AES) were diluted 1 : 3 in hexane and measured to infer the nanoparticle size with two different approaches, a model-free Guinier fit (radius  $18 \pm 3 \text{ \AA}$ <sup>30</sup>) and a Schulz polydisperse spheres form factor fit (radius  $20 \pm 2 \text{ \AA}$ , see ESI†). Generally, lipid bilayers have thicknesses around 40 Å; some theoretical reports identify a threshold of 60 Å for nanoparticles' diameter not to destroy the lipid architecture,<sup>31</sup> even if the final effect is strictly dependent on hydrophobic/hydrophilic nature of NPs.<sup>32</sup> The synthesized SPIONs have therefore an ideal size to be embedded in a lipid membrane without disrupting the bilayer.

GMO cubic phases (50% w/w lipid–water fraction) were prepared, as described in the Experimental section (see ESI†), with different amounts of SPIONs, ranging from 0.23% w/w to 1.1% w/w with respect to GMO quantity. If expressed as number of nanoparticles per lipid unit surface, or as number of lipid molecules per nanoparticle (considering for the cubic phase a specific area of 400 m<sup>2</sup> g<sup>-1</sup> (ref. 33), see Table 1) these

**Table 1** GMO/H<sub>2</sub>O/SPIONs samples composition: SPIONs weight percentage with respect to GMO amount (w/w% SPIONs); number of SPIONs per GMO/H<sub>2</sub>O cubic phase area unit ( $N_{\text{SPIONs}}/A_{\text{GMO}}$ ) and volume unit ( $N_{\text{SPIONs}}/V_{\text{GMO}}$ ); number of GMO molecules per SPION ( $N_{\text{GMO}}/N_{\text{SPIONs}}$ )

w/w% SPIONs	$N_{\text{SPIONs}}/A_{\text{GMO}}$ ( $\mu\text{m}^{-2}$ )	$N_{\text{SPIONs}}/V_{\text{GMO}}$ ( $\mu\text{m}^{-3}$ )	$N_{\text{GMO}}/N_{\text{SPIONs}}$
0.23	~46	~17 312	~91 743
0.47	~93	~35 000	~45 248
0.94	~188	~70 313	~22 522
1.1	~217	~81 250	~19 493

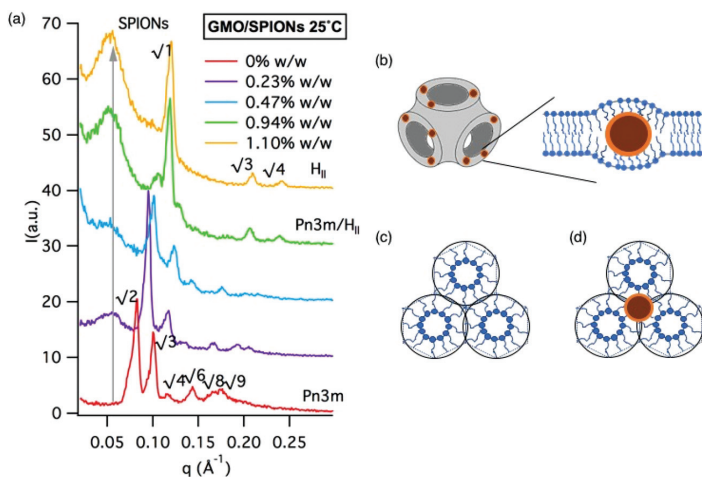
quantities result in relatively low NP concentrations, for all the investigated samples.

Fig. 1 shows the SAXS profiles of the mesophases in water at 25 °C in the absence and in the presence of increasing amounts of SPIONs. GMO 50% w/w is a *Pn3m* coexisting with water excess and represents the maximum swelling of this lipid at room temperature. When SPIONs are inserted in the liquid crystalline (LC) phase at 0.23–0.47% w/w SPIONs/GMO, the scattering peaks that describe the spatial correlation of the diamond cubic structure are preserved, but shifted to higher scattering vectors with respect to the binary system, indicating a shrinking of the liquid crystalline phase. At 0.94% w/w Fe<sub>3</sub>O<sub>4</sub>, the scattering profile shows the coexistence of the diamond cubic and another phase, whose nature, inverted hexagonal (H<sub>II</sub>), becomes clear for higher amounts of magnetic nanoparticles. It has been reported that a *Pn3m*-H<sub>II</sub> phase tran-

sition might occur upon perturbation of the lipid arrangement due to addition of alkanes or alkenes,<sup>12</sup> or inclusion of peptides.<sup>34–36</sup> To rule out that this transition is due to the partitioning of the NPs' coating agents (oleic acid and oleylamine) into the GMO bilayer, we performed a control experiment where the maximum amount of oleic acid and oleylamine was directly added to GMO without NP at 25 °C, yielding the profile of the diamond phase (see ESI† for details). No other components are present in GMO-SPIONs samples, since the SPIONs dispersions are separated from precursors (see Materials and methods section, ESI†) and milliQ water is employed for sample preparation.

Therefore, the structural transition observed for GMO is due to the insertion of SPIONs in the lipid scaffold; this NP-promoted transition could be relevant in the framework of a better understanding of nano-bio interfaces and possible toxic effects caused by SPIONs.<sup>37</sup> This finding is also consistent with recent works of Briscoe and coworkers,<sup>38</sup> who demonstrated a noteworthy effect of silica nanoparticles in shifting the phase boundaries between hexagonal H<sub>II</sub> and lamellar L<sub>α</sub> phases in phospholipids assemblies.

As clearly shown in Fig. 1, the SAXS curves in the presence of SPIONs display an additional peak at low  $q$ , attributable to spatial correlations of the SPIONs in the lipid matrix,<sup>10</sup> whose intensity increases as the amount of nanoparticles increases. The existence of a correlation distance, of about 110–120 Å if calculated as  $2\pi/q_{\text{max}}$ , implies that SPIONs exhibit a quasi-ordered arrangement within the lipid scaffold. The relatively large correlation distance can be justified taking into



**Fig. 1** (a) SAXS profiles of GMO 50% w/w water liquid crystalline phases in the presence of different SPIONs amounts: from bottom to top SAXS curves of the samples with increasing SPIONs percentages (0; 0.32; 0.47; 0.94; 1.1% w/w with respect to GMO amount) are displayed with suitable offsets; (b) (c) (d) schemes representing the effect of the SPIONs on the packing frustration energy: (b) when inserted in a lipid bilayer, the SPIONs increase the packing frustration and bring an energy penalty caused by the stretch of lipid chains to fill the voids along the equatorial position of nanoparticles, (c) in the hexagonal phase the chain ends would fall on the circles. As a result, the major packing frustration is localized in the void spaces of the cylindrical structure, (d) hexagonal phase with SPIONs: the previous frustration packing is released, with the hydrophobic nanoparticles localized in the void spaces.

account a contribution due to the spatial organization imposed by the lipid phase geometry and, probably, an additional contribution due to magnetic dipolar and van der Waals interactions between the SPIONs, similarly to what observed for concentrated dispersions of magnetic nanoparticles upon solvent evaporation.<sup>39</sup> GMO/H<sub>2</sub>O/SPIONs systems are peculiar both in terms of the polymorphic behavior of the GMO lipid matrix induced by the presence of SPIONs and in terms of SPIONs ordered arrangement within the lipid scaffold imposed by GMO phase geometry in water excess.

In order to rationalize the *Pn3m*-H<sub>II</sub> phase transition induced by the NPs from a thermodynamic point of view, we can write the total free energy of a lipid bilayer  $g_T$  as composed of three terms:<sup>33</sup>  $g_C$  free energy of elastic curvature,  $g_P$  frustration packing free energy and  $g_{inter}$  interaction energy term, that is generally negligible.

$$g_T = g_C + g_P + g_{inter} \quad (1)$$

Considering the energy difference between the hexagonal (final) and cubic (initial) phase, the variation of the total free energy of the bilayer, connected with the cubic to hexagonal phase transition  $\Delta g_T$  is:

$$\Delta g_T = g_{H_{II}} - g_{Pn3m} = \Delta g_C + \Delta g_P \quad (2)$$

It is known that the hexagonal phase<sup>40</sup> is characterized by a higher frustration packing energy than the bicontinuous cubic phase ( $\Delta g_P > 0$ ), and by a lower energy of elastic curvature ( $\Delta g_C < 0$ ).<sup>41</sup> Taking into account that, in the absence of SPIONs, the cubic to hexagonal phase transition is already favored according to the elastic contribution ( $g_C$ ), we can hypothesize that a major effect of the SPIONs on the free energy of the bilayer in the hexagonal phase is a decrease in the frustration packing energy. In fact, above a relatively low NP concentration threshold, we observe only a hexagonal phase. In a simplistic approach,  $g_P$  can be described with a harmonic oscillator-like equation:<sup>40</sup> its contribution arises from lipid chains that are stretched or compressed with respect to their relaxed state. In the presence of NPs embedded in a *Pn3m* structure, the lipids close to a NP experience a packing frustration due to the fact that their hydrocarbon chains stretch to fill the hydrophobic cavities (Fig. 1b). The increase of frustration packing contribution is thus a possible driving force to the cubic to hexagonal phase transition: NPs can fill the voids of cylindrical structure (Fig. 1d), without any stretching penalty for the lipid hydrocarbon chains (Fig. 1c). It has been shown that larger hydrophilic nanoparticles dramatically impact the organization of lipid mesophases, eventually driving completely different structural effects.<sup>42</sup> Clearly, in the above-described behaviour, the hydrophobicity of the SPIONs and their size matching with the lipid bilayer thickness, have a major role.

### Thermotropic behavior of GMO-SPIONs assemblies

Fig. 2a reports the well-known phase diagram of GMO as temperature and water percentage are varied (readapted with per-

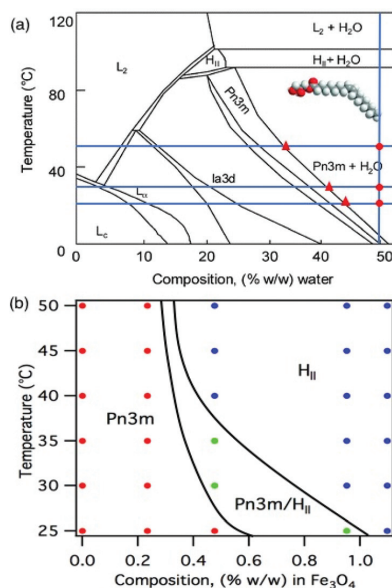


Fig. 2 (a) Phase diagram of GMO (readapted with permission from ref. 33). (b) Phase diagram of GMO/SPIONs at 50% w/w water content: structural dependence on temperature (°C) and on SPIONs content (% w/w with respect to GMO amount).

mission from ref. 33) compared to the phase behavior of GMO/SPIONs/water 50% w/w (Fig. 2b), as temperature and SPIONs content are varied. In the absence of SPIONs, the *Pn3m* to H<sub>II</sub> transition occur at 90 °C; in the presence of SPIONs, the transition temperature, Fig. 2b, decreases proportionally to the amount of NPs, down to 25 °C, for the highest Fe<sub>3</sub>O<sub>4</sub> % w/w.

To interpret this behavior, we first focus on the binary system. In the range 25 °C–50 °C, GMO 50% w/w H<sub>2</sub>O system keeps a bicontinuous diamond cubic phase structure, with the characteristic peaks progressively shifted to higher scattering vectors, with lattice parameters of  $104 \pm 2$  Å, (25 °C),  $96 \pm 2$  Å (35 °C),  $84 \pm 1$  Å (50 °C), which fully match the literature results<sup>43</sup> (see ESI† for details). If we adopt the previously described thermodynamic approach (eqn (2)), in this case  $\Delta g_T$  represents the variation of the free energy of GMO cubic phase between 50 °C (final state) and 25 °C (initial state). In the absence of a phase transition,  $\Delta g_P$  dependence on temperature is minor.<sup>41</sup> Thus,  $\Delta g_T$  can be considered in first approximation as only dependent on the variation of the free energy of elastic curvature  $\Delta g_C$ . The Helfrich's free energy of elastic curvature  $g_C$ <sup>44</sup> adapted for a lipid bilayer can be expressed as:

$$g_C = 2\kappa_B(H - H_0^B)^2 + \kappa_G^B K \quad (3)$$

with  $H_0^B$  and  $H$  mean spontaneous and mean curvatures respectively, in this case equal to zero,<sup>45</sup>  $\kappa_B$  and  $\kappa_G^B$  bending and Gaussian elastic moduli and  $K$  Gaussian curvature.  $g_C$  can be thus considered dependent on  $K$  and  $\kappa_G^B$ , which are related

to the viscoelastic properties of the lipid membrane. The Gaussian curvature  $K$  can be related to the experimentally observed lattice parameters  $d$  of the  $Pn3m$  cubic phase through the Gauss-Bonnet theorem<sup>1</sup>  $\langle K \rangle_0 = 2\pi\chi/\sigma d^2$ , where  $K_0$  is the mean Gaussian curvature to the mid-plane of lipid bilayer,  $\chi$  is the Euler-Poincaré parameter ( $\chi_{Pn3m} = -2$ ) and  $\sigma$  is a topological constant ( $\sigma_{Pn3m} = 1.919$ ).<sup>1</sup> In the absence of SPIONs, a linear decrease of the GMO  $Pn3m$  lattice parameter  $d$  with temperature increase, with slope  $-0.8 \text{ \AA } ^\circ\text{C}^{-1}$  (see ESI† for details) is observed, which, taking into account eqn (3) in combination with the Gauss-Bonnet theorem, is with a concomitant decrease in free energy of elastic curvature  $g_C$ . Thus, in the absence of any constraint due to SPIONs, as temperature increases the hydrophobic chains splay out from each other<sup>45,46</sup> and adopt a new curvature, due to a higher flexibility of the membrane, that leads to a decrease of lattice parameters.

If we consider the ternary sample containing the lowest amount of SPIONs (0.23% w/w), in the range 25 °C–50 °C the  $Pn3m$  lipid structure is preserved (see Fig. 2). The same thermodynamic considerations discussed are thus applied. Interestingly, in this case a milder dependence of the lattice parameter on temperature is observed, with a slope of  $-0.25 \text{ \AA } ^\circ\text{C}^{-1}$  (see ESI† for details). The lower sensitivity of the lattice parameters to temperature means that, in the presence of SPIONs, the decrease of the free energy of elastic curvature  $g_C$  is lower. Clearly, the SPIONs do not have effect only on the frustration packing free energy, as discussed in the previous paragraph, but affect also the viscoelastic properties of the membrane, through  $g_C$ . The effect of nanoparticles on the elastic properties of lipid mono-bilayer has been recently addressed, highlighting either softening or stiffening effects on the lipid phases depending on physico-chemical properties of NPs, generally considered with a hydrophilic coating.<sup>47</sup> In this case the modifications of the viscoelastic properties of the membrane are provoked by hydrophobic SPIONs embedded in the membrane.

Finally, we focused our attention on the sample whose phase transition is in the range 30–40 °C, close to physiological temperature, 0.47% w/w of SPIONs.

In Fig. 3 the SAXS profiles of 50% w/w GMO (25–35–50 °C Fig. 3a) and this latter sample (at 25–30–35–40–45–50 °C, Fig. 3b) are displayed. For GMO/SPIONs 0.47% w/w, the diamond cubic phase, which is the only present at 25 °C, is preserved at 30 and 35 °C, with a minor sensitivity of the lattice parameter on the temperature and the appearance of some extra peaks. Due to the coexistence with an inverse hexagonal phase  $H_{II}$ , these extra peaks are not ascribable to the  $Pn3m$  structure. The cubic phase signature completely disappears in the range 35–40 °C and since 40 °C only the  $H_{II}$  phase can be observed. With the same thermodynamic considerations, the total free energy of lipid bilayer  $\Delta g_T$  can be written in terms of  $\Delta g_p$  and  $\Delta g_C$  contributions, which can be separately considered. As already pointed out, in the absence of phase transition  $g_p$  exhibits a minor temperature dependence.<sup>41</sup>

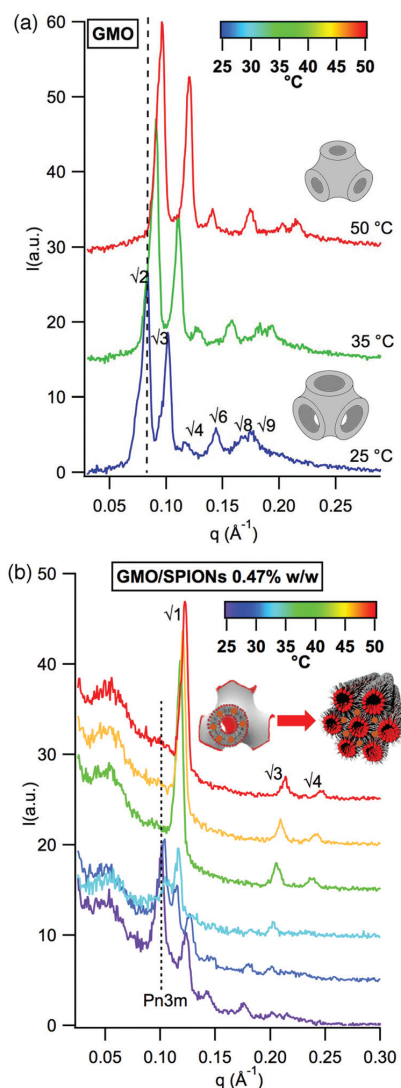


**Fig. 3** (a) SAXS curves of bulk cubic phase of GMO assembled in water at 25–35–50 °C with 50% w/w water. Water channel shrink enhancing temperature. (b) SAXS curves of GMO cubic phase assembled with 0.47% w/w SPIONs and 50% w/w water at 25–30–35–40–45–50 °C. Phase transition from cubic to hexagonal phase was observed above 35 °C.

Thus,  $\Delta g_p$  ( $H_{II}$ - $Pn3m$ ) can be considered as a temperature independent, positive value. Concerning  $\Delta g_C$ , the difference in the free energy of elastic curvature between the hexagonal (final) and the cubic (initial) phase,<sup>48</sup> can be expressed through a relatively simple equation (eqn (4)), whose extended derivation is reported in the ESI†, being the elastic moduli of the monolayers  $\kappa$  and  $\kappa_G$  related to the corresponding parameters of symmetric bilayers<sup>40</sup> through  $\kappa_B = 2\kappa$  and  $\kappa_G^B = 2(\kappa_G - 2H_0\kappa_C)$ , and

taking into account that  $K = 0$  for  $H_{II}$  while  $H = 0$  for  $Pn3m$  at the bilayer mid-plane.

$$\Delta g_C = 4\kappa H_{II}^2 - 2K_{Pn3m}(\kappa_G - 2H_0\kappa l_c). \quad (4)$$

Due to the previous considerations,  $\Delta g_C$  for a  $Pn3m$  to  $H_{II}$  transition is always negative. Thus, being the  $\Delta g_p$  term positive and practically invariant in the 25–50 °C temperature range,<sup>41</sup> the occurrence of  $Pn3m$ - $H_{II}$  phase transition can only be ascribed to the free energy of elastic curvature compensating and overcoming the frustration packing free energy at a defined temperature (eqn (5)):

$$|\Delta g_p| < |\Delta g_C(T)| \quad (5)$$

By combining eqn (4) and (5) we can write (eqn (6)):

$$\frac{\Delta g_p}{\kappa} + 4H_{II}^2 < 2K_{Pn3m}\left(\frac{\kappa_G}{\kappa} - 2H_0l_c\right) \quad (6)$$

$\kappa$ ,  $\kappa_G$ ,  $H_0$  decrease if temperature increase.  $\kappa$  and  $\kappa_G$  are related to the membrane elasticity while  $H_0$  depends on the molecular geometry. Ultimately, the prevalence of a  $H_{II}$  or a  $Pn3m$  phase depends on the balance between these two contributions,  $H_0$  and  $\kappa_G/\kappa$ . In the GMO cubic phase without NPs, the phase transition to the hexagonal phase is promoted at 90 °C. In the presence of SPIONs, as already discussed, an overall increase of the spontaneous curvature occurs, also at room temperature, determining an overall decrease of  $\Delta g_p$ , which, thus, decreases the minimum value of free energy of elastic curvature necessary to observe the phase transition (see eqn (5)). Thus, the presence of the SPIONs acts in the thermotropic behavior of the GMO liquid crystalline phase having influence both on the free energy of elastic curvature and on the free energy of packing frustration.

Overall, these energetic considerations are useful to highlight the potential of GMO/NPs systems; the thermotropism can be finely tuned through SPIONs content in lipid structure considering that magnetic nanoparticles affect both frustration packing and elastic curvature free energies.

### Thermotropic behavior of GMO-SPIONs nanoparticles

The hybrid bulk cubic phase of GMO/SPIONs with 0.47% w/w SPIONs was dispersed with Pluronic F127 as stabilizer as described in the Experimental section, to give cubosomes with a hydrodynamic radius in the range 2000–2500 Å (ref. 49) (see ESI† for details). The structure and thermotropic behavior of the cubosomes dispersion was investigated with SAXS within a temperature range of 25–49 °C. For GMO cubosomes, the structure is a primitive cubic phase  $Im3m$ <sup>50,51</sup> (Fig. 4a), *i.e.*, a more hydrated phase than  $Pn3m$ , characterized by larger water channels, which size, as in the  $Pn3m$ , decreases with temperature (from 26 Å at 25 °C to 20 Å at 49 °C in the  $Im3m$  and from 24 Å at 25 °C and 16 Å at 50 °C in the  $Pn3m$ ). In the same temperature range the lattice parameter  $d$  decreases by 2 nm (see ESI†), following a sigmoidal-like trend with inflection point at 36 °C, close to physiological temperature, making cubosomes interesting for drug delivery of both hydrophobic and hydrophilic therapeutics.

The SAXS profiles of magnetocubosomes, in the same temperature range (Fig. 4b) are consistent with a less hydrated diamond cubic phase with respect to bare cubosomes, coexisting with a  $H_{II}$  even at 25 °C. The cubic phase signature disappears above 35 °C and the hexagonal phase is the only one at 37 °C. The larger stability range of  $H_{II}$  phases for GMO-SPIONs hybrid systems is consistent with what was observed for the bulk cubic phase and is indeed very interest-

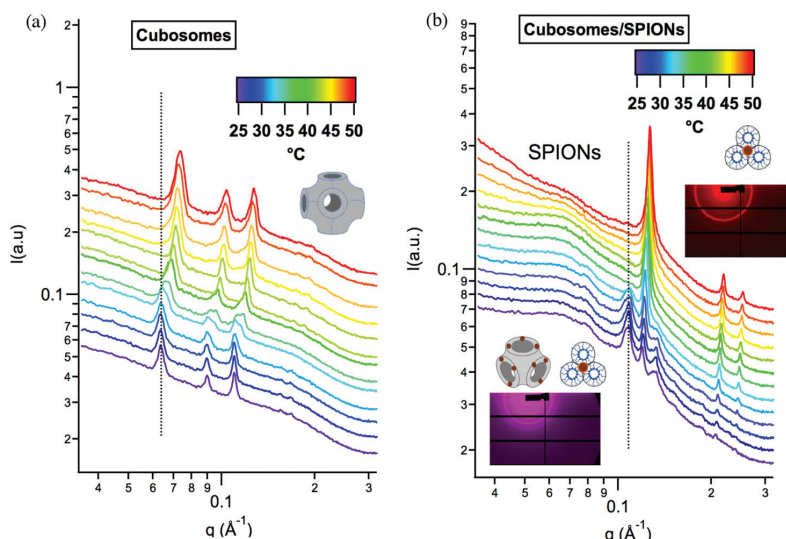


Fig. 4 SAXS curves of (a) cubosomes and (b) magnetocubosomes monitored in the 25 °C–49 °C temperature range with 2 °C temperature steps.

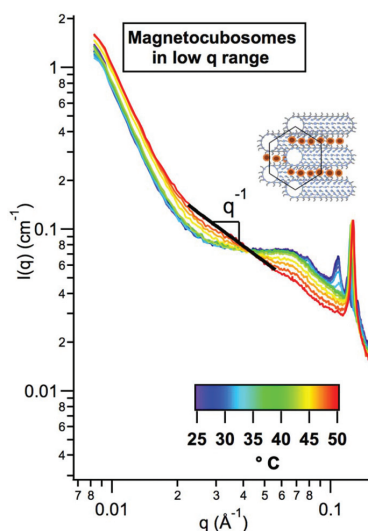


Fig. 5 Detail on low- $q$  range of SAXS curves of magnetocubosomes acquired in the 25–49 °C temperature range (see Fig. 4b). Variation of scattering intensity for magnetic nanoparticles was detected during the increase of temperature. At 49 °C self-organization of SPIONs into the lipid architecture shows a pearl-necklace like structure ( $q^{-1}$ ).

ing in order to design temperature responsive drug delivery systems: in fact, the transition to hexagonal phase implies a shrinking of the lipid nanoparticles, with water expulsion. This structural modification implies therefore a huge release

of the aqueous content of the aqueous channels with possible release of the confined active principles.

A very interesting feature emerges in the low- $q$  region of the SAXS spectra of magnetocubosomes (see Fig. 4b compared to Fig. 4a and 5): at 25 °C, the main feature of low- $q$  region is the structure factor corresponding to a correlation length of the nanoparticles embedded in the lipid architecture, observed in the same position as in the bulk cubic phase. This structure factor peak is preserved up to 40 °C. From 42 °C on, this peak disappears and a different structural feature occurs, consisting on a reorganization of the NPs. We can hypothesize that a decrease in viscosity of the lipid phase allows particle diffusion into the hydrophobic domain and the magnetic dipolar interaction drives a pearl-necklace organization.<sup>39</sup> In Fig. 5 the low- $q$  SAXS range is highlighted, showing at 49 °C a distinct and relatively extended  $q^{-1}$  scalar law beyond Guiner region. We can infer the radius of the pearls (18 Å), corresponding to the NPs radius and the length of the necklace (281 Å); from these values, we can hypothesize that 5–6 nanoparticles align in the lipid structure. Recently, modulation of nanoparticles shape or their aggregates have been proposed to overcome the so-called Brezovich effect. NPs controlled aggregation might enhance the heating power of SPIONs,<sup>52</sup> and/or modulate their magnetic properties.<sup>53</sup> With our results, we demonstrate that a fine control on the SPIONs arrangement can be achieved exploiting the polymorphic behavior of a lipid scaffold. The spontaneous controlled arrangement in linear structure can profoundly modify magnetic properties, as predicted in some computational studies<sup>54,55</sup> and finally alter magnetic properties.

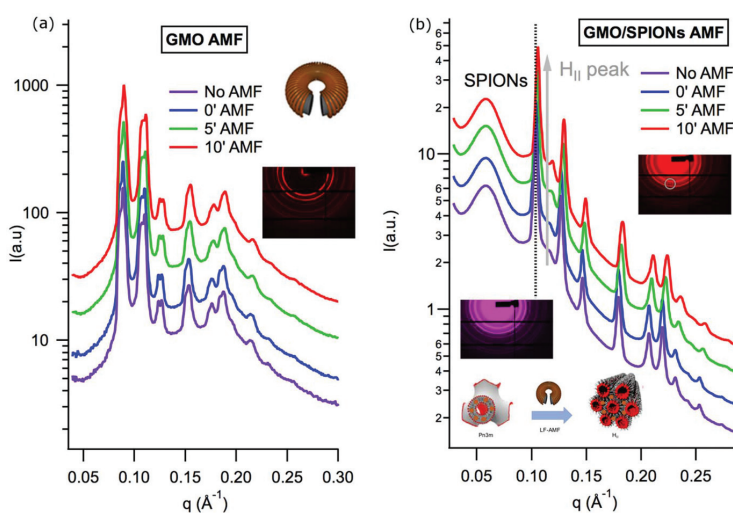


Fig. 6 SAXS curves of (a) GMO bulk cubic phase and (b) GMO bulk cubic phase with 0.47% SPIONs monitored during 10 minutes LF-AMF application at r.t. (a) A very mild shift of cubic phase Bragg peaks is present upon 10 minutes AMF application, corresponding to an temperature increase of 0.6 °C; (b) the appearance of an extra-peak at low  $q$  occur attributable to a  $H_{II}$  phase proves the occurrence of a  $Pn3m/H_{II}$  phase transition.

## Magnetotropic behavior of GMO-SPIONs assemblies

It is well known that SPIONs are responsive to an alternating magnetic field: their magnetic relaxation causes local heating. This effect is used in drug delivery systems to trigger the release from vehicles as liposomes<sup>11,26,27</sup> or magnetocubosomes<sup>4,10</sup> of model drug confined in the hydrophilic domains. For the first time, we report the structural effects of the AMF monitored “live”, *i.e.* during the AMF application, on the structure of a GMO cubic bulk phase self-assembled in the presence or in the absence of SPIONs (Fig. 6). With a dedicated experimental setup, we monitored through SAXS the structural changes in the bulk cubic phase during the application of an alternating magnetic field. As we can see from Fig. 6a, the AMF applied to GMO cubic phase (without SPIONs) does not induce structural changes, apart from a mild Joule Effect of the coil, which causes an overall minor shift ( $\sim 4.4 \times 10^{-4} \text{ \AA}^{-1}$ ) of the profile, consistent with a temperature increase of 0.6 °C.

Conversely, when SPIONs-loaded *Pn3m* GMO mesophases are subjected to AMF, Fig. 6b, the appearance of an extra peak is highlighted, which position is identical to the first reflection of the  $H_{II}$  phase (see Fig. 2b). During 10 minutes application, the intensity of the peak increases, though the transition is not complete. However, complete absence of phase transition and negligible temperature increase when NPs are not present and the perfect correspondence of this peak with the hexagonal phase allows us attributing it unambiguously to the local heating effect of the SPIONs that, probably due to the very localized effect, provoke a locally confined phase transition of the lipid scaffold.

## Conclusions

Hydrophobic magnetic nanoparticles endow GMO cubic mesophases with responsiveness to alternating magnetic fields,<sup>10</sup> allowing spatio-temporal control of the release of small molecules confined in their lipid bilayers or in the water channels. The mechanistic aspects of this process, of particular relevance in the field of controlled drug-delivery, were not yet elucidated.

In this contribution, we have explored and interpreted the structural effects of SPIONs on the thermotropic and lyotropic phase behaviour of bulk and dispersed cubic lipid phases. As the concentration of SPIONs in the lipid scaffold increases, a *Pn3m*- $H_{II}$  phase transition is promoted. For *Pn3m* GMO/SPIONs/water systems, the transition temperature to an  $H_{II}$  phase is lowered with respect to GMO/water (90 °C). The thermotropic properties of magnetocubosomes were also investigated, and the same structural effects were detected. We explain this phase behaviour in terms of changes of frustration packing and elastic features of the lipid bilayer. The same transition was induced applying an alternating magnetic field, due to local heating operated by the NPs. The structural change causes a shrinking of the mesophase, responsible for the release of hydrophilic molecules, initially confined in the water channels. Additionally, we detected in the hexagonal phase a spontaneous re-organization of the NPs into a pearl-

necklace supraparticle. This result is fully in line with our hypothesis on the NPs-induced frustration packing of the mesophase as the driving force of the transition.

These data and their interpretation open new perspectives both from fundamental and applicative standpoints. Concerning the first aspect, the results here presented contribute to the elucidation of NPs' interactions with synthetic or natural lipid membranes, demonstrating that NPs affect the viscoelastic properties of lipid bilayers, shifting the mesophases' phase boundaries. This effect can be harnessed to tune the mesophase response to AMF and drive the release of host molecules, with numerous applications in the field of drug delivery. In addition, lipid mesophases steer the organization of single NPs into magnetic supraparticles with preserved colloidal stability. This approach opens the way to control the spontaneous supraorganization of SPIONs in a lipid scaffold, possibly overcoming the Brezovich limit, which nowadays hampers clinical applicability of magnetic hyperthermia.<sup>53</sup>

## Conflicts of interest

There are no conflicts to declare.

## Acknowledgements

Annalisa Salvatore and Giacomo Becheri are acknowledged by all the authors for taking part to SAXS experiments and Annalisa Salvatore also for contribution on SPIONs synthesis. We gratefully acknowledge the allocation of beamtime at Elettra, Trieste, Italy.

## References

- 1 R. H. Templer, *Curr. Opin. Colloid Interface Sci.*, 1998, **3**, 255–263.
- 2 A. Marín-Menéndez, C. Montis, T. Díaz-Calvo, D. Carta, K. Hatzixanthis, C. J. Morris, M. McArthur and D. Berti, *Sci. Rep.*, 2017, **7**, 41242.
- 3 S. Smeazzetto, F. Tadini-Buoninsegni, G. Thiel, D. Berti and C. Montis, *Phys. Chem. Chem. Phys.*, 2016, **18**, 1629–1636.
- 4 M. Szlezak, D. Nieciecka, A. Joniec, M. Pekała, E. Gorecka, M. Emo, M. J. Stébé, P. Krysiński and R. Bilewicz, *ACS Appl. Mater. Interfaces*, 2017, **9**(3), 2796–2805.
- 5 R. Negrini and R. Mezzenga, *Langmuir*, 2012, **28**, 16455–16462.
- 6 W. Sun, J. J. Vallooran, A. Zabara and R. Mezzenga, *Nanoscale*, 2014, **6**, 6853–6859.
- 7 S. Murgia, S. Lampis, P. Zucca, E. Sanjust and M. Monduzzi, *J. Am. Chem. Soc.*, 2010, **132**, 16176–16184.
- 8 P. Huang, J. Zhao, C. Wei, X. Hou, P. Chen, Y. Tan, C.-Y. He, Z. Wang and Z.-Y. Chen, *Biomater. Sci.*, 2017, **5**, 120–127.

- 9 R. Negrini and R. Mezzenga, *Langmuir*, 2011, **27**, 5296–5303.
- 10 C. Montis, B. Castroflorio, M. Mendoza, A. Salvatore, D. Berti and P. Baglioni, *J. Colloid Interface Sci.*, 2015, **449**, 317–326.
- 11 M. Bonini, D. Berti and P. Baglioni, *Curr. Opin. Colloid Interface Sci.*, 2013, **18**, 459–467.
- 12 H. Vacklin, B. J. Khoo, K. H. Madan, J. M. Seddon and R. H. Templer, *Langmuir*, 2000, **16**, 4741–4748.
- 13 N. Tran, A. M. Hawley, J. Zhai, B. W. Muir, C. Fong, C. J. Drummond and X. Mulet, *Langmuir*, 2016, **32**, 4509–4520.
- 14 S. J. Marrink and D. P. Tieleman, *J. Am. Chem. Soc.*, 2001, **123**, 12383–12391.
- 15 T. G. Meikle, S. Yao, A. Zabara, C. E. Conn, C. J. Drummond and F. Separovic, *Nanoscale*, 2017, **9**, 2471–2478.
- 16 L. van 't Hag, A. Anandan, S. A. Seabrook, S. L. Gras, C. J. Drummond and X. Vrieling, *Soft Matter*, 2017, **13**, 1493–1504.
- 17 A. Zabara, T. G. Meikle, J. Newman, T. S. Peat, C. E. Conn and C. J. Drummond, *Nanoscale*, 2017, **9**, 754–763.
- 18 J. J. Vallooran, S. Bolisetty and R. Mezzenga, *Adv. Mater.*, 2011, **23**, 3932–3937.
- 19 J. J. Vallooran, S. Handschin, S. Bolisetty and R. Mezzenga, *Langmuir*, 2012, **28**, 5589–5595.
- 20 J. J. Vallooran, R. Negrini and R. Mezzenga, *Langmuir*, 2013, **29**, 999–1004.
- 21 R. Di Corato, A. Espinosa, L. Lartigue, M. Tharaud, S. Chat, T. Pellegrino, C. Ménager, F. Gazeau and C. Wilhelm, *Biomaterials*, 2014, **35**, 6400–6411.
- 22 L. Lartigue, P. Hugounenq, D. Alloeyau, S. P. Clarke, M. Lévy, J.-C. Bacri, R. Bazzi, D. F. Brougham, C. Wilhelm and F. Gazeau, *ACS Nano*, 2012, **6**, 10935–10949.
- 23 A. Hervault, A. E. Dunn, M. Lim, C. Boyer, D. Mott, S. Maenosono and N. T. K. Thanh, *Nanoscale*, 2016, **8**, 12152–12161.
- 24 D. Maiolo, C. Pigliacelli, P. Sánchez Moreno, M. B. Violatto, L. Talamini, I. Tirota, R. Piccirillo, M. Zucchetti, L. Morosi, R. Frapolli, G. Candiani, P. Bigini, P. Metrangolo and F. Baldelli Bombelli, *ACS Nano*, 2017, **11**, 9413–9423.
- 25 A. Salvatore, C. Montis, D. Berti and P. Baglioni, *ACS Nano*, 2016, **10**, 7749–7760.
- 26 Y. Chen, A. Bose and G. D. Bothun, *ACS Nano*, 2010, **4**, 3215–3221.
- 27 M. S. Martina, J. P. Fortin, C. Ménager, O. Clément, G. Barratt, C. Grabielle-Madellmont, F. Gazeau, V. Cabuil and S. Lesieur, *J. Am. Chem. Soc.*, 2005, **127**, 10676–10685.
- 28 S. Sun, H. Zeng, D. B. Robinson, S. Raoux, P. M. Rice, S. X. Wang and G. Li, *J. Am. Chem. Soc.*, 2004, **126**, 273–279.
- 29 L. Wang, J. Luo, Q. Fan, M. Suzuki, I. S. Suzuki, M. H. Engelhard, Y. Lin, N. Kim, J. Q. Wang and C. J. Zhong, *J. Phys. Chem. B*, 2005, **109**, 21593–21601.
- 30 G. Capuzzi, F. Pini, C. M. C. Gambi, M. Monduzzi, P. Baglioni and J. Teixeira, *Langmuir*, 1997, **53**, 6927–6930.
- 31 H. Sub Wi, K. Lee and H. Kyu Pak, *J. Phys.: Condens. Matter*, 2008, **20**, 494211.
- 32 C. M. Beddoes, J. Berge, J. E. Bartenstein, K. Lange, A. J. Smith, R. K. Heenan and W. H. Briscoe, *Soft Matter*, 2016, **12**, 6049–6057.
- 33 C. Fong, T. Le and C. J. Drummond, *Chem. Soc. Rev.*, 2012, **41**, 1297.
- 34 M. Fuhrmans, V. Knecht and S. J. Marrink, *J. Am. Chem. Soc.*, 2009, **131**, 9166–9167.
- 35 A. Yaghmur, P. Laggner, S. Zhang and M. Rappolt, *PLoS One*, 2007, **2**(5), e479.
- 36 N. Johnner, S. Mondal, G. Morra, M. Caffrey, H. Weinstein and G. Khelashvili, *J. Am. Chem. Soc.*, 2014, **136**, 3271–3284.
- 37 C. C. Piccinetti, C. Montis, M. Bonini, R. Laurà, M. C. Guerrero, G. Radaelli, F. Vianello, V. Santinelli, F. Maradonna, V. Nozzi, A. Miccoli and I. Olivotto, *Zebrafish*, 2014, **11**, 567–579.
- 38 J. M. Bulpett, T. Snow, B. Quignon, C. M. Beddoes, T.-Y. D. Tang, S. Mann, O. Shebanova, C. L. Pizzey, N. J. Terrill, S. A. Davis and W. H. Briscoe, *Soft Matter*, 2015, **11**, 8789–8800.
- 39 Y. Lalatonne, J. Richardi and M. P. Pileni, *Nat. Mater.*, 2004, **3**, 121–125.
- 40 G. C. Shearman, O. Ces, R. H. Templer and J. M. Seddon, *J. Phys.: Condens. Matter*, 2006, **18**, S1105–S1124.
- 41 R. H. Templer, J. M. Seddon, P. M. Duesing, R. Winter and J. Erbes, *J. Phys. Chem. B*, 1998, **102**, 7262–7271.
- 42 E. Venugopal, S. K. Bhat, J. J. Vallooran and R. Mezzenga, *Langmuir*, 2011, **27**, 9792–9800.
- 43 B. Angelov, A. Angelova, V. M. Garamus, G. Lebas, S. Lesieur, M. Ollivon, S. S. Funari, R. Willumeit and P. Couvreur, *J. Am. Chem. Soc.*, 2007, **129**, 13474–13479.
- 44 W. Helfrich, *Z. Naturforsch.*, 1973, **28**, 693–703.
- 45 S. T. Hyde, *J. Phys. Chem.*, 1989, **93**, 1458–1464.
- 46 S. T. Hyde, *Curr. Opin. Solid State Mater. Sci.*, 1996, **1**, 653–662.
- 47 I. Hoffmann, R. Michel, M. Sharp, O. Holderer, M.-S. Appavou, F. Polzer, B. Farago and M. Gradzielski, *Nanoscale*, 2014, **6**, 6945–6952.
- 48 D. P. Siegel and M. M. Kozlov, *Biophys. J.*, 2004, **87**, 366–374.
- 49 C. Neto, D. Berti, G. D. Aloisi, P. Baglioni and K. Larsson, *Prog. Colloid Polym. Sci.*, 2000, **115**, 295–299.
- 50 J. Y. T. Chong, X. Mulet, L. J. Waddington, B. J. Boyd and C. J. Drummond, *Soft Matter*, 2011, **7**, 4768.
- 51 B. Angelov, A. Angelova, B. Papahadjopoulos-Sternberg, S. Lesieur, J. F. Sadoc, M. Ollivon and P. Couvreur, *J. Am. Chem. Soc.*, 2006, **128**, 5813–5817.
- 52 P. Guardia, R. Di Corato, L. Lartigue, C. Wilhelm, A. Espinosa, M. Garcia-Hernandez, F. Gazeau, L. Manna and T. Pellegrino, *ACS Nano*, 2012, **6**, 3080–3091.
- 53 D. Maity, P. Chandrasekharan, P. Pradhan, K.-H. Chuang, J.-M. Xue, S.-S. Feng and J. Ding, *J. Mater. Chem.*, 2011, **21**, 14717.
- 54 P. V. Melenev, V. V. Rusakov and Y. L. Raikher, *Tech. Phys. Lett.*, 2008, **34**, 248–250.
- 55 V. Schaller, G. Wahnström, A. Sanz-Velasco, S. Gustafsson, E. Olsson, P. Enoksson and C. Johansson, *Phys. Rev. B: Condens. Matter Mater. Phys.*, 2009, **80**, 1–4.

# On the thermotropic and magnetotropic phase behavior of lipid liquid crystals containing magnetic nanoparticles

Marco Mendoza<sup>1</sup>, Costanza Montis<sup>1</sup>, Lucrezia Caselli<sup>1</sup>, Marcell Wolf<sup>2</sup>, Piero Baglioni<sup>1</sup> and Debora Berti<sup>1\*</sup>

<sup>1</sup>Department of chemistry and CSGI, University of Florence, Via della Lastruccia 3, 50019-Sesto Fiorentino, Florence, Italy.

<sup>2</sup>Institute of Inorganic Chemistry, Graz University of Technology, Stremayrgasse 9/IV, 8010 Graz, Austria

<b>Materials and Methods</b>	<b>Page</b>
<i>S.1 Materials</i>	S3
<i>S.2 Synthesis of magnetic nanoparticles</i>	S3
<i>S.3 Preparation of bulk and disperse cubic phase</i>	S3
<i>S.4 Small-Angle X-ray Scattering (SAXS) Hecus</i>	S4
<i>S.5 Small-Angle X-ray Scattering (SAXS) Elettra Synchrotron</i>	S5
<i>S.6 SAXS analysis</i>	S5
<i>S.7 LF-AMF specifications</i>	S6
<b>Supporting Figures</b>	
<i>S.8 SAXS characterization of magnetic nanoparticles</i>	S7
<i>S.9 Lattice parameters of GMO/H<sub>2</sub>O systems and SAXS curves of GMO/H<sub>2</sub>O/oleic acid-oleylamine</i>	S8
<i>S.10 SAXS curves of GMO/H<sub>2</sub>O/SPIONs</i>	S14
<i>S.11 Temperature dependence of GMO/H<sub>2</sub>O/SPIONs lattice parameters</i>	S18
<i>S.12 DLS analysis of cubosomes and magnetocubosomes</i>	S19
<i>S.13 Temperature dependence of cubosomes and magnetocubosomes lattice parameters</i>	S20
<i>S.14 Derivation of Equation 4 of the main text</i>	S20
<b>References</b>	S23

## Materials and Methods

### *S.1- Materials*

Fe(III)acetylacetonate, 1,2-hexadecanediol, oleylamine, oleic acid, diphenylether, ethanol and mixture of hexane employed for the synthesis of SPIONs, were purchased from Sigma Aldrich (St. Louis MO), the same for Glyceryl Monooleate (GMO) and Pluronic F-127.

### *S.2- Synthesis of magnetic nanoparticles*

Iron oxide nanoparticles were synthesized according to the protocol reported by Wang et al.<sup>1</sup>. Briefly, 0.71 g Fe(acac)<sub>3</sub> (2 mmol) were dissolved in 20 mL of phenyl ether with 2 mL of oleic acid (6 mmol) and 2 mL of oleylamine (4 mmol) under nitrogen atmosphere and vigorous stirring. 1,2-hexadecanediol (2.58g, 10 mmol) was then added. The solution was heated at 210 °C, refluxed for 2 h and then cooled down to RT. Ethanol was added to the dispersion and the precipitate collected, washed with ethanol to remove residual precursors and side products from the synthesis and redispersed in 20 mL hexane in the presence of 75 mM of both oleic acid and oleylamine. A stable dispersion of the SPIONs with a hydrophobic coating of oleic acid and oleylamine in hexane was obtained.

### *S.3- Preparation of bulk and disperse cubic phase*

The preparation of bulk cubic phase with or without SPIONs was carried out according to the following procedure. First, 30 mg of GMO were weighted in a 2mL glass vial. For GMO/SPIONs systems, the appropriate volume of SPIONs dispersion was then added. About 1 mL hexane was used to solubilize the mixture and then the solvent was removed with a gentle

nitrogen flux. GMO or GMO/SPIONs systems were left under vacuum overnight sheltered from light. The dry film was then hydrated with 30  $\mu\text{L}$  Milli-Q water and the sample was then centrifuged at least 5 times altering a cycle with cap facing upward with another with cap facing downward.

For the preparation of cubosomes, first GMO or GMO-SPIONs film was obtained, as previously described. 8 mg of Pluronic F-127 were then added to the dry film and the mixture was heated in a water bath at 70  $^{\circ}\text{C}$  for 5' to melt the Pluronic F-127 and then vortexed for 5'. Five cycles of heating-vortexing were carried out and then 500  $\mu\text{L}$  of preheated  $\text{H}_2\text{O}$  at 70  $^{\circ}\text{C}$  were added. The dispersion was then sonicated in a bath-sonicator at 59 kHz and 100% power for 6 h, to homogenize the system.

#### *S.4- Small-Angle X-ray Scattering (SAXS) Hecus*

SAXS measurements were carried out on a S3-MICRO SAXS/WAXS instrument (HECUS GmbH, Graz, Austria) which consists of a GeniX microfocus X-ray Sealed Cu Ka source (Xenocs, Grenoble, France) power 50 W which provides a detector focused X-ray beam with  $k = 0.1542 \text{ nm Cu Ka line}$ . The instrument is equipped with two one-dimensional (1D) position sensitive detectors, (HECUS 1D-PSD-50 M system) each detector is 50 mm long (spatial resolution 54  $\text{lm/channel}$ , 1024 channels) and cover the SAXS  $q$ -range ( $0.003 < q < 0.6 \text{ \AA}^{-1}$ ) and the WAXS  $q$ -range ( $1.2 < q < 1.9 \text{ \AA}^{-1}$ ). The temperature was controlled by means of a Peltier TCCS-3 Hecus. SAXS curves of bulk cubic phase were recorded at 25-30-35-40-45-50  $^{\circ}\text{C}$  in a solid sample-holder. Dispersion of SPIONs were recorded in a glass capillary.

### S.5- Small-Angle X-ray Scattering (SAXS) Elettra Synchrotron

Analysis of cubosomes and magnetocubosomes were carried out at SAXS beamline of synchrotron radiation Elettra, Trieste, Italy operated at 2 GeV and 300 mA ring current. The experiments were carried with  $\lambda = 1.5\text{ \AA}$  and SAXS signal was detected with Pilatus 3 1M detector in q-range from  $0.008\text{ \AA}^{-1}$  to  $0.45\text{ \AA}^{-1}$ . Thermic behavior of colloidal dispersion of cubosomes and magnetocubosomes were carried out through thermostat from  $25\text{ }^{\circ}\text{C}$  to  $49\text{ }^{\circ}\text{C}$  increasing the temperature of  $2\text{ }^{\circ}\text{C}$  each step. Equilibration time at each temperature was 5 minutes. SAXS curves were recorded in a glass capillary for cubosomes and magnetocubosomes dispersions and in a solid sample-holder for the cubic phases.

### S.6- SAXS analysis

Equation (1) was used to calculate lattice parameter of cubic and hexagonal phase:

$$q = \left(\frac{2\pi}{d}\right) \sqrt{h^2 + k^2 + l^2} \quad (S1)$$

Eq. (2) was used to calculate water channel radii  $r_w$  in cubic phase while eq (3) was used to calculate volume water fraction:

$$r_w = \sqrt{(-\sigma/2\pi\chi)d} - l_c \quad (S2)$$

$$\varphi_w = 1 - 2A_0 \left(\frac{l_c}{d}\right) - \frac{4}{3}\pi\chi \left(\frac{l_c}{d}\right)^3 \quad (S3)$$

Equation (4)<sup>2</sup> and (5)<sup>3</sup> describe water channel radii of hexagonal phase and water volume fraction respectively:

$$r_w = \frac{0.5256d - l_c}{0.994} \quad (S4)$$

$$\varphi_w = \frac{2\pi r_w^2}{\sqrt{3}d^2} \quad (S5)$$

We assumed that  $l_c$  into the range of 25-50 °C, is constant and assume value of about 17 Å. Moreover, to evaluate water fraction both for cubic and hexagonal phase we assumed that %w/w of  $Fe_3O_4$  negligible.

#### *S.7- LF-AMF specifications*

A sinusoidal magnetic field was generated in the gap of a broken toroidal magnet carrying a solenoid through which an alternating electric current (AC) from a tone generator was led as described elsewhere<sup>4</sup>. The samples to be treated with LF-AMF were placed in the middle of the gap. Due to the design of the experimental apparatus, the magnetic field inside the cell is not isotropic. During the experiments, the field frequency was set at 6.22 kHz. Magnetic field values of magnet range from 100-330 mT with 10 V and 8 A.

## Supplementary Figures

### S.8- SAXS characterization of magnetic nanoparticles

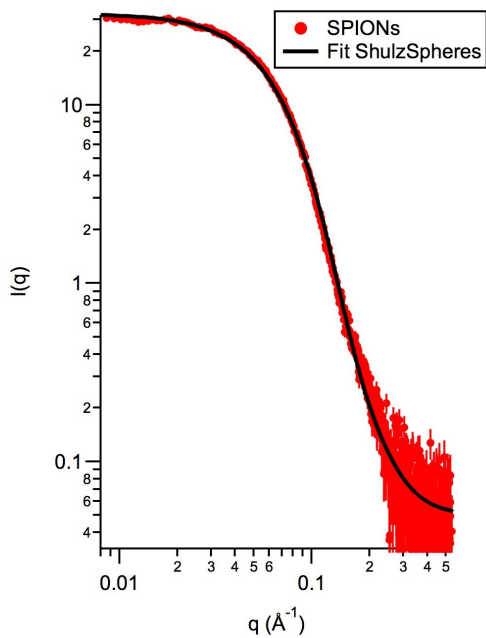


**Figure S1:** SAXS curve of magnetic nanoparticles disperse in hexane diluted 1:3 (red) fitted by polidisperse Shultz Sphere model (black line).

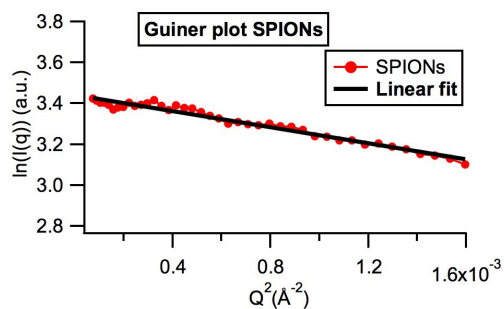


**Figure S2:** SAXS curves of magnetic nanoparticles with linear fit in Guiner region.

To investigate the dimension of magnetic nanoparticles synthesized as reported in S.2 section, we diluted 1:3 in hexane magnetic nanoparticles. We employed “SphereSchultz Model” by NIST to estimate the radius and polydispersity of SPIONs, which were found equal to  $20 \pm 3 \text{ \AA}$  and 0.35 respectively. Moreover, the SAXS curve was analyzed with the Guiner limit law finding a gyration radius of  $24 \text{ \AA}$ . In the hypothesis of spherical and monodisperse nanoparticles, the average radius of the SPIONs derived from Guinier plot is  $R = 31 \text{ \AA}$ . This result, corrected for the polydispersity of the colloidal dispersion<sup>5</sup>, is about  $18 \text{ \AA}$ , and this is fully consistent with the radius obtained from the “SphereSchultz Model” analysis.

*S.9- Lattice parameters of GMO/H<sub>2</sub>O systems and SAXS curves of GMO/H<sub>2</sub>O/oleic acid-oleylamine*

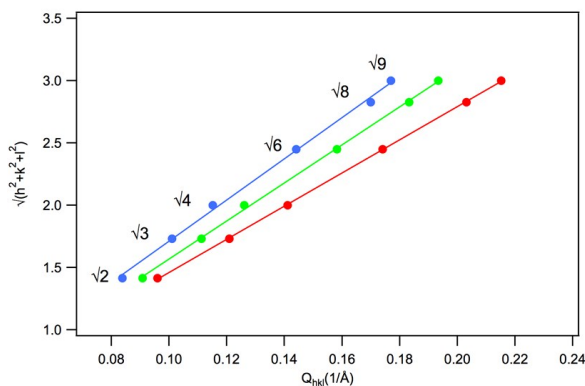


**Figure S3:** SAXS analysis of GMO/H<sub>2</sub>O mesophases at 25 °C (blue line and markers), 35 °C (green line and markers) and 50 °C (red line and markers): square root of the sum of the h,k,l Miller indexes of each peak vs q-peak position (blue, green, red circles); linear fit of the experimental data to calculate lattice parameters the different mesophases (blue, green, red line).

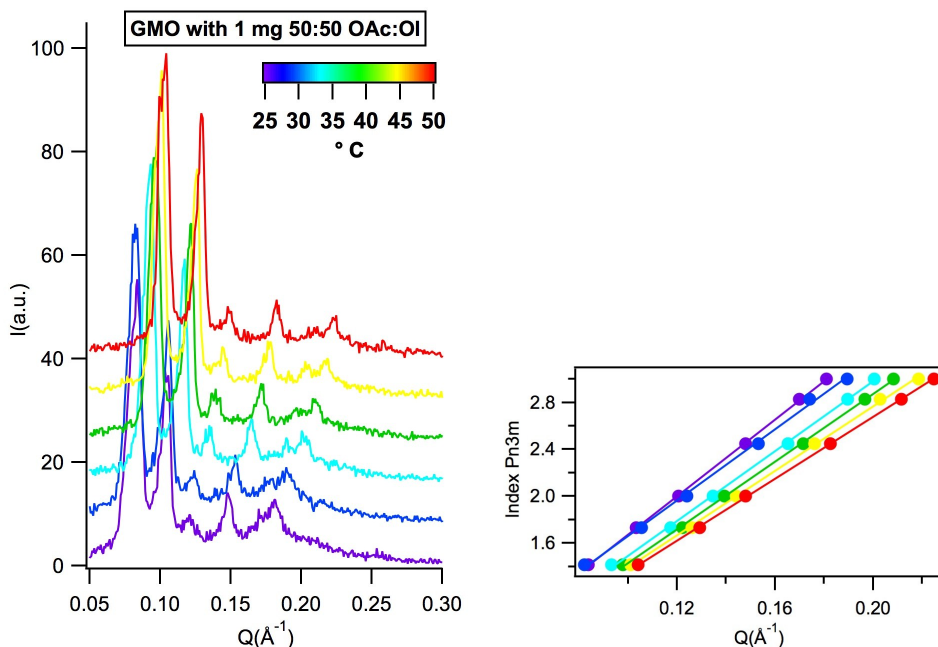


**Figure S4:** SAXS curves of GMO assembled with 1 mg of a mixture Oleic Acid/Oleylamine at 25-30-35-40-45-50 °C (respectively violet, blue, cyan, green, yellow and red) and Miller index on  $Q_{\max}$  to determine the trend of Pn3m lattice parameter with temperature. No phase transition was observed in this system.

**Table S1.** Lattice parameters, water channel radii and water volume fraction of GMO assembled with 1 mg of a mixture 50:50 of Oleic acid and oleylamine

T (°C)	Lattice parameter ( $\text{\AA}$ )	Water channel radii ( $\text{\AA}$ )	Water volume fraction
25	103	23	0.40
30	95	20	0.36
35	94	20	0.36
40	91	19	0.34
45	86	17	0.31
50	83	15	0.29

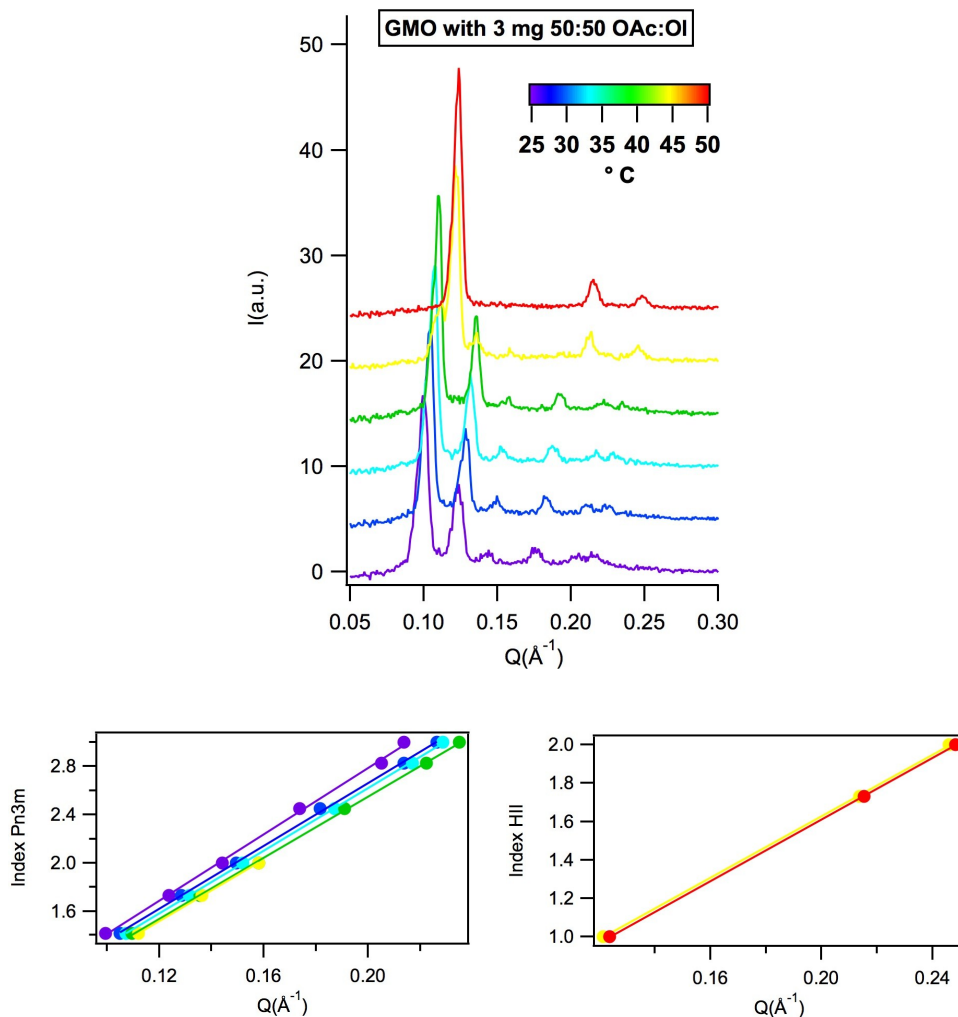


**Figure S5:** SAXS curves of GMO assembled with 3 mg of a mixture Oleic Acid/Oleylamine and Miller index on  $Q_{\max}$  to determine the trend of the lattice parameter both for cubic (violet, blue, cyan, green and yellow) and hexagonal phase (yellow and red line) with temperature in the 25-50 °C temperature range. At 45°C the coexistence of cubic and hexagonal phases was detected. Only at 50 °C a pure inverse hexagonal phase was detected.

**Table S2.** Lattice parameters, water channel radii and waer volume fraction of GMO assembled with 3 mg of a mixture 50:50 of Oleic acid and oleylamine.

<b>T (°C)</b>	<b>Lattice parameter (Å)</b>	<b>Water channel radii (Å)</b>	<b>Water volume fraction</b>
<b>25</b>	86	17	0.31
<b>30</b>	82	15	0.28
<b>35</b>	82	15	0.28
<b>40</b>	80	14	0.26
<b>45</b>	80 (Pn3m)	14	0.26
	50 (H <sub>II</sub> )	9	0.13
<b>50</b>	50	9	0.13

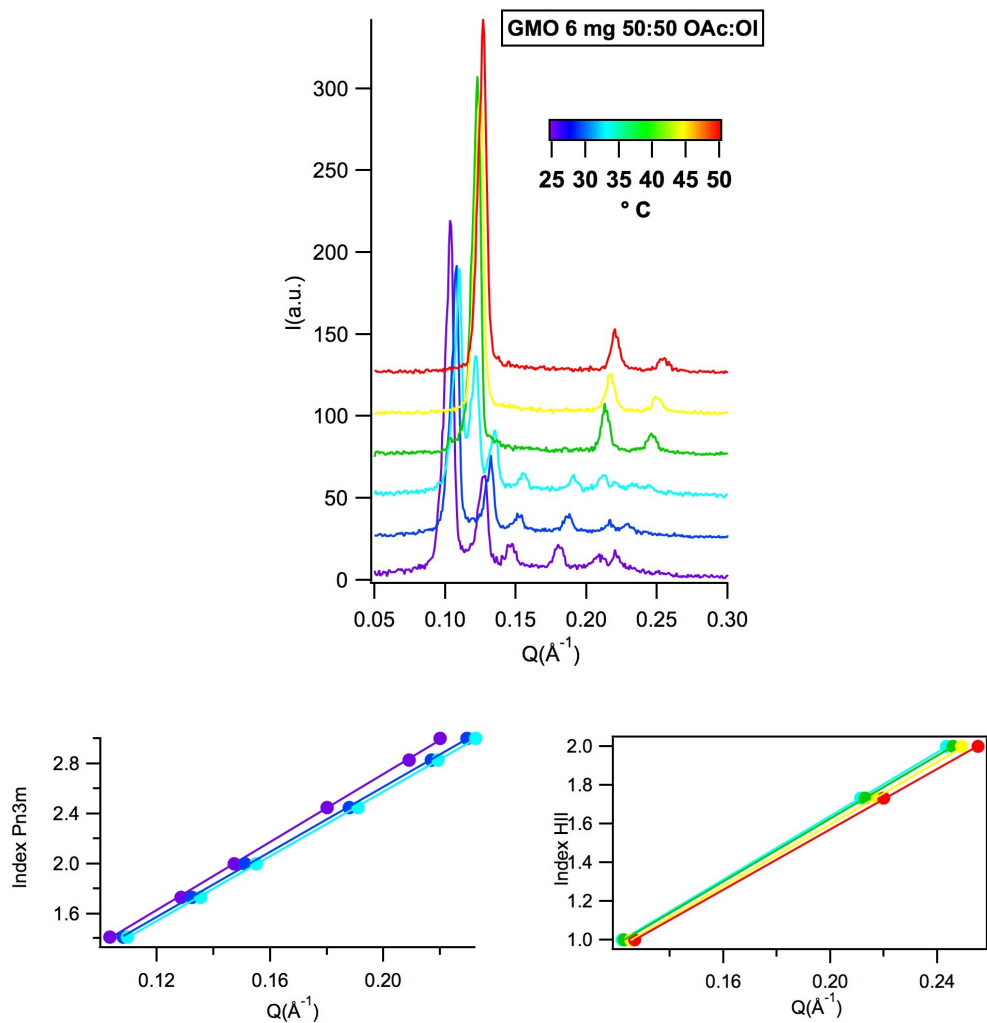


**Figure S6:** SAXS curves of GMO assembled with 6 mg of a mixture Oleic Acid/Oleylamine and Miller index on  $Q_{\max}$  to determine the trend of the lattice parameter both for cubic (violet, blue and cyan) and hexagonal phase (cyan, green and yellow and red line) with temperature in the 25-50 °C temperature range. At 35°C the coexistence of cubic and hexagonal phases was detected. From 40 °C a pure inverse hexagonal phase was detected.

**Table S3.** Lattice parameters, water channel radii and waer volume fraction of GMO assembled with 6 mg of a mixture 50:50 of oleic acid and oleylamine.

<b>T (°C)</b>	<b>Lattice parameter (Å)</b>	<b>Water channel radii (Å)</b>	<b>Water volume fraction</b>
<b>25</b>	85	16	0.3
<b>30</b>	82	15	0.28
<b>35</b>	81 (Pn3m)	15	0.27
	52(H <sub>II</sub> )	10.4	0.14
<b>40</b>	51	9.8	0.14
<b>45</b>	51	9.8	0.14
<b>50</b>	49	8.8	0.12

S.10- SAXS curves of GMO/H<sub>2</sub>O/SPIONs

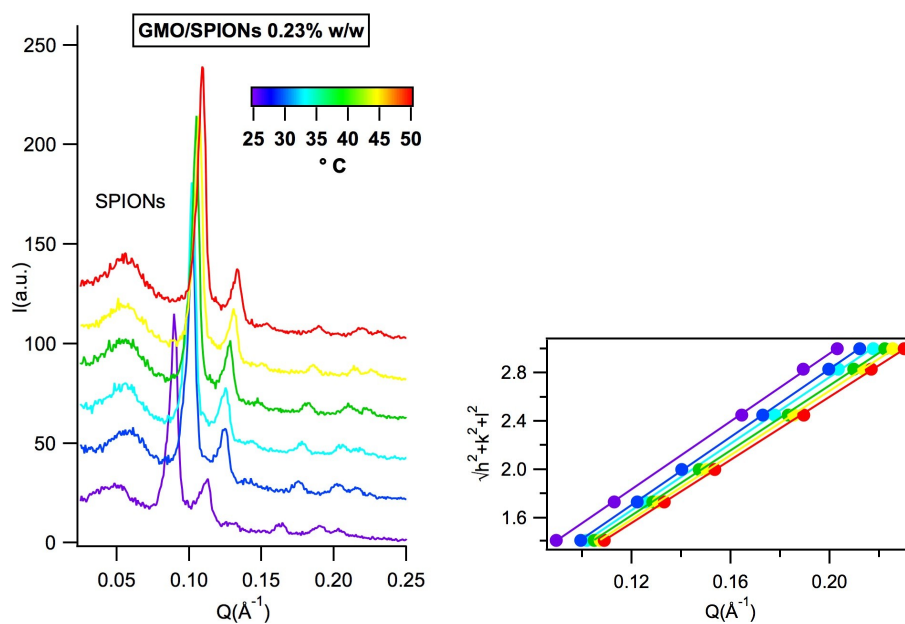


**Figure S7:** SAXS curves of GMO assembled with 0.23% w/w Fe<sub>3</sub>O<sub>4</sub> (mixture of OAc/OI is 1.33 mg) and Miller index on  $Q_{\max}$  to determine the variation of the lattice parameter for cubic phase with temperature in the 25-50 °C temperature range. No phase transition with this amount of SPIONs was detected.

**Table S4.** Lattice parameters, water channel radii and waer volume fraction of GMO assembled with 0.23% SPIONs at increasing temperatures.

<b>T (°C)</b>	<b>Lattice parameter (Å)</b>	<b>Water channel radii (Å)</b>	<b>Water volume fraction</b>
25	88	17	0.32
30	88	17	0.32
35	86	16.6	0.31
40	84	15.8	0.29
45	84	15.8	0.29
50	82	15	0.28

**Table S5.** Lattice parameters, water channel radii and waer volume fraction of GMO assembled with 0.47% SPIONs at increasing temperatures.

<b>T (°C)</b>	<b>Lattice parameter (Å)</b>	<b>Water channel radii (Å)</b>	<b>Water volume fraction</b>
25	87 (Pn3m)	17	0.31
30	86 (Pn3m)	16.6	0.31
	55 (H <sub>II</sub> )	12	0.17
35	85 (Pn3m)	16	0.3
	54 (H <sub>II</sub> )	11	0.16
40	53 (H <sub>II</sub> )	11	0.15
45	52 (H <sub>II</sub> )	10	0.14
50	51 (H <sub>II</sub> )	9.8	0.14

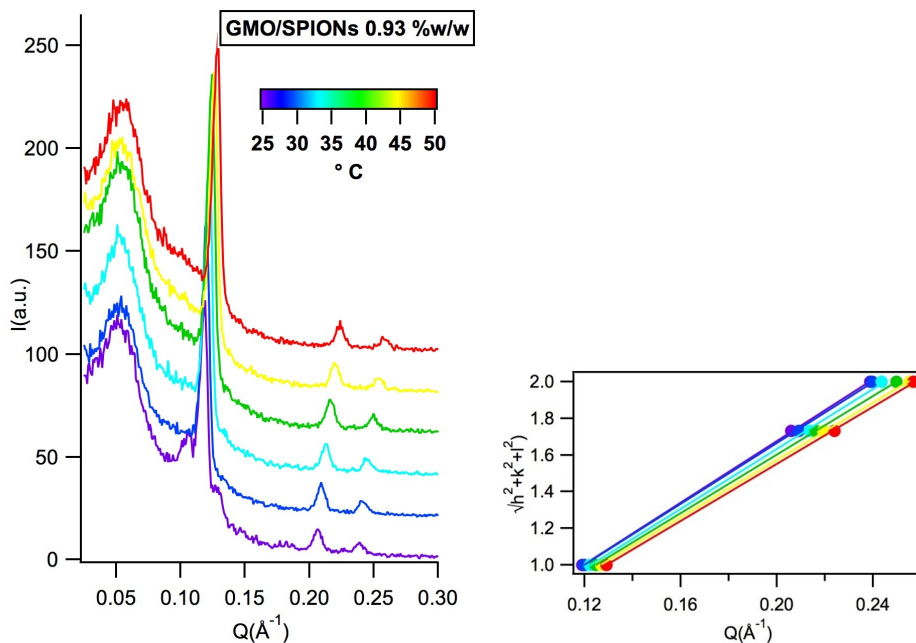


**Figure S8:** SAXS curves of GMO assembled with 0.93% w/w Fe<sub>3</sub>O<sub>4</sub> (5.33 mg of a mixture OAc/OI) and Miller index on  $Q_{\max}$  to determine the trend of the lattice parameter for the inverse hexagonal phase with temperature in the 25-50 °C temperature range.

**Table S6.** Lattice parameters, water channel radii and water volume fraction of GMO assembled with 0.93% SPIONs at increasing temperatures.

T (°C)	Lattice parameter (Å)	Water channel radii (Å)	Water volume fraction
25	53	11	0.15
30	52	10	0.14
35	51	9.8	0.13
40	50	9.3	0.13
45	49	8.8	0.12
50	49	8.8	0.12

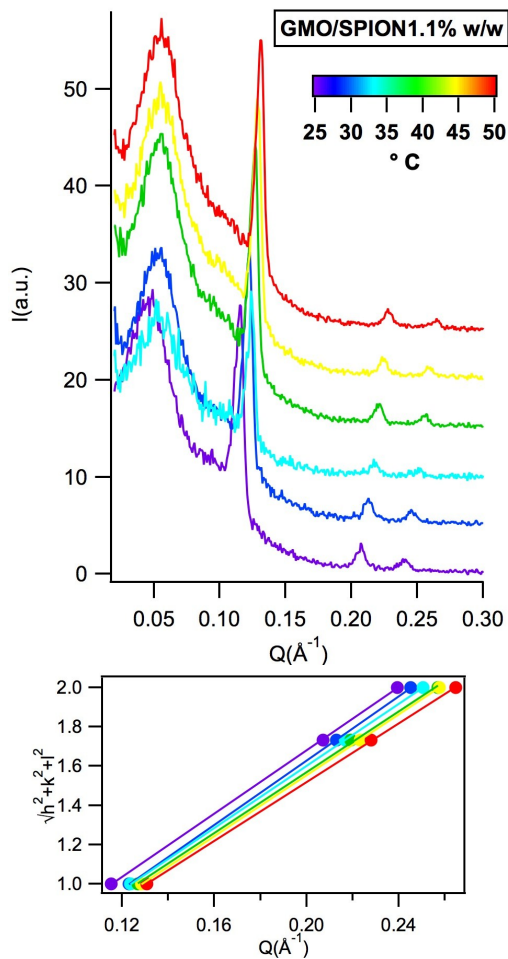


**Figure S9:** SAXS curves of GMO assembled with 1.1% w/w  $\text{Fe}_3\text{O}_4$  (6.13 mg of a mixture OAc/OI) and Miller index on  $Q_{\text{max}}$  to determine the trend of the lattice parameter for the inverse hexagonal phase with temperature in the 25-50 °C temperature rang.

**Table S7.** Lattice parameters, water channel radii and water volume fraction of GMO assembled with 1.1% SPIONs at increasing temperatures.

T (°C)	Lattice parameter ( $\text{\AA}$ )	Water channel radii ( $\text{\AA}$ )	Water volume fraction
25	50	9.3	0.13

30	51	9.8	0.14
35	49	8.8	0.12
40	49	8.8	0.12
45	49	8.8	0.12
50	47	7.7	0.1

*S.11- Temperature dependence of GMO/H<sub>2</sub>O/SPIONs lattice parameters*

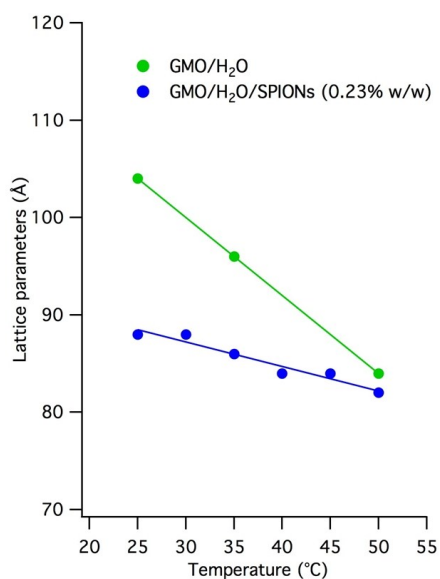


**Figure S10:** Linear fit of lattice parameters in GMO/H<sub>2</sub>O system (green line) and GMO/H<sub>2</sub>O/SPIONs (0.23% w/w) (blue line) on temperature. Both the systems have the same cubic structure (Pn3m).

*S.12- DLS analysis of cubosomes and magnetocubosomes*

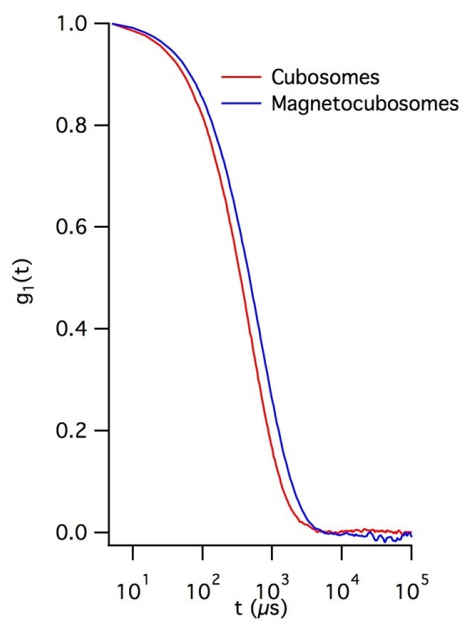


**Figure S11:** Dynamic Light Scattering (DLS) curves of cubosomes and magnetocubosomes water dispersion diluted 1:500 before the measurement.

---

**Table S8.** Hydrodynamic diameter and polydispersity of cubosomes and magnetocubosomes. DLS curves analyzed through a cumulant analysis stopped to the second order.

---

T (°C)	Hydrodynamic diameter (nm)	Polydispersity
Cubosomes	240	0.19
Magnetocubosomes	260	0.12

*S.13- Temperature dependence of cubosomes and magnetocubosomes lattice parameters*

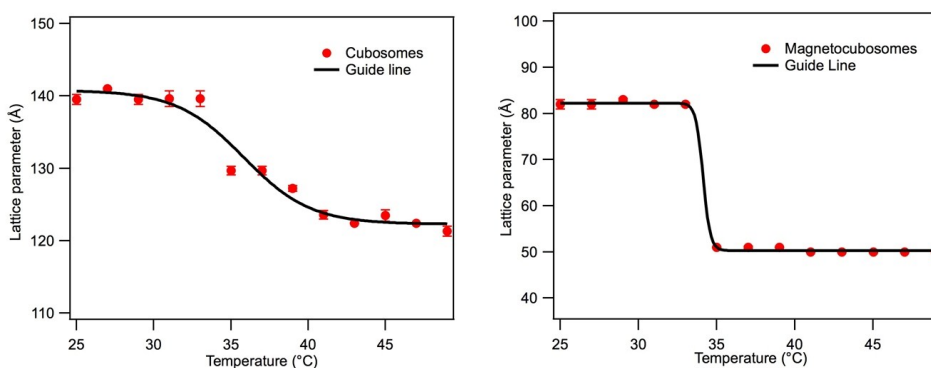


**Figure S12:** Trend of lattice parameters of cubosomes and magnetocubosomes with temperature in the 25-50°C temperature range, estimated from SAXS data. The lattice parameter  $d$  decreases following a sigmoidal-like trend. The overall lattice parameter decrease is of about 2 nm for cubosomes and 3 nm for magnetocubosomes in the 25°C-50°C temperature range. Magnetocubosomes present a phase transition  $Pn3m-H_{II}$  very close to the physiological temperature.

#### *S.14- Derivation of Equation 4 of the main text*

In the framework of Helfrich theory, the free energy of elastic curvature of a lipid bilayer  $g_c$  can be expressed as:

$$g_c = 2\kappa^B(H - H_0^B)^2 + \kappa_G^B K \quad (S6)$$

where  $\kappa^B$  and  $\kappa_G^B$  are the bending and Gaussian elastic moduli respectively, H and K are the mean and Gaussian curvatures and  $H_0^B$  is the spontaneous curvature of the bilayer. Considering that for a symmetric lipid bilayer  $H_0^B = 0$ , the  $H_{II}$  phase is characterized by a Gaussian curvature  $K=0$  and that the mean curvature for a Pn3m at the mid-plane  $H=0$ , we can write equation (6) for the hexagonal and cubic phases as follows:

$$g_c(H_{II}) = 2\kappa_B H^2 \quad (S7)$$

$$g_c(Pn3m) = \kappa_G^B K \quad (S8)$$

If we express the bending and Gaussian elastic moduli for a bilayer in terms of the corresponding terms for a monolayer, we obtain:

$$\kappa_B = 2\kappa \quad (S9)$$

$$\kappa_G^B = 2(\kappa_G - 2H_0\kappa l_c) \quad (S10)$$

and can rewrite (7) and (8) as follows:

$$g_c(H_{II}) = 4\kappa H^2 \quad (S11)$$

$$g_c(Pn3m) = 2(\kappa_G - 2H_0\kappa l_c)K \quad (S12)$$

Considering a cubic-to-hexagonal phase transition, we can write the variation of elastic curvature as:

$$\Delta g_C = 4\kappa H_{H11}^2 - 2K_{Pn3m}(\kappa_G - 2H_0\kappa l_c) \quad (S13)$$

## REFERENCES

- (1) Wang, L.; Luo, J.; Fan, Q.; Suzuki, M.; Suzuki, I. S.; Engelhard, M. H.; Lin, Y.; Kim, N.; Wang, J. Q.; Zhong, C. J. *J. Phys. Chem. B* **2005**, *109* (46), 21593.
- (2) Reese, C. W.; Strango, Z. I.; Dell, Z. R.; Tristram-Nagle, S.; Harper, P. E. *Phys. Chem. Chem. Phys.* **2015**, *17* (14), 9194.
- (3) Marsh, D. *Handbook of lipid bilayers*; 2013.
- (4) Salvatore, A.; Montis, C.; Berti, D.; Baglioni, P. *ACS Nano* **2016**, *10* (8), 7749.
- (5) Kotlarchyk, M.; Chen, S.-H. *J. Chem. Phys.* **1983**, *79* (5), 2461.

# Paper II





## Regular Article

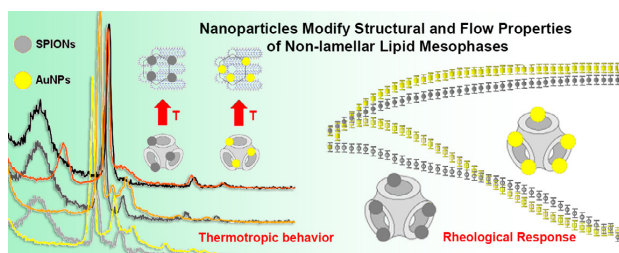
# Inorganic nanoparticles modify the phase behavior and viscoelastic properties of non-lamellar lipid mesophases

Marco Mendozza, Lucrezia Caselli, Costanza Montis, Stefano Orazzini, Emiliano Carretti, Piero Baglioni, Debora Berti\*

Department of Chemistry Ugo Schiff, University of Florence and CSGI, Via della Lastruccia 3, 50019 Florence, Italy



## GRAPHICAL ABSTRACT



## ARTICLE INFO

## Article history:

Received 3 December 2018  
 Revised 21 January 2019  
 Accepted 22 January 2019  
 Available online 23 January 2019

## Keywords:

Liquid crystalline mesophases  
 AuNPs  
 SPIONs  
 Phytantriol  
 Cubic lipid phases

## ABSTRACT

The inclusion of inorganic nanoparticles (NPs) within organized lipid assemblies combines the rich polymorphism of lipid phases with advanced functional properties provided by the NPs, expanding the applicative spectrum of these materials. In spite of the relevance of these hybrid systems, fundamental knowledge on the effects of NPs on the structure and physicochemical properties of lipid mesophases is still limited. This contribution combines Small-Angle X-ray Scattering (SAXS) and Rheology to connect the structural properties with the viscoelastic behavior of liquid crystalline mesophases of Phytantriol (Phyt) containing two kinds of hydrophobic NPs of similar size, i.e., gold NPs (AuNPs) and Superparamagnetic Iron Oxide NPs (SPIONs). Both types of NPs spontaneously embed in the hydrophobic domains of the liquid crystalline mesophase, deeply affecting its phase behavior, as SAXS results disclose. We propose a general model to interpret and predict the structure of cubic mesophases doped with hydrophobic NPs, where the effects on lipid phase behavior depend only on NPs' size and volume fraction but not on chemical identity. The rheological measurements reveal that NPs increase the solid-like behavior of the hybrid and, surprisingly, this effect depends on the chemical nature of the NPs. We interpret these results by suggesting that the long-range dipolar interactions of SPIONs affect the viscoelastic response of the material and provide an additional control parameter on mechanical properties. Overall, this study discloses new fundamental insights into hybrid liquid crystalline mesophases doped with hydrophobic NPs, highly relevant for future applications, e.g. in the biomedical field as smart materials for drug delivery.

© 2019 Published by Elsevier Inc.

**Abbreviations:** LLCs, lyotropic liquid crystals; DDS, drug-delivery systems; Phyt, phytantriol; SPIONs, superparamagnetic iron oxide nanoparticles; AuNPs, gold nanoparticles.

\* Corresponding author.

E-mail address: [debora.berti@unifi.it](mailto:debora.berti@unifi.it) (D. Berti).

## 1. Introduction

The inclusion of inorganic nanoparticles into organized lipid assemblies has the potential to combine the properties of the two components to produce smart materials and nanodevices for

a variety of diverse applications in the biomedical field. For instance, gold nanorods have been embedded in lipid vesicles for applications in hyperthermia [1,2]; quantum dots-loaded liposomes have been proposed for diagnostic purposes [3–6]; superparamagnetic iron oxide nanoparticles (SPIONs) have been included in liposomes, to form magnetoliposomes, applied both for MRI [7,8] and as drug delivery systems that can release their payload in a space- and time-controlled manner, thanks to responsiveness to static and alternating magnetic fields [9–11]. The most explored amphiphilic scaffolds are lipid vesicles, but more recently some studies have addressed the insertion of inorganic NPs [12,13] into non-lamellar lipid assemblies formed through self-assembly of polymorphic lipids. While some applicative examples have been reported, a fundamental understanding of the impact of NPs on lipid phase behavior, necessary to design these materials for a specific biomedical application is, to date, very limited.

It is well known that lipid self-assembly in water gives rise to a rich phase diagram, with a complex variety of architectures and morphologies, as in the case of glyceryl-monoleate (GMO) and Phytantriol (Phyt). For these latter systems, the phase diagrams have been thoroughly investigated over the years [14]. Depending on the water content, lamellar structures ( $L_c$  and  $L_\alpha$ ) and bicontinuous cubic mesophases (gyroid Ia3d and diamond Pn3m) are observed at room temperature, while hexagonal structures and inverted micelles are formed at higher temperatures. The presence of additives modifies and controls the geometry of these lipid architectures. This is the case for fatty acids [15,16], photo-switchable molecules [17–19], and proteins [20] that can be even crystallized within the lyotropic phase [21,22]. Recently, Briscoe et al. [23,24] investigated the effects of hydrophobic silica NPs on dioleoyl-phosphatidylethanolamine mesophases, highlighting a temperature and pressure-dependent lamellar to hexagonal phase transition. Mezzenga and coauthors studied the inclusion of hydrophilic SPIONs in monolinolein assemblies, observing the structural responsiveness of the lipid-SPION hybrids to static magnetic fields [25,26]. In a previous work, we showed that the addition of hydrophobic SPIONs to a GMO Pn3m cubic phase induces a transition to hexagonal phase, which can be understood as a balance between the free energies of membrane elastic curvature and lipid frustration packing [27]. Additionally, we highlighted that the same phase transition occurs by applying a low frequency alternating magnetic field (AMF), due to the local heating produced by the magnetic relaxation of NPs [27,28].

The central purpose of this study is the separation of thermodynamic effects, due to insertion of hydrophobic hard spheres with a given curvature into locally bilayered structures, from functional effects, specifically originating from the chemical nature of the NPs. To this aim, we leverage our previous studies on hybrid lipid cubic mesophases [27,28] to investigate two kinds of hydrophobic NPs and map the phase and flow behavior with SAXS and Rheology. Phytantriol (Phyt), endowed with lyotropic and thermotropic polymorphism, was doped with NPs characterized by the same size and similar hydrophobic coating, but different core, i.e., AuNPs and SPIONs.

The ensemble of results here gathered, besides providing fundamental knowledge on the phase behavior of such hybrid systems, discloses new insights on the interaction between nanomaterials and non-lamellar biomimetic interfaces at the molecular level, fostering the applicative potentials of these smart materials in the biomedical field [29–32].

## 2. Materials and methods

### 2.1. Materials

Fe(III)-acetylacetonate (97%), 1,2-hexadecanediol (90%), oleylamine (70%), oleic acid (90%), diphenylether (99%), denatured

ethanol and hexane mixture of isomers employed for the synthesis of hydrophobic SPIONs, were purchased from Sigma Aldrich (St. Louis MO), the same for Gold-(III) tetrachloride (99.995%) and tetraoctylammonium bromide (TOAB 98%). Phytantriol (Phyt) was a gift of Royal DSM. The synthesis of AuNPs and SPIONs is reported in the SI.

### 2.2. Preparation of bulk cubic mesophases

Bulk cubic phases with or without SPIONs and AuNPs were prepared according to the following procedure: 30 mg of Phyt were weighted in 2 mL glass vessels in the absence (for neat Phyt mesophases) or in the presence (for NPs-loaded Phyt mesophases) of appropriate volumes of SPIONs and AuNPs dispersions in hexane. About 1 mL of hexane was used to solubilize the mixtures, then the solvent was removed under a gentle nitrogen flux. The dry films were left under vacuum overnight, then hydrated with 50  $\mu$ L Milli-Q water and centrifuged ten times, 5 min each time, at 9000 rpm, alternating a run with the cap facing upward with another with the cap facing downward.

### 2.3. Small-Angle X-ray Scattering (SAXS)

SAXS measurements were performed on a S3-MICRO SAXS/WAXS instrument (HECUS GmbH, Graz, Austria) which consists of a GeniX microfocus X-ray Sealed Cu K $\alpha$  source (Xenocs, Grenoble, France) with power 50 W. The source provides a focused X-ray beam with  $\lambda = 0.1542$  nm Cu K $\alpha$  line [33,34]. The instrument is equipped with two one-dimensional (1D) position sensitive detectors, (HECUS 1D-PSD-50M system) each detector is 50 mm long (spatial resolution 54  $\mu$ m/channel, 1024 channels) and covers a q-range of  $0.003 < q < 0.6 \text{ \AA}^{-1}$  (SAXS) and  $1.2 < q < 1.9 \text{ \AA}^{-1}$ , (WAXS). The temperature was controlled by means of a Peltier TCSS-3 Hecus. SAXS curves of bulk cubic phases were recorded at 25, 35 and 50 °C in a solid sample-holder. The hexane dispersions of SPIONs and AuNPs were inserted in a glass capillary to record SAXS profiles. NPs dry films were prepared as follows: the NPs dispersion in hexane was placed in a glass capillary and dried under vacuum overnight to remove the solvent.; SAXS profiles were then recorded. SAXS data analysis is detailed in the SI.

### 2.4. Rheology

All rheology tests were performed using a Physica-Paar UDS 200 rheometer, equipped with a plate-plate geometry measuring system (diameter of the upper plate 20 mm, measuring gap: 200  $\mu$ m). The temperature was controlled with a Peltier device. All the oscillatory measurements were performed within the linear viscoelastic range (1 Hz about the amplitude sweep curves). For all the measurements, once the samples were deposited on the surface of the measuring plate, a delay time of 10 min was set in order to ensure the complete equilibration of the sample; in that way no loading effect was observed for all the investigated samples. In order to minimize the evaporation of water, silicone oil was applied to the rim of the samples when temperature was varied in 25–50 °C. The instrumental setups for the rheology tests are the following:

- i. Frequency sweep test: frequency range 100–0.001 Hz; amplitude 0.1% strain;
- ii. Amplitude sweep test: strain % from 0.001% to 10%; frequency 1 Hz.

### 3. Results and discussion

#### 3.1. Structure of Phyt mesophases doped with hydrophobic NPs

Fig. 1 summarizes the physicochemical characterization of the NPs (AuNPs and SPIONs) employed in the study. Briefly, AuNPs with a dodecanethiol coating in hexane were synthesized according to Brust et al. [35] (see SI for details), leading to slightly polydisperse nanospheres, as visible from the TEM images (Fig. 1d). The analysis of the NPs' SAXS profile yielded an average core diameter of 3.0 nm and a polydispersity index of 0.28, as estimated through a Schultz distribution [36] (see Fig. 1c): a similar value was obtained from TEM (average diameter 2.8 nm, see SI for details). Hydrophobic SPIONs were synthesized according to Wang et al. [37], leading to a stable hexane dispersion of magnetite nanospheres coated with oleic acid/oleylamine, with slightly larger size than AuNPs, as visible from TEM images (Fig. 1b) and from SAXS (Fig. 1a) curve fitting results: core diameter of 3.6 nm (3.8 nm by TEM) and polydispersity 0.30. The two different NPs' samples are therefore characterized by a hydrophobic coating, which is expected to drive their inclusion in the hydrophobic domains of the mesophase, and by relatively small core size, which is a necessary prerequisite to determine a minimum local perturbation to the bilayered arrangement of Phyt, of 2.8 nm thickness [38].

The effects of increasing amounts of hydrophobic NPs (SPIONs and AuNPs) on the structure of the liquid crystalline mesophases of Phyt in water excess at 25 °C were monitored with SAXS (Fig. 2b, 2c).

It is well known that the binary system Phyt/H<sub>2</sub>O with excess water at room temperature is a Pn3m cubic mesophase, with the amphiphilic Phyt molecules assembled as bilayers folded in

a tridimensional cubic structure [39]. Accordingly, the Bragg peaks of the cubic phase are clearly recognizable in the corresponding SAXS profile (Fig. 2b, Fig. 2c, blue dashed lines).

Before discussing the phase behavior of hybrid NPs/Phyt systems, some consideration should be made about the Phyt bilayer thickness as compared with NPs' size. While the former is 2.8 nm [39], the overall sizes of magnetic and gold nanoparticles, considering their shell composed by oleic acid (chain length 2 nm [40]) and dodecanethiol (1.4 nm [41]), are 7.6 nm and 5.8 nm respectively. In the hypothesis of interdigitation between Phyt and the coating alkyl chains, it is mainly the hindrance of NPs' cores to determine a local perturbation in the bilayer (see the sketch in Fig. 2d). Dodecanethiol is covalently bound to the surface of AuNPs (the excess is removed during the synthesis work-up, see SI for details), while oleic acid and oleylamine are in excess in SPIONs dispersion. Therefore, to better compare Phyt/SPIONs and Phyt/AuNPs data without coating effects, Phyt/AuNPs samples were prepared adding the same quantity of SPIONs stabilizing agent (see sections S-4 and S-5 in SI for details).

The addition of increasing amounts of both SPIONs and AuNPs results in a clear modification of the mesostructure. Even small amounts of NPs ( $1 \times 10^{-5}$  NPs/Phyt) causes the appearance of an additional peak, broad and centered at  $0.18 \text{ \AA}^{-1}$  for AuNPs and more intense and centered at  $0.06 \text{ \AA}^{-1}$  for SPIONs. These peaks are present for all Phyt/NPs SAXS profiles (see Fig. 2b, 2c), without any significant shift of the maximum, irrespectively of the amounts of NPs. To gain more insight on this effect, we recorded SAXS profiles of dry NPs films (see Section 2 for details on samples preparation). The dry AuNPs film (Fig. 2b, red curve) exhibits a broad peak, centered at  $0.18 \text{ \AA}^{-1}$ , which perfectly matches the q-value of the extra-peak in the mixed mesophase (see Fig. 2b). The SAXS profile

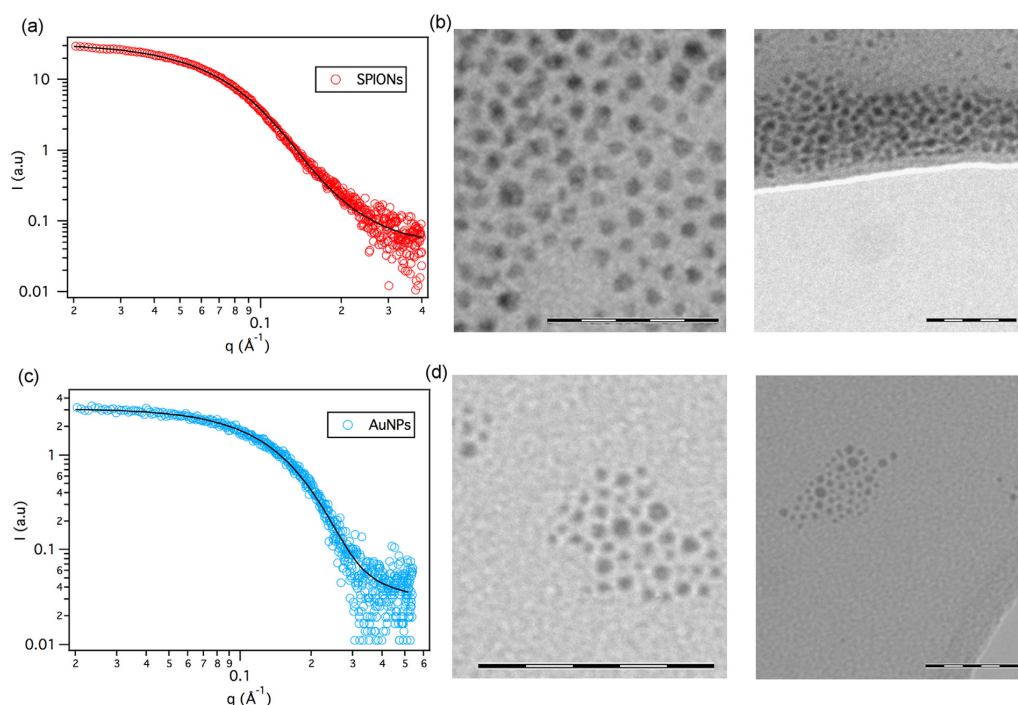


Fig. 1. Structural characterization of hydrophobic AuNPs and SPIONs: (a, c) Small-Angle X-ray Scattering profiles of SPIONs (a) and AuNPs (c) in hexane: the continuous lines represent the best fitting curves according to a Schultz polydisperse spheres distribution; (b, d) representative TEM images of (b) SPIONs and (d) AuNPs. The scale bar in TEM images is 50 nm.



[13,42,43]. The difference in the correlation length of SPIONs and AuNPs in the dry film might be both related to the core differences or to the slightly different hydrophobic coating of NPs, which might lead to a different arrangement of the alkyl chains between neighboring NPs. The shift of the correlation peak from  $0.07 \text{ \AA}^{-1}$  (dry film) to  $0.06 \text{ \AA}^{-1}$  (NPs inside Phyt) observed for SPIONs, which corresponds to a variation in the NP-NP correlation distance from 8.90 to 10.5 nm, hints at the coexistence of SPIONs at the grain boundaries with particles effectively embedded in the mesophase. The same effect is clearer for AuNPs, where an additional correlation peak at  $0.097 \text{ \AA}^{-1}$  is detected, which can unambiguously attributed the appearance of the peak to AuNPs embedded inside the lipid architecture. Interestingly, the estimated correlation distance (6.5 nm) closely matches the nanometric organization of the mesophase.

Upon increasing the NPs amount, a phase transition from cubic (Pn3m) to hexagonal ( $H_{II}$ ) phase is detected. In particular, at the lowest NPs amount (light blue lines, Fig. 2b, c), both mixed mesophases retain the Pn3m cubic structure; the intermediate amount of SPIONs ( $2 \times 10^{-5}$  NPs/Phyt, Fig. 2b, green curve) is sufficient to induce the phase transition, while the same number of AuNPs induces a partial transition to the hexagonal phase, highlighted by the coexistence of the typical Bragg reflections of both phases (Fig. 2c, green curve); finally, at the highest amount of NPs ( $4 \times 10^{-5}$  NPs/Phyt) (Fig. 2b, c, yellow curve), both mesophases are  $H_{II}$ . In a recent study we reported the same Pn3m- $H_{II}$  phase transition induced by hydrophobic SPIONs on GMO mesophases, ascribing it to the balance between free energies of elastic curvature and frustration packing [27]. The results here gathered extend our previous findings to a different lipid (Phyt vs GMO), additionally showing that the effect of the hydrophobic nature of SPIONs and AuNPs is similar; it has to be pointed out that even if NPs' number is the same, their different size results in a difference in volume fractions (see SI for details). This value, higher for SPIONs, fully justifies the less pronounced phase transition of Phyt/AuNPs with respect to the SPIONs mesophase with lower and intermediate amount of NPs. We can conclude that the structural arrange-

ment of the hybrid lipid/hydrophobic NPs mesophases is dependent on: (i) the equilibrium structure of the lipid binary phase; (ii) the hydrophobic nature of the coating of the NPs, leading to their preferential partition in the hydrophobic domains of the lipid scaffold; (iii) the size of NPs, which determines the degree of perturbation of the bilayer curvature at the NPs inclusions, thereby affecting the frustration packing energy of the lipid scaffold [27]. The relevance of this latter parameter is also suggested by the slight variation between SPIONs and AuNPs amounts required to completely trigger the phase transition, fully in line with the slight size and polydispersity difference between the two NPs types.

We then fixed the NPs/Phyt ratio to  $1 \times 10^{-5}$  and varied the temperature from 25 °C to 50 °C, to explore the thermotropic phase behavior of the hybrid mesophases (Fig. 3).

Fig. 3a displays the profiles of the binary Phyt/ $H_2O$  system in excess water, which shows the characteristic Pn3m- $H_{II}$  transition at 50 °C, in full agreement with the literature [39].

Upon loading with the same number of SPIONs and AuNPs, (Fig. 3b and 3c, respectively) the Pn3m phase persists at room temperature (blue curves); a temperature increase to 35 °C partially promotes the phase transition to the hexagonal phase, both for SPIONs (more pronounced) and for AuNPs (Fig. 3b, c green curves). Therefore, the Pn3m- $H_{II}$  transition can be induced both by increasing the amounts of NPs and, at a fixed amount of NPs, by raising the temperature up to a value which is considerably lower than the transition temperature of the binary phase. The correlation peak, observed for higher NPs concentrations (see Fig. 2), also appears increasing the temperature for the sample with the lower amount of nanoparticles (Fig. 3c) and the sharp signal is preserved after 24 h of the thermal cycle (see SI for details). This effect might be related to a reorganization of the NPs which, at higher temperature, are characterized by a higher mobility inside the mesophase. Nevertheless, the present results further prove that this behavior is not specifically related to a defined lipid molecule or NP kind but can be considered as a general phenomenon. In addition, in this description, the nature of the NPs core does not show major impact.

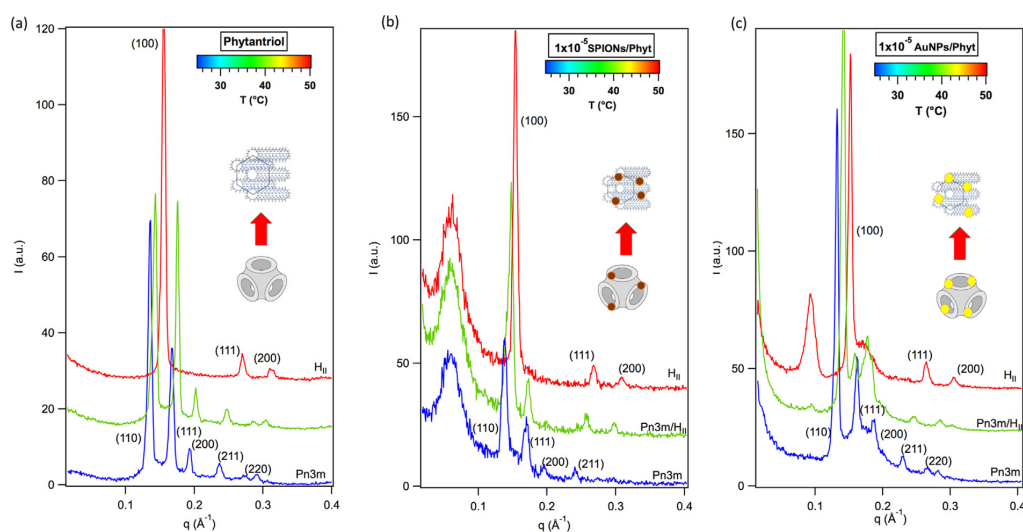


**Fig. 3.** SAXS profiles of Phyt/ $H_2O$  mesophases in the absence (a) and in the presence of (b, c)  $1 \times 10^{-5}$  NPs (b) SPIONs and (c) AuNPs per Phyt molecule at 25 °C (blue), 35 °C (green curves) and 50 °C (red curves); the Miller indexes assignments ( $hkl$ ) of the Pn3m and hexagonal phase are also reported. (For interpretation of the references to colours in this figure legend, the reader is referred to the web version of this article.)

### 3.2. Rheological behavior of Phyt mesophases doped with hydrophobic NPs

In order to understand the effect of NPs on the viscoelastic properties of Phyt/NPs systems, rheological experiments were performed on the same hybrid mesophases.

Amplitude sweep measurements at a fixed frequency of 1 Hz and at  $T = 25\text{ }^{\circ}\text{C}$  are shown in Fig. 4, where the storage modulus  $G'$  (the elastic component of the complex modulus  $G^*$ ) and the loss modulus  $G''$  (the dissipative component of  $G^*$ ) of the different liquid crystalline mesophases are displayed as a function of the applied strain. The curves measured for the hybrid Pn3m mesophases doped with  $1 \times 10^{-5}$  NPs per Phyt molecule (red markers, SPIONs in Fig. 4a, AuNPs in Fig. 4c) are compared to those measured for Phyt/ $\text{H}_2\text{O}$  in the absence of NPs (blue markers). Fig. 4b, d show the profiles measured for hybrid  $\text{H}_{\text{II}}$  mesophases doped with increasing amounts (light blue markers  $2 \times 10^{-5}$  NPs per Phyt molecule, green markers  $4 \times 10^{-5}$  NPs per Phyt molecule) of NPs (SPIONs in Fig. 4b, AuNPs in Fig. 4d).

It is known that different structural arrangements of liquid crystalline mesophases are characterized by markedly diverse rheological responses [42,44]. Accordingly, the inclusion of NPs (both SPIONs and AuNPs) in the Phyt/ $\text{H}_2\text{O}$  cubic mesophase, which induces a cubic-to-hexagonal phase transition, is associated with a striking variation in the rheological behavior: as a matter of fact, for Phyt/ $\text{H}_2\text{O}$  system and for low NPs loading, the amplitude sweep curves (Fig. 4a, c) are characterized by the typical behavior of a 3D isotropic network, with no preferential directionality, e.g., similarly to Xantan Gum [45] and PVA [46]-based gels. In particular,  $G''$

shows a non-monotonic behavior: after an initial increase for low strain values, it reaches a maximum, above which a strain increase causes the disruption of the network, resulting in the decrease of both  $G'$  and  $G''$ , previously interpreted by McLeish and coworkers with a “slip-plane” model, where the local cubic order is disrupted along the direction of applied shear, while the bulk connectivity of the 3D network is preserved [47,48].

As discussed in the previous section, NPs promote the Pn3m to  $\text{H}_{\text{II}}$  phase transition (see Fig. 2). The 1D-directional nature of the hexagonal phase, whose domains are able to align along the shear direction [49], determines a very different behavior, with monotonic decrease of both moduli with increasing strain (Fig. 4b, d).

In summary, the arrangement of the lipid scaffold appears as the main factor affecting the rheological behavior, as inferred from amplitude sweep measurements. Within the same structural arrangement (Pn3m or  $\text{H}_{\text{II}}$ ), increasing the NPs number density does not have major effects. This evidence also suggests an overall structural integrity of the mesophase, where lipid assembly persists in the presence of NPs embedded in the hydrophobic domains.

To gather additional insight into the flow behavior, we investigated the dependence of the storage and loss moduli of the material on the frequency of the applied shear perturbation, by performing frequency sweep measurements in the linear viscoelastic regime (strain 0.1%, see Materials and Methods for details). The main results are reported in Fig. 5.

In line with the amplitude sweep profiles, the results highlight a different dependence of both  $G'$  and  $G''$  on the frequency of the applied strain for Pn3m (Fig. 5a, c) and  $\text{H}_{\text{II}}$  (Fig. 5b, d) mesophases.

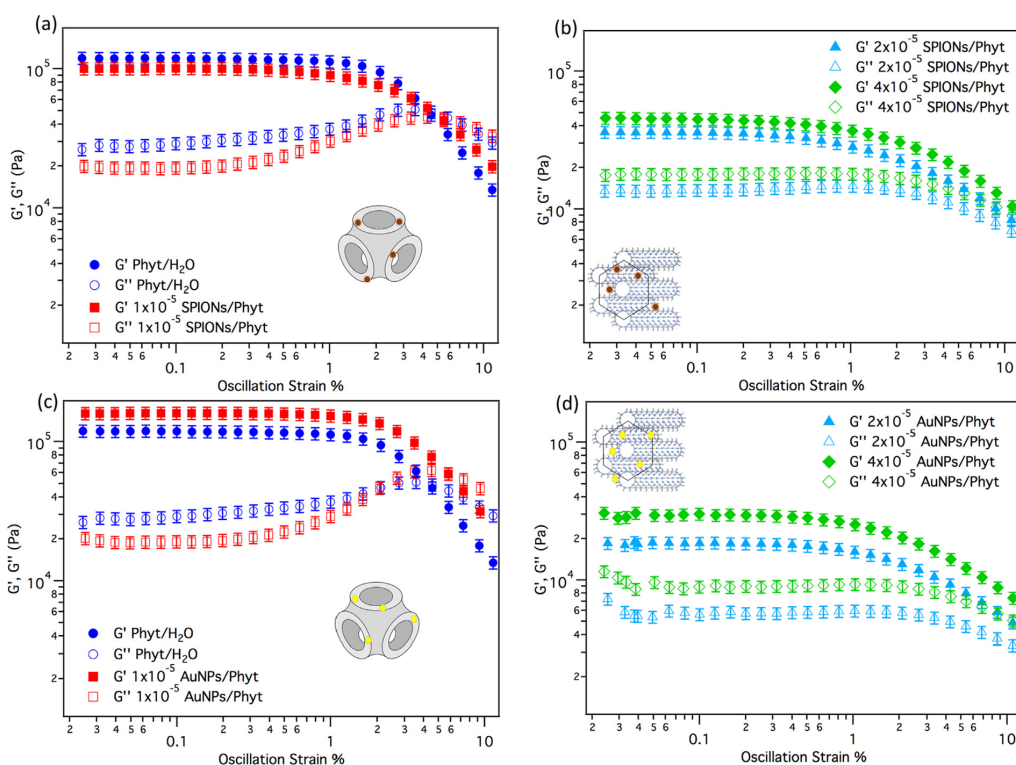


**Fig. 4.** Amplitude sweep analysis performed at 1 Hz and  $25\text{ }^{\circ}\text{C}$  for: (a, c) Phyt/ $\text{H}_2\text{O}$  Pn3m mesophase in the absence (blue markers) and in the presence (red markers) of  $1 \times 10^{-5}$  SPIONs (a) and AuNPs (c) per Phyt molecule; (b, d) Phyt/ $\text{H}_2\text{O}$   $\text{H}_{\text{II}}$  mesophase in the presence of  $2 \times 10^{-5}$  (light blue markers) and  $4 \times 10^{-5}$  (green markers) SPIONs (b) and AuNPs (d) per Phyt molecule. (For interpretation of the references to colours in this figure legend, the reader is referred to the web version of this article.)

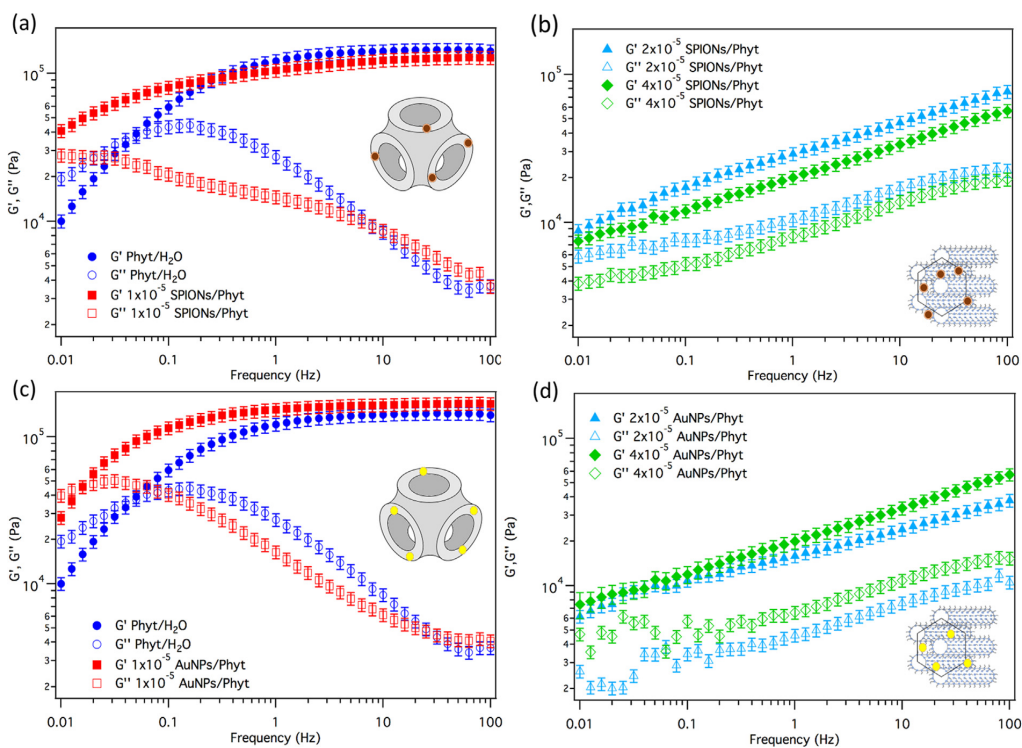


**Fig. 5.** Frequency sweep curves measured at 25 °C for: (a, c) Phyt/H<sub>2</sub>O Pn3m mesophase in the absence (blue markers) and in the presence (red markers) of  $1 \times 10^{-5}$  SPIOs (a) and AuNPs (c) per Phyt molecule; (b, d) Phyt/H<sub>2</sub>O H<sub>II</sub> mesophase in the presence of  $2 \times 10^{-5}$  (light blue markers) and  $4 \times 10^{-5}$  (green markers) SPIOs (b) and AuNPs (d) per Phyt molecule. (For interpretation of the references to colours in this figure legend, the reader is referred to the web version of this article.)

As a first observation, the transition from Pn3m to H<sub>II</sub> induces a decrease of  $\omega_c$ , highlighting the lower rigidity of the hexagonal phase [50,51], which can be again attributed to the transition from a 3D-to-1D geometry, as confirmed by the trend of  $\tan \delta$  ( $\tan \delta = G''/G'$ ) reported in the SI.

The Pn3m mesophases (Fig. 5a, c) behave as a viscoelastic fluid: for  $\omega > \omega_c$  (with  $\omega_c$  crossover frequency between  $G'$  and  $G''$  curves),  $G'$  is higher than  $G''$ , which indicates a predominantly elastic behavior, while the viscous character is dominant for  $\omega < \omega_c$ . Concerning the H<sub>II</sub> mesophase (Fig. 5b, d), the material is characterized by a solid-like behavior, with  $G'$  higher than  $G''$  in the whole range of investigated frequencies. In this region of the phase diagram, increasing the number density of NPs does not significantly affect the viscoelastic properties, probably due to the alignment of nanoparticles along the hexagonal domains.

Conversely, the inclusion of nanoparticles in a Pn3m mesophase, significantly modifies its rheological behavior. In particular, although the same general trend described for the binary phase is preserved for the cubic phases doped with SPIOs (Fig. 5a, red markers) and AuNPs (Fig. 5c, red markers), the crossover frequency between  $G'$  and  $G''$  is shifted to lower  $\omega$  values. This effect is particularly marked for SPIOs, with the crossover frequency located outside the accessible frequency range of our rheometer.

The crossover frequency marks the transition from the rubbery plateau to the viscous regime and corresponds to the longest relaxation time ( $\tau_{max} = 1/\omega_c$ ) of the system, i.e. the longest characteristic time required to relax back to the equilibrium configuration. According to the model proposed by Mezzenga et al. [44,52], the

physical meaning of this relaxation time  $\tau_{max} = 1/\omega_c$  can be attributed to the diffusion time of the lipid molecules at the water-lipid interface; this value provides therefore a characteristic order of magnitude for the diffusion processes occurring at the interface and can be used as an indication for the release kinetics of the active molecules through the hydrophobic/hydrophilic interface [52]. The  $\tau_{max}$  value markedly increases in the presence of  $1 \times 10^{-5}$  NPs/Phyt, passing from 3.1 s to 10 s for AuNPs and to >10 s for SPIOs, accounting for a slower response of the material to the applied stress, which is a clear signature of an enhanced solid-like behavior.

To rule out that this effect is caused by the partition of the SPIOs coating agents in the bilayer (added also to Phyt/AuNPs, to better compare the two systems, see SI for details), we performed a control experiment where the same amount of oleic acid and oleylamine was directly added to Phyt without NPs (see SI for details). This results in a negligible shift in the crossover frequency with respect to the neat binary phase. Therefore, the possible compositional change of the lipid scaffold determined by these hydrophobic molecular additives, does not substantially affect the lipid/water interface relaxation time.

Moreover, as discussed in the SAXS section, NPs affect the lattice parameter of the mesostructure, shrinking the water channels. Since it has been reported [51] that the swelling of the cubic phase has a major impact on the crossover frequency values, as a further control experiment we performed rheological experiments on Phyt/oleic acid/oleylamine Pn3m mesophases, tuning the composition to match the lattice parameter of NPs/Phyt (see SI). The

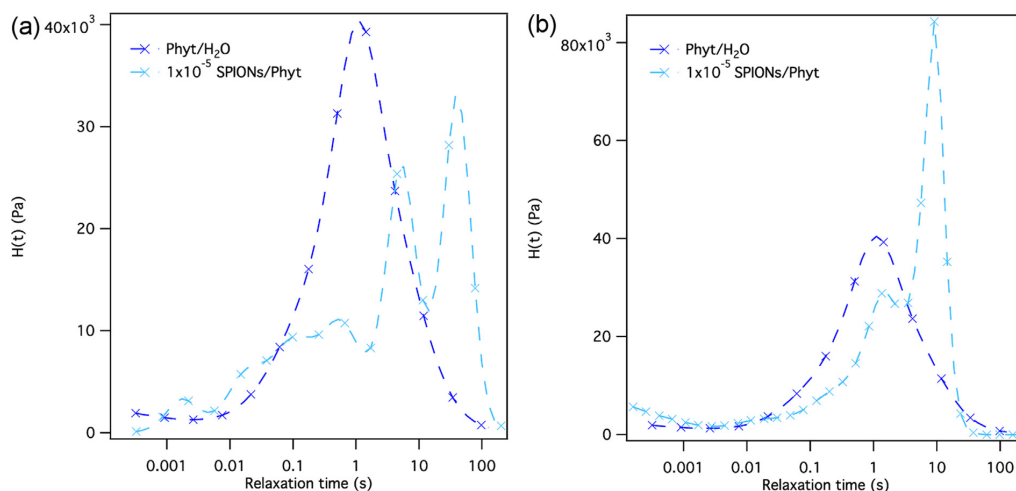


**Fig. 6.** Viscoelastic relaxation spectra of Pn3m mesophases: Phyt/H<sub>2</sub>O (blue markers and line in both plots), Phyt/SPIONs (cyan markers and line in (a)), and Phyt/AuNPs (cyan markers and line in (b)). (For interpretation of the references to colours in this figure legend, the reader is referred to the web version of this article.)

variation of the frequency sweep profile is indeed negligible and therefore possible effects due to a different degree of swelling of the cubic phase can be safely ruled out.

In summary, the presence of NPs is the main factor that tunes the viscoelastic relaxation of the cubic mesophase. To better appreciate this point, the frequency sweep curves were transformed in continuum relaxation spectra [44,51] (Fig. 6, see SI for the different inversion methods tested). The behavior of Pn3m cubic mesophases can be described with a monomodal distribution of relaxation times: the main term is identified with the characteristic diffusion time of lipids at the water–lipid interface, i.e.  $\tau_{max}$ .

With NPs, the relaxation mode distribution broadens and the spectrum complexity increases, indicating a higher polydispersity [51]. For both kinds of NPs, the main relaxation mode splits into a multimodal distribution, suggesting a non-trivial effect on the rheological properties of lipid bilayer. This feature can be interpreted in terms of the coexistence of lipids freely diffusing at the lipid/water interface, with a slower relaxation time, i.e.  $\tau_{max}$ , ascribable to a hampered lipid diffusion at the NPs' surface. Interestingly, this is a similar effect highlighted through Fluorescence Correlation Spectroscopy [53,54], for hydrophilic AuNPs interacting with free-standing lipid membrane. Moreover, although the NPs' diameter is comparable, the concentration identical and the effects on phase behavior similar (as highlighted from SAXS measurements), the addition of SPIONs is related to a significantly higher  $\tau_{max}$  value with respect to AuNPs (9.1 s vs 37.9 s), as the comparison between Fig. 6a and b, highlights. Therefore, the chemical nature of NPs might be critical for the rheological response of the material. This significant effect is, we believe, well beyond what can be expected considering the slight difference in NPs sizes, therefore hinting to a “core” effect in the viscoelastic response. A working hypothesis is that the long-range dipolar interactions between the SPIONs, which are absent in the AuNPs-doped systems, act as a structuring factor on the material, increasing the elastic over viscous response of the material upon the applied stress. This stiffening effect likely originates at the nanoscale level, where dipolar interactions between SPIONs inside the bilayer may additionally hamper the free diffusion of lipids. Indeed, while AuNPs do not significantly influence the diffusion times of lipid molecules at the lipid/water interface, corresponding to the higher- $\tau$  peak in the relaxation spectrum (Fig. 6b, light blue dashed line), SPIONs cause a substantial shift in the “free-

diffusion” time of lipids, suggesting an alteration of molecular mobility in the whole bilayer.

#### 4. Conclusions

In this contribution we explored the structural and rheological effects of the insertion of hydrophobic SPIONs and AuNPs of similar size in liquid crystalline mesophases of Phytantriol at maximum water swelling. SAXS results highlighted that both types of NPs are embedded in the liquid crystalline mesophase and that their presence promotes a cubic to hexagonal phase transition, with no noteworthy dependence on the type of NPs, but only on their number density, in line with previous data on glycerol-monooleate/SPIONs hybrid mesophases [27]. These results are consistent with the fact that simple thermodynamic considerations, related to the mesophase geometry, the coating and size of NP, can describe in general terms the phase behavior.

The rheological response of such architectures, addressed here for the first time, reveals that the presence of NPs enhances the solid-like behavior of the material. Interestingly, this effect is significantly more pronounced for SPIONs, evidencing possible long-range dipolar interactions between SPIONs that may constitute an additional structuring factor for the material, decreasing its deformability upon stress deformation.

Overall, the comparison of structural and rheological results highlights that different features of the NPs are relevant in affecting the properties of the mesophase: NPs surface (i.e., hydrophobic nature of the coating, driving localization in the lipid scaffold) and size, modulate the local perturbation of the lipid assemblies and affect the phase behavior at rest, while the core composition (AuNPs vs SPIONs) seems to become relevant for the rheological response and for the relaxation to mechanical perturbation.

These results shed light on the structural and physicochemical properties of lipid/NPs mixed liquid crystalline mesophases, disclosing new fundamental knowledge for future biomedical applications.

#### Acknowledgment

Mirko Severi is gratefully acknowledged for ICP-AES analysis; CSGI is acknowledged by all the authors for partial funding.

## Appendix A. Supplementary material

Supplementary data to this article can be found online at <https://doi.org/10.1016/j.jcis.2019.01.091>.

## References

- [1] W.K. Fong, T.L. Hanley, B. Thierry, A. Tilley, N. Kirby, L.J. Waddington, B.J. Boyd, Understanding the photothermal heating effect in non-lamellar liquid crystalline systems, and the design of new mixed lipid systems for photothermal on-demand drug delivery, *Phys. Chem. Chem. Phys.* 16 (2014) 24936–24953, <https://doi.org/10.1039/c4cp03635b>.
- [2] W.K. Fong, T.L. Hanley, B. Thierry, N. Kirby, B.J. Boyd, Plasmonic nanorods provide reversible control over nanostructure of self-assembled drug delivery materials, *Langmuir* 26 (2010) 6136–6139, <https://doi.org/10.1021/la100644s>.
- [3] I.L. Medintz, H.T. Uyeda, E.R. Goldman, H. Mattoussi, Quantum dot bioconjugates for imaging, labelling and sensing, *Nat. Mater.* 4 (2005) 435–446, <https://doi.org/10.1038/nmat1390>.
- [4] J.A. Kloepfer, N. Cohen, J.L. Nadeau, FRET between CdSe quantum dots in lipid vesicles and water- And lipid-soluble dyes, *J. Phys. Chem. B* 108 (2004) 17042–17049, <https://doi.org/10.1021/jp048094c>.
- [5] G. Gopalakrishnan, C. Danelon, P. Izweska, M. Prummer, P.Y. Bolinger, I. Geissbühler, D. Demurtas, J. Dubochet, H. Vogel, Multifunctional lipid/quantum dot hybrid nanocontainers for controlled targeting of live cells, *Angew. Chemie – Int. Ed.* 45 (2006) 5478–5483, <https://doi.org/10.1002/anie.200600545>.
- [6] W.T. Al-jamal, K.T. Al-jamal, B. Tian, L. Lacerda, P.H. Bomans, P.M. Frederik, K. Kostarelos, Lipid quantum dot bilayer vesicles, *ACS Nano* 2 (2008).
- [7] K. Yang, Y. Liu, Y. Liu, Q. Zhang, C. Kong, C. Yi, Z. Zhou, Z. Wang, G. Zhang, Y. Zhang, N.M. Khashab, X. Chen, Z. Nie, Cooperative assembly of magnetonanosomes with tunable wall thickness and permeability for MRI-guided, *Drug Deliv.* (2018), <https://doi.org/10.1021/jacs.8b00884>.
- [8] M.S. Martina, J.P. Fortin, C. Ménager, O. Clément, G. Barratt, C. Grabielle-Madelmont, F. Gazeau, V. Cabuil, S. Lesieur, Generation of superparamagnetic liposomes revealed as highly efficient MRI contrast agents for in vivo imaging, *J. Am. Chem. Soc.* 127 (2005) 10676–10685, <https://doi.org/10.1021/ja0516460>.
- [9] E. Amstad, J. Kohlbrecher, E. Müller, T. Schweizer, M. Textor, E. Reimhult, Triggered release from liposomes through magnetic actuation of iron oxide nanoparticle containing membranes, *Nano Lett.* 11 (2011) 1664–1670, <https://doi.org/10.1021/nl2001499>.
- [10] A. Salvatore, C. Montis, D. Berti, P. Baglioni, Multifunctional magnetoliposomes for sequential controlled release, *ACS Nano* 10 (2016) 7749–7760, <https://doi.org/10.1021/acsnano.6b03194>.
- [11] C.C. Piccinetti, C. Montis, M. Bonini, R. Laurà, M.C. Guerrero, G. Radaelli, F. Vianello, V. Santinelli, F. Maradonna, V. Nozzi, A. Miccoli, I. Olivetto, Transfer of silica-coated magnetic ( $\text{Fe}_3\text{O}_4$ ) nanoparticles through food: a molecular and morphological study in Zebrafish 11 (2014) 567–579, <https://doi.org/10.1089/zeb.2014.1037>.
- [12] M. Szlezak, D. Nieciecka, A. Joniec, M. Pekała, E. Gorecka, M. Emo, M.J. Stébé, P. Krysiński, R. Bilewicz, Monoolein cubic phase gels and cubosomes doped with magnetic nanoparticles-hybrid materials for controlled drug release, *ACS Appl. Mater. Interfaces* *acsami*.6b12889 (2017), <https://doi.org/10.1021/acsnano.6b12889>.
- [13] E. Venugopal, S.K. Bhat, J.J. Vallooran, R. Mezzenga, Phase behavior of lipid-based lyotropic liquid crystals in presence of colloidal nanoparticles, *Langmuir* 27 (2011) 9792–9800, <https://doi.org/10.1021/la201767p>.
- [14] C. Fong, T. Le, C.J. Drummond, Lyotropic liquid crystal engineering—ordered nanostructured small molecule amphiphile self-assembly materials by design, *Chem. Soc. Rev.* 41 (2012) 1297, <https://doi.org/10.1039/c1cs15148g>.
- [15] N. Tran, A.M. Hawley, J. Zhai, B.W. Muir, C. Fong, C.J. Drummond, X. Mulet, High-throughput screening of saturated fatty acid influence on nanostructure of lyotropic liquid crystalline lipid nanoparticles, *Langmuir* 32 (2016) 4509–4520, <https://doi.org/10.1021/acs.langmuir.5b03769>.
- [16] N. Tran, X. Mulet, A.M. Hawley, C. Fong, J. Zhai, T.C. Le, J. Ratcliffe, C.J. Drummond, Manipulating the ordered nanostructure of self-assembled monoolein and phytantriol nanoparticles with unsaturated fatty acids, *Langmuir* 34 (2018) 2764–2773, <https://doi.org/10.1021/acs.langmuir.7b03541>.
- [17] S. Aleandri, C. Speziale, R. Mezzenga, E.M. Landau, Design of light-triggered lyotropic liquid crystal mesophases and their application as molecular switches in ‘On Demand’ release, *Langmuir* 31 (2015) 6981–6987, <https://doi.org/10.1021/acs.langmuir.5b01945>.
- [18] K.J. Tangso, W.K. Fong, T. Darwish, N. Kirby, B.J. Boyd, T.L. Hanley, Novel spirocyan amphiphiles and their application as light-responsive liquid crystalline components, *J. Phys. Chem. B* 117 (2013) 10203–10210, <https://doi.org/10.1021/jp403840m>.
- [19] S. Jia, J.D. Du, A. Hawley, W.K. Fong, B. Graham, B.J. Boyd, Investigation of donor-acceptor stenhouse adducts as new visible wavelength-responsive switching elements for lipid-based liquid crystalline systems, *Langmuir* 33 (2017) 2215–2221, <https://doi.org/10.1021/acs.langmuir.6b03726>.
- [20] Q. Liu, Y. Da Dong, B.J. Boyd, Selective sequence for the peptide-triggered phase transition of lyotropic liquid-crystalline structures, *Langmuir* 32 (2016) 5155–5161, <https://doi.org/10.1021/acs.langmuir.6b00547>.
- [21] L. Van'T Hag, L. De Campo, C.J. Garvey, G.C. Feast, A.E. Leung, N.R. Yepuri, R. Knott, T.L. Greaves, N. Tran, S.L. Gras, C.J. Drummond, C.E. Conn, Using SANS with contrast-matched lipid bicontinuous cubic phases to determine the location of encapsulated peptides, proteins, and other biomolecules, *J. Phys. Chem. Lett.* 7 (2016) 2862–2866, <https://doi.org/10.1021/acs.jpclett.6b01173>.
- [22] L. van 't Hag, A. Anandan, S.A. Seabrook, S.L. Gras, C.J. Drummond, A. Vrielink, C.E. Conn, Direct demonstration of lipid phosphorylation in the lipid bilayer of the biomimetic bicontinuous cubic phase using the confined enzyme lipid A phosphoethanolamine transferase, *Soft Matter*. 13 (2017) 1493–1504, <https://doi.org/10.1039/C6SM02487D>.
- [23] J.M. Bulpitt, T. Snow, B. Quignon, C.M. Beddoes, T.-Y.D. Tang, S. Mann, O. Shebanova, C.L. Pizzey, N.J. Terrill, S.A. Davis, W.H. Briscoe, Hydrophobic nanoparticles promote lamellar to inverted hexagonal transition in phospholipid mesophases, *Soft Matter*. 11 (2015) 8789–8800, <https://doi.org/10.1039/c5sm01705j>.
- [24] C.M. Beddoes, J. Berge, J.E. Bartenstein, K. Lange, A.J. Smith, R.K. Heenan, W.H. Briscoe, Hydrophilic nanoparticles stabilising mesophase curvature at low concentration but disrupting mesophase order at higher concentrations, *Soft Matter*. 12 (2016) 6049–6057, <https://doi.org/10.1039/C6SM00393A>.
- [25] J.J. Vallooran, R. Negrini, R. Mezzenga, Controlling anisotropic drug diffusion in lipid- $\text{Fe}_3\text{O}_4$  nanoparticle hybrid mesophases by magnetic alignment, *Langmuir* 29 (2013) 999–1004, <https://doi.org/10.1021/la304563r>.
- [26] J.J. Vallooran, S. Bolisetty, R. Mezzenga, Macroscopic alignment of lyotropic liquid crystals using magnetic nanoparticles, *Adv. Mater.* 23 (2011) 3932–3937, <https://doi.org/10.1002/adma.201101760>.
- [27] M. Mendoza, C. Montis, L. Caselli, M. Wolf, P. Baglioni, D. Berti, On the thermotropic and magnetotropic phase behavior of lipid liquid crystals containing magnetic nanoparticles, *Nanoscale* 10 (2018) 3480–3488, <https://doi.org/10.1039/c7nr08478a>.
- [28] C. Montis, B. Castrorfforio, M. Mendoza, A. Salvatore, D. Berti, P. Baglioni, Magnetocubosomes for the delivery and controlled release of therapeutics, *J. Colloid Interface Sci.* 449 (2015) 317–326, <https://doi.org/10.1016/j.jcis.2014.11.056>.
- [29] L. Boge, A. Västberg, A. Umerska, H. Byssell, J. Eriksson, K. Edwards, A. Millqvist-Fureby, M. Andersson, Freeze-dried and re-hydrated liquid crystalline nanoparticles stabilized with disaccharides for drug-delivery of the plectasin derivative AP114 antimicrobial peptide, *J. Colloid Interface Sci.* 522 (2018) 126–135, <https://doi.org/10.1016/j.jcis.2018.03.062>.
- [30] U. Bazylińska, J. Kulbacka, J. Schmidt, Y. Talmon, S. Murgia, Polymer-free cubosomes for simultaneous bioimaging and photodynamic action of photosensitizers in melanoma skin cancer cells, *J. Colloid Interface Sci.* 522 (2018) 163–173, <https://doi.org/10.1016/j.jcis.2018.03.063>.
- [31] N. Tran, M. Hocquet, B. Eon, P. Sangwan, J. Ratcliffe, T.M. Hinton, J. White, B. Özcelik, N.P. Reynolds, B.W. Muir, Non-lamellar lyotropic liquid crystalline nanoparticles enhance the antibacterial effects of rifampicin against *Staphylococcus aureus*, *J. Colloid Interface Sci.* 519 (2018) 107–118, <https://doi.org/10.1016/j.jcis.2018.02.048>.
- [32] Q. Liu, J. Hu, M.R. Whittaker, T.P. Davis, B.J. Boyd, Nitric oxide-sensing actuators for modulating structure in lipid-based liquid crystalline drug delivery systems, *J. Colloid Interface Sci.* 508 (2017) 517–524, <https://doi.org/10.1016/j.jcis.2017.08.079>.
- [33] M. Raudino, G. Selvolini, C. Montis, M. Baglioni, M. Bonini, D. Berti, P. Baglioni, Polymer films removed from solid surfaces by nanostructured fluids: microscopic mechanism and implications for the conservation of cultural heritage, *ACS Appl. Mater. Interfaces* 7 (2015), <https://doi.org/10.1021/acsnano.6b00534>.
- [34] M. Mamusa, L. Sitia, F. Barbero, A. Ruyra, T.D. Calvo, C. Montis, A. Gonzalez-Paredes, G.N. Wheeler, C.J. Morris, M. McArthur, D. Berti, Cationic liposomal vectors incorporating a bolaamphiphile for oligonucleotide antimicrobials, *Biochim. Biophys. Acta – Biomembr.* 1859 (2017), <https://doi.org/10.1016/j.bbmem.2017.06.006>.
- [35] M. Brust, M. Walker, D. Bethell, D.J. Schiffrin, R. Whyman, Synthesis of thiol-derivatised gold nanoparticles in a two-phase liquid-liquid system, *J. Chem. Soc. Chem. Commun.* (1994) 801–802, <https://doi.org/10.1039/C39940000801>.
- [36] M. Kotlarchyk, S.-H. Chen, Analysis of small angle neutron scattering spectra from polydisperse interacting colloids, *J. Chem. Phys.* 79 (1983) 2461, <https://doi.org/10.1063/1.446055>.
- [37] L. Wang, J. Luo, Q. Fan, M. Suzuki, I.S. Suzuki, M.H. Engelhard, Y. Lin, N. Kim, J.Q. Wang, C.J. Zhong, Monodispersed core-shell  $\text{Fe}_3\text{O}_4/\text{Au}$  nanoparticles, *J. Phys. Chem. B* 109 (2005) 21593–21601, <https://doi.org/10.1021/jp0543429>.
- [38] H. Sub Wi, K. Lee, H. Kyu Pak, Interfacial energy consideration in the organization of a quantum dot–lipid mixed system, *J. Phys. Condens. Matter*. 20 (2008) 494211, <https://doi.org/10.1088/0953-8984/20/49/494211>.
- [39] J. Barauskas, T. Landh, Phase behavior of the phytantriol/water system, *Langmuir* 19 (2003) 9562–9565, <https://doi.org/10.1021/la0350812>.
- [40] J. Xie, C. Xu, N. Kohler, Y. Hou, S. Sun, Controlled PEGylation of monodisperse  $\text{Fe}_3\text{O}_4$  nanoparticles for reduced non-specific uptake by macrophage cells, *Adv. Mater.* 19 (2007) 3163–3166, <https://doi.org/10.1002/adma.200701975>.
- [41] J. Chen, M.A. Reed, C.L. Asplund, A.M. Cassell, M.L. Myrick, A.M. Rawlett, J.M. Tour, P.G. Van Patten, Placement of conjugated oligomers in an alkanethiol matrix by scanned probe microscope lithography, *Appl. Phys. Lett.* 75 (1999) 624–626, <https://doi.org/10.1063/1.124461>.
- [42] J.B. Marlow, M.J. Pottage, T.M. McCoy, L. De Campo, A. Sokolova, T.D.M. Bell, R. F. Tabor, Structural and rheological changes of lamellar liquid crystals as a result of compositional changes and added silica nanoparticles, *Phys. Chem. Chem. Phys.* 20 (2018) 16592–16603, <https://doi.org/10.1039/C8CP02101E>.

- [43] J.J. Vallooran, S. Handschin, S. Bolisetty, R. Mezzenga, Twofold light and magnetic responsive behavior in nanoparticle-lyotropic liquid crystal systems, *Langmuir* 28 (2012) 5589–5595, <https://doi.org/10.1021/la300449q>.
- [44] R. Mezzenga, C. Meyer, C. Servais, A.I. Romoscanu, L. Sagalowicz, R.C. Hayward, Shear rheology of lyotropic liquid crystals: a case study, *Langmuir* 21 (2005) 3322–3333, <https://doi.org/10.1021/la046964b>.
- [45] K. Hyun, M. Wilhelm, C.O. Klein, K.S. Cho, J.G. Nam, K.H. Ahn, S.J. Lee, R.H. Ewoldt, G.H. McKinley, A review of nonlinear oscillatory shear tests: analysis and application of large amplitude oscillatory shear (LAOS), *Prog. Polym. Sci.* 36 (2011) 1697–1753, <https://doi.org/10.1016/j.progpolymsci.2011.02.002>.
- [46] K. Hyun, S.H. Kim, K.H. Ahn, S.J. Lee, Large amplitude oscillatory shear as a way to classify the complex fluids, *J. Nonnewton. Fluid Mech.* 107 (2002) 51–65. [https://doi.org/10.1016/S0377-0257\(02\)00141-6](https://doi.org/10.1016/S0377-0257(02)00141-6).
- [47] S. Radiman, C. Toprakcioglu, T. McLeish, Rheological Study of ternary cubic phases, *Langmuir* 10 (1994) 61–67, <https://doi.org/10.1021/la00013a009>.
- [48] J.L. Jones, T.C.B. McLeish, Rheological response of surfactant cubic phases, *Langmuir* 11 (1995) 785–792, <https://doi.org/10.1021/la00003a020>.
- [49] G. Schmidt, P. Lindner, I. Laue-langevin, Small-angle neutron scattering from a hexagonal phase under shear, *Colloid Polym. Sci.* 88 (1996) 85–88, <https://doi.org/10.1007/BF00658914>.
- [50] M. Pouzot, R. Mezzenga, M. Leser, L. Sagalowicz, S. Guillote, O. Glatter, Structural and rheological investigation of Fd3m inverse micellar cubic phases, *Langmuir* 23 (2007) 9618–9628, <https://doi.org/10.1021/la701206a>.
- [51] C. Speziale, R. Ghanbari, Rheology of Ultraswollen Bicontinuous Lipidic Cubic Phases, 2018. <https://doi.org/10.1021/acs.langmuir.8b00737>.
- [52] L. Sagalowicz, R. Mezzenga, M.E. Leser, Investigating Reversed Liquid Crystalline Mesophases, 11 (2006) 224–229. <https://doi.org/10.1016/j.cocis.2006.07.002>.
- [53] C. Montis, A. Zandrini, F. Valle, S. Busatto, L. Paolini, A. Radeghieri, A. Salvatore, D. Berti, P. Bergese, Size distribution of extracellular vesicles by optical correlation techniques, *Colloids Surfaces B Biointerfaces*. 158 (2017), <https://doi.org/10.1016/j.colsurfb.2017.06.047>.
- [54] C. Montis, D. Maiolo, I. Alessandri, P. Bergese, D. Berti, Interaction of nanoparticles with lipid membranes: a multiscale perspective, *Nanoscale* 6 (2014) 6452–6457, <https://doi.org/10.1039/C4NR00838C>.

# Inorganic Nanoparticles Modify the Phase Behavior and Viscoelastic Properties of Non-lamellar Lipid Mesophases

Marco Mendoza, Lucrezia Caselli, Costanza Montis, Stefano Orazzini, Emiliano Carretti, Piero Baglioni, Debora Berti\*

<sup>1</sup>Department of chemistry “Ugo Schiff” and CSGI, University of Florence, Via della Lastruccia 3, 50019-Sesto Fiorentino, Florence, Italy.

<b>Materials and Methods</b>	<b>Page</b>
S.1 <i>Synthesis of SPIONs</i>	S2
S.2 <i>Synthesis of AuNPs</i>	S2
S.3 <i>SAXS data analysis</i>	S3
<b>Supplementary Figures</b>	
S.4 <i>ICP-AES analysis of SPIONs, AuNPs and TEM image analysis</i>	S6
S.5 <i>SAXS of Phytantriol mesophases loaded with Oleic Acid/Oleylamine</i>	S9
S.6 <i>SAXS of Phytantriol mesophases loaded with SPIONs and AuNPs</i>	S12
S.7 <i>SAXS: Thermal reversibility of phytantriol with SPIONs and AuNPs</i>	S18
S.8 <i>Supplementary Amplitude sweep curves</i>	S19
S.9 <i>Supplementary Frequency sweep curves and data analysis</i>	S20
S.10 <i>Continuum time relaxation spectra</i>	S22
S.11 <i>Plot of <math>\tan\delta</math> vs frequency</i>	S27
S.12 <i>Frequency Sweep curves and relaxation spectra of Phytantriol assembled with oleic acid-oleylamine</i>	S26
<b>References</b>	S25



## Materials and Methods

### *S.1- Synthesis of SPIONs*

Iron oxide nanoparticles were synthesized according to the protocol reported by Wang et al.[1]. Briefly, 0.71 g  $\text{Fe}(\text{acac})_3$  (2 mmol) were dissolved in 20 mL of phenyl ether with 2 mL of oleic acid (6 mmol) and 2 mL of oleylamine (4 mmol) under nitrogen atmosphere and vigorous stirring. 1,2-hexadecanediol (2.58g, 10 mmol) was added into the solution. The solution was heated to 210 °C, refluxed for 2 h and then cooled to RT. Ethanol was added to the solution and the precipitate collected, washed with ethanol and redispersed in 20 mL of hexane in the presence of 75 mM each of oleic acid and oleylamine. A stable dispersion of the magnetic SPIONs with a hydrophobic coating of oleic acid and oleylamine in hexane was obtained.

### *S.2- Synthesis of AuNPs*

Hydrophobic gold nanoparticles are synthesized according to the protocol reported by Brust et al.[2] Briefly, an aqueous solution of  $\text{HAuCl}_4$  (30 ml, 30 mM) was mixed with a solution of tetraoctylammonium bromide (TOAB) in toluene (80 ml, 50 mM). The two-phase mixture was vigorously stirred until all the Gold-(III) compound was transferred into the organic layer. Then, dodecanethiol (170 mg) was added to the organic phase. A freshly prepared aqueous solution of sodium borohydride (25 ml, 0.4 M) was slowly added with vigorous stirring. After 3 h stirring the organic phase was separated, evaporated to 10 ml in a rotavapor and mixed with 400 ml ethanol to remove excess thiol. The mixture was kept for 24 h at  $-18^\circ\text{C}$  and the dark brown precipitate was filtered off and washed with ethanol. The crude product was dissolved in 10 ml toluene and again precipitated with 400 ml ethanol. Then, the twice washed precipitated was dispersed in 20 mL hexane.

### S.3- SAXS data analysis

Equation (1) was used to calculate lattice parameter (d) of cubic and hexagonal phase:

$$q = \left(\frac{2\pi}{d}\right) \sqrt{h^2 + k^2 + l^2} \quad (1)$$

where (hkl) are Miller index related to the considered structures. In a Pn3m structure are (110), (111), (200), (211), (220)... while in H<sub>II</sub> mesophases are (100), (111), (200)... Eq. (2)[3] was used to calculate water channel radii  $r_w$  in Pn3m cubic phase while Eq. (3)[3] was used to calculate volume water fraction  $\varphi_w$ :

$$r_w = \sqrt{(-A_0/2\pi\chi)d} - l_c \quad (2)$$

$$\varphi_w = 1 - 2A_0 \left(\frac{l_c}{d}\right) - \frac{4}{3}\pi\chi \left(\frac{l_c}{d}\right)^3 \quad (3)$$

where  $A_0$  and  $\chi$  are topological parameters respectively the ratio of the area of the minimal surface in a unit cell to (unit cell volume)<sup>2/3</sup> and the Euler–Poincaré characteristic, that for the diamond cubic mesophase (Pn3m), are  $A_0=1.919$  and  $\chi=-2$ . Equation (4)[4] and (5)[5] describe water channel radii ( $r_w$ ) of hexagonal phase H<sub>II</sub> and water volume fraction ( $\varphi_w$ ) respectively:

$$r_w = \frac{0.5256d - l_c}{0.994} \quad (4)$$

$$\varphi_w = \frac{2\pi r_w^2}{\sqrt{3}d^2} \quad (5)$$

We assumed that chain length  $l_c$  into the range of 25-50 °C, is constant and assume value of about 9 Å calculated by the data reported in literature through Eq.(2-3) [6]. Moreover, we assumed that %w/w of Fe<sub>3</sub>O<sub>4</sub> and Au was negligible to evaluate water fraction both for cubic and hexagonal phase.

To Fit SAXS curves of both dispersed gold and iron oxide nanoparticles, we used Sphere-Schulz Model by NIST[7,8]. This model calculates the scattering for a polydisperse population of sphere

with uniform Scattering Length Density (SLD). The distribution of radii is a Schulz distribution as in Eq. (6):

$$f(R) = (z + 1)^{z+1} x^z \frac{\exp [-(z + 1)x]}{R_{avg} \Gamma(z + 1)} \quad (6)$$

Where  $R_{avg}$  is the mean radius,  $x=R/R_{avg}$ ,  $z$  is related to the polydispersity,  $p=\sigma/R_{avg}$ , by  $z=1/p^2-1$ .  $\sigma^2$  is the variance of distribution. The scattering intensity is modeled as reported in Eq. (7):

$$I(q) = \left(\frac{4\pi}{3}\right)^2 N_0 \Delta\rho^2 \int_0^\infty f(R) R^6 F^2(qR) dR \quad (7)$$

where  $N_0$  is the total number of particles per unit volume, and  $\Delta\rho$  is the difference in scattering length density,  $F(qR)$  the scattering amplitude for a sphere reported in Eq. (8):

$$F(x) = \frac{3[\sin(x) - x\cos(x)]}{x^3} \quad (8)$$

No interparticle interference effects are included in this calculation.

## Supplementary Figures

### *S.4- ICP-AES analysis of SPIONs, AuNPs and TEM image analysis*

The ICP-AES analyses were performed to determine the weight concentration of both types of NPs and the results are 2.19 mg/mL and 3.78 mg/mL for SPIONs and AuNPs respectively. Thus, considering the density of Fe<sub>3</sub>O<sub>4</sub> and Au, which are 5.17 g/cm<sup>3</sup> and 19.31 g/cm<sup>3</sup> respectively, the amounts of NPs added in the Phyt mesophase in order to have the same number of AuNPs or SPIONs in each samples are reported in table S1:

<b>Table S1: Percentage in weight of nanoparticles with respect to lipid, mg of oleic acid and oleylamine, number of nanoparticles and volume fraction of SPIONs and AuNPs</b>				
<b>N° nanoparticles</b>	<b>N° nanoparticles/lipid molecule</b>	<b>mg of oleic acid and oleylamine</b>	<b>SPIONs Volume fraction #</b>	<b>AuNPs Volume fraction #</b>
<b>5.57x10<sup>14</sup></b>	<b>1x10<sup>-5</sup></b>	1*	4.2x10 <sup>-4</sup>	1.9x10 <sup>-4</sup>
<b>1.13x10<sup>15</sup></b>	<b>2x10<sup>-5</sup></b>	3*	8.5x10 <sup>-4</sup>	3.9x10 <sup>-4</sup>
<b>2.26x10<sup>15</sup></b>	<b>4x10<sup>-5</sup></b>	6*	1.7x10 <sup>-3</sup>	7.9x10 <sup>-4</sup>

\* dispersed as stabilizer agent in SPIONs or added to lipids with the appropriate amount of AuNPs dispersion

# calculated as ratio of the NPs and phytantriol volumes, taking into account that 30 mg of phytantriol (density 0.935 g/cm<sup>3</sup>) were used to prepare each sample

In order to proof that nanoparticles are embedded in the hydrophobic regions, we performed an experiment's control: we prepared a Phyt/SPIONs sample with the lower concentration of nanoparticles (See Table S1). Briefly, 100 mg of Phyt was dissolved with a volume of SPIONs dispersion to obtain 0.234 mg of magnetite into the mesophase. We added 0.15 mL of MilliQ water and we placed the sample at 50 °C for 1 h. Thus, we analyzed water solution with ICP-AES to determine the iron concentration (SPIONs released from the mesophase) after phase

transition. The magnetite concentration is  $1.29 \times 10^{-4}$  mg/mL in 0.15 mL of analyzed water solution thus, the ratio of released amount of SPIONs and 0.234 mg at the beginning correspond to  $8.35 \times 10^{-3}\%$ , a value negligible, allowing us to be sure that nanoparticles are into the lipid matrix.

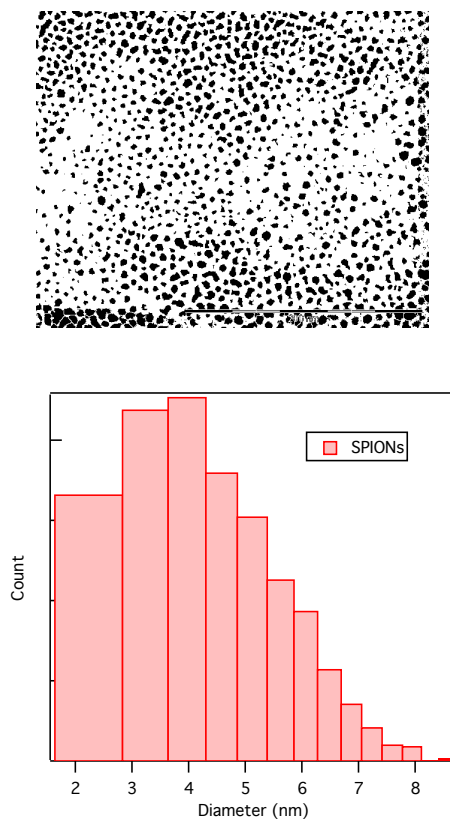


**Figure S1:** Size distribution of SPIONs estimated from three different TEM images through Image J.

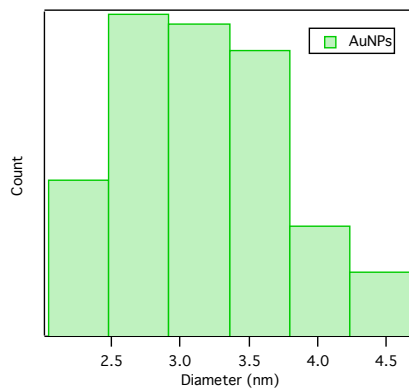
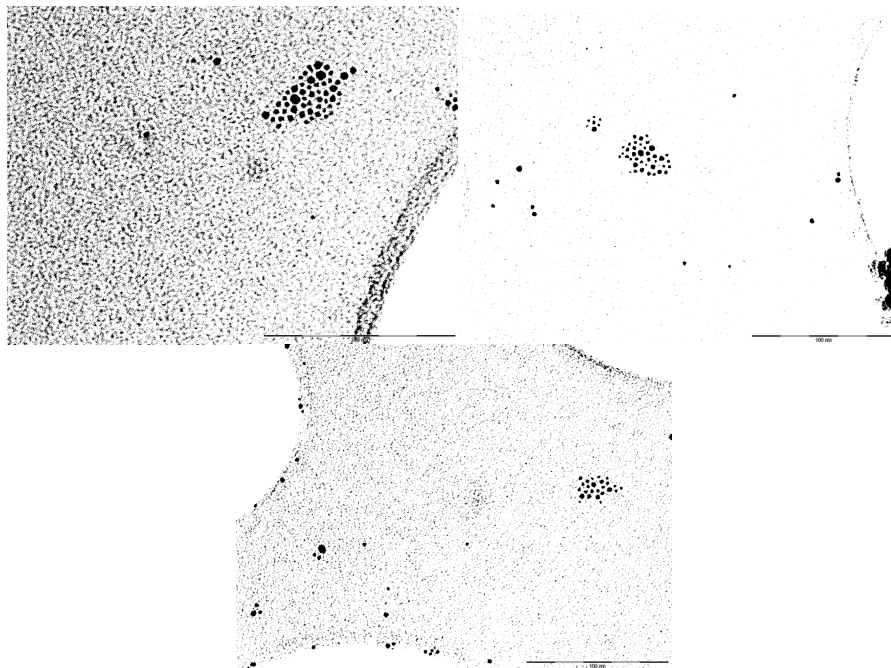


**Figure S2:** Size distribution of AuNPs estimated from three different TEM images through Image J.

S.5- SAXS of Phytantriol mesophases loaded with Oleic Acid/Oleylamine

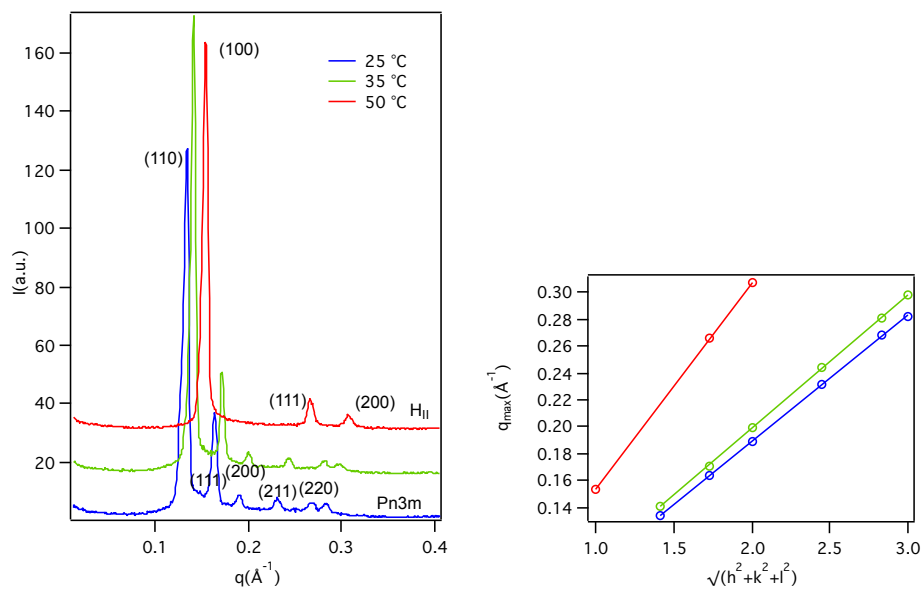


**Figure S3:** SAXS curves of phytantriol assembled with 1 mg of a mixture Oleic Acid/Oleylamine at 25-35-50 °C (respectively blue, cyan, green, and red) and Miller index on  $q_{\max}$  to determine variation of lattice parameter with temperature.

**Table S2.** Lattice parameters, water channel radii and water volume fraction of phytantriol assembled with 1 mg of a mixture 50:50 of oleic acid and oleylamine

T (°C)	Lattice parameter (Å)	Water channel radii (Å)	Water volume fraction
25	67	17	0.505
35	63	16	0.476
50	41	13	0.347

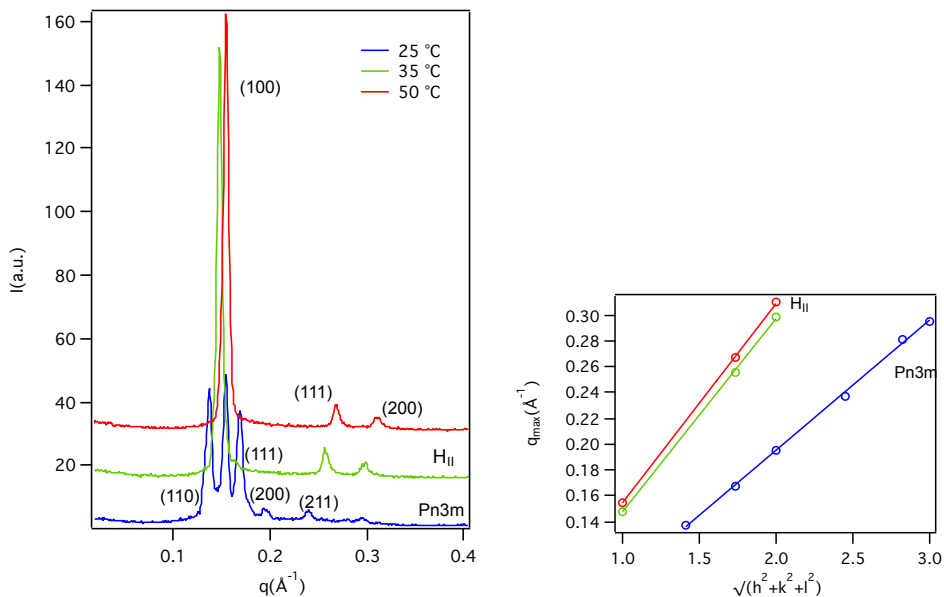


**Figure S4:** SAXS curves of phytantriol assembled with 3 mg of a mixture Oleic Acid/Oleylamine and Miller index on  $q_{\max}$  to determine variation of lattice parameter both for cubic (blue) and hexagonal phase (cyan, green, red) with temperature into the range from 25-50 °C.

**Table S3.** Lattice parameters, water channel radii and waer volume fraction of phytantriol assembled with 3 mg of a mixture 50:50 of Oleic acid and oleylamine.

T (°C)	Lattice parameter (Å)	Water channel radii (Å)	Water volume fraction
25	62	15	0.468
35	42	13	0.347
50	40	12	0.326

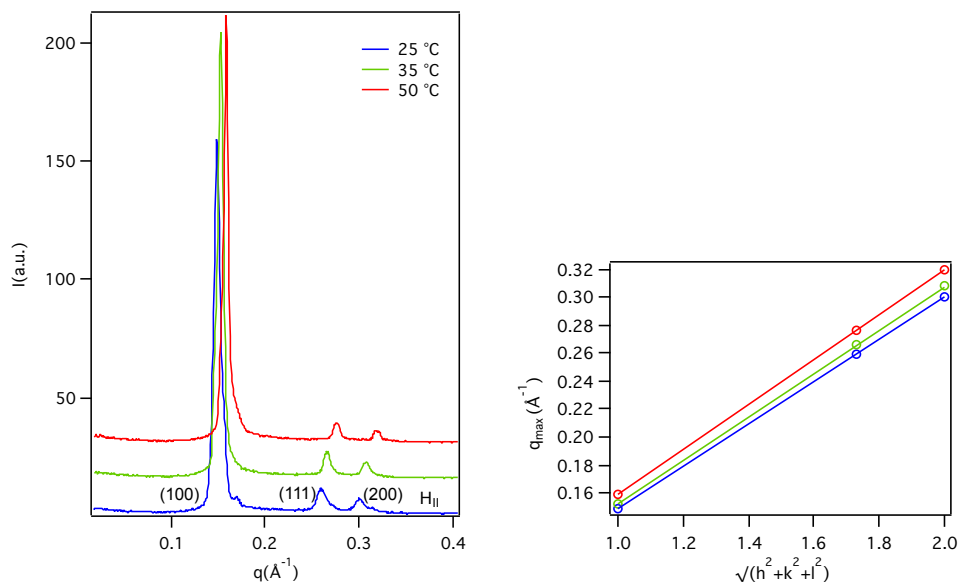


**Figure S5:** SAXS curves of phytantriol assembled with 6 mg of a mixture Oleic Acid/Oleyleamine and Miller index on  $q_{\max}$  to determine variation of lattice parameter of hexagonal phase with temperature into the range from 25-50 °C.

**Table S4.** Lattice parameters, water channel radii and water volume fraction of phytantriol assembled with 6 mg of a mixture 50:50 of oleic acid and oleylamine.

T (°C)	Lattice parameter (Å)	Water channel radii (Å)	Water volume fraction
25	42	13	0.347
35	40	12	0.326
50	39	12	0.326

S.6- SAXS: Thermal reversibility of phytantriol with SPIONs and AuNPs

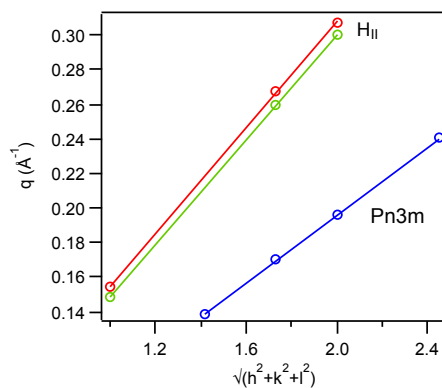


**Figure S6.** Lattice parameter of phytantriol assembled with  $1 \times 10^{-5}$  SPIONs/Phyt of Pn3m mesophase at 25 °C (blue curve) and hexagonal phase at 35-50 °C. SAXS profiles are showed in main text.

**Table S5.** Lattice parameters, water channel radii and water volume fraction of phytantriol assembled with  $1 \times 10^{-5}$  SPIONs/Phyt (data showed in main text)

T (°C)	Lattice parameter (Å)	Water channel radii (Å)	Water volume fraction
25	64	16	0.484
35	42	13	0.347
50	41	12	0.326

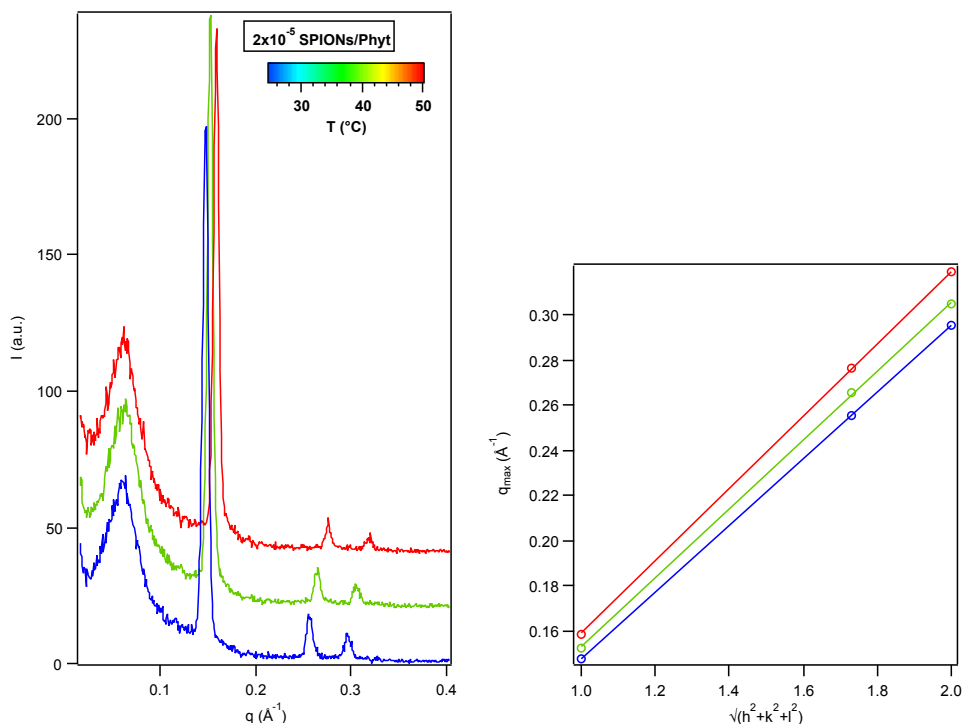


**Figure S7.** SAXS curves of phytantriol assembled with  $2 \times 10^{-5}$  SPIONs/Phyt and Miller index on  $q_{\text{max}}$  to determine variation of lattice parameter of hexagonal phase with temperature into the range from 25-50 °C.

**Table S6.** Lattice parameters, water channel radii and water volume fraction of phytantriol assembled with  $2 \times 10^{-5}$  SPIONs/Phyt

T (°C)	Lattice parameter (Å)	Water channel radii (Å)	Water volume fraction
25	43 ( $H_{II}$ )	14	0.384
35	41 ( $H_{II}$ )	13	0.347
50	39 ( $H_{II}$ )	12	0.326

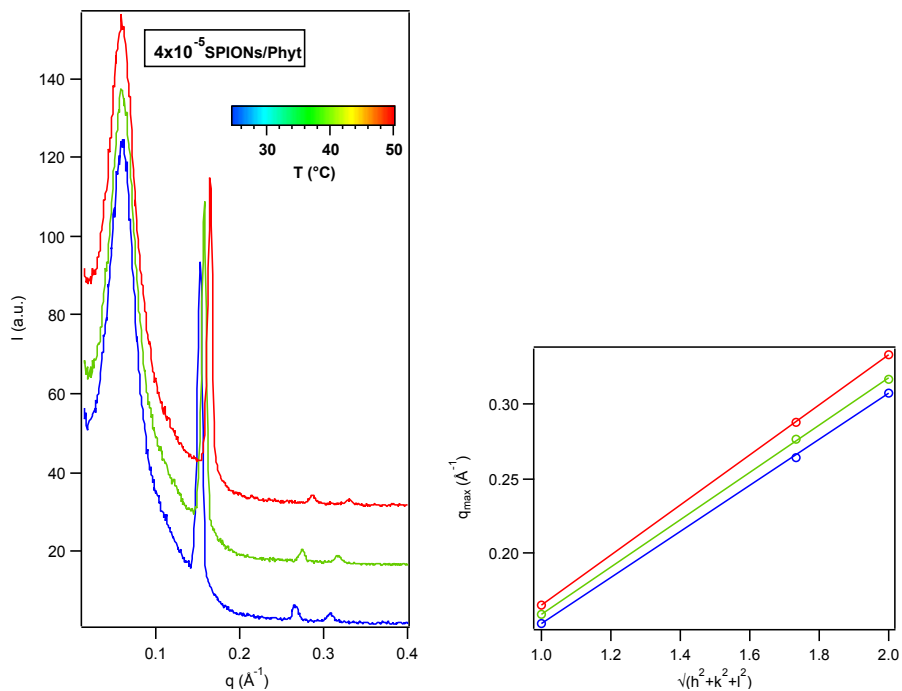


**Figure S8.** SAXS curves of phytantriol assembled with  $4 \times 10^{-5}$  SPIONs/Phyt and Miller index on  $q_{\text{max}}$  to determine variation of lattice parameter of hexagonal phase with temperature into the range from 25-50 °C.

**Table S7.** Lattice parameters, water channel radii and water volume fraction of phytantriol assembled with  $4 \times 10^{-5}$  SPIONs/Phyt

T (°C)	Lattice parameter (Å)	Water channel radii (Å)	Water volume fraction
25	41 ( $H_{II}$ )	13	0.347
35	39 ( $H_{II}$ )	12	0.326
50	38 ( $H_{II}$ )	11	0.324

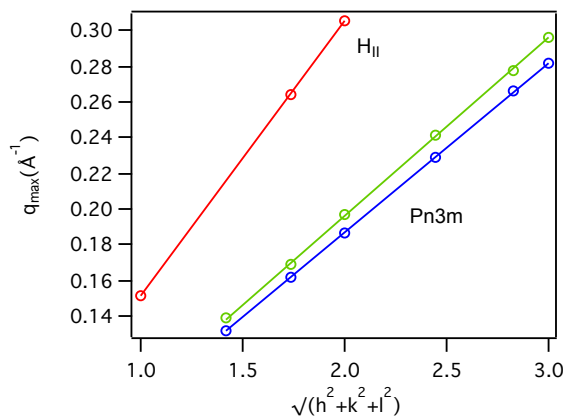


**Figure S9.**  $Q_{\max}$  as function of Miller Index to calculate lattice parameter of phytantriol mesophases assembled with  $1 \times 10^{-5}$  AuNPs/Phyt

**Table S8.** Lattice parameters, water channel radii and water volume fraction of phytantriol assembled with  $1 \times 10^{-5}$  AuNPs/Phyt (data showed in main text)

T (°C)	Lattice parameter (Å)	Water channel radii (Å)	Water volume fraction
25	66	17	0.505
35	63	16	0.476
50	41	13	0.347

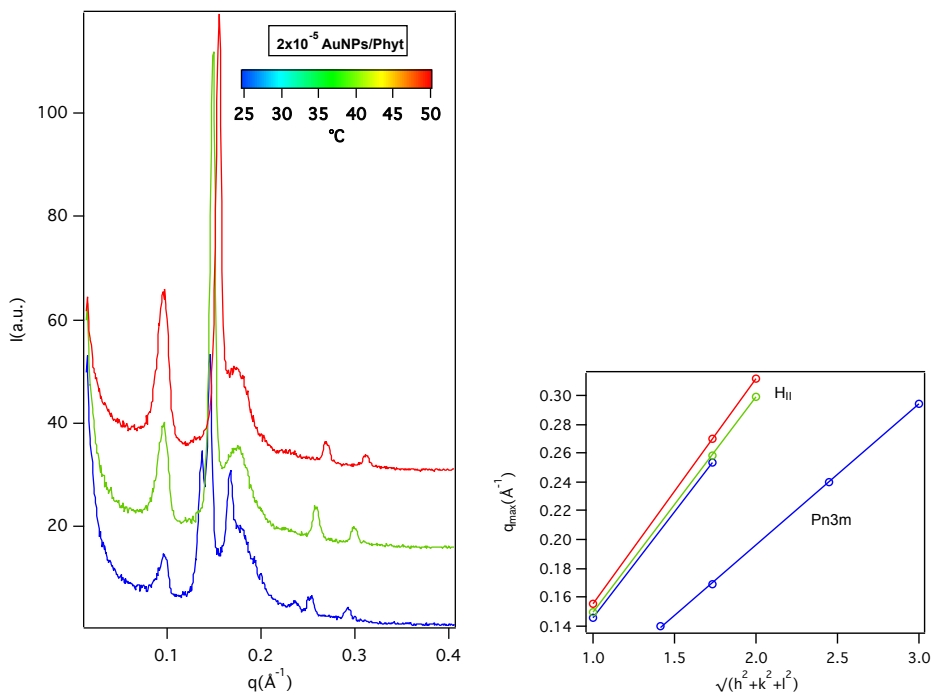


**Figure S10:** Lattice parameter of phytantriol mesophases assembled with  $2 \times 10^{-5}$  AuNPs/Phyt and lattice parameter into the range 25-50 °C.

**Table S9.** Lattice parameters, water channel radii and water volume fraction of phytantriol assembled with  $2 \times 10^{-5}$  AuNPs/Phyt varying the temperature.

T (°C)	Lattice parameter (Å)	Water channel radii (Å)	Water volume fraction
25	64 (Pn3m)	16	0.484
	43 (H <sub>II</sub> )	14	0.384
35	42	13	0.347
50	40	12	0.326

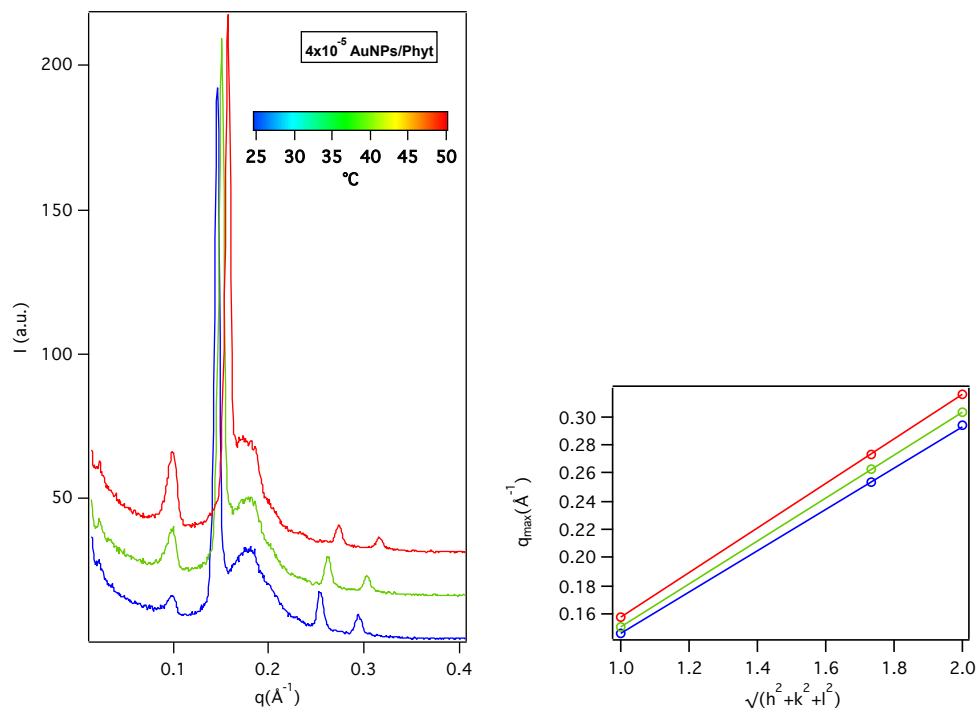


**Figure S11:** Lattice parameter of phytantriol mesophases assembled with  $4 \times 10^{-5}$  AuNPs/Phyt and lattice parameter into the range 25-50 °C.

**Table S10.** Lattice parameters, water channel radii and waer volume fraction of phytantriol assembled with  $4 \times 10^{-5}$  AuNPs/Phyt varying the temperature.

T (°C)	Lattice parameter ( $\text{\AA}$ )	Water channel radii ( $\text{\AA}$ )	Water volume fraction
25	43	14	0.384
35	41	13	0.347
50	40	12	0.326

S.7 SAXS: Thermal reversibility of phytantriol with SPIONs and AuNPs

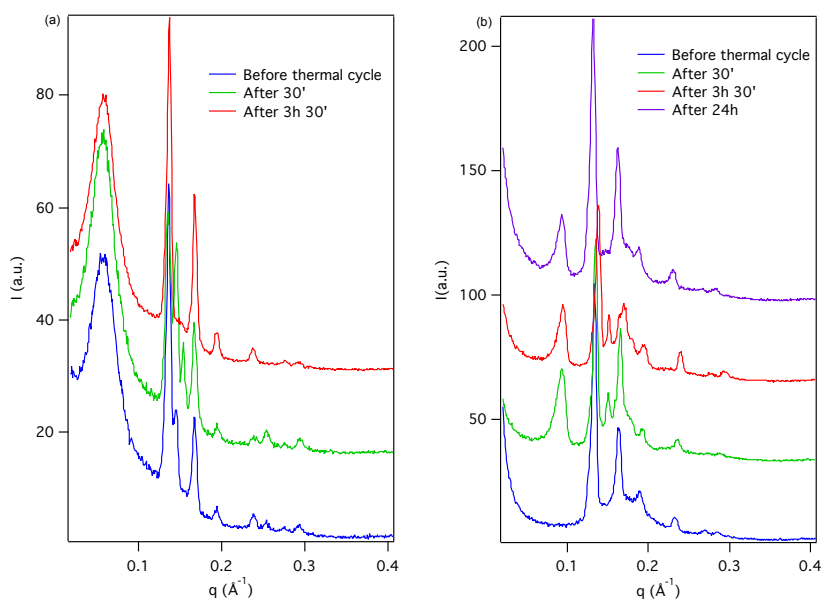


**Figure S12.** SAXS profiles of Phytantriol assembled with  $1 \times 10^{-5}$  (a) SPIONs/Phyt and (b) AuNPs/Phyt before and after the thermal cycle of 50 °C to detect the recovery of the lipid structures. Phyt/SPIONs assemblies shows a recovery of Bragg reflex after 3h and 30 minutes, while Phyt/AuNPs shows the recovery only after 24 h.

### S.8-Supplementary Amplitude Sweep curves

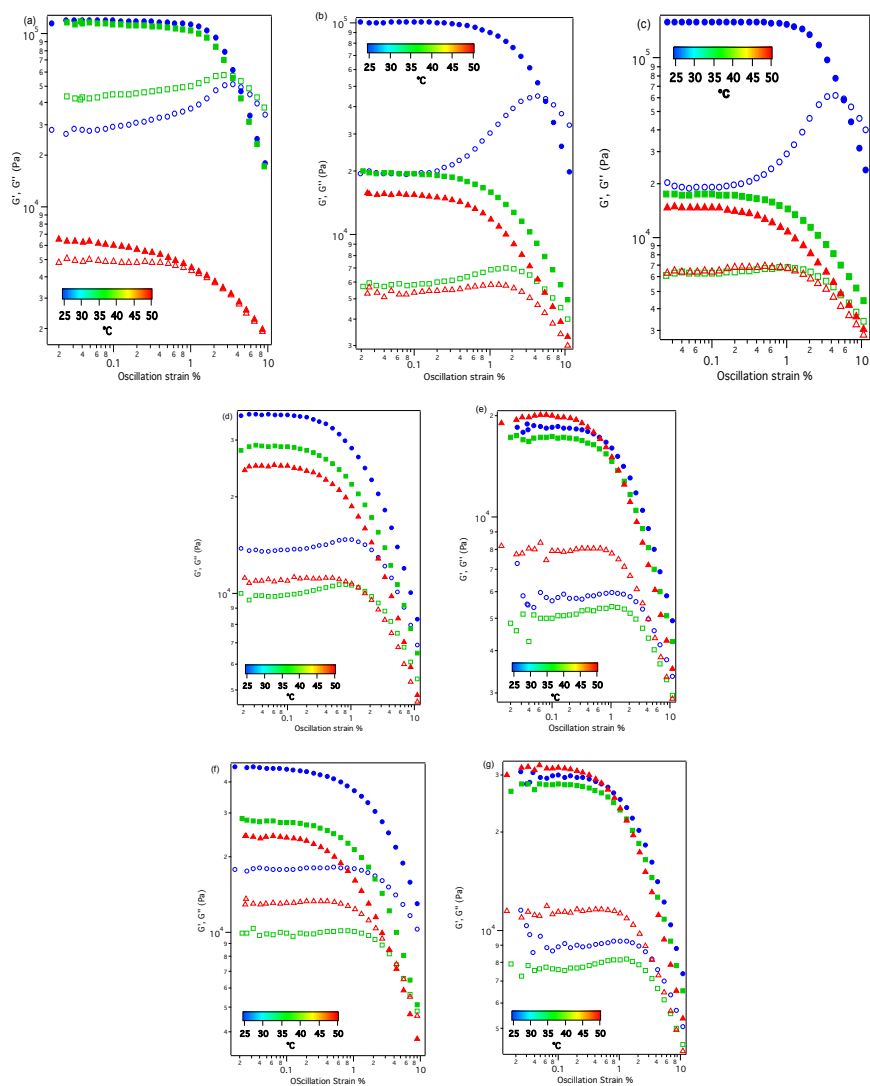


**Figure S13.** Amplitude sweep curves at 25 °C (blue), 35 °C (green) and 50 °C (red) for (a) phytantriol binary matrix, (b)  $1 \times 10^{-5}$  SPIONs/Phyt, (c)  $1 \times 10^{-5}$  AuNPs/Phyt, (d)  $2 \times 10^{-5}$  SPIONs/Phyt, (e)  $2 \times 10^{-5}$  AuNPs/Phyt, (f)  $4 \times 10^{-5}$  SPIONs/Phyt and (g)  $4 \times 10^{-5}$  AuNPs/Phyt.

S.9- Supplementary Frequency Sweep curves and data analysis

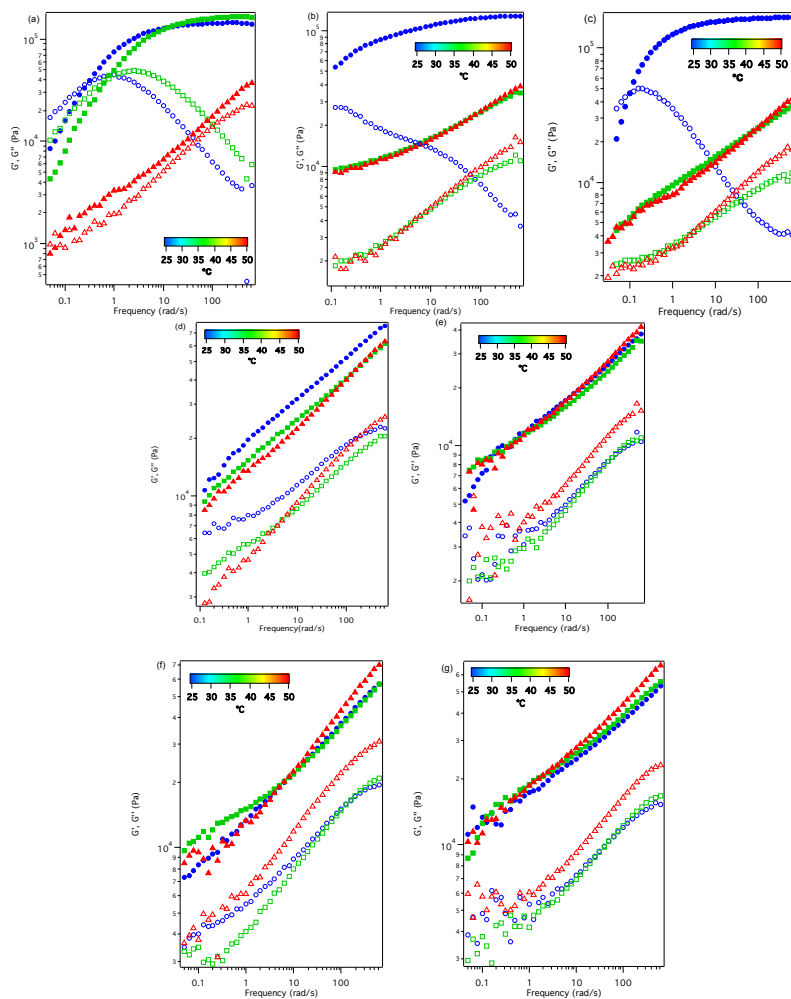


**Figure S14.** Frequency sweep curves at 25 °C (blue), 35 °C (green) and 50 °C (red) for (a) phytantriol binary matrix, (b)  $1 \times 10^{-5}$  SPIONs/Phyt, (c)  $1 \times 10^{-5}$  AuNPs/Phyt, (d)  $2 \times 10^{-5}$  SPIONs/Phyt, (e)  $2 \times 10^{-5}$  AuNPs/Phyt, (f)  $4 \times 10^{-5}$  SPIONs/Phyt and (g)  $4 \times 10^{-5}$  AuNPs/Phyt.

Frequency Sweep curves were fitted with three terms Maxwell Model, which are describe by Eq. (9-10):

$$G'(\omega) = \sum_{i=1}^3 \frac{\omega^2 \tau_i^2}{1 + \omega^2 \tau_i^2} G_i^0 \quad (9)$$

$$G''(\omega) = \sum_{i=1}^3 \frac{\omega^2 \tau_i}{1 + \omega^2 \tau_i^2} G_i^0 \quad (10)$$

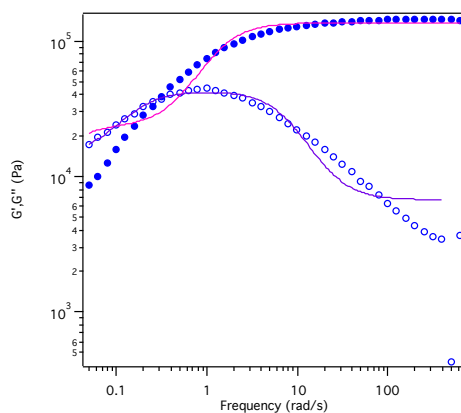


**Figure S15.** Three terms Maxwell model fitting of storage and loss modulus of Phyt/H<sub>2</sub>O at 25°C.

The curve fitting of Phyt/H<sub>2</sub>O rheological profiles with this model are displayed in Figure S13. Clearly, the adopted model does not fully describe the system, that is likely to be characterized by a high polydispersity. A suitable approach to describe polydisperse systems the continuum spectrum  $H(t)$  of relaxation times, which depends from  $G'$  and  $G''$  through the following equations (11-12):

$$G'(\omega) = G_0 + \int_0^{\infty} H(\tau) \frac{(\omega\tau)^2}{1 + (\omega\tau)^2} \frac{d\tau}{\tau} \quad (11)$$

$$G''(\omega) = G_0 + \int_0^{\infty} H(\tau) \frac{\omega\tau}{1 + (\omega\tau)^2} \frac{d\tau}{\tau} \quad (12)$$

H(t) can be extracted according to different algorithms for the inversion of the equation (11-12) [9]. In the following section the continuum relaxation spectra of the experimental frequency sweep curves are displayed.

*S.10-Continuum time relaxation spectra:*

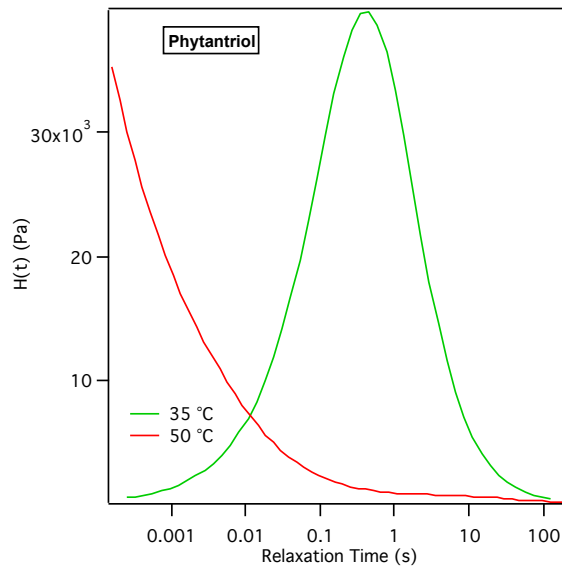


**Figure S16:** Continuum time relaxation spectra of Phyt/H<sub>2</sub>O assemblies without nanoparticles at 35 °C (green curve) and 50 °C (red curve)

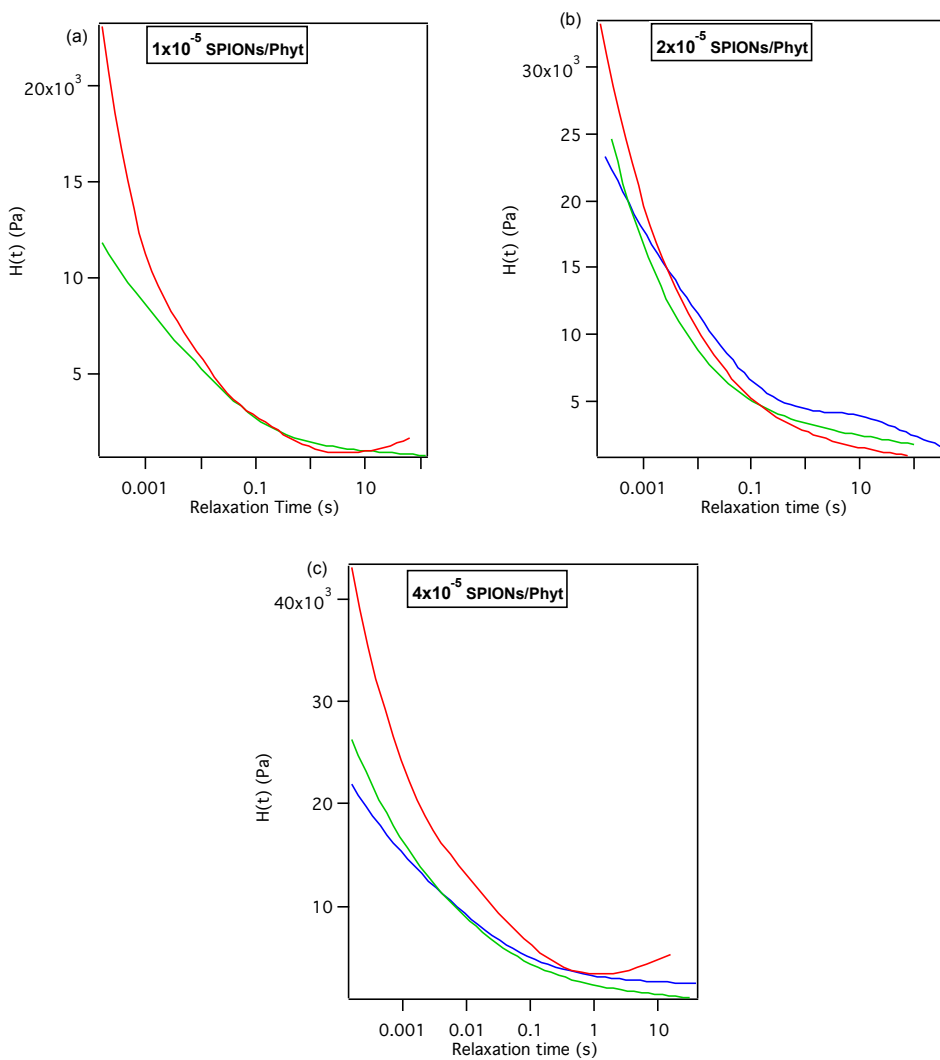


**Figure S17.** Continuum time relaxation spectra of phytantriol mesophases assembled with  $1 \times 10^{-5}$  SPIONs/Phyt (a),  $2 \times 10^{-5}$  SPIONs/Phyt (b) and  $4 \times 10^{-5}$  SPIONs/Phyt (c) at 25 (blue curves), 35 (green curves) and 50 °C (red curves). The curve of cubic mesophase at 25 °C doped with  $1 \times 10^{-5}$  SPIONs/Phyt is shown in main text.

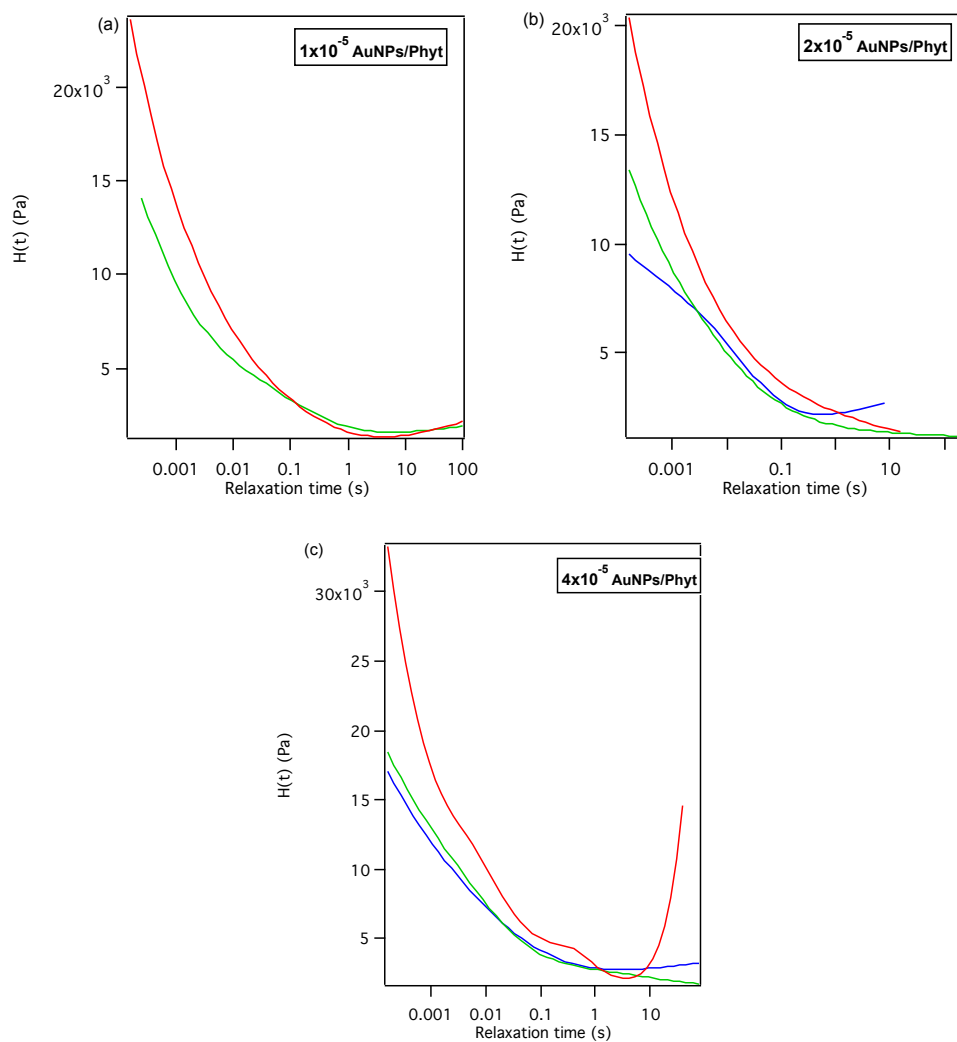


**Figure S18.** Continuum time relaxation spectra of phytantriol mesophases assembled with  $1 \times 10^{-5}$  AuNPs/Phyt (a),  $2 \times 10^{-5}$  AuNPs/Phyt (b) and  $4 \times 10^{-5}$  AuNPs/Phyt (c) at 25 (blue curves), 35 (green curves) and 50 °C (red curves). The curve of cubic mesophase at 25 °C doped with  $1 \times 10^{-5}$  AuNPs/Phyt is shown in main text.

S11- Plot of  $\tan\delta$  vs frequency

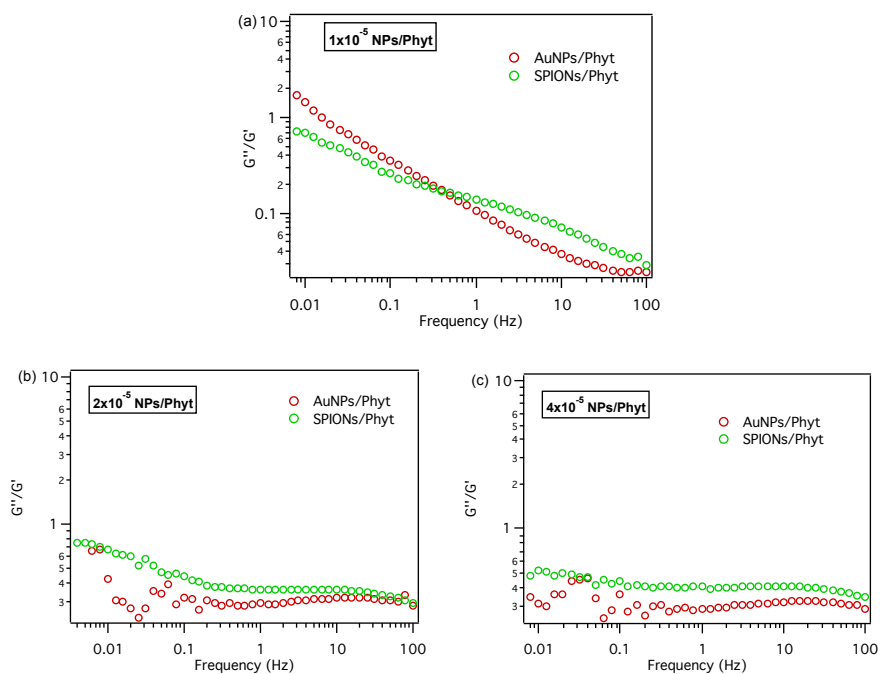


**Figure S19:** Loss and storage modulus ratio as function of frequency at 25 °C relative to mesophases doped with different amount of both nanoparticles; (a) shows  $\tan\delta$  curves of Phyt/NPs cubic mesophases to the lower amount of nanoparticles  $1 \times 10^{-5}$  NPs/Phyt, (b) shows  $\tan\delta$  curves of Phyt assembled with  $2 \times 10^{-5}$  NPs/Phyt and (c) Phyt hexagonal mesophases with  $4 \times 10^{-5}$  NPs/Phyt.

S.12 Frequency Sweep curves and relaxation spectra of Phytantriol assembled with oleic acid-oleylamine

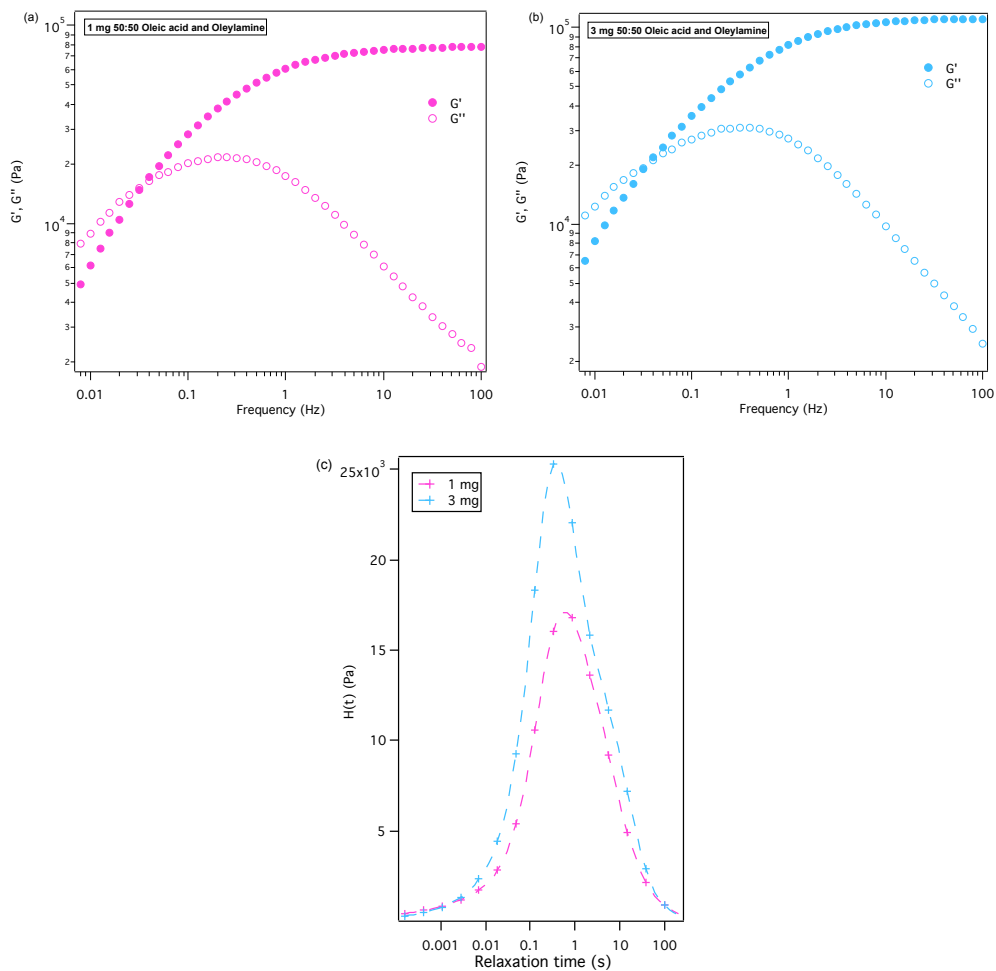


**Figure S20:** Storage ( $G'$ ) and Loss ( $G''$ ) moduli of phytantriol assembled with different amount of stabilizer agents (oleic acid and oleylamine 50:50 ratio). (a)  $G'$  (purple full markers) and  $G''$  (purple empty markers) of Phyt/1 mg of the mixture; (b)  $G'$  (cyan full markers) and  $G''$  (cyan empty markers) of Phyt/3 mg of the mixture; (c) both relaxation spectra extracted by frequency sweep curves of (a) Phyt/1 mg and (b) Phyt/3 mg.

## REFERENCES

- [1] S.H. Sun, H. Zeng, Size-controlled synthesis of magnetite nanoparticles, *J. Am. Chem. Soc.* 124 (2002) 8204–8205. doi:10.1021/ja026501x.
- [2] M. Brust, M. Walker, D. Bethell, D.J. Schiffrin, R. Whyman, Synthesis of thiol-derivatised gold nanoparticles in a two-phase liquid-liquid system, *J. Chem. Soc. Chem. Commun.* (1994) 801–802. doi:10.1039/C39940000801.
- [3] R. Negrini, R. Mezzenga, Diffusion, molecular separation, and drug delivery from lipid mesophases with tunable water channels, *Langmuir*. 28 (2012) 16455–16462. doi:10.1021/la303833s.
- [4] C.W. Reese, Z.I. Strango, Z.R. Dell, S. Tristram-Nagle, P.E. Harper, Structural insights into the cubic-hexagonal phase transition kinetics of monoolein modulated by sucrose solutions., *Phys. Chem. Chem. Phys.* 17 (2015) 9194–204. doi:10.1039/c5cp00175g.
- [5] D. Marsh, *Handbook of lipid bilayers*, 2013. doi:10.1201/b11712.
- [6] Y. Da Dong, I. Larson, T. Hanley, B.J. Boyd, Bulk and dispersed aqueous phase behavior of phytantriol: Effect of vitamin E acetate and F127 polymer on liquid crystal nanostructure, *Langmuir*. 22 (2006) 9512–9518. doi:10.1021/la061706v.
- [7] M. Kotlarchyk, S. Chen, Analysis of small angle neutron scattering spectra from polydisperse interacting colloids, *J. Chem. Phys.* 79 (1983) 2461. doi:10.1063/1.446055.
- [8] D. Begriff, A. Hand, D. Zerlegung, D. Fraktionierung, A. Grund, D. Fraktionierbarkeit, S. Kurven, S.- Dinger, I. Authenticated, D. Date, Die Verteilungsfunktionen polymolekularer Stoffe und ihre Ermittlung durch Zerlegung in Fraktionen ., 70 (1940) 155–193.
- [9] J. Honerkamp, J. Weese, A nonlinear regularization method for the calculation of relaxation spectra, *Rheol. Acta.* 32 (1993) 65–73. doi:10.1007/BF00396678.

# Paper III





Cite this: *Soft Matter*, 2019, 15, 8951

Received 8th August 2019,  
Accepted 25th October 2019

DOI: 10.1039/c9sm01601e

rsc.li/soft-matter-journal

## Nanoparticles and organized lipid assemblies: from interaction to design of hybrid soft devices

Marco Mendoza,  Lucrezia Caselli,  Annalisa Salvatore,  Costanza Montis \* and Debora Berti \*

This contribution reviews the state of art on hybrid soft matter assemblies composed of inorganic nanoparticles (NP) and lamellar or non-lamellar lipid bilayers. After a short outline of the relevant energetic contributions, we address the interaction of NPs with synthetic lamellar bilayers, meant as cell membrane mimics. We then review the design of hybrid nanostructured materials composed of lipid bilayers and some classes of inorganic NPs, with particular emphasis on the effects on the amphiphilic phase diagram and on the additional properties contributed by the NPs. Then, we present the latest developments on the use of lipid bilayers as coating agents for inorganic NPs. Finally, we remark on the main achievements of the last years and our vision for the development of the field.

### 1. Introduction

Lipid bilayers are ubiquitous structural motifs in natural and synthetic soft matter assemblies. Their interaction with nanostructured matter, and in particular with nanoparticles (NPs), is therefore of interest both for natural and engineered systems. In addition, the shared length and energy scales, combined with the peculiar properties of inorganic matter at the nano-scale, can be harnessed to use NPs to probe selected physical

properties of membranes or to modify the amphiphilic phase diagram under external stimuli.

In this contribution we will review the state of the art concerning research on hybrid soft matter assemblies composed of inorganic NPs and synthetic lipid bilayers, either in lamellar or non-lamellar arrangement.

This topic is currently a very active area of research, with implications ranging from the design of smart nanostructured hybrid devices, where nanoparticles are included or functionalized with lipid bilayers, to the quest for mechanistic understanding of events taking place at the nano-bio-interface, relevant for nanomedicine and toxicity of nanomaterials.

*Department of Chemistry "Ugo Schiff", University of Florence, and CSGI (Italian Center for Colloid and Surface Science, Via della Lastruccia 3, Sesto Fiorentino, 50019 Firenze, Italy. E-mail: montis@csgi.unifi.it, debora.beriti@unifi.it*



**Marco Mendoza**

*Marco Mendoza received his MSc in Chemical Sciences-Physical Chemistry from University of Florence in 2016. Currently he is pursuing his PhD in Physical Chemistry under the supervision of Prof. Debora Berti at the University of Florence. His research focuses on the investigation of the phase behavior and viscoelastic properties of non-lamellar lipid membranes assembled with hydrophobic inorganic stimuli responsive nanoparticles (iron oxide and*

*gold nanoparticles) in order to design new functional materials, with envisaged applications the biomedical field.*



**Lucrezia Caselli**

*Lucrezia Caselli obtained her MSc degree in Chemical Sciences from the University of Florence in Italy in 2017. She is now a PhD student in Chemical Sciences at the University of Florence. Her main research interest concerns Physical Chemistry of Soft Matter, with particular focus on self-assemblies with biological relevance. Her research topics include the interaction of inorganic nanomaterials with synthetic model cellular membranes, engineering of*

*hybrid nanoparticle/lipid assemblies for responsive drug delivery, microfluidic design and application of innovative model systems for the study of the nano-bio interfaces.*

This review will focus on some selected classes of inorganic nanomaterials, namely metals (Au and Ag), metal oxides (like iron and zinc oxide) and silica NPs. The interaction of several other kinds of nanomaterials with lipid bilayers has been described in the literature and we refer the readers to some excellent recent reports on these topics.<sup>1–8</sup>

In this contribution, particular attention will be devoted to non-covalent interactions that take place when NPs and lipid bilayers are put into contact. Understanding the nature and the key determinants of these interactions is instrumental both for fundamental and applied soft matter research.

This review is organized as follows: a short theoretical section will introduce the main energetic contributions at stake when NPs interact with lipid bilayers (Section 2). Then, we will provide an overview of the most relevant studies which have recently addressed the interaction of NPs with synthetic phospholipid bilayers, meant as simplified and highly controllable

mimics of cell membranes (Section 3). In this section, we will emphasize some examples where the investigation on model systems contributed disclosing non-covalent interactions at play in living systems. Then, we will review (Section 4) the design of hybrid nanostructured materials composed of lipid bilayers and inorganic nanoparticles, with particular emphasis on the effects on the amphiphilic phase diagram and on the additional properties contributed by the NPs. Then, we will present the latest developments on the use of lipid bilayers as coating agents for inorganic NPs (Section 5), whose aim is the improvement of dispersibility, biocompatibility and pharmacokinetic properties. Finally, a conclusive Section will remark the main achievements of the last years and our vision for the development of the field.

## 2. Interaction of nanoparticles with lipid membranes: the role of non-covalent forces

In this section we will consider the events following the exposure of a free-standing synthetic lipid bilayer to NPs, by outlining the different contributions to the total interaction energy.

### 2.1 Theoretical description of NPs–lipid membrane interaction

The interaction between a NP and a lipid bilayer might lead to NP's adhesion on the bilayer, which can be followed by partial or total engulfment by the membrane. In a well-defined medium and at a given temperature, the NP docking to lipid membranes is thermodynamically favoured if the adhesion energy  $E_{\text{adh}} < 0$ , *i.e.*, if the attractive terms overcome the repulsive ones. Considering a prototypical model of a bioinorganic interface, with a spherical NP of radius  $R_1$  interacting with a liposomal membrane with curvature  $1/R_2$ , the energetic balance between repulsive and attractive forces can be approximately described



**Annalisa Salvatore**

*Annalisa Salvatore obtained her MSc degree in Chemical Sciences-Physical Chemistry at University of Florence in 2013 and started her PhD research under the supervision of Prof. Debora Berti, in the same year. Her doctoral research focused on the interaction of natural and synthetic lipid assemblies with inorganic nanoparticles. During her postdoctoral fellowship, she extended her interests to the synthesis of inorganic nanoparticles as consolidants for bone remains of archeological interest, as well as in the preparation and stabilization of graphene derivatives.*

*Annalisa Salvatore obtained her MSc degree in Chemical Sciences-Physical Chemistry at University of Florence in 2013 and started her PhD research under the supervision of Prof. Debora Berti, in the same year. Her doctoral research focused on the interaction of natural and synthetic lipid assemblies with inorganic nanoparticles. During her postdoctoral fellowship, she extended her interests to the synthesis of inorganic nanoparticles as consolidants for bone remains of archeological interest, as well as in the preparation and stabilization of graphene derivatives.*



**Costanza Montis**

*Costanza Montis obtained her PhD in Chemical Sciences from the University of Florence (Italy) in 2013. She is now a researcher in the Department of Chemistry of the University of Florence and member of the Italian Consortium for Colloid and Surface Science (CSGI). Her scientific background is Physical Chemistry of Soft Matter. Her main research topics include the biophysical understanding of nano-bio interfaces; the design of lipid-nanoparticles hybrid materials for biomedical applications; the study of nanostructured materials for applications in restoration of works of art.*

*Costanza Montis obtained her PhD in Chemical Sciences from the University of Florence (Italy) in 2013. She is now a researcher in the Department of Chemistry of the University of Florence and member of the Italian Consortium for Colloid and Surface Science (CSGI). Her scientific background is Physical Chemistry of Soft Matter. Her main research topics include the biophysical understanding of nano-bio interfaces; the design of lipid-nanoparticles hybrid materials for biomedical applications; the study of nanostructured materials for applications in restoration of works of art.*



**Debora Berti**

*Debora is Full Professor of Physical Chemistry at the Department of Chemistry of the University of Florence and member of the Italian Consortium for Colloid and Surface Science (CSGI). Debora's scientific background is Physical Chemistry of Soft Matter. Her research topics include hybrid nano and micro particle/lipid assemblies for responsive drug delivery, interaction of nanostructured assemblies with model membranes, design and application of nanostructured fluids for the conservation of cultural heritage. Debora has a well-established track record of her work, with more than 130 authored or co-authored research papers and several chapters contributed in specialized books.*

*Debora is Full Professor of Physical Chemistry at the Department of Chemistry of the University of Florence and member of the Italian Consortium for Colloid and Surface Science (CSGI). Debora's scientific background is Physical Chemistry of Soft Matter. Her research topics include hybrid nano and micro particle/lipid assemblies for responsive drug delivery, interaction of nanostructured assemblies with model membranes, design and application of nanostructured fluids for the conservation of cultural heritage. Debora has a well-established track record of her work, with more than 130 authored or co-authored research papers and several chapters contributed in specialized books.*

by a classical DLVO (Derjaguin–Landau–Verwey–Overbeek) formalism, as in eqn (1), including only the electrical double layer ( $E^{\text{EL}}$ ) and the London–van der Waals ( $E^{\text{LW}}$ ) contributions to the total energy of adhesion:

$$E_{\text{adh}} = E^{\text{EL}} + E^{\text{LW}} \quad (1)$$

where the terms  $E^{\text{EL}}$ , derived as a combination between the linear Debye–Hückel and the Derjaguin approximations and valid for surface potentials  $< 25$  mV, and  $E^{\text{LW}}$  are described in eqn (2) and (3), respectively:<sup>9</sup>

$$E^{\text{EL}} = \frac{\varepsilon R_1 R_2 (\psi_1^2 + \psi_2^2)}{4(R_1 + R_2)} \left[ \frac{2\psi_1 \psi_2}{(\psi_1^2 + \psi_2^2)} \ln \left( \frac{1 + e^{-kd}}{1 - e^{-kd}} \right) + \ln(1 - e^{-2kd}) \right] \quad (2)$$

$$E^{\text{LW}} = -A \frac{R_1 R_2}{6(R_1 + R_2)} \left( \frac{1}{d} - \frac{1}{d+h} \right) - \frac{A}{6} \ln \left( \frac{d}{d+h} \right) \quad (3)$$

where  $\psi_1^2$  and  $\psi_2^2$  are the surface potentials of the NP and the membrane,  $d$  the NP–membrane distance,  $k$  the Debye length,  $h$  the membrane's thickness, and  $A$  is the Hamaker constant. Although the DLVO theory generally succeeds in predicting the colloidal stability of hard colloids (e.g., inorganic NPs) suspended in a liquid medium, it often fails in describing the interaction of NPs with free-standing bilayers; a more comprehensive description for  $E_{\text{adh}}$  includes additional repulsive hydration forces establishing at short NPs–membrane distances, as well as hydrophobic NP–lipid chain attraction (the interested reader is referred to a recent report for the analytical expression of the these two supplementary energetic contributions<sup>9</sup>).

Once the NP is adsorbed onto the lipid surface (i.e.,  $E_{\text{adh}} < 0$ ), the elastic properties of the membrane comes into play, and their balance with the adhesion forces determines the degree of membrane deformation and NP's wrapping. Specifically, the energetic gain due to the adhesion forces is maximized by increasing the contact area between the NP and the lipid membrane, according to eqn (4):<sup>10</sup>

$$E_{\text{adh}} = -w \int_0^{S_{\text{ad}}} dS \quad (4)$$

with  $w$  adhesion energy per unit area and  $S_{\text{ad}}$  the contact area between the membrane and the NP. On the other side, the NP's wrapping is associated with a free energy cost of imposing membrane deformation ( $E_{\text{el}}$ ), which is expressed through the Cahn–Helfrich–Evans formalism:<sup>10</sup>

$$E_{\text{el}} = \int_0^S dS \left[ \gamma + 2k_{\text{B}}(H - c_0)^2 + \bar{k}K \right] \quad (5)$$

with  $S$  the entire interfacial area.

As we can see from eqn (5), the deformation penalty depends both on the membrane's topology, through the mean  $H$  and Gaussian  $K$  curvatures, and on the interface's mechanical and elastic properties, expressed by the surface tension  $\gamma$ , bending rigidity  $k_{\text{B}}$ , spontaneous curvature  $c_0$  and Gaussian saddle splay modulus  $\bar{k}$ . It is the fine interplay between  $E_{\text{adh}}$  and  $E_{\text{el}}$  that ultimately defines the NP–membrane arrangement which

minimizes the system's energy, ranging from completely unwrapped NPs (e.g., for small nanoparticles and/or weakly interacting with the lipid phase), to larger and/or strongly adhered nano-objects, eventually fully engulfed by the lipid membrane (see Fig. 1A).

Based on the above treatment, we will now discuss the several NPs- and membrane-related factors implicated in this interaction, with particular attention on size, shape, surface coating of NPs and NP–NP correlations; on the “membrane” side, we will take into account some selected physicochemical properties and the zero or non-zero curvature.

Depending on their size, the adhesion of NPs on a target planar membrane can result in different effects: small NPs can either remain embedded in the lipid membrane or directly diffuse through it; relatively larger particles ( $> 10$  nm) can be wrapped by the membrane.<sup>11</sup> This process is finely controlled by the energetic balance between the adhesion forces (eqn (4)) and the membrane's elastic deformation penalty (eqn (5)), leading to an optimal size for wrapping, as first observed by Roiter *et al.*<sup>12</sup> In particular, two characteristic NPs' limiting radii for a successful engulfment by lipid membranes can be theoretically predicted:<sup>10</sup>

$$R_{\text{kw}} = \sqrt{\frac{2k_{\text{B}}}{E_{\text{adh}}}} \quad (6)$$

$$R_{\text{ky}} = \sqrt{\frac{2k_{\text{B}}}{E_{\text{adh}} - \gamma}} \quad (7)$$

within the bending-dominated regime (i.e., for relatively small membrane's deformation), the membrane tension can be neglected, and the wrapping process is mainly controlled by the competition between membrane's bending and NP's adhesion strength, defining a critical radius  $R_{\text{kw}}$ . NPs with  $R < R_{\text{kw}}$  remain unwrapped, while larger NPs ( $R > R_{\text{kw}}$ ) are fully engulfed inside the lipid scaffold. For larger membrane's deformation (e.g., induced by micron-sized particles), a characteristic length scale  $\lambda = (2k_{\text{B}}/\gamma)^{1/2}$ , which depends solely on membrane's properties, marks the crossover from the bending-dominated to the stretching-dominated regime<sup>9,13</sup> (Fig. 1B), where the  $\gamma$ -dependent wrapping extent gradually increases with NP's size. The full engulfment is reached for a second crossover NP's radius  $R_{\text{ky}}$  (eqn (7)), representing a larger NP's limiting size, which is required for the internalization in the case of finite tension-membranes.

## 2.2 Key NPs features in the interaction with lipid membranes

Concerning NPs shape, the increase of the surface area/volume ratio from spherical to asymmetrical NPs (e.g., nanorods, nanoprisms and nanocubes), maximizes the surface available for absorption onto lipid membranes (eqn (4)), enhancing their reactivity;<sup>14</sup> on the other side, the local particle's surface curvature is predicted to increase the energy barrier associated to membrane's deformation, stabilizing partial-wrapping states also for tensionless membranes.<sup>9,10</sup> Moreover, the interaction of asymmetric NPs with target lipid membranes can lead to

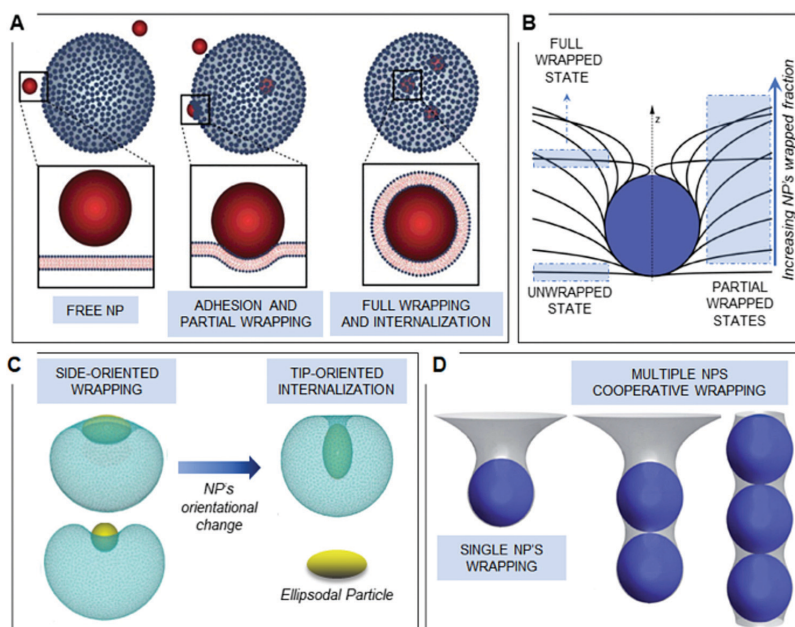


**Fig. 1** Theory of NPs–lipid membranes interactions. Panel A: illustration of the three possible configurations for a NP interacting with a lipid membrane: from left to right, (i) NP free in the environment (repulsive contribution to the NP–bilayer total interaction overcoming the attractive one), (ii) NP's adhesion to the membrane, causing NP's partial wrapping and (iii) NP's full engulfment (strong attractive NP–bilayer forces). Readapted from open access ref. 13. Panel B: illustrative picture representing unwrapped, fully wrapped and different wrapping degree–intermediate configurations for a NP interacting with a fluid interface. Reproduced from ref. 101 with permission from The Royal Society of Chemistry. Panel C: ellipsoidal NP's reorganization from a side-oriented configuration, adopted during the wrapping process, to a tip-oriented configuration, minimizing the energy required for full NP's engulfment and internalization. Reproduced from ref. 16 with permission from The Royal Society of Chemistry. Panel D: illustrative picture of (from left to right) a single NP wrapped by a fluid interface, two and three NPs wrapped in a membrane tube. Reproduced from ref. 101 with permission from The Royal Society of Chemistry.

preferential wrapping orientations, to minimize the energy cost for wrapping<sup>15,16</sup> (see Fig. 1C). Eventually, the asymmetric shape of NPs can drive peculiar self-assembly phenomena at the nanobio interface, some examples of which are given in Section 3.

The NPs surface functionalization represents another important factor affecting the interaction with membranes; in particular, NPs surface charge has a major impact on adhesion both onto charged and zwitterionic interfaces, setting the sign and magnitude of the electrostatic long-range contribution of (eqn (1)).<sup>3,17–21</sup> Furthermore, the adhesion of charged NPs to a target membrane is also associated to an entropic gain, deriving from the release of small counterions from the NP surface<sup>22</sup> (see Fig. 1D). On the other side, the presence of polymeric steric stabilizers on the NPs surface, like for PEGylated particles, often decreases the adhesion energy; this effect can be understood considering the mobility loss experienced by the polymer chains approaching the lipid surface, which entails a considerable entropic penalty for membrane adhesion. Moreover, NPs' surface functionalization determines their polarity, which is key in controlling their spontaneous localization when challenging a free-standing lipid membrane: generally, hydrophilic nanomaterials with size larger than 10 nm reside at the membrane surface, with the possibility to be partially or fully wrapped by

the membrane. Conversely, depending on their hydrophobicity,<sup>23</sup> small particles can either spontaneously cross<sup>24,25</sup> or be entrapped<sup>24</sup> within the lipid membrane, provoking an alteration of the bilayer's frustration packing energy.<sup>26–31</sup>

Eventually, interparticle forces between different membrane-bound NPs may originate cooperative phenomena, ultimately leading to the simultaneous wrapping and engulfment of multiple NPs (see Fig. 1D), which will be discussed in detail in Section 3.

### 2.3 Key membrane features in the interaction with NPs

Membrane-related characteristics have a crucial role in the interaction with NPs. In particular, the composition of lipid bilayers determines specific physico-chemical, viscoelastic and thermodynamic properties of relevance in the interaction with NPs. Membrane's surface potential, determined by the percentage of non-ionic, anionic and cationic lipids, strongly affects the electrostatic contribution to NPs adhesion (eqn (1)), while the presence of specific components (*e.g.*, cholesterol) and their relative abundance, give rise to characteristic behaviours, which will be extensively discussed in Section 3.

Equally important, the molecular geometry of the membrane's components determines the equilibrium arrangement of lipids within the bilayer. The molecular packing represents the main

factor affecting both the physical state and the overall topological curvature of membranes, which are two prominent determinants in the interactions with nanomaterials.

In particular, the interactions at the nano-lipid interface is extremely affected by the gel–liquid crystalline phase behaviour of lipid membranes: by increasing temperature, lipid bilayers undergo a main phase transition from the so-called “gel state” ( $L_{\beta}$ ), where hydrocarbon chains are tightly packed and almost locked in place, to a “fluid state” ( $L_{\alpha}$ ), where lipids freely diffuse within the 2D membrane’s plane. The “melting transition temperature” ( $T_m$ ) is specific for a given lipid composition and determines the elastic response of membranes at a given temperature. In particular, gel phase bilayers show a reduced reactivity with nanomaterials, mostly due to the high value of their bending rigidity ( $k_b$ ) with respect to the fluid phase,<sup>9</sup> which strongly hampers the membrane’s bending and wrapping around NPs (see eqn (5)–(7)). On the other side, the interaction with NPs, which can proceed through polar headgroups (hydrophilic NPs) or hydrophobic chains (hydrophobic NPs), might affect the lipid molecular packing, leading to micro and macroscopic modifications in the membrane structure and thermotropic behaviour (specific examples will be provided in the following Section).

As predicted from eqn (5), the membrane’s topology plays a crucial role in its elastic response to NP’s induced deformations. Although lipid membranes are generally visualized as flat bilayers ( $H$  and  $G$  in eqn (5) equal to zero), both biomembranes and synthetic lipid assemblies may fold into more organized non-lamellar bilayered structures.<sup>32</sup> The interaction of nanomaterials with such non-lamellar structures may have a noteworthy relevance both for biomimetic and technological applications,<sup>33,34</sup> (as discussed in details in the following Section) while it remains, to date, a highly unexplored research area.

Differently from planar membranes, curved membranes are defined by positive (direct phases) or negative (inverse phases) mean curvature ( $H$ ) and non-zero Gaussian curvature ( $K$ )<sup>35</sup> in each point of their surface, with  $H$  and  $G$  described by eqn (8) and (9), respectively:

$$H = \frac{1}{2}(c_1 + c_2) \quad (8)$$

$$K = c_1 c_2 \quad (9)$$

with  $c_1$  and  $c_2$  minimum and maximum values of curvature at a specific point of membrane surface.

The non-zero values of  $H$  and  $K$  lead, as predicted from eqn (5), to a modification of their Helfrich energy and elastic response towards externally induced deformations (*e.g.*, NPs’ wrapping) with respect to the case of lamellar membranes. Moreover, different topologies are associated with a frustration packing free energy ( $E_p$ ), which varies according to eqn (10):<sup>36</sup>

$$E_p = k(l - l_r)^2 \quad (10)$$

with  $k$  stretching rigidity of lipid chains,  $l$  and  $l_r$  hydrophobic chain extension in the stretched and relaxed state, respectively. Phase transitions between different geometries, including changes in both elastic and frustration packing energies, have

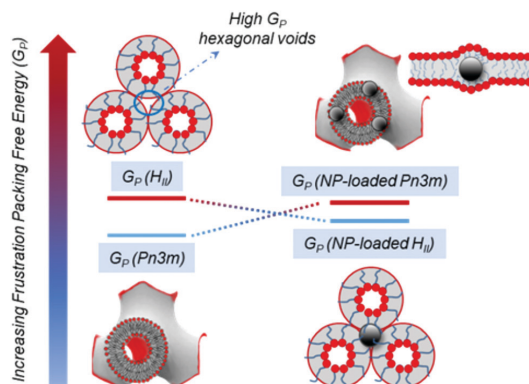


Fig. 2 Effects of NPs on lipid mesophases architectures. Illustrative scheme of the NP-induced modification of the Frustration Packing Energy of both cubic and hexagonal mesophases.

high biological relevance, sharing similar energy barriers and molecular re-arrangements with membrane fusion processes.<sup>37</sup> Several recent studies, which will be addressed in Section 4, demonstrated that both hydrophilic and hydrophobic NPs can promote phase transitions between model mesophases with different geometry,<sup>26,27,34,37–41</sup> lowering the energy barrier required to switch from low to high curvature phases. One of the first attempts to elucidate this effect is represented by recent works,<sup>26,42</sup> where the transition temperature from cubic to hexagonal phases in monoolein liquid crystals is demonstrated to be finely controlled by inclusion of hydrophobic iron oxide NPs (see Section 4). This behaviour was explained by combining the Helfrich theory in eqn (5) with geometrical considerations: NPs increase the frustration packing energy of the cubic phase (eqn (10)), while they have a milder effect on the hexagonal arrangement, by inserting into its hydrophobic voids (see Fig. 2).

In the framework of this theoretical description, in recent years the interaction of NPs with lipid membranes has been explored with different approaches and for different purposes: from fundamental studies employing lipid bilayers as biomimetic platforms of tuneable physicochemical feature for investigating the interaction with prototypical nanoparticles, aimed at a better understanding of the efficiency and possible adverse effects of nanomaterials designed for biomedical applications, to applicative studies, where the interaction of NPs and lipid membranes is exploited for analytical purposes; from the engineering of lipid assemblies with NPs inclusion, in order to form smart hybrid materials for applications in materials science, to the functionalization of NPs with a lipid coating, to improve their biocompatibility and pharmacokinetic properties.

In Section 3 we will review the interaction of NPs with synthetic lipid bilayers, taken as simplified models of real plasma membranes: in line with Section 2, we will consider the main physicochemical factors, either related to NPs or to the lipid membrane, affecting the interaction under simplified conditions. We will provide relevant examples from the recent

literature, highlighting the connections, whenever they are relevant, between the findings on cell models and the *in vitro*/*in vivo* observations.

### 3. NPs/biomembrane interactions: from biophysical studies of nano–bio interfaces to applications

One of the main issues limiting the development of nanomedicine and the translation of engineered nanomaterials into medical practice, is the poor understanding of their fate in biological fluids, and their short-term and long-term possible adverse cytotoxic effects.<sup>37,43–49</sup> Recent reports have also highlighted how nanodevices designed for nanomedicine applications, whose functionality/efficiency has been proved at the lab-scale, completely fail reaching their biological targets once in a living organism.<sup>50</sup> As a matter of fact, to date, nano-therapeutics available on the market are mainly limited to polymeric- and liposomal-based formulations,<sup>51,52</sup> while, apart from some iron oxide NPs-based formulations, inorganic and metallic particles are at research stage or in clinical trials.<sup>53</sup> With the ultimate aim to fill the gap between the design/synthesis/development of nanomaterials for nanomedicine and their end use application, it is necessary to improve our fundamental knowledge on the interaction of nanomaterials with biologically relevant interfaces, particularly, cell membranes.

Plasma membrane, primarily composed by a mixed phospholipid bilayer with embedded proteins, protects the cell interior and ensures its communication with the external environment. The mechanisms of cell signalling processes are extremely complex and length scale-dependent, with smaller molecules spontaneously crossing the lipid barrier and larger and/or polar molecules harnessing protein-mediated transportations across the membrane.<sup>13</sup> The nanoscale, shared by engineered particles and biologically relevant macromolecules (*i.e.*, DNA, viruses, surface proteins), is mostly associated with endocytic pathways, where the internalisation of nano-objects is generally controlled by the membrane through specific receptor–protein binding for the case of biological species.<sup>54,55</sup> However, it has been demonstrated that synthetic NPs can be wrapped and internalized by both model and real cell membranes in the absence of any receptor-mediated interaction,<sup>43,55,56</sup> under exclusive control of non-specific interactions taking place at the nano–bio interface, and membrane's elasticity.

In this context, synthetic lipid membranes (together with more complex systems, as organ-on-a-chip and 3D cells arrays, mimicking an entire tissue<sup>57</sup>), are interesting biomimetic systems, which, by mimicking the main structural unit of plasma membranes, allow investigating phenomena at the nano–bio interface in simplified and highly controlled conditions.<sup>44,45,58</sup>

In recent years, both experimental and theoretical studies have addressed the interaction of NPs with synthetic lipid membranes, aimed at establishing clear connections between the results in simplified model systems and what observed in real cells, in order to enabling predictive strategies for the

design of evermore efficient and non-toxic nanomaterials for nanomedicine.

In the following sections recent relevant studies on NPs–synthetic lipid membranes interactions, together with their implications for the understanding of real nano–bio interfaces, will be revised, particularly focusing on: the effect of NPs coating (surface charge, exchangeability of the ligand, steric hindrance of the coating, impact of the protein corona) (Section 3.1); the effect of NPs size and shape (with particular interest on the relevance of NPs clusterization in cell uptake) (Section 3.2); the effect of NPs adhesion on the composition, integrity and viscoelastic properties of the target membrane (Section 3.3). In addition, the interaction of inorganic NPs and lipid membranes has been exploited for analytical purposes, in order to label/signal/probe selected properties of cells or lipid assemblies in complex biological media, both exploiting specific and non-specific interactions of NPs with the target membranes. This latter research field will be reviewed in Section 3.4.

#### 3.1 Biophysics of nano–bio interfaces: NPs coating

**3.1.1 NPs surface charge.** The intrinsic characteristics of NPs (*i.e.*, core composition, size, shape) often have a secondary impact on the interaction with a target lipid membrane, which is primarily mediated by the ligands coating the NP's surface: the surface characteristics of NPs determine polarity and interfacial properties, directly involved in the electrostatic and London–van der Waals contributions to NPs' adhesion to a lipid interface (see Section 2.1 for the theoretical background). The interaction of NPs with target membranes is primarily affected by the charge of both components (see eqn (2)). In order to closely resemble real plasma membranes, most of the employed model bilayers in biomimetics are characterized by a zwitterionic or slightly anionic nature. Therefore, negatively charged NPs tend to be electrostatically repelled from the membrane, undergoing to weaker interactions with respect to cationic ones: remarkably, this is also observed for real cell membranes, where the uptake is generally much lower for anionic NPs than for cationic ones.<sup>59–61</sup> However, the situation of real cells is complicated by the presence of other interaction pathways of specific nature, representing an alternative with respect to non-specific forces. Several studies have highlighted that nonionic, anionic and cationic NPs of similar sizes undergo different internalization routes, from clathrin- or caveolae-mediated endocytosis to non-endocytic pathways, like passive diffusion.<sup>62,63</sup> Even if characterized by limited interaction capability, yet anionic NPs are attractive for biomedical applications, due to limited adverse cytotoxic effects. In addition, despite the dominantly repulsive electrostatic forces, several reports have shown successful internalization of anionic NPs, as silica or Gold NPs (AuNPs).<sup>63–65</sup> Conversely, cationic NPs have a strong tendency to interact with negatively charged membranes: it has been shown that cationic NPs adhere and clusterize onto synthetic target membranes, extract lipids from the membrane, ultimately provoking localized membrane disruption or integrity loss.<sup>22,66,67</sup> In line with this findings, they are often characterized by limited stability in biological media and,

above all, relevant toxic effects on real cells.<sup>13,68,69</sup> Recently, Lee *et al.*<sup>70</sup> hypothesized, by means of a systematic study using a charge library of modified AuNPs, that the magnitude of the positive charge is not the sole factor determining the extent of interaction with target membranes and, thereby cytotoxicity. They conclude that spatial proximity of positively charged functional groups within a hydrophobic moiety is a common characteristic of toxic gold colloids.

**3.1.2 NPs coated with steric stabilizers.** A common strategy to increase the colloidal stability of NPs in biological media consists in the passivation of NPs with bulky ligands, to endow them with steric stabilization. This kind of coating also improves the pharmacokinetic properties of NPs: for instance, it is well known that PEGylation prevents opsonisation, improving the circulation time of the nanomaterial. This stealth effect of PEG in preventing opsonisation depends on its steric hindrance: it has been shown that both NPs uptake and circulation time depend on the molecular weight of PEG coating the NPs.<sup>71</sup> Moreover, thanks to molecular dynamic simulations, Lin *et al.*<sup>72</sup> elucidated the effect of both the grafting density and polymer's chain length on the shielding ability of PEG layers bounded to gold NPs of varying size. Similar examples of steric stabilization of NPs have recently been proposed by Jiang and co-workers, who have employed poly(zwitterionic)protein functionalization (for instance poly(carboxybetaine)) to improve pharmacokinetic properties of NPs,<sup>73,74</sup> while other examples of polyzwitterionic coatings are poly(acrylic acid) derivatives, poly(maleic anhydride-*alt*-1-alkene) derivatives or poly(sulfobetaine) derivatives, which offer several advantages over PEGylation (see as a reference the Review from Garcia *et al.*<sup>73</sup>).

PEGylation or steric stabilization affects the interaction of NPs with synthetic target membranes, with possible implications also at the real membranes' level. Indeed, the use of steric stabilizers, like PEG, is theoretically predicted to decrease the adhesion of NPs to lipid membranes, due to the high entropic loss associated to the adsorption process (see Section 2).

In a recent study,<sup>75</sup> through large scale molecular dynamic simulations, Gal and coworkers extensively characterized the interaction of PEGylated SPIONs of different size with both synthetic membranes of different composition and real cancer and kidney cells. In the frame of classic DLVO theory (Section 2), they presented a direct comparison of NP-synthetic and real membrane interactions, linking weak NP adsorption to anionic lipid membranes, due to NP-bilayer electrostatic interactions, with eukaryote cell uptake, without membrane penetration. Moreover, they showed that the NP-membrane electrostatic attraction is suppressed by increasing PEG molecular weight and NP size, which they correlated with low cell uptake and no cytotoxicity in two cell lines.

A common strategy to circumvent the poor ability of steric-stabilized NPs to interact with cells *via* non-specific interactions, limiting their cell uptake and therapeutic/diagnostic efficiency, is to exploit the NP-membrane specific interactions, which are available for the case of real plasma membranes: endowing NPs surface with targeting moieties, might result in promoting the effective docking of NPs on cell membranes and

improving the successful achievement of their biological target. For instance, in a proof-of-concept study it was shown that adding biotin or streptavidin moieties allows specific binding of polymer-coated NPs to beads carrying the complementary unit;<sup>76</sup> Kaaki *et al.*<sup>77</sup> highlighted the efficient targeting of human breast carcinoma cells by folic acid-conjugated iron oxide NPs with a PEG coating. However, partially contradictory results were obtained by Kraiss *et al.* on similar system, where no folate-dependent targeting was highlighted.<sup>78</sup>

**3.1.3 NPs coating with exchangeable ligands.** The binding mode and strength between the NPs and the coating agent determine both single NP-membrane interactions and collective NP-NP interactions at the nano-bio interface: physisorbed ligands, which can be easily displaced from the NP's surface through ligand-exchange, are associated to enhanced reactivity of NPs, which can be considered as "naked". Recently, hydrophobic physisorbed ligands, *i.e.*, oleic acid/oleylamine coatings on iron oxide NPs, have been associated to small NPs' pearl-necklace aggregation inside monoolein bilayers.<sup>26</sup> Moreover it has been shown that hydrophilic weakly adsorbed ligands on the surface of AuNPs can promote peculiar aggregation phenomena occurring on the lipid membrane,<sup>18,19</sup> which are particularly significant also for the case of repulsive NPs/membrane electrostatic interactions (*e.g.*, between negatively charged gold NPs and slightly anionic synthetic free-standing bilayers). Moreover, weakly bound physisorbed ligand onto the NPs surface can be easily replaced with other molecules establishing covalent or stronger non-specific interaction with the bare NPs surface: remarkably, it has been recently demonstrated by Wang *et al.*,<sup>79</sup> that weak ligands, as citrate and short DNA fragments onto the gold surface, can be effectively replaced with lipid components of cell membranes, resulting in unique interfacial phenomena. Indeed, when ligand exchange processes occur at the interface, NPs might aggregate into ordered monolayers on the lipid membrane, which might affect membrane integrity and cell internalization efficiency and pathway.

**3.1.4 Protein corona coating of NPs.** An interesting aspect is the functionalization of NPs surface with the so-called protein corona.<sup>14,55,80,81</sup> From the pioneering studies of K. Dawson<sup>82-84</sup> and coauthors, it has been progressively established that NPs in biological fluids are spontaneously covered by a self-assembled layer of proteins (an inner non-exchangeable layer and an external exchangeable one), which determines a "biological identity" of the NPs and, ultimately, their ability to interact with cells.<sup>44,80,85,86</sup> The composition of the protein corona depends on the nature of NPs core, on their shape and on their surface coating. In particular, the surface charge of NPs also affects the adhesion of biomolecules present in biological media, modifying the protein corona, in terms of composition and orientation.<sup>62,87,88</sup> It has also been highlighted that during NPs internalization, the tendency of corona proteins is, at least partially, to remain attached to NPs surface.<sup>83,89,90</sup> Since proteins are generally characterized by significant steric hindrance and amphiphilic nature, they specifically mediate the interaction of the NPs with plasma membranes. In this context, it has been highlighted that slight physicochemical

modifications of the proteins modify their binding and orientation on NPs, strongly affecting the biological uptake of NPs.<sup>91</sup> Recently, the controlled formation of the protein corona has been exploited both for application purposes (e.g., for applications in cancer vaccines<sup>92</sup>) and also to control in a predictable way the protein-corona-mediated interaction of NPs with cell membranes. For instance, pre-incubation of NPs with serum has been exploited to prevent NPs aggregation in biological media, improve their cell uptake and decrease their cytotoxic effects.<sup>69</sup> The comprehension, control and exploitation of protein corona formation is therefore a key milestone in determining and predicting NPs fate in living organisms.

### 3.2 Biophysics of nano-bio interfaces: NPs size and shape

As discussed in Section 2, when a NP adheres to a planar lipid membrane, it locally imposes a curvature modification, which depends on the size of NPs and on the viscoelastic properties of the membrane (eqn (5)), which eventually controls the occurrence and extent of NPs wrapping by the membrane; therefore, NPs size also determines the response of the bilayer to its adhesion and, ultimately, the effects on the target membrane and the internalization pathway. NPs with size comparable or smaller than the lipid bilayer thickness can either be entrapped within the membrane<sup>30</sup> or translocate across the lipid bilayer by diffusing through<sup>25,93,94</sup> or by opening pores in the membrane,<sup>95</sup> which is normally associated to a high cytotoxicity *in vivo*.<sup>56,96</sup> On the contrary, wrapping represents the dominant mechanism for larger particles (> 10 nm) interacting with bilayers, which is associated to their entrance into cells in living organisms.<sup>11</sup> Often, depending on NPs size, adhesion to a target membrane might result in the NPs clusterization: indeed, under specific conditions, membranes actively drive the self-assembly of adsorbed NPs, as a result of the tendency of the membrane to minimize the NP-induced deformation and its associated elastic cost (eqn (5)).<sup>97</sup> As a result, small-sized NPs have been observed to preferentially interact with membranes as clusters,<sup>67,98</sup> while fluid membranes have been theoretically predicted to mediate the asymmetric aggregation of spherical nanoparticles onto lipid surface.<sup>99</sup> This aspect is particularly significant for medical application of nanomaterials, since NPs uptake in model and real membranes is often preceded by aggregation at the nano-bio interface.<sup>11</sup> In addition, mathematical models and molecular dynamic simulations have revealed that membrane-induced interactions between bound particles can lead to collective NPs wrapping and internalization: in particular, Zhang *et al.*<sup>100</sup> revealed that NPs translocation proceeds in a cooperative way, with a key role played by NPs quantity, while Lipowsky *et al.*<sup>101,102</sup> showed that spherical NPs can be cooperatively wrapped in tubular membrane invaginations.

While the effect of NP's size has been extensively investigated, much less is known on the impact of NP's geometry. Asymmetrically shaped NPs, like nanorods, nanodisks and nanostars, are particularly attractive materials, due to the peculiar properties (optical, magnetic, electronic and so on) arising from anisotropy.<sup>103</sup> Depending on their shape, anisotropic NPs can

efficiently interact with a target membrane and translocate across it. MD studies on the interaction of NPs of different non-spherical shapes highlighted reorientation of NPs in proximity to the target membrane, to maximize the interaction, leading to strong shape and orientational dependence on the translocation<sup>104</sup> (see Fig. 3A). In addition, it has to be considered that, from a theoretical standpoint, it is thermodynamically more favourable for a lipid membrane to wrap a spherocylinder than a sphere of the same radius.<sup>105</sup> Consistently with the theoretical predictions, non-spherical NPs, from nanostars to nanorods, are efficiently internalized by cells, in a shape and, for nanorods, aspect-ratio dependent manner.<sup>106,107</sup> Experimental studies on biomimetic membranes have shown that the asymmetric shape of NPs can drive peculiar self-assembly phenomena at the nano-bio

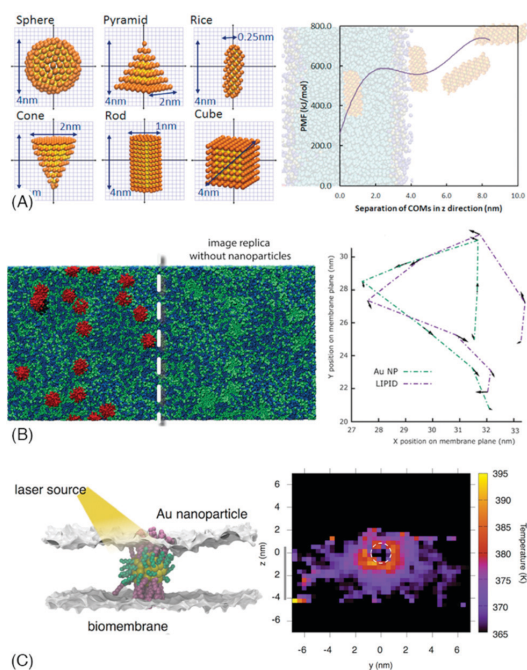


**Fig. 3** Theoretical studies on nano-bio interfaces. Panel A: molecular dynamics study to compute translocation rate constants of NPs of different shapes through lipid membranes; (left) coarse-grained gold nanoparticles setup; (right) analysis of rice NP translocation: potential of mean force, PMF ( $\text{kJ mol}^{-1}$ ) profile as a function of distance of the NP from the lipid bilayer. Adapted with permission from ref. 104. Copyright (2012) American Chemical Society. Panel B: lipid membrane modifications upon interaction with cationic gold NPs: (left) lateral phase separation of 1:1 anionic (green) and zwitterionic (blue) lipids in the presence of gold NPs (red); (right) trajectories of NP (green) and anionic lipid (blue) highlighting the slowed diffusion of anionic lipids upon interaction with NPs. Adapted with permission from ref. 22. Copyright (2019) American Chemical Society. Panel C: nonequilibrium molecular dynamics simulations to investigate photoporation of lipid membranes through the irradiation of AuNPs: the NPs, stably bound to cell membranes, convert the radiation into heat; a quantitative prediction of the temperature gradient around the NP upon irradiation is evaluated. Adapted with permission from ref. 197 Copyright (2017) American Chemical Society.

interface:<sup>10,37</sup> as an example, we recently demonstrated that gold nanorods (Au NRs) are wrapped by model and real cell membranes as end-to-end NPs' clusters,<sup>67</sup> reducing the energy penalty required for the membrane to bend around highly curved edges. The induced tension due to the adhesion of asymmetric NPs determines effects of lipid extraction, observed both on model membranes and macrophage cells, eventually provoking extensive disruption of the membrane, related to a significant *in vitro* cytotoxicity.<sup>67</sup>

### 3.3 Biophysics of nano-bio interfaces: membrane composition

Cell membranes are characterized by a high degree of compositional heterogeneity, typically comprising of thousands of different lipids, carbohydrates and proteins,<sup>108</sup> which is reproduced, at different complexity levels, by model membranes. The chemical composition of both synthetic and natural bilayers strongly affects their elasticity, physical state and structure, thereby determining their response towards external stimuli. A clear example is the recent work of Lunnoo *et al.*,<sup>109</sup> in which model bilayers with different compositional complexity levels correspond, as predicted by their proposed MD simulations, to diverse cellular uptake pathways of neutral 10 nm gold NPs. Going more into details, the presence of charges on the lipid membrane emphasizes the interaction with oppositely charged particles, as expected from eqn (2)<sup>96</sup> in Section 2; however, it has been demonstrated that electrostatic interactions play a major role also for neutral zwitterionic lipids facing anionic and cationic NPs.<sup>110,111</sup> In addition, it has been observed that the molecular structure of membrane's lipid components (*e.g.*, saturation degree of hydrophobic chains) represents another factor to take into account, affecting the penetration level of NPs inside the lipid region.<sup>112</sup> Furthermore, cholesterol, one of the most abundant sterols in real lipid membranes, deeply affects the structure and fluidity of lipid bilayers; moreover, it is involved in the formation of lipid rafts,<sup>113</sup> which, for reasons not yet fully understood, increase the extent of NPs-membrane interactions: as an example, Melby *et al.*<sup>114</sup> showed that positively charged AuNPs bind significantly more to phase-segregated bilayers with respect to single phase ones, while Hartono *et al.*<sup>115</sup> associated higher cholesterol concentrations in lipid monolayers to stronger interactions with protein-coated AuNPs, leading to monolayer disruption.

### 3.4 Biophysics of nano-bio interfaces: NPs-induced membrane modifications

The self-assembled nature and lateral fluidity of plasma membranes determine a capability of the membrane to reorganize and locally and transiently restructure itself in response to biological stimuli. This is the case considering for instance the transient formation of lipid rafts, in relationship with cell trafficking phenomena, or considering ligand (drug)-receptor interactions at cell surface, triggering complex biological responses. In this respect, several studies have addressed the effects on NPs on a target lipid membrane upon adhesion. A first effect is the induced lateral phase separation within the target

membrane: theoretical studies on cationic NPs have highlighted their tendency to recruit anionic lipids in the adhesion area, determining the formation of phase separated patches within the membrane (see Fig. 3B).<sup>22,116</sup> The alteration of membrane's phase behaviour induced by NPs is a growing research topic, with several studies contributing building-up a complex picture, which is far from being understood. As an example, the group of Granick<sup>111</sup> reported a different effect of silica anionic<sup>117</sup> and cationic particles on phospholipid membranes, with negative NPs inducing gelation and positive ones provoking fluidification. Considering anionic silica NPs with different size, the group of Zhang *et al.*<sup>118</sup> reports that the gelation, or "freeze effect" on DOPC giant unilamellar vesicles (GUV) is promoted by small NPs (18 nm), while large particles (>78 nm) promote membrane wrapping. By significantly decreasing the phospholipid lateral mobility, the release of tension through stress-induced fracture mechanics results in a microsize hole in the GUVs after interaction. On the other hand, membrane wrapping leads to increased lipid lateral mobility and the eventual collapse of the vesicles.

Von White *et al.*<sup>30</sup> registered an increase in the gel-to-liquid crystalline transition temperature of synthetic lipid vesicles induced by the embedding of hydrophobic AuNPs, while Chakraborty *et al.*<sup>119</sup> reported the opposite effect, *i.e.*, phospholipid bilayer softening, due to hydrophobic AuNPs inclusions; on the other side, recent studies demonstrated that hydrophilic (negatively and positively charged) AuNPs induce the same effect at the nanoscale, promoting the formation of rigidified lipid domains around the NPs' surface, characterized by a reduced lipid motion with respect to the surrounding fluid phase.<sup>21,22,120,121</sup> Both the induced lateral phase separation on a target membrane and the induced modification of the viscoelastic properties might represent, at the biological level, both biologically relevant signals, activating cell entry pathways, or else might be of relevance in inducing cytotoxic effects (Fig. 3C).

### 3.5 Analytical applications of NP-lipid membrane interactions

An interesting research topic related to the interaction of NPs with lipid membranes is its exploitation for analytical purposes. Inorganic NPs are characterized by peculiar properties, making them suitable to provide a readout, generally an optical (fluorescence, scattering) or magnetic signal, which can provide qualitative or quantitative information of different nature. Knowles and coworkers have shown how the spontaneous formation of a supported lipid bilayer on a polystyrene NPs patterned support can be exploited to form membrane regions of high curvature, due to NPs partial wrapping: these areas spontaneously accumulate specific, single-tailed lipids, of higher spontaneous curvature, and can be exploited to monitor the interaction of biomolecules with membrane areas of high curvature;<sup>122</sup> Liu *et al.*<sup>123</sup> have formed AuNPs patterned surfaces (see Fig. 4B), for mechanical tension measurements in living cells. Cho and coworkers<sup>124</sup> have designed a nanoplasmonic biosensor made of an array of gold, silicon oxide or titanium oxide nanodisks coated with different lipid architectures

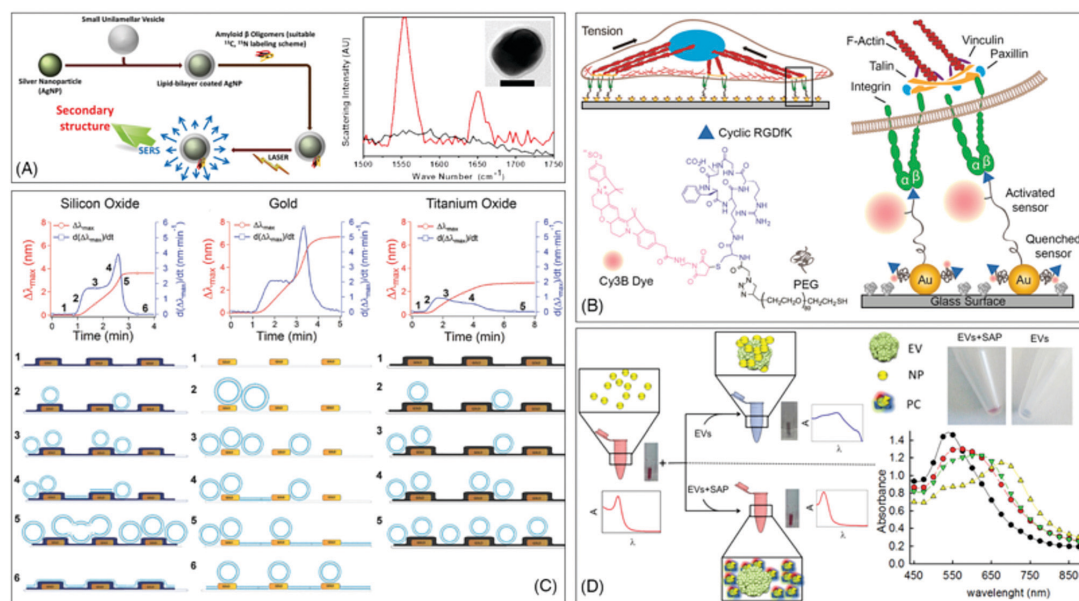


Fig. 4 Analytical applications of NP–lipid membrane interactions. Panel A: SERS technique exploiting the spontaneous binding of proteins to lipid bilayer-encapsulated AgNPs to probe lipid membrane-attached oligomers; (left) set-up of the technique (right) TEM micrograph of lipid-coated AgNPs; SERS spectrum of melittin in the presence of AgNPs (black) and lipid-coated AgNPs (red). Adapted with permission from ref. 127. Copyright (2015) American Chemical Society. Panel B: molecular tension fluorescence microscopy applied to the investigation of fibroblast cells layered on a substrate with an array of precisely spaced functionalized AuNPs: cartoon summarizing the experimental set-up. Adapted with permission from ref. 123. Copyright (2014) American Chemical Society. Panel C: self-assembly formation of lipid membranes on nanoplasmic sensor platforms. Time-resolved extinction maximum wavelength shift measurements (red) and corresponding time derivative (blue) for vesicle adsorption onto (left) silicon oxide-coated nanodisk surface, (center) bare gold nanodisks on glass surface, and (right) titanium oxide-coated nanodisk surface. Adapted with permission from ref. 124. Copyright (2014) WileyVCH Verlag GmbH & Co. KGaA, Weinheim. Panel D: (left) set-up of the nanoplasmic assay for probing by eye protein contaminants (single and aggregated exogenous proteins, SAP) in EV preparations; (right) Eppendorf tubes containing AuNPs in the presence of EVs (blue) or EVs + SAP (red), highlighting the sensitivity of the assay to EVs protein contaminants; UV-visible absorbance spectra of AuNPs, in the presence of increasing amounts of EVs, highlighting the sensitivity of the assay to EVs concentration. Adapted with permission from ref. 130. Copyright (2015) American Chemical Society.

(see Fig. 4C), vesicles arrays, supported lipid bilayers or a coexistence of the two systems, spontaneously formed due to different pathways of interaction between lipid vesicles and the nanodisks of different material: localized surface plasmon resonance experiments detecting a membrane-active peptide highlighted a strong dependence of the interaction between the peptide and the lipid bilayer, depending on the architecture of the lipid scaffold. Limaj *et al.*<sup>125</sup> designed an infrared biosensor to monitor the molecular behaviour and dynamics of lipid membranes, based on the adsorption of lipid vesicles on an engineered substrate functionalized with gold nanoantennas for surface enhanced infrared absorption (SEIRA) experiments. Suga *et al.*<sup>126</sup> exploited the interaction of hydrophobic (dodecanthiol-modified) AuNPs with phospholipids and phospholipid assemblies, to investigate the behavior of lipid membranes at a molecular length-scale through Surface-Enhanced Raman Spectroscopy (SERS). The same technique is employed by Bhowmik *et al.*,<sup>127</sup> who exploited the formation of a lipid coating wrapping Silver NPs (AgNPs) to probe through SERS the molecular behavior of protein oligomers spontaneously binding to the lipid coating of AgNPs (this example will be also discussed in Section 5) (see Fig. 4A). Recently, we have

shown that synthetic Giant Unilamellar Vesicles of POPC promote the clusterization of Turkevich–Frens citrated AuNPs on the lipid membrane itself.<sup>121</sup> This phenomenon, which has been investigated by other groups, provokes a modification of the plasmon resonance peak of AuNPs, which is visible also by naked eyes as a colour change of AuNPs dispersion from red to blue.<sup>17,128</sup> Interestingly, this effect is similarly observed when the same AuNPs challenge biogenic natural vesicles (extracellular vesicles, EVs)<sup>120,129</sup> and it has been found as strongly dependent on the concentration of EVs and on the presence of protein contaminant. Therefore, an analytical method for EVs has been developed, offering an easy and fast assay for purity and concentration of EVs, based on nonspecific interactions between NPs and lipid membranes<sup>130–132</sup> (see Fig. 4D).

#### 4. Engineering lipid assemblies: inclusion of NPs in lipid scaffolds

Depending on their molecular structure and on the environmental conditions, lipids in water self-assemble into very

diverse structures, from simple planar lamellar phases, as vesicles, to non-lamellar curved bilayered structures (as cubic mesophases),<sup>133–135</sup> to inverse monolayered tubular arrangements (as inverse hexagonal mesophases). These different structural arrangements, formed by spontaneous self-assembly, can host hydrophilic-coated NPs in the aqueous regions and/or hydrophobic-coated NPs in the hydrophobic domains.

NPs can spontaneously insert in the lipid scaffolds, due to non-specific forces, such as hydrophobic, electrostatic and van der Waals interactions (see Section 2), thus representing a facile approach to obtain a complex hybrid material with controlled structure and defined properties arising from the combination of lipid and NP building blocks.

In particular, the inclusion of NPs in lipid scaffolds allows obtaining materials with specific interesting features: (i) the biocompatibility of the lipid scaffold (dependent on its composition) allows envisioning the employment of these hybrid materials for biomedical applications; (ii) the self-organization and phase behavior of lipid mesophases is generally responsive to the inclusion of external species, to temperature, hydration and other experimental conditions, which variations can be triggered, in a space and time controlled manner, by external stimuli applied to the NPs included in the lipid scaffold (*e.g.*, magnetoliposomes). This is a very interesting opportunity for several applications, for instance the development of drug delivery systems (DDS) with controlled release abilities; (iii) the inclusion and confinement of NPs in lipid scaffolds has the effect to locally concentrate them and to impose them a spatial arrangement. This localized NPs concentration increase might be of relevance to enhance NP-related signals (for instance optical or MRI readout for diagnostic applications); in addition, the increased concentration, together with a defined structural architecture, might induce peculiar collective properties of NPs, arising from the lipid scaffold-imposed arrangement.

In the following sections we will revise this topic, in particular focusing on the effect of NPs inclusion on the overall features of lipid/NP hybrid materials (Section 4.1), and, subsequently, on applicative examples of NP/lipid hybrids made of NPs included in lamellar (Section 4.2) and non-lamellar (Section 4.3) lipid mesophases.

#### 4.1 NPs inclusion in lipid scaffolds: structural and physicochemical effects

The hydrophobic or hydrophilic nature of NPs, which depends on the coating agent, is the key factor in determining the localization in a lipid assembly. Both lamellar (*i.e.*, liposomes, Giant Unilamellar Vesicles) and non-lamellar (*i.e.*, cubic or hexagonal structures) lipid assemblies are characterized by the coexistence of hydrophobic and hydrophilic domains, capable to host NPs of different nature. In all NPs–lipid hybrids, the inclusion of NPs in the lipid architecture affects the physico-chemical and structural properties of the lipid scaffold, modifying for instance the fluidity and bending properties of the membrane, its local thickness, the phase behavior and the viscoelastic properties. For instance, it has been shown that the inclusion

of hydrophobic superparamagnetic iron oxide NPs (SPIONs) in the lipid membrane of DPPC liposomes increases the average thickness of the membrane and modifies the orientation of the phospholipid chains, affecting the lipid melting temperature.<sup>136,137</sup> In addition, depending on the chemical nature of hydrophobic NPs embedded in a lipid bilayer, they can either stabilize or destabilize the lipid ordering, causing opposite effects on the phase behavior of the lipid scaffold; it has been shown that 4 and 5.7 nm AgNPs<sup>31</sup> increase the fluidity of the membrane, reducing the degree of ordering of the lipid tails, while 5 nm maghemite NPs<sup>29</sup> increase membrane rigidity. Finally, the inclusion of nanoparticles can also modify the final structure of the bilayer: for instance, a Cryo-TEM investigation of Chen *et al.* on liposomes containing hydrophobic SPIONs has highlighted the formation of liposomes' aggregates with SPIONs clusters acting as bridging agents (see Fig. 5A and B). These local perturbations highlight that some structural rearrangement of a planar lipid membrane can be possible preserving the overall lipid mesophase architecture; however, as reported by Briscoe *et al.*,<sup>40</sup> significant amounts of NPs inclusion might promote, for defined lipid compositions and specific temperature/pressure conditions, a phase transition from lamellar to hexagonal mesophases. In general, as already pointed out in Section 2, the inclusion of NPs in a planar bilayer increases the frustration packing energy of the lipid molecules eventually promoting the re-organization in a different mesophase, characterized by a more negative curvature; the mismatch between the equilibrium curvature and the perturbed arrangement due to NP inclusion, favors the transition to a more thermodynamically stable structure.

These examples highlight how the effect of NPs on lipid membranes is variable, but possibly predictable, on the basis of minimum energy considerations; therefore, the physico-chemical properties of the target lipid membrane and of the NPs to be inserted in the lipid scaffold can be tuned in order to modify the behavior of the membrane in a desired manner, engineering the system for its final purpose.

#### 4.2 Applications of NPs/lamellar lipid assemblies hybrids

Among hybrid nanostructures where NPs are included in lamellar assemblies, particularly relevant are magnetoliposomes (MLs), where hydrophobic SPIONs are included in the lipid bilayers of lipid vesicles.<sup>138–140</sup> Their responsivity to static (SMF) and alternating magnetic fields (AMF) makes MLs good candidates in nanomedicine as DDS,<sup>141</sup> able to release drugs confined in the lumen of liposomes in a time and space controlled manner, upon application of external stimuli.<sup>142,143</sup> Despite their potentiality, the inclusion of small NPs in the bilayer can be exploited only for drug delivery purposes, while generally, no bulk heating effect can be induced by small NPs subjected to AMFs, as shown in several studies:<sup>144</sup> therefore, they cannot be applied in hyperthermia therapies, for the thermal ablation of cells; however, as reported by Di Corato *et al.*,<sup>145</sup> using hydrophilic SPIONs loaded in the vesicles' lumen combined with a photosensitizer, results in a synergistic effect, observed both *in vitro* and *in vivo*, making this strategy, which exploits a multifunctional

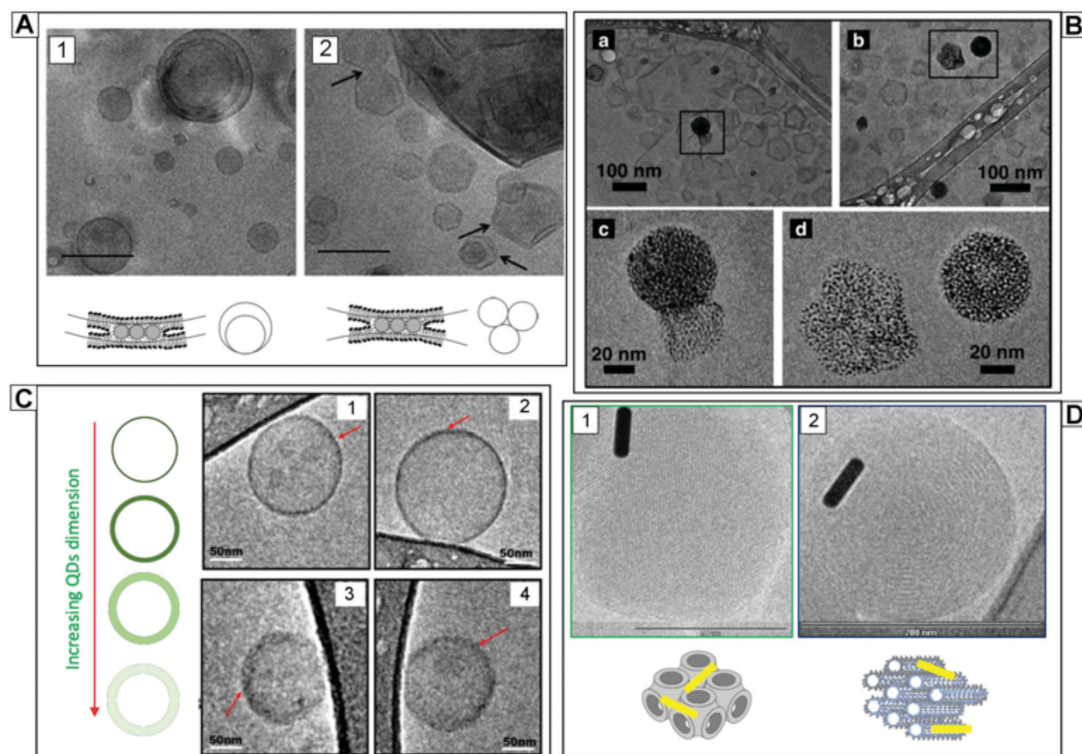


Fig. 5 Cryo-microscopies of lamellar and non-lamellar lipid membranes assembled with hydrophobic NPs. Panel A: cryo-TEM images highlighting the structural changes induced by hydrophobic SPIONs interacting with liposomes: on the left, TEM image showing liposomes arranged in a multiwalled configuration with SPIONs bridging; on the right, TEM image of liposomes' aggregates bridged by SPIONs clusters embedded in the bilayer. Adapted with permission from ref. 29. Copyright (2010) American Chemical Society. Panel B: DPPC liposomes decorated with dodecanethiol-capped AuNPs shown at different magnifications. Adapted with permission from ref. 28. Copyright (2017) American Chemical Society. Panel C: TEM images of POPC/POPE liposomes assembled with quantum dots (QDs) of different sizes embedded in the bilayer. The size increase of QDs (from 1 to 4 progressively) increases the perturbation of the lipid membrane: lipid membrane appears sharp when small QDs are included (1 and 2), while with the larger ones the membrane becomes fuzzier (3 and 4). Reproduced from ref. 150 with permission from The Royal Society of Chemistry. Panel D: cryo-SEM of non-lamellar mesophases interacting with Au NRs. On the left Phytantriol cubic mesophase, on the right Phytantriol hexagonal mesophase, both assembled with Au NRs. Adapted with permission from ref. 156. Copyright (2012) American Chemical Society.

nanomaterial, very promising for therapeutic applications. Recently, MLs decorated both with hydrophobic and hydrophilic SPIONs have been shown to release on-demand hydrophilic or hydrophobic payloads, depending on the frequency and application time of an AMF.<sup>127</sup>

Besides SPIONs, hydrophobic AuNPs were recently used<sup>146</sup> to build-up photoresponsive and thermosensitive hybrid liposomes. In addition, multifunctional hybrid liposomes containing magnetoplasmonic nanoparticles (SPIONs@Au), merging the possibility to combine hypothermic and photothermal treatments were recently shown<sup>147,148</sup> for image-guided delivery of anti-HIV drugs to the brain: generally, the successful delivery of antiretroviral drugs to the brain is limited due to the presence of the blood-brain barrier (BBB); in this case the authors reported an enhanced BBB transmigration efficiency under AMF without its disruption; moreover, the treatment of HIV virus with multifunctional liposomes successfully reduced the viral replication.

Several studies have addressed the inclusion of quantum dots in lipid assemblies: despite their unique optical properties, they are characterized by significant acute cytotoxic effects. With the aim to realize a contrast agent for imaging applications,<sup>138,149,150</sup> several studies have shown that the confinement of CdSe dots in lipid bilayers increases their biocompatibility, while preserving their fluorescence features, making the system more suitable for biomedical applications (see Fig. 5C).

#### 4.3 Applications of NPs/non-lamellar lipid assemblies hybrids

As anticipated in Section 2, the inclusion of NPs into non-lamellar lipid assemblies mostly affects the structure of the mesophase, in terms of the lattice parameter and, consequently, of the diameter of the nanochannels and amount of water contained in the lipid architecture. If the size of NPs is similar or smaller than the lattice parameter, NPs can be easily encapsulated in the architectures. Venugopala *et al.*<sup>38</sup> investigated

the encapsulation of hydrophilic Silica NPs of 8 nm diameter in monolinolein mesophase: in this case, the NPs were too large to be encapsulated in the nanochannels (of 3–3.8 nm diameter); nevertheless, the addition of NPs determined the overall dehydration of the lipid scaffold, eventually causing, for high concentrations, the transition of the assembly geometry to a gyroid cubic structure (*Ia3d*). The authors interpret this behavior considering that, since the energy cost to include the NPs in the nanochannels is extremely high (above  $100k_{\text{B}}T$ ), the NPs tend to minimize their interfacial energy, aggregating along the grain boundaries of the mesophase, similarly to what reported concerning lamellar structures.<sup>151</sup> The same authors investigated also the structural features of monolinolein mesophases loaded with hydrophilic SPIONS. Upon application of a static magnetic field, a reorganization of the lipid domains along the direction of the field<sup>152,153</sup> was found, highlighting how the responsiveness of SPIONS to magnetic fields can be exploited to induce structural modifications in the whole lipid mesophase. This effect has been applied for instance to control the release of drugs confined in the lipid mesophases<sup>152</sup> or, as the same authors reported,<sup>154</sup> for the application in optical memory storage.

The inclusion of hydrophobic NPs in non-lamellar mesophases can be easily achieved exploiting the hydrophobic interactions that spontaneously drive the NPs localization in the hydrophobic regions of the self-assembly. However, also in this case, the size of NPs is of paramount importance, to avoid the disruption of the lipid scaffold. Recently, the inclusion of hydrophobic SPIONS into 1-monoolein diamond cubic phase was reported, highlighting that the amount of included NPs, together with temperature, controls the phase transition from cubic to hexagonal phase. Since this transition is accompanied by a significant dehydration of the mesophase, the structural rearrangement is accompanied by the release of most of the water content of the nanochannels. This thermoresponsive hybrid material was also found to be responsive to AMFs, representing, therefore, a promising system for the delivery of hydrophilic drugs in a time and space-controlled manner.<sup>33</sup> Recently, it was shown that this thermotropic effect of liquid crystalline phases loaded with hydrophobic NPs is a general phenomenon, highlighted also for cubic mesophases formed of phytantriol and hydrophobic AuNPs.<sup>20</sup>

Very few examples in the literature address the inclusion of non-spherical NPs in non-lamellar lipid assemblies: Boyd *et al.*<sup>155</sup> reported on hydrophobic NRs included in phytantriol, selachyl alcohol and monoolein lipid mesophases, with the aim to build-up photo-responsive hybrid materials (see Fig. 5D). The authors investigated the effect of NRs on the cubic mesophases, highlighting a slight reduction in the phase transition temperature and in the lattice parameter. Interestingly, similarly to spherical hydrophobic NPs, gold NRs shift the cubic-to-hexagonal boundaries to lower temperatures.<sup>156</sup> For hexosomes of selachyl alcohol, it was shown that the lattice parameter or water volume fraction<sup>26,27</sup> are not affected by the presence of AuNRs; the authors suggested that NRs are positioned along the direction of hexosomes, but, due to their large sizes

(55.5 nm in length and 16 nm in width) they are in close proximity of the lipid bilayer, without being efficiently included inside it. Nevertheless, the application of a NIR laser on the hybrid structure promoted the phase transition from cubic to hexagonal phase, similarly to what observed with the application of AMF on monoolein-SPIONS hybrids.

## 5. Surface engineering of inorganic NPs: functionalization of NPs with a lipid coating

Recently, several research groups have addressed the functionalization of inorganic NPs or clusters of NPs with lipids to form lipid-coated NPs with a supported lipid bilayer (SLB and liposomes<sup>3</sup>). The validity of this approach is twofold: first, a lipid coating of appropriate composition might strongly improve the biocompatibility of inorganic NPs: this is particularly critical for the very toxic quantum dots. The second advantage is the increased dispersibility in body fluids and improved pharmacokinetic properties. As a matter of fact, without a proper coating, bare NPs introduced by parenteral administration, are rapidly opsonized and removed by phagocytes from the blood stream<sup>54</sup> and accumulated in liver and spleen,<sup>157,158</sup> often causing oxidative stress.<sup>159,160</sup>

Although this could be even convenient for those treatments where the desired aim is to modulate local immune responses,<sup>161</sup> it is worth considering the use of a capping agent that prevents leakage of the drug, protects the carriers from degrading enzymes, and shields them from the immune system avoiding side effects.<sup>162,163</sup> Among several potential capping systems, lipid bilayers are especially advantageous<sup>164</sup> for several reasons: (i) the escape from endosomal vesicles of the nanomaterial and successful reaching of its biological target, upon endocytic uptake, is strongly favoured in the presence of a lipid coating, improving the ability of NPs to passively permeate to the inner core of the cell;<sup>165,166</sup> (ii) the presence of a lipid coating is helpful in preventing NPs aggregation in biological environment; (iii) lipid coating is highly tuneable in composition (for instance PEGylated lipids, to further improve nanoparticle pharmacokinetic properties,<sup>167</sup> can be easily incorporated, as well as cholesterol, added as a controlling fluidity agent) and can be easily functionalized and designed to match the specific requirements of the desired application.<sup>168–170</sup> As introduced in Section 2, the achievement of such a coating depends on the size of the NP to be coated and on the viscoelastic properties of the membrane. Generally, relatively large NPs, imposing a low curvature to the target membrane, can be successfully completely wrapped and coated by a lipid membrane, while small particles need to be wrapped and coated as clusters. In the following sections we will review the most relevant examples and applications of lipid-coated inorganic nanoparticles, considering one by one the different types of nanoparticles, silica NPs (Section 5.1), gold and silver NPs (Section 5.2) and iron oxide NPs (Section 5.3).

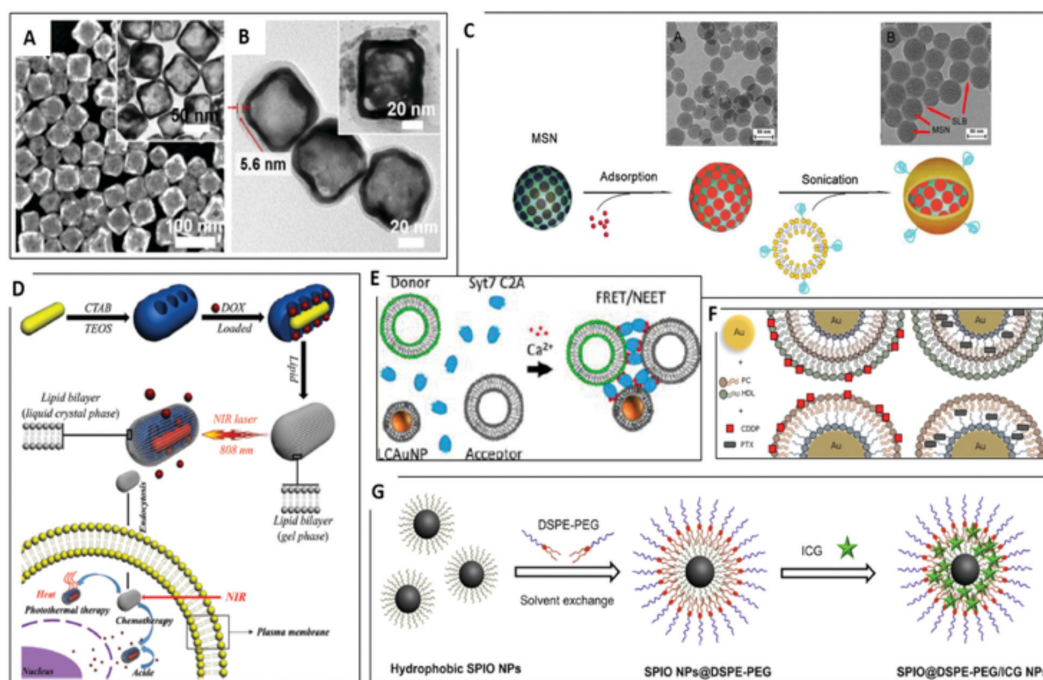


Fig. 6 Lipid-coated NPs. Panel A and B: TEM images of bare Au nanocages (A) and the same nanocages covered by a lipid bilayer (B) used as nanovaccine for cancer immunotherapy. Reprinted with permission from ref. 187 © Elsevier; panel C: schematic overview of the procedure for the fabrication of doxorubicin (DOX)-loaded SLB-mesoporous silica NPs. The thermal responsiveness of the lipids circumvents the premature leakage of the payload. The insets show the related TEM images. Adapted and reprinted with permission from ref. 178 © Elsevier; panel D: schematic illustration of the fabrication process of DOX-AuNR@mSiO<sub>2</sub> covered by a lipid bilayer and the corresponding NIR laser-controlled intracellular DOX release. Reprinted with permission from ref. 192 © RSC; panel E: model of the Ca<sup>2+</sup>-dependent liposome and lipid-coated AuNPs clustering in presence of synaptotagmin (Syt). Reprinted with permission from ref. 185 © ACS; panel F: conceptual scheme of lipid-coated gold carriers for the release of paclitaxel and cisplatin. Reprinted with permission from ref. 183 © Elsevier; panel G: schematic illustration of the preparation protocol of SPION@DSPE-PEG loaded with indocyanine green. Reprinted with permission from ref. 193 © Elsevier.

### 5.1 Lipid-coated silica NPs

Leveraging the pioneering works of Rapuano's group,<sup>171,172</sup> over the last years several research groups have addressed the decoration of silica nanoparticles with SLBs.<sup>173</sup> Recently, Mousseau *et al.* showed an example of fluorescent silica NPs covered by a pulmonary surfactant Curosurf<sup>®</sup>. They found that a complete SLB coverage of silica nanoparticles is obtained only through sonication, which disrupts lipid vesicles and promotes full wrapping of the NPs. *In vitro* assays confirmed that the presence of the SLB mitigated the particle toxicity and improved internalization rates.<sup>174</sup>

Tada and co-workers tested the impact of a lipid coating (using different types of lipid bilayers) on the cytolocalization of silica NPs prepared with methylene blue, for applications in Photodynamic Therapy (PDT).<sup>175,176</sup>

Mackowiak *et al.*<sup>177</sup> showed an example of mesoporous silica NPs surrounded by a cationic DOPC/DOTAP SLB with targeting ligands on the surface of the nanoconstruct and a photosensitizer molecule covalently attached to the surface of mesoporous silica NPs, for controlled and targeted drug delivery applications. In this case, the presence of the SLB coating was also

aimed at improving the capability of the system to retain a drug inside the mesoporous structure of NPs before photoactivation to induce the release of the cargo.

An alternative route to obtain controlled release of drugs from lipid-coated mesoporous silica NPs, based on the use of thermo-responsive lipids, was recently presented by Zhang *et al.*: they combined the high drug loading capacity of mesoporous silica NPs with the thermal responsiveness of a mixture of lipids, DPPC/DSPC/Chol/DSPE-PEG2000, allowing the possibility to release on-demand the payload at hyperthermia temperature, circumventing the premature leakage at physiological temperature<sup>178</sup> (see Fig. 6C).

### 5.2 Lipid-coated gold and silver NPs

Taking advantage of their antimicrobial properties, AgNPs have been widely used in the last decades both in industrial and in biomedical applications.<sup>179–181</sup> Furthermore, due the localized surface plasmon resonance (LSPR) of AgNPs, they can be exploited for the development of biosensors. For this purpose, Bhowmik and co-workers<sup>127</sup> developed a method to determine the conformation of membrane-bound proteins: unlike conventional

SERS, that requires immobilization of molecules, they exploited the spontaneous binding of proteins to lipid bilayer-coated AgNPs. In this way, they probed the behavior of membrane-attached oligomers of Amyloid- $\beta$ 40 (A $\beta$ 40), whose conformation is of relevance in Alzheimer's disease. AuNPs are the most widely studied inorganic NPs, thanks to their facile synthetic and functionalization routes, and their plasmonic properties that can be harnessed in a plethora of applications, ranging from optical imaging, spectroscopy and photothermal therapy. Du *et al.* formed a liposomes–AuNPs hybrid system as a vector for nucleic acids, for applications in gene therapy.<sup>182</sup>

England and co-workers<sup>183,184</sup> (see Fig. 6F) prepared AuNPs functionalized with multiple layers (two or three) of phosphatidylcholine, alkanethiol, high density lipoprotein and phosphatidylcholine/alkanethiol for the delivery of hydrophobic and hydrophilic drugs for the treatment of solid tumours. By exploiting the optical properties of AuNPs, Reed *et al.* developed a novel hybrid for sensitive detection of proteins based on apposition and aggregation of liposomes induced by Ca<sup>2+</sup> ions using Förster resonance energy transfer (FRET) assays<sup>185</sup> (see Fig. 6E). Wang *et al.* recently proposed a novel approach to overcome the low delivery efficiency of plasmids by condensing them on peptide-modified AuNPs, successively covered with a mixture of phospholipids.<sup>186</sup>

In addition to spherical NPs, liposomes-coated gold nanocages<sup>187</sup> (see Fig. 6A and B) have been reported as possible nanovaccines for cancer immunotherapy: the authors demonstrated that the hybrid carrier exhibited enhanced antitumor effects, inhibiting tumour growth in lung metastasis models. In addition, lipid-coated hollow gold nanoshells have been recently developed for synergistic chemotherapy and photothermal therapy for the treatment of pancreatic cancer.<sup>188</sup> By taking advantage of the unique structure of hollow gold nanoshells, the authors successfully demonstrated the co-delivery of two drugs, one loaded in the lipid bilayer and the other one loaded in the hydrophilic interior of the nanoshell.

Furthermore, the possibility to extend lipid coverage to Au NRs has been recently explored. Recent studies have addressed the functionalization of Au NRs with a phospholipid bilayer, composed of POPC<sup>189</sup> and, more recently, DMPC,<sup>190</sup> to increase biocompatibility and bioavailability of NRs. In addition, lipid capped Au NRs (obtained with DPPC vesicles containing lipids with a thiol headgroup) have been demonstrated to be suitable label-free biosensors<sup>191</sup> for the detection of lipophilic drugs in aqueous solutions or lipopeptides in serum. Finally, moving to a more complex architecture, Han *et al.*<sup>192</sup> (see Fig. 6D) demonstrated the possibility to use silica and phospholipids to cover AuNRs, coupling the photothermal and thermo-responsive properties in the same nanoplatform.

### 5.3 Lipid-coated iron oxide NPs

SPIOs are among the most attractive NPs for biomedical applications, ranging from applications in MRI to responsive nanocarriers for drug delivery to therapeutic applications in hyperthermia (see Fig. 6G). Bao *et al.*<sup>193</sup> synthesized DSPE-PEG coated SPIOs loaded with indocyanine green molecules as

superparamagnetic carriers capable to easily accumulate in tumours sites and act as biodegradable nanotheranostic agents. In the emerging field of nanovaccines, the group of Ruiz-de-Angulo<sup>194</sup> presented a biocompatible multifunctional system designed to both act as delivery vehicle and radiotracer for PET/SPECT imaging: using lipid-coated magnetite nanoparticles, they efficiently included in the construct <sup>67</sup>Ga<sup>3+</sup> as radiotracer, plus an antigen and an adjuvant. *In vivo* imaging highlighted the efficient targeting capability of the system and cell uptake. Recently, the same authors presented bacteria-mimicking NPs, that is a similar construct (*i.e.*, lipid coated magnetite nanoparticles), coated with lipooligosaccharides, which efficiently acts as adjuvants<sup>195</sup> for application in cancer vaccine field.

Enveloping a magnetic iron oxide core with a lipid shell facilitates bioconjugation, biocompatibility, and delivery, as well reported by Wang *et al.*<sup>19</sup>: in their work they provide a general solution for coating iron oxide and other metal oxides with a simple mixing in water, facilitating applications in biosensing, separation, and nanomedicine.

A multifunctional system for dual imaging (fluorescence and MRI) of hepatocellular carcinoma was reported by Liang *et al.*<sup>196</sup> through the thin film hydration method, they covered magnetite NPs previously conjugated with a NIR fluorescent dye; the lipid bilayer was decorated with a polymer targeting tumour hepatocytes, able to steer the carrier to the specific site. By flow cytometry and confocal laser scanning microscopy they assessed the specific cellular uptake, followed by *in vivo* tests on tumor-bearing mice.

## 6. Conclusions

In this contribution we have reviewed the latest developments concerning the interaction of NPs with amphiphilic bilayers arranged in lamellar and non-lamellar mesophases.

This area is a very lively research field, where efforts are motivated by several scientific purposes. First of all, the application of nanostructured materials in the biomedical field requires a precise knowledge of the nano-bio-interface: bilayered synthetic assemblies are a very convenient and simple platform to elucidate the interactions with cell membranes and internalization of nanomedical devices. In addition, the design of smart nanostructured hybrid devices, where NPs are included in soft matter assemblies to contribute new properties and modulate their phase diagram is a very relevant and active research field. Related to this latter area is the use of lipid bilayers as coating shells for inorganic nanoparticles, to improve their biocompatibility and interaction with cell membranes.

In all cases, the mechanistic understanding of the main thermodynamic parameters involved in this interaction and their dependence on the physico-chemical features both of NPs and of the bilayers, are a necessary prerequisite to engineer soft matter hybrids and formulate NPs with potential applications in the biomedical field. Soft Matter science represents therefore the central discipline, whose scientific and methodological approaches will be more and more pivotal to contribute

meaningful progresses in this field. If the promises held by this approach will be fulfilled in the next decades, many of the current hurdles that nowadays hamper the full development of nanomedicine can be overcome.

Finally, a precise knowledge of the above-mentioned features allows engineering NPs to probe the properties of complex bilayer assemblies, both of natural and synthetic origin. This is a very exciting and promising area, where fundamental and applied efforts should be directed in the next decade.

## Conflicts of interest

There are no conflicts to declare.

## Acknowledgements

Costanza Montis acknowledges the European Union's Horizon 2020 programme (evFOUNDRY grant agreement 801367). All the authors thank CSGI for financial support.

## References

- C. Lu, Y. Liu, Y. Ying and J. Liu, *Langmuir*, 2017, **33**, 630–637.
- P.-J. J. Huang, F. Wang and J. Liu, *Langmuir*, 2016, **32**, 2458–2463.
- X. Wang, X. Li, H. Wang, X. Zhang, L. Zhang, F. Wang and J. Liu, *Langmuir*, 2019, **35**, 1672–1681.
- F. Wang and J. Liu, *J. Am. Chem. Soc.*, 2015, **137**, 11736–11742.
- F. Wang and J. Liu, *Nanoscale*, 2013, **5**, 12375.
- Y. Liu and J. Liu, *Nanoscale*, 2017, **9**, 13187–13194.
- V. C. Sanchez, A. Jachak, R. H. Hurt and A. B. Kane, *Chem. Res. Toxicol.*, 2012, **25**, 15–34.
- R. Koole, M. M. van Schooneveld, J. Hilhorst, K. Castermans, D. P. Cormode, G. J. Strijkers, C. de Mello Donega, D. Vanmaekelbergh, A. W. Griffioen, K. Nicolay, Z. A. Fayad, A. Meijerink and W. J. M. Mulder, *Bioconjugate Chem.*, 2008, **19**, 2471–2479.
- A. H. Bahrami, M. Raatz, J. Agudo-Canalejo, R. Michel, E. M. Curtis, C. K. Hall, M. Gradzielski, R. Lipowsky and T. R. Weigl, *Adv. Colloid Interface Sci.*, 2014, **208**, 214–224.
- S. Dasgupta, T. Auth and G. Gompper, *J. Phys.: Condens. Matter*, 2017, **29**, 373003.
- X. Chen, F. Tian, X. Zhang and W. Wang, *Soft Matter*, 2013, **9**, 7592.
- Y. Roiter, M. Ornatska, A. R. Rammohan, J. Balakrishnan, D. R. Heine and S. Minko, *Nano Lett.*, 2008, **8**, 941–944.
- C. Contini, M. Schneemilch, S. Gaisford and N. Quirke, *J. Exp. Nanosci.*, 2018, **13**, 62–81.
- Q. Mu, G. Jiang, L. Chen, H. Zhou, D. Fourches, A. Tropsha and B. Yan, *Chem. Rev.*, 2014, **114**, 7740–7781.
- S. Dasgupta, T. Auth and G. Gompper, *Nano Lett.*, 2014, **14**, 687–693.
- A. H. Bahrami, *Soft Matter*, 2013, **9**, 8642.
- F. Wang and J. Liu, *Nanoscale*, 2015, **7**, 15599–15604.
- F. Wang, D. E. Curry and J. Liu, *Langmuir*, 2015, **31**, 13271–13274.
- F. Wang, X. Zhang, Y. Liu, Z. Y. W. Lin, B. Liu and J. Liu, *Angew. Chem., Int. Ed.*, 2016, **55**, 12063–12067.
- X. Liu, X. Li, W. Xu, X. Zhang, Z. Huang, F. Wang and J. Liu, *Langmuir*, 2018, **34**, 6628–6635.
- J. Liu, *Langmuir*, 2016, **32**, 4393–4404.
- T. Pfeiffer, A. De Nicola, C. Montis, F. Carlà, N. F. A. van der Vegt, D. Berti and G. Milano, *J. Phys. Chem. Lett.*, 2019, **10**, 129–137.
- M. Schulz, A. Olubummo and W. H. Binder, *Soft Matter*, 2012, **8**, 4849.
- C. F. Su, H. Merlitz, H. Rabbel and J. U. Sommer, *J. Phys. Chem. Lett.*, 2017, **8**, 4069–4076.
- R. C. Van Lehn and A. Alexander-Katz, *Soft Matter*, 2014, **10**, 648–658.
- M. Mendozza, C. Montis, L. Caselli, M. Wolf, P. Baglioni and D. Berti, *Nanoscale*, 2018, **10**, 3480–3488.
- M. Mendozza, L. Caselli, C. Montis, S. Orazzini, E. Carretti, P. Baglioni and D. Berti, *J. Colloid Interface Sci.*, 2019, **541**, 329–338.
- M. R. Preiss, A. Hart, C. Kitchens and G. D. Bothun, *J. Phys. Chem. B*, 2017, **121**, 5040–5047.
- Y. Chen, A. Bose and G. D. Bothun, *ACS Nano*, 2010, **4**, 3215–3221.
- G. Von White, Y. Chen, J. Roder-Hanna, G. D. Bothun and C. L. Kitchens, *ACS Nano*, 2012, **6**, 4678–4685.
- G. D. Bothun, *J. Nanobiotechnol.*, 2008, **6**, 1–10.
- Z. A. Almsherqi, T. Landh, S. D. Kohlwein and Y. Deng, in *International Review of Cell and Molecular Biology*, Elsevier Inc., 1st edn, 2009, vol. 274, pp. 275–342.
- D. P. Chang, J. Barauskas, A. P. Dabkowska, M. Wadsäter, F. Tiberg and T. Nylander, *Adv. Colloid Interface Sci.*, 2015, **222**, 135–147.
- W. K. Fong, R. Negrini, J. J. Vallooran, R. Mezzenga and B. J. Boyd, *J. Colloid Interface Sci.*, 2016, **484**, 320–339.
- I. W. Hamley, *Angew. Chem.*, 2003, **115**, 1730–1752.
- G. C. Shearman, O. Ces, R. H. Templer and J. M. Seddon, *J. Phys. Condens. Matter*, 2006, **18**, S1105–S1124.
- C. M. Beddoes, C. P. Case and W. H. Briscoe, *Adv. Colloid Interface Sci.*, 2015, **218**, 48–68.
- E. Venugopal, S. K. Bhat, J. J. Vallooran and R. Mezzenga, *Langmuir*, 2011, **27**, 9792–9800.
- M. Szlezak, D. Nieciecka, A. Joniec, M. Pękała, E. Gorecka, M. Emo, M. J. Stébé, P. Krysiński and R. Bilewicz, *ACS Appl. Mater. Interfaces*, 2017, **9**, 2796–2805.
- J. M. Bulpett, T. Snow, B. Quignon, C. M. Beddoes, T.-Y. D. Tang, S. Mann, O. Shebanova, C. L. Pizzey, N. J. Terrill, S. A. Davis and W. H. Briscoe, *Soft Matter*, 2015, **11**, 8789–8800.
- C. M. Beddoes, J. Berge, J. E. Bartenstein, K. Lange, A. J. Smith, R. K. Heenan and W. H. Briscoe, *Soft Matter*, 2016, **12**, 6049–6057.
- C. Montis, B. Castroflorio, M. Mendozza, A. Salvatore, D. Berti and P. Baglioni, *J. Colloid Interface Sci.*, 2015, **449**, 317–326.
- K. L. Chen and G. D. Bothun, *Environ. Sci. Technol.*, 2014, **48**, 873–880.

- 44 M. Henriksen-Lacey, S. Carregal-Romero and L. M. Liz-Marzán, *Bioconjugate Chem.*, 2017, **28**, 212–221.
- 45 E. Rascol, J.-M. Devoisselle and J. Chopineau, *Nanoscale*, 2016, **8**, 4780–4798.
- 46 E. Blanco, H. Shen and M. Ferrari, *Nat. Biotechnol.*, 2015, **33**, 941–951.
- 47 P. Falagan-Lotsch, E. M. Grzincic and C. J. Murphy, *Proc. Natl. Acad. Sci. U. S. A.*, 2016, **113**, 13318–13323.
- 48 C. J. Murphy, A. M. Vartanian, F. M. Geiger, R. J. Hamers, J. Pedersen, Q. Cui, C. L. Haynes, E. E. Carlson, R. Hernandez, R. D. Klaper, G. Orr and Z. Rosenzweig, *ACS Cent. Sci.*, 2015, **1**, 117–123.
- 49 L. J. Fox, R. M. Richardson and W. H. Briscoe, *Adv. Colloid Interface Sci.*, 2018, **257**, 1–18.
- 50 S. Wilhelm, A. J. Tavares, Q. Dai, S. Ohta, J. Audet, H. F. Dvorak and W. C. W. Chan, *Nat. Rev. Mater.*, 2016, **1**, 16014.
- 51 D. Bobo, K. J. Robinson, J. Islam, K. J. Thurecht and S. R. Corrie, *Pharm. Res.*, 2016, **33**, 2373–2387.
- 52 Y. H. Choi and H. K. Han, *J. Pharm. Investig.*, 2018, **48**, 43–60.
- 53 J. M. Caster, A. N. Patel, T. Zhang and A. Wang, *Wiley Interdiscip. Rev.: Nanomed. Nanobiotechnol.*, 2017, **9**, e1416.
- 54 C. D. Walkey and W. C. W. Chan, *Chem. Soc. Rev.*, 2012, **41**, 2780–2799.
- 55 A. E. Nel, L. Mädler, D. Velegol, T. Xia, E. M. V. Hoek, P. Somasundaran, F. Klaessig, V. Castranova and M. Thompson, *Nat. Mater.*, 2009, **8**, 543–557.
- 56 S. Zhang, H. Gao and G. Bao, *ACS Nano*, 2015, **9**, 8655–8671.
- 57 N. S. Bhise, J. Ribas, V. Manoharan, Y. S. Zhang, A. Polini, S. Massa, M. R. Dokmeci and A. Khademhosseini, *J. Controlled Release*, 2014, **190**, 82–93.
- 58 G. Rossi and L. Monticelli, *Biochim. Biophys. Acta, Biomembr.*, 2016, **1858**, 2380–2389.
- 59 V. Pillay, K. Murugan, Y. E. Choonara, P. Kumar, D. Bijukumar and L. C. du Toit, *Int. J. Nanomed.*, 2015, **10**, 2191.
- 60 I. Canton and G. Battaglia, *Chem. Soc. Rev.*, 2012, **41**, 2718.
- 61 M. Calero, L. Gutiérrez, G. Salas, Y. Luengo, A. Lázaro, P. Acedo, M. P. Morales, R. Miranda and A. Villanueva, *Nanomedicine*, 2014, **10**, 733–743.
- 62 S. Behzadi, V. Serpooshan, W. Tao, M. A. Hamaly, M. Y. Alkawareek, E. C. Dreaden, D. Brown, A. M. Alkilany, O. C. Farokhzad and M. Mahmoudi, *Chem. Soc. Rev.*, 2017, **46**, 4218–4244.
- 63 Y. Jiang, S. Huo, T. Mizuhara, R. Das, Y. W. Lee, S. Hou, D. F. Moyano, B. Duncan, X. J. Liang and V. M. Rotello, *ACS Nano*, 2015, **9**, 9986–9993.
- 64 K. A. Dawson, A. Lesniak, F. Fenaroli, M. P. Monopoli, A. Christoffer and A. Salvati, *ACS Nano*, 2012, 5845–5857.
- 65 J. Blechinger, A. T. Bauer, A. A. Torrano, C. Gorzelanny, C. Bräuchle and S. W. Schneider, *Small*, 2013, **9**, 3970–3980.
- 66 S. Tatur, M. MacCarini, R. Barker, A. Nelson and G. Fragneto, *Langmuir*, 2013, **29**, 6606–6614.
- 67 C. Montis, V. Generini, G. Boccalini, P. Bergese, D. Bani and D. Berti, *J. Colloid Interface Sci.*, 2018, **516**, 284–294.
- 68 E. Fröhlich, *Int. J. Nanomed.*, 2012, **7**, 5577–5591.
- 69 J. A. Yang, S. E. Lohse and C. J. Murphy, *Small*, 2014, **10**, 1642–1651.
- 70 E. Lee, H. Jeon, M. Lee, J. Ryu, C. Kang, S. Kim, J. Jung and Y. Kwon, *Sci. Rep.*, 2019, **9**, 2494.
- 71 Y. C. Park, J. B. Smith, T. Pham, R. D. Whitaker, C. A. Sucato, J. A. Hamilton, E. Bartolak-Suki and J. Y. Wong, *Colloids Surf, B*, 2014, **119**, 106–114.
- 72 J. Lin, H. Zhang, V. Morovati and R. Dargazany, *J. Colloid Interface Sci.*, 2017, **504**, 325–333.
- 73 K. P. Garcia, K. Zarschler, L. Barbaro, J. A. Barreto, W. O'Malley, L. Spiccia, H. Stephan and B. Graham, *Small*, 2014, **10**, 2516–2529.
- 74 L. Zhang, H. Xue, C. Gao, L. Carr, J. Wang, B. Chu and S. Jiang, *Biomaterials*, 2010, **31**, 6582–6588.
- 75 N. Gal, A. Lassenberger, L. Herrero-Nogareda, A. Scheberl, V. Charwat, C. Kasper and E. Reimhult, *ACS Biomater. Sci. Eng.*, 2017, **3**, 249–259.
- 76 E. Giovanelli, E. Muro, G. Sitbon, M. Hanafi, T. Pons, B. Dubertret and N. Lequeux, *Langmuir*, 2012, **28**, 15177–15184.
- 77 K. Kaaki, K. Hervé-Aubert, M. Chiper, A. Shkilnyy, M. Soucé, R. Benoit, A. Paillard, P. Dubois, M. L. Saboungi and I. Chourpa, *Langmuir*, 2012, **28**, 1496–1505.
- 78 A. Kraus, L. Wortmann, L. Hermanns, N. Feliu, M. Vahter, S. Stucky, S. Mathur and B. Fadeel, *Nanomedicine*, 2014, **10**, 1421–1431.
- 79 X. Wang, X. Wang, X. Bai, L. Yan, T. Liu, M. Wang, Y. Song, G. Hu, Z. Gu, Q. Miao and C. Chen, *Nano Lett.*, 2019, **19**, 8–18.
- 80 P. Vedantam, G. Huang and T. R. J. Tzeng, *Cancer Nanotechnology*, 2013, **4**, 13–20.
- 81 B. Pelaz, G. Charron, C. Pfeiffer, Y. Zhao, J. M. De La Fuente, X. J. Liang, W. J. Parak and P. Del Pino, *Small*, 2013, **9**, 1573–1584.
- 82 M. P. Monopoli, D. Walczyk, A. Campbell, G. Elia, I. Lynch, F. Baldelli Bombelli and K. A. Dawson, *J. Am. Chem. Soc.*, 2011, **133**, 2525–2534.
- 83 F. Bertoli, D. Garry, M. P. Monopoli, A. Salvati and K. A. Dawson, *ACS Nano*, 2016, **10**, 10471–10479.
- 84 S. Milani, F. Baldelli Bombelli, A. S. Pitek, K. A. Dawson and J. Rädler, *ACS Nano*, 2012, **6**, 2532–2541.
- 85 G. Caracciolo, O. C. Farokhzad and M. Mahmoudi, *Trends Biotechnol.*, 2017, **35**, 257–264.
- 86 A. Lesniak, A. Salvati, M. J. Santos-Martinez, M. W. Radomski, K. A. Dawson and C. Åberg, *J. Am. Chem. Soc.*, 2013, **135**, 1438–1444.
- 87 D. Hühn, K. Kantner, C. Geidel, S. Brandholt, I. De Cock, S. J. H. Soenen, P. Riveragil, J. M. Montenegro, K. Braeckmans, K. Müllen, G. U. Nienhaus, M. Klapper and W. J. Parak, *ACS Nano*, 2013, **7**, 3253–3263.
- 88 W. Lin, T. Insley, M. D. Tuttle, L. Zhu, D. A. Berthold, P. Král, C. M. Rienstra and C. J. Murphy, *J. Phys. Chem. C*, 2015, **119**, 21035–21043.
- 89 C. C. Fleischer and C. K. Payne, *Acc. Chem. Res.*, 2014, **47**, 2651–2659.
- 90 F. Wang, L. Yu, M. P. Monopoli, P. Sandin, E. Mahon, A. Salvati and K. A. Dawson, *Nanomedicine*, 2013, **9**, 1159–1168.

- 91 L. Treuel, S. Brandholt, P. Maffre, S. Wiegele, L. Shang and G. U. Nienhaus, *ACS Nano*, 2014, **8**, 503–513.
- 92 S. Fogli, C. Montis, S. Paccosi, A. Silvano, E. Michelucci, D. Berti, A. Bosi, A. Parenti and P. Romagnoli, *Nanomedicine*, 2017, **12**, 1647–1660.
- 93 R. P. Carney, T. M. Carney, M. Mueller and F. Stellacci, *Biointerphases*, 2012, **7**, 17.
- 94 F. Simonelli, D. Bochicchio, R. Ferrando and G. Rossi, *J. Phys. Chem. Lett.*, 2015, **6**, 3175–3179.
- 95 S. Li and N. Malmstadt, *Soft Matter*, 2013, **9**, 4969.
- 96 A. M. Farnoud and S. Nazemidashtarjandi, *Environ. Sci.: Nano*, 2019, **6**, 13–40.
- 97 A. Šarić and A. Cacciuto, *Soft Matter*, 2013, **9**, 6677–6695.
- 98 K. Jaskiewicz, A. Larsen, D. Schaeffel, K. Koynov, I. Lieberwirth, G. Fytas, K. Landfester and A. Kroeger, *ACS Nano*, 2012, **6**, 7254–7262.
- 99 A. Šarić and A. Cacciuto, *Phys. Rev. Lett.*, 2012, **108**, 118101.
- 100 H. Zhang, Q. Ji, C. Huang, S. Zhang, B. Yuan, K. Yang and Y. Q. Ma, *Sci. Rep.*, 2015, **5**, 10525.
- 101 M. Raatz, R. Lipowsky and T. R. Weigl, *Soft Matter*, 2014, **10**, 3570–3577.
- 102 A. H. Bahrami, R. Lipowsky and T. R. Weigl, *Phys. Rev. Lett.*, 2012, **109**, 188102.
- 103 N. D. Burrows, A. M. Vartanian, N. S. Abadeer, E. M. Grzincic, L. M. Jacob, W. Lin, J. Li, J. M. Dennison, J. G. Hinman and C. J. Murphy, *J. Phys. Chem. Lett.*, 2016, **7**, 632–641.
- 104 S. Nangia and R. Sureshkumar, *Langmuir*, 2012, **28**, 17666–17671.
- 105 R. Vácha, F. J. Martinez-Veracoechea and D. Frenkel, *Nano Lett.*, 2011, **11**, 5391–5395.
- 106 Y. Qiu, Y. Liu, L. Wang, L. Xu, R. Bai, Y. Ji, X. Wu, Y. Zhao, Y. Li and C. Chen, *Biomaterials*, 2010, **31**, 7606–7619.
- 107 A. Espinosa, A. K. A. Silva, A. Sánchez-Iglesias, M. Grzelczak, C. Péchoux, K. Desboeufs, L. M. Liz-Marzán and C. Wilhelm, *Adv. Healthcare Mater.*, 2016, **5**, 1040–1048.
- 108 H. I. Ingólfsson, M. N. Melo, F. J. Van Eerden, C. Arnarez, C. A. Lopez, T. A. Wassenaar, X. Periole, A. H. De Vries, D. P. Tieleman and S. J. Marrink, *J. Am. Chem. Soc.*, 2014, **136**, 14554–14559.
- 109 T. Lunnoo, J. Assawakhajornsak and T. Puangmali, *J. Phys. Chem. C*, 2019, **123**, 3801–3810.
- 110 M. Laurencin, T. Georgelin, B. Malezieux, J. M. Siaugue and C. Ménager, *Langmuir*, 2010, **26**, 16025–16030.
- 111 B. Wang, L. Zhang, S. C. Bae and S. Granick, *Proc. Natl. Acad. Sci. U. S. A.*, 2008, **105**, 18171–18175.
- 112 G. D. Bothun, N. Ganji, I. A. Khan, A. Xi and C. Bobba, *Langmuir*, 2017, **33**, 353–360.
- 113 T. Róg, M. Pasenkiewicz-Gierula, I. Vattulainen and M. Karttunen, *Biochim. Biophys. Acta, Biomembr.*, 2009, **1788**, 97–121.
- 114 E. S. Melby, A. C. Mensch, S. E. Lohse, D. Hu, G. Orr, C. J. Murphy, R. J. Hamers and J. A. Pedersen, *Environ. Sci. Nano*, 2016, **3**, 45–55.
- 115 D. Hartono, Hody, K.-L. Yang and L.-Y. Lanry Yung, *Biomaterials*, 2010, **31**, 3008–3015.
- 116 F. Lolicato, L. Joly, H. Martinez-Seara, G. Fragneto, E. Scoppola, F. Baldelli Bombelli, I. Vattulainen, J. Akola and M. Maccarini, *Small*, 2019, **15**, 1805046.
- 117 R. Michel, E. Kesselman, T. Plostica, D. Danino and M. Gradzielski, *Angew. Chem., Int. Ed.*, 2014, **53**, 12266.
- 118 S. Zhang, A. Nelson and P. A. Beales, *Langmuir*, 2012, **28**, 12831–12837.
- 119 S. Chakraborty, A. Abbasi, G. D. Bothun, M. Nagao and C. L. Kitchens, *Langmuir*, 2018, **34**, 13416–13425.
- 120 C. Montis, A. Zandrini, F. Valle, S. Busatto, L. Paolini, A. Radeghieri, A. Salvatore, D. Berti and P. Bergese, *Colloids Surfaces B Biointerfaces*, 2017, **158**, 331–338.
- 121 C. Montis, D. Maiolo, I. Alessandri, P. Bergese and D. Berti, *Nanoscale*, 2014, **6**, 6452–6457.
- 122 J. C. Black, P. P. Cheney, T. Campbell and M. K. Knowles, *Soft Matter*, 2014, **10**, 2016–2023.
- 123 Y. Liu, R. Medda, Z. Liu, K. Galior, K. Yehl, J. P. Spatz, E. A. Cavalcanti-Adam and K. Salaita, *Nano Lett.*, 2014, **14**, 5539–5546.
- 124 G. H. Zan, J. A. Jackman, S.-O. Kim and N.-J. Cho, *Small*, 2014, **10**, 4828–4832.
- 125 O. Limaj, D. Etezadi, N. J. Wittenberg, D. Rodrigo, D. Yoo, S. H. Oh and H. Altug, *Nano Lett.*, 2016, **16**, 1502–1508.
- 126 K. Suga, T. Yoshida, H. Ishii, Y. Okamoto, D. Nagao, M. Konno and H. Umakoshi, *Anal. Chem.*, 2015, **87**, 4772–4780.
- 127 D. Bhowmik, K. R. Mote, C. M. MacLaughlin, N. Biswas, B. Chandra, J. K. Basu, G. C. Walker, P. K. Madhu and S. Maiti, *ACS Nano*, 2015, **9**, 9070–9077.
- 128 K. Sugikawa, T. Kadota, K. Yasuhara and A. Ikeda, *Angew. Chem., Int. Ed.*, 2016, **55**, 4059–4063.
- 129 C. Montis, S. Busatto, F. Valle, A. Zandrini, A. Salvatore, Y. Gerelli, D. Berti and P. Bergese, *Adv. Biosyst.*, 2018, **2**, 1700200.
- 130 D. Maiolo, L. Paolini, G. Di Noto, A. Zandrini, D. Berti, P. Bergese and D. Ricotta, *Anal. Chem.*, 2015, **87**, 4168–4176.
- 131 S. Busatto, A. Giacomini, C. Montis, R. Ronca and P. Bergese, *Anal. Chem.*, 2018, **90**, 7855–7861.
- 132 A. Mallardi, N. Nuzziello, M. Liguori, C. Avolio and G. Palazzo, *Colloids Surf., B*, 2018, **168**, 134–142.
- 133 J. Zhai, C. Fong, N. Tran and C. J. Drummond, *ACS Nano*, 2019, **13**, 6178–6206.
- 134 R. Mezzenga, J. M. Seddon, C. J. Drummond, B. J. Boyd, G. E. Schröder-Turk and L. Sagalowicz, *Adv. Mater.*, 2019, 1900818.
- 135 H. M. G. Barriga, M. N. Holme and M. M. Stevens, *Angew. Chem., Int. Ed.*, 2019, **58**, 2958–2978.
- 136 A. Salvatore, C. Montis, D. Berti and P. Baglioni, *ACS Nano*, 2016, **10**, 7749–7760.
- 137 O. Bixner and E. Reimhult, *J. Colloid Interface Sci.*, 2016, **466**, 62–71.
- 138 R. Martínez-González, J. Estelrich and M. A. Busquets, *Int. J. Mol. Sci.*, 2016, **17**, 1–14.
- 139 B. Drasler, P. Budime Santhosh, D. Drobne, M. Erdani Kreft, S. Kralj, D. Makovec and N. Poklar Ulrih, *Int. J. Nanomed.*, 2015, **10**, 6089.

- 140 S. Saesoo, S. Sathornsumetee, P. Anekwiang, C. Treetidnipa, P. Thuwajit, S. Bunthot, W. Maneeprakorn, L. Maurizi, H. Hofmann, R. U. Rungsardthong and N. Saengkrit, *Colloids Surf., B*, 2018, **161**, 497–507.
- 141 E. Amstad, J. Kohlbrecher, E. Müller, T. Schweizer, M. Textor and E. Reimhult, *Nano Lett.*, 2011, **11**, 1664–1670.
- 142 S. Nappini, S. Fogli, B. Castroflorio, M. Bonini, F. Baldelli Bombelli and P. Baglioni, *J. Mater. Chem. B*, 2016, **4**, 716–725.
- 143 J. Haša, J. Hanuš and F. Štěpánek, *ACS Appl. Mater. Interfaces*, 2018, **10**, 20306–20314.
- 144 P. Pradhan, J. Giri, F. Rieken, C. Koch, O. Mykhaylyk, M. Döblinger, R. Banerjee, D. Bahadur and C. Plank, *J. Controlled Release*, 2010, **142**, 108–121.
- 145 R. Di Corato, G. Béalle, J. Kolosnjaj-Tabi, A. Espinosa, O. Clément, A. K. A. Silva, C. Ménager and C. Wilhelm, *ACS Nano*, 2015, **9**, 2904–2916.
- 146 A. K. Rengan, A. B. Bukhari, A. Pradhan, R. Malhotra, R. Banerjee, R. Srivastava and A. De, *Nano Lett.*, 2015, **15**, 842–848.
- 147 A. Tomitaka, H. Arami, Z. Huang, A. Raymond, E. Rodriguez, Y. Cai, M. Febo, Y. Takemura and M. Nair, *Nanoscale*, 2018, **10**, 184–194.
- 148 M. E. Khosroshahi, L. Ghazanfari, Z. Hassannejad and S. Lenhart, *J. Nanomed. Nanotechnol.*, 2015, **6**, 298.
- 149 R. B. Lira, M. A. B. L. Seabra, A. L. L. Matos, J. V. Vasconcelos, D. P. Bezerra, E. De Paula, B. S. Santos and A. Fontes, *J. Mater. Chem. B*, 2013, **1**, 4297–4305.
- 150 M. Wlodek, M. Kolasinska-Sojka, M. Szuwarzynski, S. Kereiche, L. Kovacic, L. Zhou, L. Islas, P. Warszynski and W. H. Briscoe, *Nanoscale*, 2018, **10**, 17965–17974.
- 151 J. B. Marlow, M. J. Pottage, T. M. McCoy, L. De Campo, A. Sokolova, T. D. M. Bell and R. F. Tabor, *Phys. Chem. Chem. Phys.*, 2018, **20**, 16592–16603.
- 152 J. J. Vallooran, R. Negrini and R. Mezzenga, *Langmuir*, 2013, **29**, 999–1004.
- 153 J. J. Vallooran, S. Handschin, S. Bolisetty and R. Mezzenga, *Langmuir*, 2012, **28**, 5589–5595.
- 154 J. J. Vallooran, S. Bolisetty and R. Mezzenga, *Adv. Mater.*, 2011, **23**, 3932–3937.
- 155 W. K. Fong, T. L. Hanley, B. Thierry, A. Tilley, N. Kirby, L. J. Waddington and B. J. Boyd, *Phys. Chem. Chem. Phys.*, 2014, **16**, 24936–24953.
- 156 W. K. Fong, T. L. Hanley, B. Thierry, N. Kirby, L. J. Waddington and B. J. Boyd, *Langmuir*, 2012, **28**, 14450–14460.
- 157 S. M. Moghimi, A. C. Hunter and T. L. Andresen, *Annu. Rev. Pharmacol. Toxicol.*, 2011, **52**, 481–503.
- 158 S. Mitravotri and J. Lahann, *Adv. Mater.*, 2012, **24**, 3717–3723.
- 159 W. H. De Jong, W. I. Hagens, P. Krystek, M. C. Burger, A. J. A. M. Sips and R. E. Geertsma, *Biomaterials*, 2008, **29**, 1912–1919.
- 160 P. Aggarwal, J. B. Hall, C. B. McLeland, M. A. Dobrovolskaia and S. E. McNeil, *Adv. Drug Delivery Rev.*, 2009, **61**, 428–437.
- 161 T. A. Wynn, A. Chawla and J. W. Pollard, *Nature*, 2013, **496**, 445–455.
- 162 B. Illes, P. Hirschle, S. Barnert, V. Cauda, S. Wuttke and H. Engelke, *Chem. Mater.*, 2017, **29**, 8042–8046.
- 163 K. Raemdonck, K. Braeckmans, J. Demeester and S. C. De Smedt, *Chem. Soc. Rev.*, 2014, **43**, 444–472.
- 164 A. Luchini and G. Vitiello, *Front. Chem.*, 2019, **7**, 1–16.
- 165 M. E. Davis, Z. Chen and D. M. Shin, *Nat. Rev. Drug Discovery*, 2008, **7**, 771–782.
- 166 N. Kamaly, Z. Xiao, P. M. Valencia, A. F. Radovic-Moreno and O. C. Farokhzad, *Chem. Soc. Rev.*, 2012, **41**, 2971.
- 167 Z. Shen, H. Ye, M. Kröger and Y. Li, *Phys. Chem. Chem. Phys.*, 2017, **19**, 13294–13306.
- 168 A. Luchini, R. K. Heenan, L. Paduano and G. Vitiello, *Phys. Chem. Chem. Phys.*, 2016, **18**, 18441–18449.
- 169 T. M. Allen and P. R. Cullis, *Adv. Drug Delivery Rev.*, 2013, **65**, 36–48.
- 170 E. Terreno, F. Uggeri and S. Aime, *J. Controlled Release*, 2012, **161**, 328–337.
- 171 R. Rapuano and A. M. Carmona-Ribeiro, *J. Colloid Interface Sci.*, 1997, **193**, 104–111.
- 172 R. Rapuano and A. M. Carmona-Ribeiro, *J. Colloid Interface Sci.*, 2000, **226**, 299–307.
- 173 A. L. Troutier and C. Ladavière, *Adv. Colloid Interface Sci.*, 2007, **133**, 1–21.
- 174 F. Mousseau, C. Puisney, S. Mornet, R. Le Borgne, A. Vacher, M. Airiau, A. Baeza-Squiban and J. F. Berret, *Nanoscale*, 2017, **9**, 14967–14978.
- 175 L. M. Rossi, P. R. Silva, L. L. R. Vono, A. U. Fernandes, D. B. Tada and M. S. Baptista, *Langmuir*, 2008, **24**, 12534–12538.
- 176 D. B. Tada, E. Suraniti, L. M. Rossi, C. A. P. Leite, C. S. Oliveira, T. C. Tumolo, R. Calemczuk, T. Livache and M. S. Baptista, *J. Biomed. Nanotechnol.*, 2014, **10**, 519–528.
- 177 S. A. Mackowiak, A. Schmidt, V. Weiss, C. Argyo, C. Von Schirnding, T. Bein and C. Bräuchle, *Nano Lett.*, 2013, **13**, 2576–2583.
- 178 Q. Zhang, X. Chen, H. Shi, G. Dong, M. Zhou, T. Wang and H. Xin, *Colloids Surf., B*, 2017, **160**, 527–534.
- 179 S. Chernousova and M. Epple, *Angew. Chem., Int. Ed.*, 2013, **52**, 1636–1653.
- 180 R. R. Arvizo, S. Bhattacharyya, R. A. Kudgus, K. Giri, R. Bhattacharya and P. Mukherjee, *Chem. Soc. Rev.*, 2012, **41**, 2943.
- 181 L. Cheng, M. D. Weir, H. H. K. Xu, J. M. Antonucci, N. J. Lin, S. Lin-Gibson, S. M. Xu and X. Zhou, *J. Biomed. Mater. Res., Part B*, 2012, **100**, 1378–1386.
- 182 B. Du, L. Tian, X. Gu, D. Li, E. Wang and J. Wang, *Small*, 2015, **11**, 2333–2340.
- 183 C. G. England, A. M. Gobin and H. B. Frieboes, *Eur. Phys. J. Plus*, 2015, **130**, 231.
- 184 H. Frieboes, C. England, T. Priest, G. Zhang, X. Sun, D. Patel, L. McNally, V. van Berkel and A. Gobin, *Int. J. Nanomed.*, 2013, 3603.
- 185 D. J. Hamilton, M. D. Coffman, J. D. Knight and S. M. Reed, *Langmuir*, 2017, **33**, 9222–9230.
- 186 P. Wang, L. Zhang, W. Zheng, L. Cong, Z. Guo, Y. Xie, L. Wang, R. Tang, Q. Feng, Y. Hamada, K. Gonda, Z. Hu,

- X. Wu and X. Jiang, *Angew. Chem., Int. Ed.*, 2018, **57**, 1491–1496.
- 187 R. Liang, J. Xie, J. Li, K. Wang, L. Liu, Y. Gao, M. Hussain, G. Shen, J. Zhu and J. Tao, *Biomaterials*, 2017, **149**, 41–50.
- 188 B. K. Poudel, B. Gupta, T. Ramasamy, R. K. Thapa, S. Pathak, K. T. Oh, J. H. Jeong, H. G. Choi, C. S. Yong and J. O. Kim, *Colloids Surf., B*, 2017, **160**, 73–83.
- 189 C. J. Orendorff, T. M. Alam, D. Y. Sasaki, B. C. Bunker and J. A. Voigt, *ACS Nano*, 2009, **3**, 971–983.
- 190 P. B. Santhosh, N. Thomas, S. Sudhakar, A. Chadha and E. Mani, *Phys. Chem. Chem. Phys.*, 2017, **19**, 18494–18504.
- 191 E. T. Castellana, R. C. Gamez and D. H. Russell, *J. Am. Chem. Soc.*, 2011, **133**, 4182–4185.
- 192 X. Cui, W. Cheng and X. Han, *J. Mater. Chem. B*, 2018, **6**, 8078–8084.
- 193 Y. Ma, S. Tong, G. Bao, C. Gao and Z. Dai, *Biomaterials*, 2013, **34**, 7706–7714.
- 194 A. Ruiz-De-Angulo, A. Zabaleta, V. Gómez-Vallejo, J. Llop and J. C. Mareque-Rivas, *ACS Nano*, 2016, **10**, 1602–1618.
- 195 G. Traini, A. Ruiz-de-Angulo, J. B. Blanco-Canosa, K. Zamacola Bascarán, A. Molinaro, A. Silipo, D. Escors and J. C. Mareque-Rivas, *Small*, 2019, **15**, 1803993.
- 196 J. Liang, X. Zhang, Y. Miao, J. Li and Y. Gan, *Int. J. Nanomed.*, 2017, **12**, 2033–2044.
- 197 A. Torchi, F. Simonelli, R. Ferrando and G. Rossi, *ACS Nano*, 2017, **11**, 12553–12561.

# Paper IV



**Phase transition induced ordering of SPIONs liquid crystalline lipid mesophases**

*Marco Mendoza, Beatrice Muzzi, Alessandra Toti, Lucrezia Caselli, Costanza Montis, Tommaso Mello, Claudia Innocenti, Claudio Sangregorio, Lorenzo Di Cesare Mannelli and Debora Berti\**

M. Mendoza, L. Caselli, Dr. C. Montis, Prof. D. Berti  
Department of chemistry “Ugo Schiff” and CSGI  
University of Florence  
Sesto Fiorentino (FI), 50019, Italy  
E-mail: [debora.berti@unifi.it](mailto:debora.berti@unifi.it)

B. Muzzi  
Department of Biotechnology, Chemistry and Pharmacy, University of Siena 1240, I-53100  
Siena, Italy  
I.C.C.O.M. - C.N.R., I-50019 Sesto Fiorentino (FI), Italy

Dr. C. Innocenti  
I.C.C.O.M. - C.N.R., I-50019 Sesto Fiorentino (FI), Italy  
Department of Chemistry “U. Schiff”, University of Florence, I-50019 Sesto Fiorentino (FI), Italy

Dr. C. Sangregorio  
I.C.C.O.M. - C.N.R., I-50019 Sesto Fiorentino (FI), Italy  
Department of Chemistry “U. Schiff”, University of Florence and INSTM, I-50019 Sesto Fiorentino (FI), Italy

Dr. A. Toti, Dr. T. Mello, Dr. L. D. C. Mannelli  
Dipartimento di Neuroscienze, Psicologia, Area del Farmaco e Salute del Bambino  
University of Florence  
Firenze, 50019, Italy

Keywords: SPIONs, lipids, cubosomes, nanoparticles, functional materials

Hybrid smart materials composed by magnetic nanoparticles encapsulated in lipid membranes, allow the realization of functional systems appealing in the biomedical field as drug delivery vehicles. SPIONs inclusion in the lipid membrane modifies the hierarchical organization of mesophases preserving the responsiveness of magnetic NPs upon an oscillating magnetic field. The coexistence of both hydrophobic and hydrophilic domains, combined with the responsiveness of the materials to the nanoscale level, make of the modified functional materials controllable with an ON-OFF mechanism, the release of active molecules with different polarity. The magnetic features of SPIONs doping GMO LCs were

investigated, correlating the results to the structure, investigate through Small Angle X-Ray Scattering. In-Situ Detection of magnetocubosomes upon an alternate magnetic field to the Synchrotron radiation source was performed, showing a transition from the diamond cubic phase to hexagonal array induced by the local hyperthermia feature of loaded SPIONs. Finally, after an evaluation of the internalization time of cubosomes and magnetocubosome performed through Confocal Microscopy, the in-vitro test experiments on HT29 adenocarcinoma cancer cells were performed, and the cell viability revealed with a colorimetric assay.

### **1. Introduction**

Magnetic nanoparticles (MNPs) provide stimuli-responsive multifunctional platforms with well-explored applications in the biomedical field as contrast agents in MRI<sup>[1-3]</sup> and drug delivery system (DDS).<sup>[4,5]</sup> The hyperthermia features showed exposing MNPs to an oscillating magnetic field, were exploited to trigger the release of active molecules with a higher efficiency dependent by the chemical composition, the dimension and the anisotropy of NPs' shape. In the latter case, as reported by Di Corato et al.<sup>[6,7]</sup> the final shape of nanocrystals, controlled during their synthesis, can be a helpful approach to improve the hyperthermia efficiency. However, controlling the supra-particles organization, as predicted and demonstrated by theoretical and experimental works,<sup>[8-10]</sup> improvement of the thermal efficiency can be achieved. These features, combined with molecular compounds used to functionalize MNPs, could exert a highly localized action on cancer cells: with high amplitude (H) and low frequency (f) of oscillating field respecting the biological exposure safety limit Hf factor, the highest ability of magnetic systems is reached.<sup>[11]</sup>

The inclusion of MNPs in lipid membranes provides a smart strategy to assemble complex structures coexisting with nanocrystals; in this way, due to the high fusogenic tendency of lipid-architectures with cell membranes<sup>[12]</sup>, a short internalization time is needed leaving a small amount of MNPs outside the cell membranes. According to molecular dynamic

simulations<sup>[13]</sup> and some experimental works reported in literature,<sup>[14–16]</sup> the encapsulation of MNPs in lipid bilayer, is promoted controlling the particle size; generally, a dimension around 6 nm is sufficiently small with respect to the lattice parameter describing the mesophase to embed NPs into the membrane.<sup>[17,18]</sup> The combination of soft matter and inorganic stimuli-responsive nanoparticles are extensively reported in literature, especially about lamellar lipid membrane<sup>[19–22]</sup> and recently about non-lamellar mesophases;<sup>[23,24]</sup> these classes of smart material are of relevance from a technological point of view to build-up new functional materials for the uptake and release of active molecule, with spatial and temporal control upon external stimuli, as demonstrated in a previous work.<sup>[24]</sup> 1-monoolein (GMO) lyotropic liquid crystals are the most reported in the literature due to the biocompatibility and biodegradability; its rich polymorphism, with both hydrophobic and hydrophilic domains, make of GMO assembly the ideal scaffold to encapsulate drugs<sup>[25]</sup> and nucleic acids.<sup>[26–28]</sup> Moreover, the addition of different chemical species to the lipid mesophases provides to control the symmetry of the final structure, as extensively reported, i.e., fatty acids,<sup>[29,30]</sup> photoresponsive molecules,<sup>[31–33]</sup> glycolipids<sup>[34,35]</sup> and only recently hydrophobic nanoparticles.<sup>[23,36]</sup>

In literature are reported some works who demonstrate the high potential of colloidal dispersion of lyotropic liquid crystals (cubosomes) tested on tumor cells;<sup>[37–40]</sup> the extended hydrophobic domains allow the encapsulation of enormous quantity of hydrophobic chemotherapeutic, i.e. Paclitaxel,<sup>[25]</sup> 5-Fluor Uracil<sup>[41]</sup> above their bioavailability in biological fluids offering the unique properties to eliminate or reduce the toxicity of the anti-cancer agents. Indeed, that systems have shown a higher efficiency of the drugs compared to the "free" chemotherapeutic and that make of hybrid lipid-SPIONs systems appealing in the biomedical field as DDs. Nevertheless, on the best of our knowledge, cubosomes SPIONs loaded were never tested on cells even if they were deepen described and characterized in the literature.

In this work, it was studied the magnetic response of bulk and disperse GMO assemblies doped with SPIONs upon the alternate magnetic field. After a complete characterization of SPIONs through SAXS, XRD, SQUID measurements, it was investigated the structure and magnetic features of SPIONs-lipid systems. Then, the in-situ structural change induced by AMF on colloidal dispersion of cubosomes and magnetocubosomes are showed and discussed. Finally, we performed in-vitro test experiments on adenocarcinoma cancer cells HT29 with the aim to demonstrate the biocompatibility of magnetic cubic phases under certain conditions.

## 2. Results and Discussion

### 2.1. SPIONs and Bulk cubic phase

**Figure 1** shows SAXS, XRD, FC-ZFC, and magnetization curve of superparamagnetic nanoparticles synthesized according to a well-defined protocol (See Experimental section 4.1).<sup>[42,43]</sup> The Small-Angle Scattering curve showed in Figure 1a was fitted with SphereSchultz Model by NIST (See Section S.2) where the calculated diameter was around 3.8 nm, and the polydispersity was 0.3; the result of ICP-AES analysis to determine the NPs concentration was 6.22 mg/mL of Fe<sub>3</sub>O<sub>4</sub>. X-ray diffraction pattern (Figure 1b), recorded on nanoparticles powder (See Experimental Section 4.5), shows typical magnetic spinel structure of magnetite ( $Fd\bar{3}m$ ) with a lattice parameter of 0.8397 (1) nm. Moreover, the Rietveld analysis of the pattern shows Fe<sub>3</sub>O<sub>4</sub> NPs an average crystal size of 5(1) nm, this value is , quite close to the SAXS fit one. For the uncoated SPIONs, the data of Magnetization (M) vs. Temperature (T) for the zero field-cooled (ZFC) and field-cooled (FC) cases in Figure 1 c are shown. The average blocking temperature TB is 12.5 K: thus, by the well-known equation derived by the Néel-Brown model, the diameter of spherical nanoparticles was calculated equal to 4.3 nm. Magnetic measurements of Fe<sub>3</sub>O<sub>4</sub> nanoparticles (Figure 1d) indicate that SPIONs are superparamagnetic at 293 K and 320 K, while at 2.5 K, below the blocking temperature, the typical ferromagnetic hysteresis loop can be observed with coercivity value

of 242 Oe. Under a large external field, the magnetization, aligns with the field direction, reaches its saturation value of 39.2 emu/g at 2.5 K, 31.6 emu/g at 293 K and 30.6 emu/g at 320 K. Their size and the responsivity upon the magnetic field make them good candidates to evaluate the magnetotropic behavior when SPIONs are embedded within lipid bilayers, obtaining hybrid materials with tunable magnetic features.

GMO lipid, in water excess, can assemble in diamond cubic mesophase (Pn3m) which is preserved into the investigated temperature range (25-50 °C) as confirmed by the Small-Angle Scattering curves.<sup>[23]</sup> As the temperature increases, a shift to higher scattering vectors ( $q$ ) of SAXS curves was detected, producing a shrinking of water nanochannels. As we can see from **Figure 2**, nanoparticles affect the GMO phase behavior; with 0.26 mM SPIONs, the Pn3m structure is preserved since 35 °C, while with 0.39 mM nanoparticles, the hexagonal array can be observed starting from 25 °C. In agreement with the literature, SPIONs embedded into the lyotropic mesophases, produce a shrinking of water nanochannels compared to the neat binary system.<sup>[23]</sup> The lattice parameters ( $d$ ), describing the lipid assembly, vary in a linear fashion as a function of temperature; in the case of 0.26mM SPIONs the decrease of  $d$  Vs.  $T$  is around  $-0.46 \text{ \AA}/^\circ\text{C}$ , and  $d$  is decrease in absolute value with respect to the GMO/H<sub>2</sub>O system or with systems contain lower amount of SPIONs (See **Figure S3**). Moreover, enhancing the nanoparticles concentration until 0.39 mM SPIONs, the variation of  $d$  Vs.  $T$  is  $-0.12 \text{ \AA}/^\circ\text{C}$ ; these results suggest that nanoparticles stiffen the bulk mesophases in agreement with the model proposed by Mezzenga et al.<sup>[44]</sup> and recent rheological investigation<sup>[36,45]</sup>, a hampered diffusion of lipid located onto the SPIONs was described.<sup>[46]</sup> The SPIONs inclusion in LLCs is confirmed by the insourgence of an additional broad peak in low  $q$  region, which is not ascribable to the Bragg reflexes of the lipid architectures. The  $q$  value of the peak maximum is around  $0.050 \text{ \AA}^{-1}$  in the 0.26 mM SPIONs samples and it is related to the NPs-NPs's average distance by  $q=2\pi/d$  relation, corresponding to a length of 12.5 nm, which perfectly matches the literature.<sup>[24]</sup> Remarkably, a slight shift of

NPs correlation peak to higher scattering vectors can be observed; indeed by increasing the T: indeed, at 50 °C, 0.26 mM SPIONs sample shows a peak around  $0.053 \text{ \AA}^{-1}$  (11.8 nm), which could be related to a structural SPIONs reorganization.

To gain more insights on the magnetic features of bulk mesophases with SPIONs, the variation of magnetization as a function of temperature, was investigated for different structure: in particular, the samples with 0.26 mM and 0.39 mM SPIONs, showing at 25 °C a Pn3m and a H<sub>II</sub> mesophases, respectively, are compared with the results obtained for uncoated nanoparticles. Magnetization of uncoated SPIONs as a function of temperature was recorded at 10 Oe and the result shows a linear decay into the range 20-47 °C, typical of superparamagnetic nanoparticles (see **Figure S1**) in agreement to the well-known Curie Law. **Figure 3** shows the M Vs. T profile for 0.26 mM SPIONs (green and blue line and markers) and 0.39 mM SPIONs (red line and markers) samples. First, a brief discussion about a large number of interactions involved should be taken into account to discuss these results. A change in the magnetization can be detected with a nanoparticles' spatial correlation variation: Van der Waal interactions, electrostatic interactions, steric repulsion, magnetic attraction/repulsion and the relative direction of the magnetic dipoles,<sup>[10]</sup> are the main forces involved in the energetics of the system. Considering hydrophobic nanoparticles entrapped in a highly viscous material, the Brownian relaxation process, which is the main term in nanoparticles dispersion, is negligible to the Néel one, due to the reduced mobility of MNPs in a viscous medium; moreover, due to the hydrophobic nature and the small size of the nanoparticles coating agent, the electrostatic and steric repulsion are negligible. Thus, according to the SAXS data of GMO LLCs, where the phase behavior is affected by nanoparticles, we can hypothesize a reorganization of SPIONs, which are locked into the bilayer, as due to the new structural configuration adopted by the membrane.

In the Pn3m cubic structure assembled with SPIONs (Figure 3a), the magnetization follows a typical linear decay until 32 °C, over which a non-monotonal variation of M can be observed

since 35 °C; a further increase of the temperature produces a decrease with a linear trend until 40 °C, characterized by different scale law. The temperature values are in agreement SAXS profiles, where it is shown (Figure 2) that SPIONs embedded into the LLCs structure promote a transition to the H<sub>II</sub> array. The behavior of LLCs-embedded NPs, following the structural change of the lipid scaffold, significantly deviates by from the one of free SPIONs, due to their lipid-membrane-induced reorganization. Indeed, at 32 °C, it is likely that the provided thermal energy, producing a decrease in the bilayer viscosity with respect to the RT, allows for SPIONs diffusion within the membrane, with a deviation of  $M$  Vs.  $T$  detectable as result. The same experiment was repeated on the same sample after a thermal cycle (green markers and line Figure 3a), with no magnetic transitions observed, highlighting the presence of a hysteresis of the process. However, it should be noted that the green markers and lines of Figure 3a follow the same scalar law of the system after the transition into the 40-45 °C temperature range; it is reasonable to think that, since, as demonstrated in a previous work,<sup>[36]</sup> a recovery of the Pn3m structure after the transition requires long time (3-4 h), the hexagonal structure is thus preserved during the during the experimental time. In order to demonstrate that the magnetic variation is related to the Pn3m-H<sub>II</sub> transition, MO with 0.39 mM SPIONs was investigated (See Figure 3b), and, as can be observed, the red curve displays a typical linear decay without deviation. This suggests that the hump observed in Figure 3a can be associated univocally to the transition of lipid scaffold which drives SPIONs to follow the new arrangement. In a recent study, we observed a peculiar pearl-necklace like organization of SPIONs in dispersed LLCs characterized by an H<sub>III</sub> arrangement;<sup>[23]</sup> however, the details of the reorganization process and the final disposition of SPIONs are still not completely clarified and future studies are required in order to shades some lights on the intriguing behavior of SPIONs during a bilayer transition.

## 2.2 In-Vitro experiments on HT29 cancer cells of Cubosomes and Magnetocubosomes

Pluronic F-127 is the most used block copolymer to disperse LLCs, obtaining water colloidal dispersions of cubosomes, characterized by an average diameter of 200-250 nm<sup>[47]</sup>; poly-ethylene oxide blocks are hydrophilic and strongly interact with the aqueous environment, stabilizing the colloidal particle through steric repulsions, while the polypropylene oxide hydrophobic block is responsible for the anchoring of the stabilizer to the lipid membrane of cubosomes and for a slight modification of the cubic structure. In agreement with the literature<sup>[48]</sup>, structural investigation of cubosomes stabilized by F127 allowed to detect a primitive cubic phase (Im3m) structure characterizing cubosomes, as a difference from the diamond cubic structure observed at the bulk level. The mesophases are more swollen than bulk assemblies, hinting to a larger diameter of the nanochannels. There are some works in the literature about the interaction of cubosomes with cell membranes and their ability to deliver chemotherapeutics for cellular death. In order to prove that cubosomes doped with SPIONs are suitable as DDs, the in-vitro test experiments were performed on tumor cells: on the best of our knowledge, it is the first time that LLCs combined with SPIONs are tested on cells.

HT29 adenocarcinoma colorectal cells have been used to test the capacity of cubosomes to enter into cells. In order to determine the time of internalization,  $1 \times 10^4$  HT29 cells have been incubated in suspension with Octadecyl-Rhodamine B conjugated cubosomes (0.01% mol with respect to the GMO amount) at 0.6  $\mu\text{g/ml}$ , 6  $\mu\text{g/ml}$ , and 60  $\mu\text{g/ml}$  at 37°C. The entrance has been evaluated by confocal microscopy, detecting the fluorescence intensity of the probe encapsulated into the cells after different cubosomes interaction time: 2, 20, and 40 minutes. The best time has been estimated to be 40 minutes at the concentration of 60  $\mu\text{g/ml}$  and the images are reported in **Figure 4**. The advantage of cubosomes with respect to "free" hydrophobic drugs can be related to the low bioavailability in biological fluids of no-

conjugated therapeutics; in fact, the enormous hydrophobic domain allows to efficiently transport a significant amount of drugs (compared to the solubility of the active molecules in bio-fluids) in a relatively short interaction time. Moreover, it is noted in the literature that Pluronic F127, stabilizer agents of cubosomes, presents a typical Enhanced Permeability and Retention effect (EPR),<sup>[49-51]</sup> due to the PEO blocks of the copolymer, allowing localization of dispersed liquid crystals in tumor tissues.

Moreover, the toxicity of cubosomes, magnetocubosomes (0.26 mM SPIONs) and magnetoheosomes (0.39 mM SPIONs) has been evaluated incubating  $2 \times 10^5$  HT29 in suspension with 0.6  $\mu\text{g/ml}$ , 6  $\mu\text{g/ml}$ , and 60  $\mu\text{g/ml}$  of cubosomes, NPs-cubo and NPs-hexo for 40 minutes at 37°C. After incubation, the same volume of each suspension (corresponding to  $2 \times 10^4$  cells of control) has been seeded in cell plate for 48 hours; cell viability has been evaluated by MTT assay (Figure 4b). Results suggest that these colloids are able to be internalized and they are not toxic for cells with that experimental conditions (See SI for details). Since the exposure of NPs-cubo and NPs-hexo to an alternate magnetic field (AMF) should cause an increase of their temperature, HT29 cells have been treated at the higher dose (60  $\mu\text{g/ml}$ ) of cubosomes, NPs-cubo and NPs-hexo for 40 minutes and then they were exposed for 60 minutes to the AMF.

The viability of HT29 cells, plated in MW96 as previously described (based on control sample without AMF), has been assayed after 48 hours in order to evaluate if AMF could cause the death of treated cells. The graph (Figure 4c) doesn't show toxic effect in samples under AMF compared to samples without AMF. These results demonstrate the complete biocompatibility of cubosomes, NPs-cubo and NPs-hexo for their use on human cells in presence of AMF.

Recently Drummond et al. have studied the interaction of cubosomes with Supported Lipid Bilayer (SLB) in order to elucidate the origin of interaction with cells membrane. The results suggest a fusion of cubosomes with biomimetic membranes where, in the beginning, a lipid

exchange of MO molecules with phospholipids composing the SLB can be seen, until complete disappearance of the typical cubosomes structure. Thus, the SPIONs hyperthermia efficiency is lowered with the theoretical and experimental works reported in the literature about the SPIONs pearl-necklace structure. Moreover, in agreement with other works, it is demonstrated that the hyperthermia of small nanoparticles is not enough to induce apoptosis. The effort reported by Di Corato et al. has demonstrated that a synergistic behavior between hyperthermia and other effects (in that case, photosensitizers) is a useful approach to induce cellular death. Analogously to our results, since the efficiency of cubosomes loaded with chemotherapeutic is demonstrated, we retain that cubosomes doped with SPIONs and loaded by bioactive molecules could exert a significant impact on cells.

However, from a physico-chemical point of view, it is of relevance evaluate in simplified conditions, the AMF effects on cubosomes.

Firstly, thermotropic studies on cubosomes, magnetocubosomes (0.26 mM SPIONs) and magnetohexosomes (0.39 mM) were performed into T range of 25-50 °C: data, collected at the Synchrotron Radiation Source, ESRF, Grenoble (France), are not showed in the main text and reported in Supporting Information (**Figure S4**). The investigation provides a reference for the experiments on the in-situ structural change induced by SPIONs loaded in dispersed lyotropic liquid crystals upon AMF. Data reported in Figure 4 show that primitive structure is preserved into the investigated temperature range and a decrease of the lattice parameter is observed by increasing temperature (See **Figure S5**). The insertion of SPIONs within cubosomes modify their phase behavior; a coexistence of both diamond and hexagonal arrangement can be detected for the 0.26 mM SPIONs sample. With respect to the bulk lyotropic liquid crystals containing the same nanoparticles amount, SPIONs dramatically affect the architectures, due probably to a higher surface/volume ratio of the cubosomes dispersion. However, the diamond structure of magnetocubosomes is still present at higher temperatures range and an almost complete Pn3m-H<sub>II</sub> transition is only detectable at around

45-50 °C (See Figure S4). Very interesting are LLCs assembled with 0.39 mM SPIONs where the  $H_{II}$  mesophase is already detectable just to 25 °C: the temperature increase does not produce a significant shift of  $q$  vectors, but the magneto-hexosomes dispersion curves exhibit a slight modification in the low- $q$  region. In particular, the low- $q$  region peak is associated to the nanoparticle's correlation within the lipid scaffold, which is modified up to 45 °C; the promoted Pn3m- $H_{II}$  transition combined with a viscosity's decrease, allows for SPIONs diffusion, giving rise to a supra-particles organization in a pearl-necklace like structure.<sup>[23]</sup> These data are of relevance to evaluate the effect of the alternating magnetic field generated through a broken toroidal solenoid (See Section S5), where the frequency was around 4.55 kHz. In particular, during the experiments a fan to cool down the temperature of the coil was used, to neglect the Joule effect of the magnetic field generator. In that way, the hyperthermia, shown for SPIONs exposed to AMF, is the main term to consider during the investigation (See Section S5 for details). **Figure 5** shows the results of in-situ SAXS experiments of cubosomes and magnetocubosomes upon the oscillating magnetic field. As we can see from Figure 4a, during the application of AMF, no relevant shift of cubosomes Bragg reflexes can be observed; moreover, the intensity of the peaks, compared to the case of cubosomes references as function of the  $T$  (See Figure S4), does not change, suggesting that, with the chosen experimental setup, the temperature reached by the coil is below 37 °C. Comparing the lattice parameter of the beginning, to the  $d$  values of cubosomes calculated from the last SAXS profiles registered, the increase of the temperature is around 2°C which can be justified in terms of a weak Coil Joule Effects. The experiments on magnetocubosomes, performed in the same condition of cubosomes in Figure 4b, shows different behavior. After 90 seconds of AMF applications, the first Bragg reflex starts to shift to higher  $q$  values together with an increase of the intensity of the first Bragg hexagonal reflex. This latter peak becomes progressively higher at 120 sec, and a decrease in the Pn3m reflexes is seen. Finally, at 150 sec, a complete transition is reached, and the diamond cubic structure almost disappears.

Comparing the lattice parameters of magnetocubosomes (Table S4) with the Table S5, the temperature reached by the sample exposed to AMF after 150 sec is around 39 °C that is not enough to induce a phase transition (heating the magnetocubosomes sample, the transition is observed at 41-43 °C). For this reason, we can conclude that, with the experimental setup considered here, no Coil Joule Effect is detectable, or it is negligible, and it does not affect the results, suggesting that the leading term involved in the re-arrangement of the bilayers is the hyperthermia effect produced by nanoparticles. This phase transition, that was observed in a previous work on the bulk cubic mesophases, is preserved on the magneto-colloidal dispersion level; however, comparing the time needed by bulk and dispersed systems to re-arrange in a new architecture, a difference can be highlighted. Indeed, after 10-15 minutes upon AMF, bulk Pn3m structure shows a weak increase of  $I^\circ$  Bragg hexagonal reflex, while after around 3 minutes, a complete transition is detectable for cubosomes.

### 3. Conclusion

In summary, in this work, the magnetic features of lipid liquid crystals combined with SPIONs were investigated in order to apply these hybrids' functional materials in the biomedical field as drug-delivery systems. On bulk cubic phase, after the phase diagram of diamond cubic structure loaded with SPIONs, it was investigated the magnetization term during the increase of the temperature and the results suggest that during the structural change promoted by thermal energy, consequently to a re-arrangement of lipid scaffold, SPIONs change their relative position, interacting in a different way, and observable with an higher value of magnetization. In situ detection of dispersed cubic mesophases were studied on Synchrotron Radiation Source ESRF upon AMF: phase transition Pn3m-H<sub>II</sub> was detected, in analogy to the bulk SPIONs-lipid mesophases. Finally, the MTT test proves the biocompatibility of magnetocubosomes on HT29 cell lines. This work aims to demonstrate

how SPIONs inclusion affects the magnetic properties of lyotropic liquid crystals, how their responsivity can be used in the biomedical field since colloids are biocompatible.

#### 4. Experimental Section

*4.1 materials:* Fe(III)-acetylacetonate (97%), 1,2-hexadecanediol (90%), oleylamine (70%), oleic acid (90%), diphenyl ether (99%), denatured ethanol and hexane mixture of isomers employed for the synthesis of hydrophobic SPIONs, were purchased from Sigma Aldrich (St. Louis MO), the same for 1-oleyl-rac-glycerol (>99.9%) purchased by Sigma Aldrich (St. Louis MO).

*4.2 Synthesis of magnetic nanoparticles:* Iron oxide nanoparticles were synthesized according to the methods used by Wang et al.<sup>[52]</sup> Briefly, 0.71 g Fe(acac)<sub>3</sub> (2 mmol) were dissolved in 20 mL of phenyl ether with 6 mmol of oleic acid (2 mL) and 4 mmol of oleylamine (2 mL) under N<sub>2</sub> atmosphere and vigorous stirring. 1,2-hexadecanediol (2.58g, 10 mmol) was added into the solution. The solution was heated to 210 °C, refluxed for 2 h and then cooled to RT. Ethanol was added to the solution and the precipitate collected, washed with ethanol and dispersed again in 20 mL of hexane in the presence of 75 mM each of oleic acid and oleylamine. In that way, no impurities of salts, or other compound are present in dispersion. Dispersion of the magnetic SPIONs with a hydrophobic coating of oleic acid and oleylamine in hexane are stable; SPIONs were stored in a dark flask with N<sub>2</sub> gas on top in order to prevent the oxidation.

*4.3 Preparation of Bulk and dispersed cubic mesophases:* Bulk cubic phases in absence or in presence of magnetic nanoparticles follows this procedure. First, 30 mg of 1-monoolein was weighted in glass flask of 2 mL with or without the appropriate volume SPIONs dispersion. About 0.5 mL of hexane was added to dissolve lipids and SPIONs, then the mixture was dried

through gentle nitrogen flux, removing the solvent. Lipid or mixture GMO/SPIONs was left under vacuum overnight sheltered by light source. Lipid film was then hydrate with 50  $\mu\text{L}$  of Milli-Q water and sample was then centrifuged alternating a cycle with cap facing upward with another where cap facing downward. Bulk systems were leaved in a dark place for at least 12 h in order to stabilize the system. Cubosomes and SPIONs-loaded cubosomes were prepared following the procedure of bulk mesophase preparation until the dried film under vacuum. Then, 8 mg of Pluronic F-127 were added to the dry films and the mixture was heated in a water bath at 70  $^{\circ}\text{C}$  for 5' to melt the Pluronic F-127 and then vortexed for 5'. Five cycles of heating-vortexing were carried out and then 500  $\mu\text{L}$  of preheated  $\text{H}_2\text{O}$  at 70  $^{\circ}\text{C}$  were added. The dispersion was then sonicated in a bath-sonicator at 59 kHz and 100% of power for 6 h, to homogenize the system.

*4.4 Small Angle X-Ray Scattering:* SAXS measurements were carried out on a S3-MICRO SAXS/WAXS instrument (HECUS GmbH, Graz, Austria) which consists of a GeniX microfocus X-ray Sealed Cu Ka source (Xenocs, Grenoble, France) power 50 W which provides a detector focused X-ray beam with  $k = 0.1542 \text{ nm Cu Ka line}$ . The instrument is equipped with two one-dimensional (1D) position sensitive detectors, (HECUS 1D-PSD-50 M system) each detector is 50 mm long (spatial resolution 54  $\text{lm/channel}$ , 1024 channels) and cover the SAXS q-range ( $0.003 < q < 0.6 \text{ \AA}^{-1}$ ) and the WAXS q-range ( $1.2 < q < 1.9 \text{ \AA}^{-1}$ ). The temperature was controlled by means of a Peltier TCCS-3 Hecus. SAXS curves of bulk cubic phase were recorded at 25-30-35-40-45-50  $^{\circ}\text{C}$  in a solid sample-holder. Dispersion of SPIONs were recorded in a glass capillary.

*4.5 X-Ray Diffractometer:* The structure of the NPs was investigated by X-ray powder diffraction (XRD) using a Bruker New D8 ADVANCE ECO diffractometer equipped with a

Cu K $\alpha$  (1.5406 Å) radiation. The measurements were carried out in the range 20–70°, with a step size of 0.03° and a collection time of 1 s.

*4.6 Magnetic properties:* The magnetic properties of the NPs and bulk phases in absence or in presence of SPIONs were measured using a Quantum Design MPMS SQUID magnetometer. The field was always applied parallel to the pellet plane. The Zero Field Cooled/Field Cooled (ZFC/FC) procedure was performed applying a 5 mT probe field. The magnetization versus temperature measurements were performed in zero-field-cooled (ZFC) condition with a 10 mT probe field.

*4.7 Small Angle X-Ray Scattering Synchrotron Radiation Source:* The source is located at a high- $\beta$  section of the storage ring. Two undulators U21.4 and one U35 provide high photon flux with a low divergence. The beamline optics consist of a cryogenic (liquid nitrogen) cooled Si-111 channel-cut monochromator and a double mirror focusing setup. The standard beam size is 40  $\mu\text{m}$  x 600  $\mu\text{m}$  (vertical and horizontal, respectively) with divergence of 20  $\mu\text{rad}$  x 30  $\mu\text{rad}$ . The beamline is optimized for experiments using a fixed wavelength around 0.1 nm (12.4 keV). The SAXS signal was collected with a Pilatus 300 K detector. The experiments were performed in glass capillary with a diameter 1.5 mm. Of each sample, it was registered the background. Thermic behavior of colloidal dispersion of cubosomes and magnetocubosomes were carried out through thermostat from 25 °C to 49 °C increasing the temperature of 2 °C each step. Equilibration time at each temperature was 5 minutes. In-situ structural detection upon AMF was performed as in the setup showed in Supporting Information.

*4.8 Low Frequency Alternate Magnetic Field (LF-AMF):* A sinusoidal magnetic field was generated in the gap of a broken toroidal magnet carrying a solenoid through which an alternating electric current (AC) from a tone generator was led. The samples to be treated with

LF-AMF were placed in the middle of the gap with a Teflon sample holder. Due to the design of the experimental apparatus, the magnetic field inside the cell is not isotropic. During the experiments, the field frequency was set at 4.22 kHz. Magnetic field values of magnet range from 100-330 mT.

*4.9 Cell Culture:* Colorectal adenocarcinoma cancer cells HT29 were purchased from European Collection of Cell Culture (ECACC). Cells were routinely cultured in Dulbecco's Modified Eagle's Medium (DMEM) – high glucose (4500mg/L) supplemented with 2 mM glutamine, with penicillin (100 U/mL) and streptomycin (100 µg/mL), and with 10% fetal bovine serum (FBS, Euroclone). Cells were incubated at 37°C in a humidified atmosphere of 5% CO<sub>2</sub>- 95% air.

*4.10 Cubosomes internalization assay:*  $1 \times 10^4$  colorectal adenocarcinoma cells HT29 were plated and 24 hours later were treated with culture medium in presence or absence of different concentrations (0.6 µg/ml, 6 µg/ml, and 60 µg/ml) of octadecyl-rhodamine conjugated cubosomes loaded with 190 µl SPIONs. Cells were incubated 2, 20 and 40 minutes at 37°C in humidified 5% CO<sub>2</sub> atmosphere and then were washed with PBS 1x and imaged with a Leica AM 6000 microscope equipped with a DFC350FX camera and 40x 0.60NA air objective. All images were equally adjusted for display purposes using Fiji-Image J smart LUT.<sup>[53]</sup>

*4.11 Incubation with Cubosomes and SPIONs-loaded Cubosomes:*  $2 \times 10^5$  cells for each condition were incubated in suspension with different concentration (0.6 µg/ml, 6 µg/ml, and 60 µg/ml) of cubosomes, magnetocubosomes (NPs-cubo) and magnetohehexosomes (NPs-hexo), for 40 minutes at 37 °C and 5% CO<sub>2</sub> to allow the internalization of the molecules. In order to evaluate their toxicity, the same volume of each suspension (corresponding to  $2 \times 10^4$  cells of control) has been seeded in MW96 in triplicates for 48 hours and cell viability

has been assayed. Otherwise, in order to evaluate the effect of the AMF, cells were exposed to the alternate magnetic field for 30 minutes after the internalization.

*4.12 Cell viability assay:* 5mM MTT (3-(4,5-Dimethylthiazol- 2-yl)-2,5-diphenyltetrazolium bromide (Sigma) was added to cells and incubated for 1h at 37°C. Cells were suspended in 200 µL of Dimethyl sulfoxide: wavelength measuring was performed at 595 nm using a spectrophotometer.

### Supporting Information

Supporting Information is available from the Wiley Online Library or from the author.

### Acknowledgements

Costanza Montis acknowledges the European Union's Horizon 2020 program (evFOUNDRY grant agreement 801367). Marco Mendoza, Lucrezia Caselli, Dr. Costanza Montis, and Prof. Debora Berti acknowledge CSGI for financial support. Prof. Marcello Carlà and Dr. Giovanni Domenico Aloisi are acknowledged to furnish the magnetic field generator. All the authors acknowledge Dr. Francesco Tadini, Martin Albino, Elena Trallori, and Marco Tintori for the in-vitro test experiments. Beatrice Muzzi and Dr. Alessandra Toti equally contributed to this work.

Received: ((will be filled in by the editorial staff))

Revised: ((will be filled in by the editorial staff))

Published online: ((will be filled in by the editorial staff))

### References

- [1] M. S. Martina, J. P. Fortin, C. Ménager, O. Clément, G. Barratt, C. Grabielle-Madelmont, F. Gazeau, V. Cabuil, S. Lesieur, *J. Am. Chem. Soc.* **2005**, *127*, 10676.
- [2] K. Yang, Y. Liu, Y. Liu, Q. Zhang, C. Kong, C. Yi, Z. Zhou, Z. Wang, G. Zhang, Y. Zhang, N. M. Khashab, X. Chen, Z. Nie, *J. Am. Chem. Soc.* **2018**, *140*, 4666.
- [3] N. Tran, N. Bye, B. A. Moffat, D. K. Wright, A. Cuddihy, T. M. Hinton, A. M. Hawley, N. P. Reynolds, L. J. Waddington, X. Mulet, A. M. Turnley, M. C. Morganti-Kossmann, B. W. Muir, *Mater. Sci. Eng. C* **2017**, *71*, 584.
- [4] K. Kaaki, K. Hervé-Aubert, M. Chipper, A. Shkilnyy, M. Soucé, R. Benoit, A. Paillard,

- P. Dubois, M. L. Saboungi, I. Chourpa, *Langmuir* **2012**, *28*, 1496.
- [5] Y. C. Park, J. B. Smith, T. Pham, R. D. Whitaker, C. A. Sucato, J. A. Hamilton, E. Bartolak-Suki, J. Y. Wong, *Colloids Surfaces B Biointerfaces* **2014**, *119*, 106.
- [6] P. Guardia, R. Di Corato, L. Lartigue, C. Wilhelm, A. Espinosa, M. Garcia-Hernandez, F. Gazeau, L. Manna, T. Pellegrino, *ACS Nano* **2012**, *6*, 3080.
- [7] R. Di Corato, A. Espinosa, L. Lartigue, M. Tharaud, S. Chat, T. Pellegrino, C. Ménager, F. Gazeau, C. Wilhelm, *Biomaterials* **2014**, *35*, 6400.
- [8] S. L. Saville, B. Qi, J. Baker, R. Stone, R. E. Camley, K. L. Livesey, L. Ye, T. M. Crawford, O. Thompson Mefford, *J. Colloid Interface Sci.* **2014**, *424*, 141.
- [9] D. Serantes, K. Simeonidis, M. Angelakeris, O. Chubykalo-Fesenko, M. Marciello, M. del P. Morales, D. Baldomir, C. Martinez-Boubeta, *J. Phys. Chem. C* **2014**, *118*, 5927.
- [10] J. Faraudo, J. S. Andreu, C. Calero, J. Camacho, *Adv. Funct. Mater.* **2016**, *26*, 3837.
- [11] R. Di Corato, G. Béalle, J. Kolosnjaj-Tabi, A. Espinosa, O. Clément, A. K. A. Silva, C. Ménager, C. Wilhelm, *ACS Nano* **2015**, *9*, 2904.
- [12] A. Tan, L. Hong, J. D. Du, B. J. Boyd, *Adv. Sci.* **2019**, *6*, 1801223.
- [13] H. Sub Wi, K. Lee, H. Kyu Pak, *J. Phys. Condens. Matter* **2008**, *20*, 494211.
- [14] S. Chakraborty, A. Abbasi, G. D. Bothun, M. Nagao, C. L. Kitchens, *Langmuir* **2018**, *34*, 13416.
- [15] M. R. Preiss, A. Hart, C. Kitchens, G. D. Bothun, *J. Phys. Chem. B* **2017**, *121*, 5040.
- [16] E. Amstad, J. Kohlbrecher, E. Müller, T. Schweizer, M. Textor, E. Reimhult, *Nano Lett.* **2011**, *11*, 1664.
- [17] J. J. Vallooran, S. Handschin, S. Bolisetty, R. Mezzenga, *Langmuir* **2012**, *28*, 5589.
- [18] E. Venugopal, S. K. Bhat, J. J. Vallooran, R. Mezzenga, *Langmuir* **2011**, *27*, 9792.
- [19] K. Y. Vlasova, A. Piroyan, I. M. Le-Deygen, H. M. Vishwasrao, J. D. Ramsey, N. L. Klyachko, Y. I. Golovin, P. G. Rudakovskaya, I. I. Kireev, A. V. Kabanov, M. Sokolsky-Papkov, *J. Colloid Interface Sci.* **2019**, *552*, 689.

- [20] S. Saesoo, S. Sathornsumetee, P. Anekwiang, C. Treetidnipa, P. Thuwajit, S. Bunthot, W. Maneeprakorn, L. Maurizi, H. Hofmann, R. U. Rungsardthong, N. Saengkrit, *Colloids Surfaces B Biointerfaces* **2018**, *161*, 497.
- [21] A. Salvatore, C. Montis, D. Berti, P. Baglioni, *ACS Nano* **2016**, *10*, 7749.
- [22] J. Haša, J. Hanuš, F. Štěpánek, *ACS Appl. Mater. Interfaces* **2018**, *10*, 20306.
- [23] M. Mendoza, C. Montis, L. Caselli, M. Wolf, P. Baglioni, D. Berti, *Nanoscale* **2018**, *10*, 3480.
- [24] C. Montis, B. Castroflorio, M. Mendoza, A. Salvatore, D. Berti, P. Baglioni, *J. Colloid Interface Sci.* **2015**, *449*, 317.
- [25] J. Zhai, R. B. Luwor, N. Ahmed, R. Escalona, F. H. Tan, C. Fong, J. Ratcliffe, J. A. Scoble, C. J. Drummond, N. Tran, *ACS Appl. Mater. Interfaces* **2018**, *10*, 25174.
- [26] S. Murgia, S. Lampis, P. Zucca, E. Sanjust, M. Monduzzi, *J. Am. Chem. Soc.* **2010**, *132*, 16176.
- [27] C. Leal, N. F. Bouxsein, K. K. Ewert, C. R. Safinya, *J. Am. Chem. Soc.* **2010**, *132*, 16841.
- [28] C. R. Safinya, J. Deek, R. Beck, J. B. Jones, C. Leal, K. K. Ewert, Y. Li, *Liq. Cryst.* **2013**, *40*, 1748.
- [29] N. Tran, A. M. Hawley, J. Zhai, B. W. Muir, C. Fong, C. J. Drummond, X. Mulet, *Langmuir* **2016**, *32*, 4509.
- [30] N. Tran, X. Mulet, A. M. Hawley, C. Fong, J. Zhai, T. C. Le, J. Ratcliffe, C. J. Drummond, *Langmuir* **2018**, *34*, 2764.
- [31] S. Jia, A. Tan, A. Hawley, B. Graham, B. J. Boyd, *J. Colloid Interface Sci.* **2019**, *548*, 151.
- [32] K. J. Tangso, W. K. Fong, T. Darwish, N. Kirby, B. J. Boyd, T. L. Hanley, *J. Phys. Chem. B* **2013**, *117*, 10203.
- [33] S. Jia, J. D. Du, A. Hawley, W. K. Fong, B. Graham, B. J. Boyd, *Langmuir* **2017**, *33*,

2215.

- [34] R. Negrini, R. Mezzenga, *Langmuir* **2012**, *28*, 16455.
- [35] J. J. Vallooran, S. Assenza, R. Mezzenga, *Angew. Chemie - Int. Ed.* **2019**, *58*, 7289.
- [36] M. Mendoza, L. Caselli, C. Montis, S. Orazzini, E. Carretti, P. Baglioni, D. Berti, *J. Colloid Interface Sci.* **2019**, *541*, 329.
- [37] S. Murgia, S. Bonacchi, A. M. Falchi, S. Lampis, V. Lippolis, V. Meli, M. Monduzzi, L. Prodi, J. Schmidt, Y. Talmon, C. Caltagirone, *Langmuir* **2013**, *29*, 6673.
- [38] C. Caltagirone, A. M. Falchi, S. Lampis, V. Lippolis, V. Meli, M. Monduzzi, L. Prodi, J. Schmidt, M. Sgarzi, Y. Talmon, R. Bizzarri, S. Murgia, *Langmuir* **2014**, *30*, 6228.
- [39] S. Biffi, L. Andolfi, C. Caltagirone, C. Garrovo, A. M. Falchi, V. Lippolis, A. Lorenzon, P. Macor, V. Meli, M. Monduzzi, M. Obiols-Rabasa, L. Petrizza, L. Prodi, A. Rosa, J. Schmidt, Y. Talmon, S. Murgia, *Nanotechnology* **2017**, *28*, 055102.
- [40] S. Murgia, A. M. Falchi, V. Meli, K. Schillén, V. Lippolis, M. Monduzzi, A. Rosa, J. Schmidt, Y. Talmon, R. Bizzarri, C. Caltagirone, *Colloids Surfaces B Biointerfaces* **2015**, *129*, 87.
- [41] P. Astolfi, E. Giorgini, V. Gambini, B. Rossi, L. Vaccari, F. Vita, O. Francescangeli, C. Marchini, M. Pisani, *Langmuir* **2017**, *33*, 12369.
- [42] S. Sun, H. Zeng, D. B. Robinson, S. Raoux, P. M. Rice, S. X. Wang, G. Li, *J. Am. Chem. Soc.* **2004**, *126*, 273.
- [43] L. Wang, J. Luo, Q. Fan, M. Suzuki, I. S. Suzuki, M. H. Engelhard, Y. Lin, N. Kim, J. Q. Wang, C. J. Zhong, *J. Phys. Chem. B* **2005**, *109*, 21593.
- [44] R. Mezzenga, C. Meyer, C. Servais, A. I. Romoscanu, L. Sagalowicz, R. C. Hayward, *Langmuir* **2005**, *21*, 3322.
- [45] J. B. Marlow, M. J. Pottage, T. M. McCoy, L. De Campo, A. Sokolova, T. D. M. Bell, R. F. Tabor, *Phys. Chem. Chem. Phys.* **2018**, *20*, 16592.
- [46] C. Montis, D. Maiolo, I. Alessandri, P. Bergese, D. Berti, *Nanoscale* **2014**, *6*, 6452.

- [47] C. Neto, D. Berti, G. D. Aloisi, P. Baglioni, K. Larsson, *Prog. Coll. Polym. Sci.* **2000**, *115*, 295.
- [48] J. Y. T. Chong, X. Mulet, L. J. Waddington, B. J. Boyd, C. J. Drummond, *Soft Matter* **2011**, *7*, 4768.
- [49] H. Meng, M. Xue, T. Xia, Z. Ji, D. Y. Tam, J. I. Zink, A. E. Nel, *ACS Nano* **2011**, *5*, 4131.
- [50] E. Blanco, H. Shen, M. Ferrari, *Nat. Biotechnol.* **2015**, *33*, 941.
- [51] Q. He, Z. Zhang, F. Gao, Y. Li, J. Shi, *Small* **2011**, *7*, 271.
- [52] S. H. Sun, H. Zeng, *J. Am. Chem. Soc.* **2002**, *124*, 8204.
- [53] J. Schindelin, I. Arganda-Carreras, E. Frise, V. Kaynig, M. Longair, T. Pietzsch, S. Preibisch, C. Rueden, S. Saalfeld, B. Schmid, J.-Y. Tinevez, D. J. White, V. Hartenstein, K. Eliceiri, P. Tomancak, A. Cardona, *Nat. Methods* **2012**, *9*, 676.
- [54] M. Kotlarchyk, S. Chen, *J. Chem. Phys.* **1983**, *79*, 2461.
- [55] D. Begriff, A. Hand, D. Zerlegung, D. Fraktionierung, A. Grund, D. Fraktionierbarkeit, S. Kurven, S.- Dinger, I. Authenticated, D. Date, **1940**, *70*, 155.

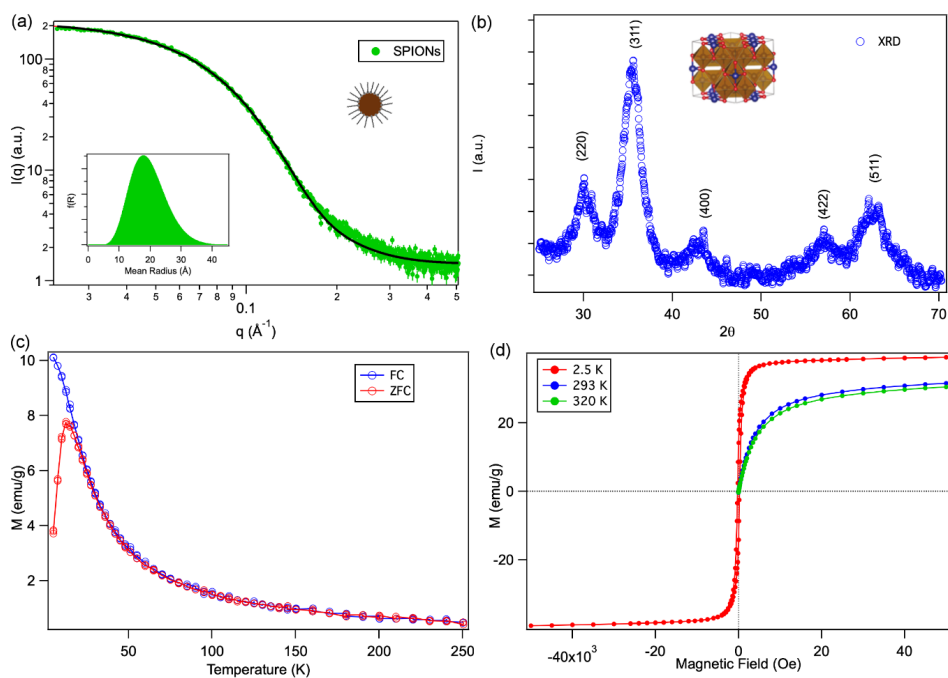


**Figure 1.** Characterization of Superparamagnetic Iron Oxide Nanoparticles  $\text{Fe}_3\text{O}_4$ : (a) Small Angle X-ray Scattering (SAXS) performed on the dispersed sample in hexane, (b) X-Ray Diffractogram (XRD) measured on dry SPIONs powder as also for (c) Field Cooled (FC) and Zero Field Cooled (ZFC) performed to 50 Oe. (d) Magnetization measurement performed on dry SPIONs powder at 2.5 K (red line and markers), 293 K (violet line and markers) and 320 K (green line and markers) are reported.

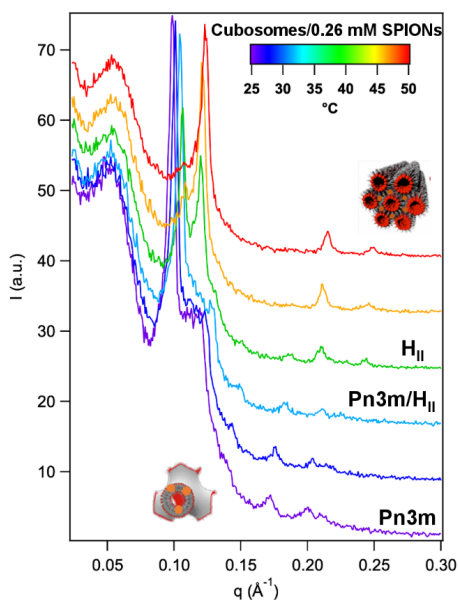


**Figure 2.** Small Angle X-Ray Scattering of bulk cubic mesophases loaded with 0.26 mM SPIONs into the range of temperature 25-50 °C increasing each step of 5 °C.

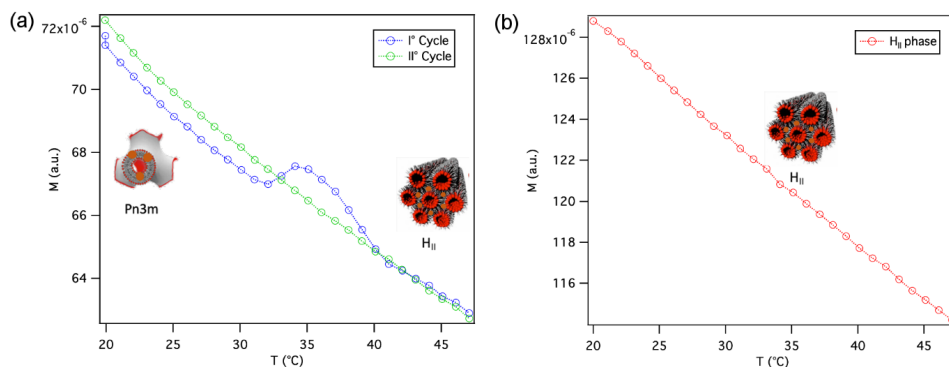


**Figure 3.** The magnetization of cubic (a) and hexagonal (b) mesophases doped with SPIONs was investigated into the range 20-47 °C. In (a) blue markers and line shows magnetization of Pn3m structure before phase transition and green line and markers shows the same experiment performed on the sample after phase transition. In (b) it is reported the curve which describe the magnetic behavior of hexagonal mesophase where no phase transition can be detected.

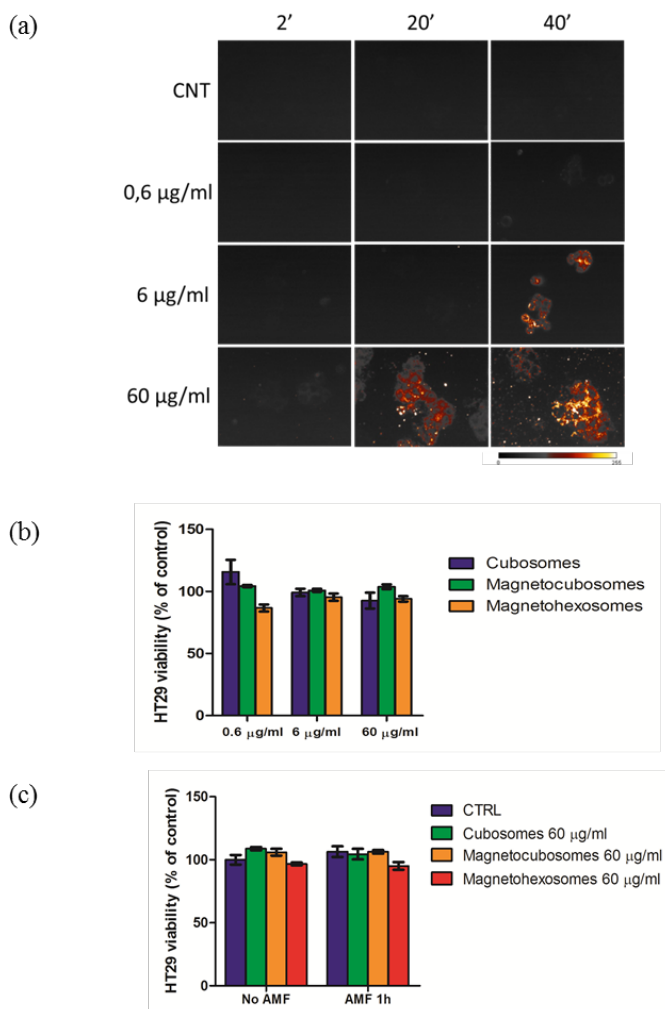


**Figure 4.** Confocal images of Octadecyl-Rhodamine B conjugated cubosomes internalization in HT29 cells at 2, 20 and 40 minutes at different concentrations (0.6 µg/ml, 6 µg/ml, and 60 µg/ml) (a). Cell viability of HT29 treated with different concentration (0.6 µg/ml, 6 µg/ml, and 60 µg/ml) of cubosomes, magnetocubosomes and magnetohehexosomes (b). Cell viability of HT29 treated with cubosomes, magnetocubosomes and magnetohehexosomes at 60 µg/ml under the alternate magnetic field (c).

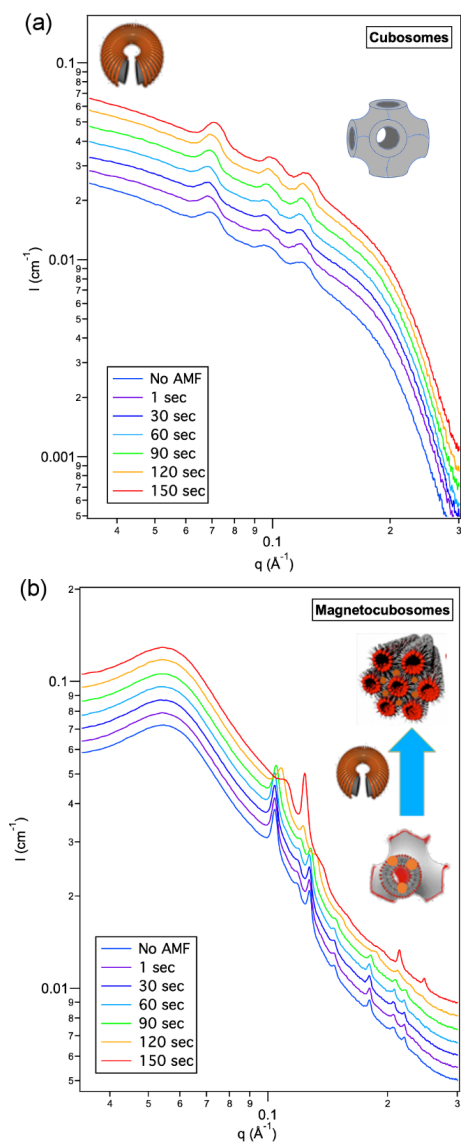


**Figure 5.** In situ SAXS experiments of cubosomes (a) and cubosomes assembled with 0.26 mM SPIONs (b) under the alternate magnetic field of 4.22 kHz. Each 30 seconds were recorded a curve to control the hyperthermic effect of nanoparticles. In (b) it is showed the transition to a hexagonal array the dispersion after 150 sec upon AMF (red curve).

Self-assembly of liquid crystals assembled with magnetic nanoparticles was investigated to describe the structure and magnetic features of lipid liquid crystals modified by nanoparticles. The responsivity upon an oscillating magnetic field was tested both on bulk and dispersed mesophases. The biocompatibility with MTT proved the toxicity of dispersed liquid crystals on cells.

**Keyword** SPIONs, lipids, cubosomes, nanoparticles, functional materials

Marco Mendoza, Beatrice Muzzi, Alessandra Toti, Lucrezia Caselli, Costanza Montis, Tommaso Mello, Claudio Sangregorio, Lorenzo Di Cesare Mannelli and Debora Berti\*

**Phase transition induced ordering of SPIONs liquid crystalline lipid mesophases**

ToC figure ((Please choose one size: 55 mm broad × 50 mm high **or** 110 mm broad × 20 mm high. Please do not use any other dimensions))

## Supporting Information

**Phase transition induced ordering of SPIONs liquid crystalline lipid mesophases**

*Marco Mendozza, Beatrice Muzzi, Alessandra Toti, Lucrezia Caselli, Costanza Montis, Tommaso Mello, Claudio Sangregorio, Lorenzo Di Cesare Mannelli and Debora Berti\**

	<b>Index</b>	<b>Page</b>
<b>S.1</b>	<i>Magnetization Vs Temperature SPIONs</i>	28
<b>S.2</b>	<i>SAXS data elaboration</i>	28
<b>S.3</b>	<i>SAXS curves of bulk mesophases</i>	30
<b>S.4</b>	<i>SAXS curves of Cubosomes and Magnetocubosomes</i>	32
<b>S.5</b>	<i>In-Situ structural investigation</i>	33

## S.1 Magnetization Vs. Temperature

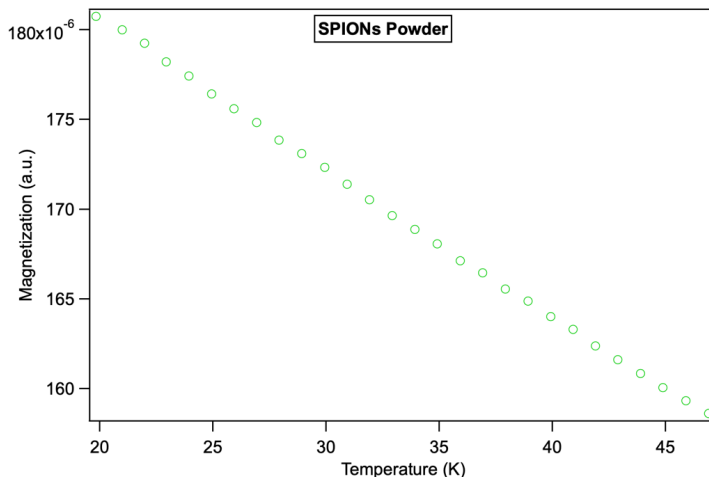


**Figure S1** Magnetization measurement performed as function of the temperature on SPIONs powder purified by oleic acid and oleylamine capping agents. The intensity of the magnetic field was 10 Oe.

In agreement to the literature (cit), SPIONs powder shows a magnetization following a linear decay into the range 20-47 °C. No deviation from this trend is detectable into the range 32-40 °C.

## S.2 SAXS data elaboration

**Equation (S1)** was used to calculate lattice parameter (d) of cubic and hexagonal phase:

$$q = \left(\frac{2\pi}{d}\right) \sqrt{h^2 + k^2 + l^2} \quad (\text{S1})$$

where (hkl) are Miller index related to the considered structures. In a Pn3m structure are (110), (111), (200), (211), (220), etc. while in H<sub>II</sub> mesophases are (100), (111), (200) etc.

To Fit SAXS curves of both dispersed gold and iron oxide nanoparticles, we used Sphere-Schulz Model by NIST<sup>[54,55]</sup>. This model calculates the scattering for a polydisperse population of spheres with uniform Scattering Length Density (SLD). The distribution of radii is a Schulz distribution as in **Equation (S2)**:

$$f(R) = (z + 1)^{z+1} x^z \frac{\exp [-(z + 1)x]}{R_{avg} \Gamma(z + 1)} \quad (S2)$$

Where  $R_{avg}$  is the mean radius,  $x=R/R_{avg}$ ,  $z$  is related to the polydispersity,  $p=\sigma/R_{avg}$ , by  $z=1/p^2-1$ .  $\sigma^2$  is the variance of distribution. The scattering intensity is modeled as reported in

**Equation (S3):**

$$I(q) = \left(\frac{4\pi}{3}\right)^2 N_0 \Delta\rho^2 \int_0^\infty f(R) R^6 F^2(qR) dR \quad (S3)$$

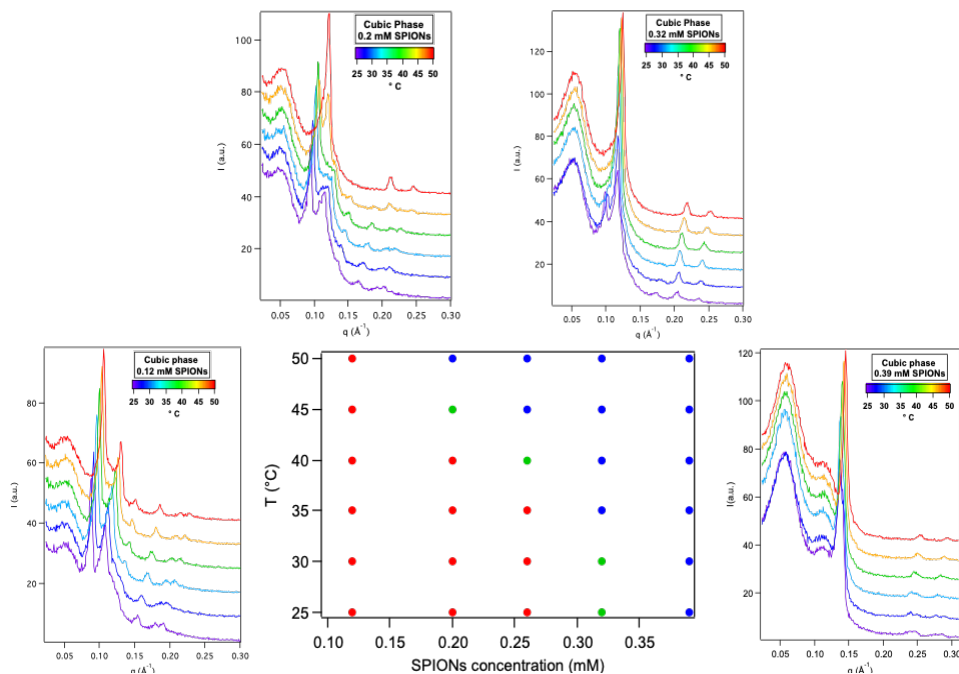
where  $N_0$  is the total number of particles per unit volume, and  $\Delta\rho$  is the difference in scattering length density,  $F(qR)$  the scattering amplitude for a sphere reported in **Equation**

**(S4):**

$$F(x) = \frac{3[\sin(x) - x\cos(x)]}{x^3} \quad (S4)$$

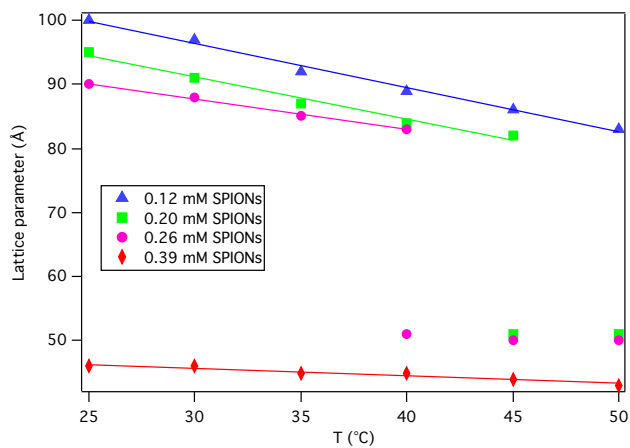
No interparticle interference effects are included in this calculation.

## S.3 SAXS curves of bulk mesophases



**Figure S2** Phase Diagram in the middle of the image and all the SAXS curves of cubic phases doped with increased amount of SPIONs: 0.12-0.2-0.26-0.32-0.39 mM. Data of cubic phase loaded by 0.26 mM SPIONs are showed in main text.

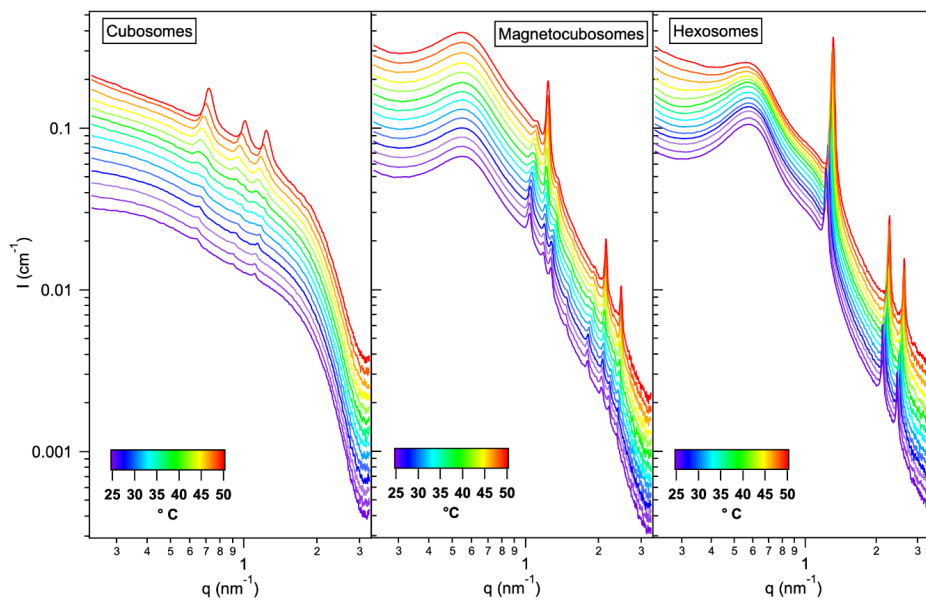
<b>Table S1</b> Lattice Parameters ( $\text{\AA}$ ) of cubic phases doped with different number of nanoparticles					
<b>Temperature (<math>^{\circ}\text{C}</math>)</b>	<b>0.12 mM SPIONs</b>	<b>0.2 mM SPIONs</b>	<b>0.26 mM SPIONs</b>	<b>0.32 mM SPIONs</b>	<b>0.39 mM SPIONs</b>
25	100 (Pn3m)	94 (Pn3m)	90 (Pn3m)	89 (Pn3m) 54 (H <sub>II</sub> )	46 (H <sub>II</sub> )
30	97 (Pn3m)	91 (Pn3m)	88 (Pn3m)	87 (Pn3m) 53 (H <sub>II</sub> )	46 (H <sub>II</sub> )
35	92 (Pn3m)	87 (Pn3m)	85 (Pn3m)	53 (H <sub>II</sub> )	45 (H <sub>II</sub> )
40	89 (Pn3m)	84 (Pn3m)	83 (Pn3m) 52 (H <sub>II</sub> )	52 (H <sub>II</sub> )	45 (H <sub>II</sub> )
45	86 (Pn3m)	83 (Pn3m) 52 (H <sub>II</sub> )	52 (H <sub>II</sub> )	51 (H <sub>II</sub> )	44 (H <sub>II</sub> )
50	83 (Pn3m)	51 H <sub>II</sub>	51 (H <sub>II</sub> )	50 (H <sub>II</sub> )	43 (H <sub>II</sub> )



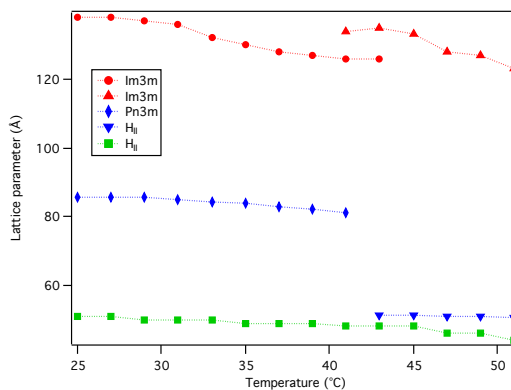
**Figure S3** Lattice parameter as function of the temperature for cubic phases doped with 0.12-0.2-0.26-0.39 mM SPIONs. The slope of linear fit performed into the range of temperature where the structure is preserved, are showed in Table S2.

Table S2 Slope of linear fit showed in Figure S3	
Samples	Slope ( $\text{\AA} \text{ } ^\circ\text{C}^{-1}$ )
<b>0.12 mM</b>	-0.69
<b>0.2 mM</b>	-0.66
<b>0.26 mM</b>	-0.48
<b>0.39 mM</b>	-0.12

## S.4 SAXS curves of cubosomes and magnetocubosomes



**Figure S4** Small Angle Scattering data of cubosomes, magnetocubosomes (0.26 mM SPIONs) and magnetohexosomes (0.39 mM SPIONs) scanning the temperature into the range 25-50 °C increasing each step by 2 °C.



**Figure S5** Lattice parameters as function of temperature into the range 25-51 °C for cubosomes (red markers), magnetocubosomes (blue markers) and magnetohexosomes (green markers).

**Table S4** Lattice parameter ( $\text{\AA}$ ) of cubosomes, magnetocubosomes, magnetohexosomes into the range 25-51  $^{\circ}\text{C}$

Temperature ( $^{\circ}\text{C}$ )	Cubosomes	MagnetoCubosomes	MagnetoHexosome
25	138	86 (Pn3m)	51 ( $H_{II}$ )
27	138	86 (Pn3m)	51 ( $H_{II}$ )
29	137	86 (Pn3m)	50 ( $H_{II}$ )
31	136	85 (Pn3m)	50 ( $H_{II}$ )
33	133	84 (Pn3m)	50 ( $H_{II}$ )
35	131	84 (Pn3m)	49 ( $H_{II}$ )
37	128	83 (Pn3m)	49 ( $H_{II}$ )
39	127	82 (Pn3m)	49 ( $H_{II}$ )
41	126 (Im3m Type I) 134 (Im3m Type II)	81 (Pn3m)	48 ( $H_{II}$ )
43	126 (Im3m Type I) 135 (Im3m Type II)	51 ( $H_{II}$ )	48 ( $H_{II}$ )
45	133 (Im3m Type II)	51 ( $H_{II}$ )	48 ( $H_{II}$ )
47	128	51 ( $H_{II}$ )	46 ( $H_{II}$ )
49	127	51 ( $H_{II}$ )	46 ( $H_{II}$ )
51	123	51 ( $H_{II}$ )	44 ( $H_{II}$ )

### S.5- In Situ structural investigation

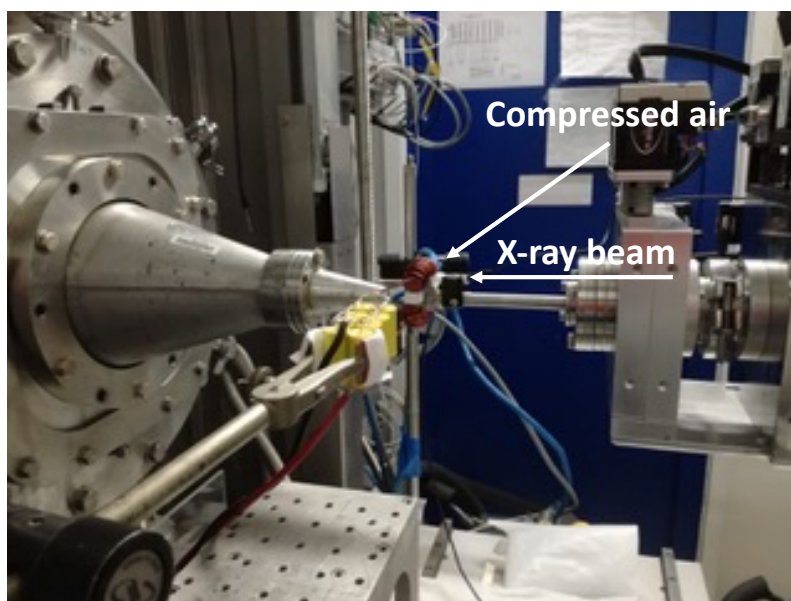


**Figure S6** Experimental setup of the experiments performed on ID02 beamline ESRF Synchrotron Radiation Source. The coil was placed between the beam and the detector; the ON-OFF alternate magnetic field was remotely controlled, and the teflon sample holder was placed in the empty space of toroidal broken part.

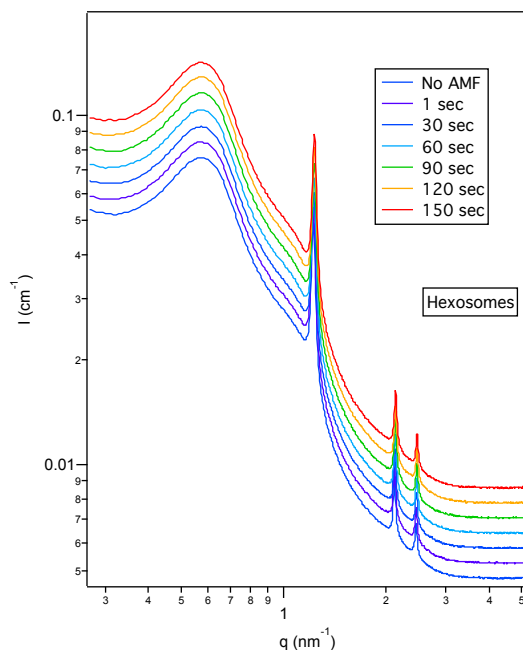


**Figure S7** In situ structural detection of magneohexosomes exposed to an oscillating magnetic field. No structural change can be seen and the lattice parameter remains constant.

Table S5 Lattice parameter ( $\text{\AA}$ ) of cubosomes, magnetocubosomes, magneohexosomes exposed to an oscillating magnetic field.			
Time (s)	Cubosomes	Magnetocubosomes	Magneohexosomes
No AMF	131 (Im3m)	85 (Pn3m)	51 (H <sub>II</sub> )
1	130 (Im3m)	85 (Pn3m)	51 (H <sub>II</sub> )
30	129 (Im3m)	85 (Pn3m)	51 (H <sub>II</sub> )
60	129 (Im3m)	85 (Pn3m)	51 (H <sub>II</sub> )
90	128 (Im3m)	84 (Pn3m) 51 (H <sub>II</sub> )	51 (H <sub>II</sub> )
120	128 (Im3m)	82 (Pn3m) 51 (H <sub>II</sub> )	51 (H <sub>II</sub> )
150	128 (Im3m)	51 (H <sub>II</sub> )	51 (H <sub>II</sub> )

# Paper V



# **Lipid Liquid Crystalline Mesophases with tuneable size of aqueous nanochannels: effects on enzymatic reaction rates.**

Debora Berti\*<sup>1</sup>, Marco Mendoza<sup>1</sup>, Costanza Montis<sup>1</sup>, Arianna Balestri<sup>1</sup>

Address: <sup>1</sup>Department of Chemistry “Ugo Schiff” and CSGI, Via della Lastruccia 3-13, Sesto Fiorentino 50019 (FI)

E-mail: Debora Berti – [debora.berti@unifi.it](mailto:debora.berti@unifi.it)

\* Corresponding author

## **Abstract**

Lipid Liquid Crystalline (LLC) mesophases, resulting from the self-assembly of polymorphic lipids in water, have been widely explored as possible biocompatible drug delivery systems over the past years. In particular, non-lamellar structures are characterized by complex 3D architectures, where hydrophobic and hydrophilic domains can conveniently host drugs of different polarity. However, one drawback in their applicability, lies in the poor tunability of their phase diagram. In this work, we investigate the phase behavior of Phytantriol (Phyt)/water mesophases, upon addition of increasing amounts of the additive Sucrose Stearate (SS). A Small-Angle X-ray Scattering (SAXS) analysis allowed determining the structural parameters of the different Phyt/SS/H<sub>2</sub>O mesophases, highlighting the possibility to finely control the structure/size of the mesophases with the amount of additive. Finally, the loading, retention and release capacities of Phyt mesophases, containing different amounts of SS, was determined through UV-Vis spectroscopy, monitoring the effect of confinement on the reaction kinetics of Alkaline Phosphatase catalysing the enzymatic reaction of p-nitrophenyl phosphate conversion into p-nitrophenol: we show that the alternative inclusion of either the substrate or the enzyme, which are smaller or of comparable size to the dimensions of the mesophases, have different impacts on the reaction kinetics, which is deeply affected by the structure of the mesophase.

# Keywords

Lipid Mesophases; Phytantriol; Drug Delivery; Enzyme Kinetics; Confinement

## 1. Introduction

Polymorphic lipids have been widely studied over the years, for their unique self-assembly properties: in water, they can form lyotropic liquid crystals with long-range order promoted by hydrophobic and H-bonds driving forces<sup>1</sup>, with different arrangements and a complex phase diagram highly dependent on temperature, pressure<sup>2</sup>, water content, and ionic strength<sup>3-6</sup>. For instance, glycerol monooleate (GMO, a glycerol monoester) and phytantriol (Phyt, a terpenoid polyalcohol) are among the most studied polymorphic amphiphiles, characterized by a rich phase diagram. Depending on the experimental conditions, they assemble in hexagonal mesophases (consisting of lipid monolayered cylinders arranged into a hexagonal network), lamellar mesophases (consisting of lipid bilayers arranged in stacked infinite plans divided by water regions), or inverse bicontinuous cubic mesophases (consisting of a lipid bilayer wrapped on a periodic minimal surface<sup>7</sup>). Cubic Mesophases, stable in excess water and at room temperature conditions, can exhibit different arrangements, namely the Schwarz Diamond, the Primitive and the Schoen Gyroid, characterized by different Infinite Periodical Minimal Surfaces (IPMS) with spatial groups Pn3m, Im3m and Ia3d respectively. While Gyroid and Diamond phase are in thermodynamic equilibrium with excess water, the primitive cubic phase is observed with additives<sup>8</sup> and polymers<sup>9</sup> swelling the water channels; thus, the hydration level and curvature increase from gyroid, diamond and primitive mesophases<sup>7</sup>.

Due to their unique structure, characterized by the coexistence of extended hydrophobic and hydrophilic regions arranged in a continuous 3D complex

architecture, cubic mesophases have been widely studied as possible alternatives to the most common lamellar phases (in particular in their dispersed form, as liposomes) for the development of vectors for drugs of different size and polarity for biomedical applications<sup>6,10-12</sup>. For instance, they have been employed to transport small hydrophobic molecules as drugs quercetin<sup>13,14</sup> and camptothecin<sup>15</sup>, and photosensitizers<sup>16</sup>, as well as macromolecules as proteins<sup>10,17,18</sup>; in addition, cubic mesophases have been successfully loaded with hydrophobic or hydrophilic superparamagnetic iron oxide nanoparticles, to build-up smart drug delivery systems, able to release the encapsulated drugs in a spatially and temporally controlled manner<sup>19,20</sup>; finally, it has been shown that cubic mesophases have a strong ability to interact with phospholipid cell membranes, making them particularly interesting for the intracellular delivery of drugs.

Despite these promising features, one drawback in the application of cubic mesophases as drug delivery systems is the fact that, once temperature and pressure are defined, their structural parameters in excess are poorly tunable, which might result in a limited control of the pharmacokinetic properties (i.e., the release profile upon loading) of drugs encapsulated in the cubic mesophases.

In recent years the effects of additives on the phase diagram of cubic mesophases has started to be explored as a possible strategy to tune the arrangement of the lipid scaffold and to widen the dimension ranges of hydrophobic and hydrophilic domains, in order to better host and retain hydrophobic and hydrophilic drugs of different sizes, and/or tune the physical-chemical features of the liquid crystalline mesophases. For instance, fatty acids<sup>21,22</sup>, phospholipids<sup>23,24</sup>, photo-switchable molecules<sup>25-27</sup> or also nanoparticles as iron oxide<sup>20,28</sup>, gold<sup>29</sup>, quantum-dots<sup>30</sup> have been shown to effectively modify the phase diagram of cubic mesophases, both in terms of lattice parameters and in terms of shift of the phase borders.

Recently, Mezzenga et al. have reported on the swelling of monolinolein Pn3m modified by sucrose stearate<sup>8,18</sup>; the additive promotes a transition to Im3m cubic mesophase, with water nanochannels about 2.5 times larger than in pure lipid/water systems. This variation, as highlighted in several studies, can modify the confinement level of the encapsulated drug, ultimately controlling its release profile<sup>8,31,32</sup>. For instance, in a recent work by Assenza et al.<sup>33</sup> it has been hypothesized that for relatively large channels the diffusion coefficient of an encapsulated molecule can be related to the average of the Gaussian curvature; conversely, in the case of narrow channels, a symmetry-dependent diffusion reduction is observed, due to the unique geometry of cubic mesophases, with the presence of cages and bottlenecks in the structure.<sup>33</sup> In general, the structure/symmetry of the mesophase, the size of the lattice parameters and of the nanochannels and, finally, the size and polarity of the drugs to be included in the mesophase will all affect the release profile of the drug in the surrounding environment.

In this contribution we address this issue, i.e., the relationship between the structural control over self-assembled cubic mesophases with determined and variable structural parameters, and their retention/release ability with different drugs. In particular, here we extend the investigation to Phyt/water system into the range 25-50 °C loaded with variable amounts of the additive Sucrose Stearate (SS), a sugar ester able to swell the water channels. Through Small-Angle X-ray Scattering (SAXS) we characterize the phase diagram of Phyt/SS/H<sub>2</sub>O, highlighting the possibility to achieve a fine structural control over the mesophases' dimensions.

In this study, we included in the aqueous channels of lipid mesophases with different lattice parameters, two model hydrophilic guest molecules, which differ in size and function, an enzyme (alkaline phosphatase, AP, M<sub>w</sub>=140 kDa) and its substrate, i.e. p-nitrophenyl phosphate, a small molecule with M<sub>w</sub>=263.05 Da.

The loading, retention and release capacities of the library of different mesophases is investigated through the enzymatic reaction catalyzed by AP converting the substrate p-nitrophenyl phosphate into p-nitrophenol, monitored through UV-vis spectroscopy in the diffusive medium: we show that the alternative inclusion of either the substrate or the enzyme, which are smaller or of comparable size to the dimensions of the mesophases, have different impacts on the reaction kinetics, which is deeply affected by the structure of the mesophase. Overall, we show that the structural control in the self-assembly of the mesophases can be suitably exploited to control the loading and release profile of drugs of different sizes (a small molecule or an enzyme) and even a reaction kinetics. The purpose of this work was to: i) verify how they diffuse and are released from the different lipid mesophases characterized by different lattice parameters and ii) evaluate the impact of confinement in the overall enzymatic reaction.

## 2. Results and Discussion

### 2.1 Structure of Phytantriol/Sucrose Stearate lipid mesophases

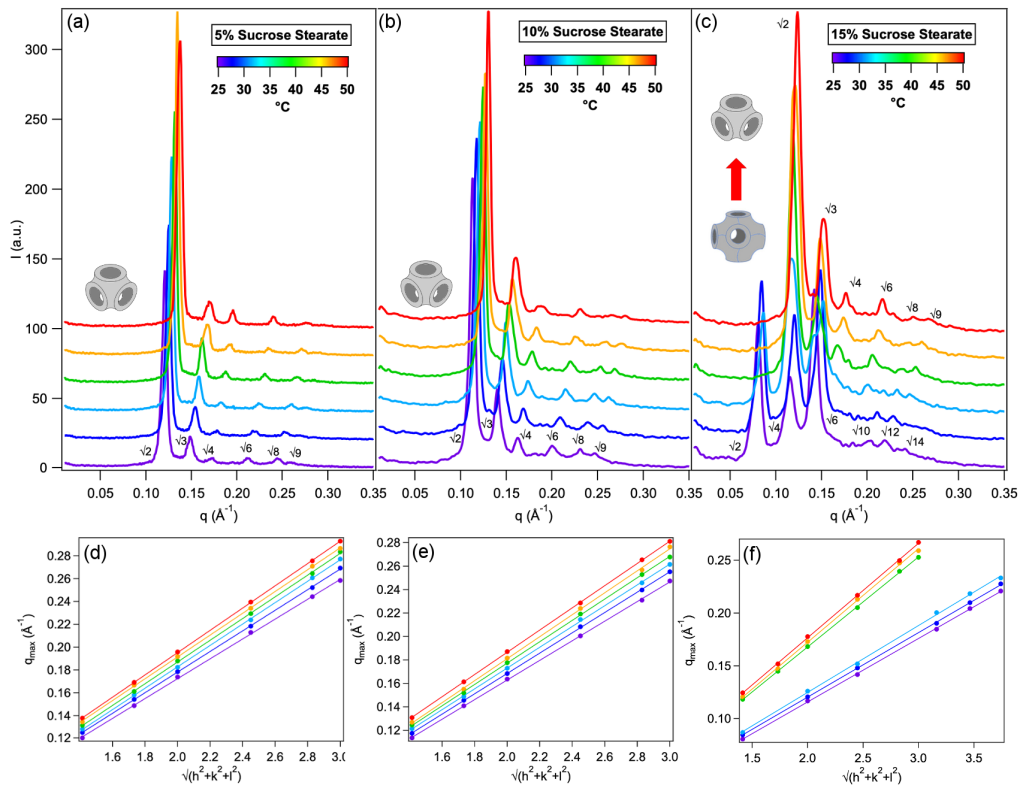


**Figure 1:** SAXS curves of Phyt mesophases added with 5% (a), 10% (b) and 15% (c) w/w SS, in excess water, measured at 25, 30, 35, 40, 45, 50  $^{\circ}\text{C}$ . (d), (e) and (f) show the linear plots to estimate the lattice parameter of the mesophases with 5%, 10% and 15% SS, respectively.

As a first experiment, in order to determine the impact of sucrose stearate (SS) on the arrangement of Phyt mesophases in excess water, we characterized the structure of Phyt/water binary systems, upon inclusion of increasing amounts of SS, at different temperatures. Phyt, in excess water, is characterized by a well-known phase diagram<sup>34</sup>, i.e., it arranges in a Pn3m cubic structure until the temperature reaches 45-50  $^{\circ}\text{C}$ , over which it undergoes a phase transition to a hexagonal phase.

Fig. 1 shows representative Small Angle X-ray Scattering (SAXS) curves of Phyt cubic mesophases with increasing concentrations of SS, namely 5% (Fig. 1a), 10% (1b) and 15% (1c) measured at 25, 30, 35, 40, 45, 50 °C.

The lattice parameters, reported in Table 1 display a well-known trend with increasing temperature, that is, a progressive decrease of the lattice parameter, associated to an overall shrinkage of the lipid mesophase; this effect is related to the conformation of the amphiphile chains splaying away each other, therefore increasing the molecule hydrophobic molecular portion. In terms of curvature of the lipid membrane, increasing the temperature results in driving a more negative spontaneous curvature of the leaflets, leading to an overall shrinking of the lipid mesophase<sup>7</sup>.

For the lowest and intermediate concentration of SS (5% and 10% w/w), the Pn3m structure of the mesophase is retained in the whole temperature range investigated (25-50 °C); however, for each temperature monitored, the lattice parameters of the liquid-crystalline phase are progressively increased by the addition of SS. This effect can be attributed to a localized perturbation of the mesophase due to the presence the additive: the sugar esters are localized at the water-lipid interface, with the hydrophobic portion inserted in the lipid bilayer and the highly hydrophilic sugar portion protruding in the water channels, enhancing the amount of water molecules in the nanochannels. This localized perturbation determines a decrease (in absolute value) of the curvature of the membrane, overall promoting a swelling of the lipid mesophase. This effect is much more pronounced for the sample where 15% w/w SS is present: in this case, at 25°C the phase arrangement is Im3m, characterized by a lower curvature of the membrane with respect to the Pn3m. We notice that increasing amounts of SS produce an opposite effect with respect to temperature increase (i.e., the addition of SS decreases the local curvature, while the temperature increase enhances it). Remarkably, at 40°C, the sample Phyt/SS(15% w/w)/H<sub>2</sub>O undergoes a transition from

Im3m to Pn3m, i.e. the thermodynamically stable structure for Phyt/H<sub>2</sub>O in the absence of additives at room temperature. Therefore, for this sample and temperature range, the swelling-deswelling effects (SS inclusion and temperature increase) are perfectly counterbalanced and the lattice parameter is similar to that observed for Phyt/H<sub>2</sub>O binary system at 25°C (see Table 1).

**Table 1:** Lattice parameter *d* (nm) of Phyt mesophases doped with increasing concentrations (5% w/w, 10% w/w, 15% w/w,) of SS in excess water, measured at different temperatures in the range T=25-50 °C.

	<b>No SS</b>		<b>5% SS</b>		<b>10% SS</b>		<b>15% SS</b>	
T (°C)	<i>d</i> (nm) <sup>#</sup>	<i>d<sub>w</sub></i> (nm)	<i>d</i> (nm)	<i>d<sub>w</sub></i> (nm)	<i>d</i> (nm)	<i>d<sub>w</sub></i> (nm)	<i>d</i> (nm)	<i>d<sub>w</sub></i> (nm)
25	6.6*±0.1	2.3	7.2*±0.1	2.8	7.5*±0.1	3.0	10.5 <sup>+</sup> ±0.2	3.6
30	6.5*±0.1	2.2	7.0*±0.1	2.6	7.2*±0.2	2.8	10.3 <sup>+</sup> ±0.1	3.4
35	6.4*±0.1	2.2	6.7*±0.1	2.4	7.1*±0.2	2.7	9.9 <sup>+</sup> ±0.2	3.2
40	6.3*±0.1	2.0	6.6*±0.1	2.3	6.9*±0.1	2.6	7.4*±0.2	2.9
45	4.8 <sup>§</sup> ±0.2	1.9	6.6*±0.2	2.3	6.7*±0.2	2.4	7.1*±0.1	2.7
50	4.0 <sup>§</sup> ±0.1	1.2	6.4*±0.2	2.2	6.6*±0.1	2.3	7.0*±0.1	2.6

\*Pn3m structure; § H<sub>II</sub> structure; + Im3m structure;

<sup>#</sup>Phyt/water lattice parameters are reported here by reference<sup>34</sup>

From these results it appears that, by playing with temperature and additive amount, it is possible to finely tune the structural parameters of a Phyt/H<sub>2</sub>O mesophase.

To this aim, we determined the size of the nanochannels from the lattice parameters (reported in Table 1) through Eq. 1 for a cubic phase

$$r_w = \sqrt{(-A_0/2\pi\chi)d} - l_c \quad (1)$$

and Eq. 2 for a hexagonal phase

$$r_w = \frac{0.525d - l_c}{0.994} \quad (2)$$

With  $r_w$  the radius of the water channel,  $A_0$  and  $\chi$  constants related to the topology of the mesophases (for a Pn3m  $A_0 = 1.919$  and  $\chi = -2$  while for an Im3m  $A_0 = 2.345$  and  $\chi = -4$ ),  $d$  is the lattice parameter, experimentally determined from the SAXS curves and the lipid bilayer thickness is considered equal to  $2l_c = 2.84$  nm both for pure Phyt/water system and for the systems additioned with SS.

The values of the diameters of water nanochannels determined through the previously reported equations reflect the trend of the lattice parameters of the mesophase: for instance, at 25°C the diameter of water nanochannels are 2.2 nm for neat Phyt/H<sub>2</sub>O system, and it progressively increases to 2.8 nm for 5% w/w SS, to 3.0 nm for 10% w/w SS and, finally, to 3.6 nm for 15% w/w SS. On the other hand, for each mesophase the temperature increase determines a progressive shrinkage of the water channels, determining a progressive water release from the mesophase. This effect is more pronounced in case of the system containing 15% w/w SS, where between 35 - 40°C a Im3m to Pn3m phase transition occurs, which is accompanied by a burst decrease of the water content of the mesophase (See SI for water volume fractions).

From this structural characterization it results that we built-up a library of liquid crystalline mesophases of cubic structure, characterized by variable and controlled size of the nanochannels. In the following paragraph we will report the characterization of the enzymatic reaction involving the enzyme alkaline phosphatase and its substrate p-nitrophenyl phosphate, which will be then included in the mesophase, to monitor the effect of confinement on the kinetics of the enzymatic reaction.

As mentioned in the introduction effect on the enzymatic kinetics were determined with UV spectroscopy in the bulk medium.

## 2.2 Alkaline Phosphatase Enzymatic reaction in aqueous solution

Alkaline phosphatase (AP) catalyses the conversion of the colourless substrate p-nitrophenyl phosphate to a yellow-green product (p-nitrophenol) in TRIS buffer pH 7.5, Figure 2a. The enzymatic reaction and the progressive formation of the reaction product can be therefore conveniently followed through UV-vis spectroscopy, observing the absorbance increase at 400 nm.

Figure 2b shows the kinetics profiles at different substrate concentrations ( $1 \times 10^{-5}$ ,  $2 \times 10^{-5}$ ,  $4 \times 10^{-5}$ ,  $5 \times 10^{-5}$ ,  $6 \times 10^{-5}$  M), monitored in the absence of the mesophase, with 0.2 U/mL of AP enzyme. The reaction is complete in around 5-15 minutes, depending on the concentration of the substrate.

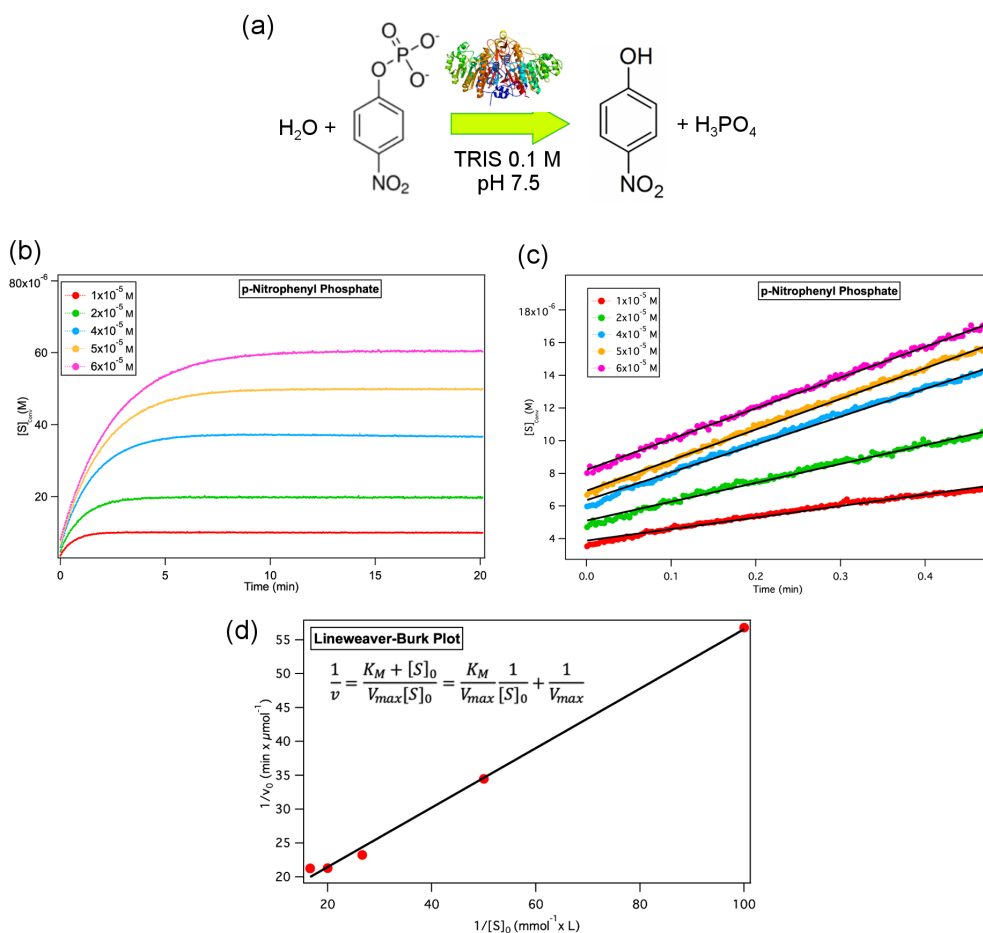


**Figure 2:** (a) Sketch of the conversion of p-nitrophenyl phosphate into p-nitrophenol catalysed by AP (b, c) reaction kinetics followed through UV-vis spectroscopy at 400 nm, varying the concentration of substrate ( $1 \times 10^{-5}$  M (red),  $2 \times 10^{-5}$  M (green),  $4 \times 10^{-5}$  M (cyan),  $5 \times 10^{-5}$  M (yellow) and  $6 \times 10^{-5}$  M (purple) in the presence of a fixed amount of enzyme (0.2 U/mL); (b) complete kinetics (c) initial absorbance increase, analysed with a linear fit (black bold lines); (d) Lineweaver-Burk plot to extract the Michaelis-Menten constant and the maximum velocity. The error bars on each point are smaller than the markers' size.

Figure 2c, displays the absorbance increase over the first 30 seconds, showing that the initial reaction rate depends on the substrate concentration. To determine the Michaelis-Menten constant,  $K_M$  and the maximum reaction rate,  $V_{max}$ , we used the linear Lineweaver-Burk plot (Eq. 3)

$$\frac{1}{v} = \frac{K_M + [S]_0}{V_{max}[S]_0} = \frac{K_M}{V_{max}} \frac{1}{[S]_0} + \frac{1}{V_{max}} \quad (3)$$

where  $v$  is the initial reaction rate,  $[S]_0$  the substrate concentration; from the plot reported in Figure 2d, the evaluated Michaelis-Menten constant  $K_M$  and  $V_{max}$  values are  $K_M = 0.034$  mM and  $V_{max} = 7.9 \times 10^{-2}$   $\mu\text{mol}$  of product/min, respectively. These results substantially agree with the literature values<sup>35</sup>, taking into account the different experimental conditions here adopted, i.e., 25°C instead of 37°C, neutral instead of alkaline pH, lower enzyme/substrate ratio.

### 2.3 Alkaline Phosphatase substrate inclusion in lipid mesophases

We then addressed the effect of confining the substrate in the mesophases aqueous channels of varying size. The experimental set-up, whose details are reported in the experimental section, can be briefly described as follows: Phyt or Phyt/SS was swollen with appropriate amounts of a p-nitrophenyl phosphate solution and placed in a UV-Vis cuvette containing 2.5 mL of a 0.2 U/mL AP aqueous solution (TRIS pH 7.5) and the absorption increase monitored for six days. This setup allows monitoring the absorbance in the external medium, excluding the mesophase region. The concentration of substrate into the mesophases was chosen to reach a theoretical absorbance value  $A=1$  (concentration of the product  $6 \times 10^{-5}$  M). Therefore, the initial absorbances of substrate and product are, for this configuration, zero.

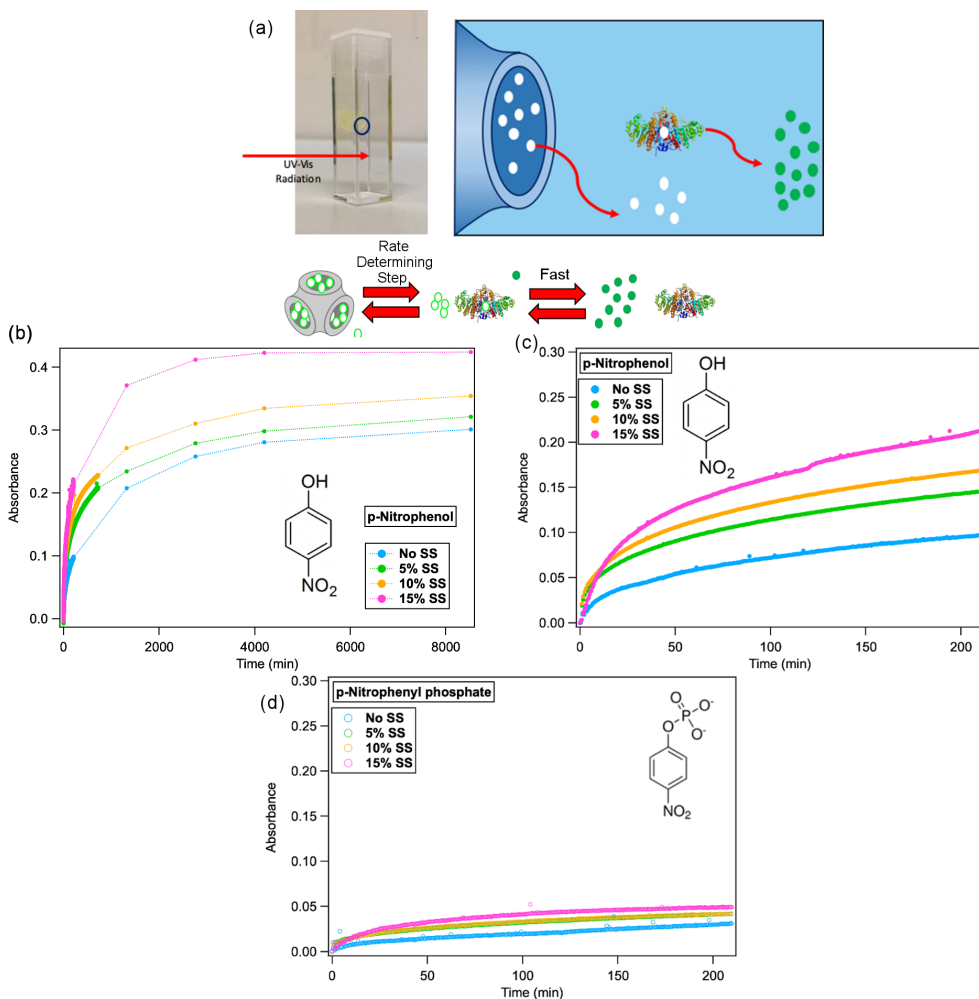


**Figure 3.** (a) Sketch of the release of substrate (green empty circles) in solution from the cubic mesophase, and its subsequent conversion by AP into p-nitrophenol (green filled circles); (b, c) kinetic profile of p-nitrophenol presence in solution, recorded at 400 nm for the substrate confined in the different mesophases with: No SS (cyan markers), 5% SS (green markers), 10% SS (orange markers) and 15% (purple markers); (b) complete kinetics (6 days); (c) first step of the kinetics (4h); (d) Release profile of p-nitrophenyl-phosphate in solution, recorded at 310 nm during the first 4 h for the substrate confined in the different mesophases with: No SS (empty cyan markers), 5% SS (empty green markers), 10% SS (orange empty markers) and 15% (purple empty markers).

Figures 3c-d display the UV-vis spectra measured for the enzymatic reaction over the first 4 hours. In particular, the release of p-nitrophenyl phosphate from the cubic phase of Phyt containing different amounts of SS (the absorbance at 310 nm is monitored over time, figure 3d), and its conversion into p-nitrophenol by the AP enzyme dispersed in the surrounding TRIS buffer solution (the absorbance at 400 nm is monitored over time, Figures 3b-3c).

To observe product formation, two different pathways for substrate/enzyme contact are possible: (i) the enzyme, diffuses inside the nanochannels, converts the substrate, the product leaves the nanochannels, (ii) the substrate diffuses from the nanochannels to the external medium and is then converted. The typical sizes of the enzyme (around 5 nm diameter) and the substrate (around 0.8 nm) are significantly different and should be compared to the sizes of the nanochannels.

From the data displayed in Figure 3c and 3d, it appears that over the first 5 minutes a steep increase of both p-nitrophenyl phosphate and p-nitrophenol absorbance is observed for all systems, (in the absence or the presence of increasing amounts of SS). This initial effect can be probably attributed to a part of the substrate localized at the interface of the lipid mesophase and the surrounding medium which freely diffuses in the buffer. There, AP readily converts it to p-nitrophenol.

Conversely, for longer times, the increase in both p-nitrophenyl phosphate and p-nitrophenol absorbance over time is slower, consistent with the conversion of the substrate confined in the aqueous channels.

For all the investigated liquid crystalline scaffolds, the size of p-nitrophenyl phosphate is smaller than the size of the water nanochannels. Therefore, we can expect an efficient encapsulation within the mesophase. However, the substrate diffusion towards the surrounding medium (driven by a chemical potential imbalance), can critically depend on the size of the mesophase nanochannels, which vary as a function

of SS amounts. As we can see from Fig. 3c, the kinetic profile at each SS concentration, shows that the reaction proceeds slowly for Phyt/H<sub>2</sub>O and that the conversion rate gradually increases with addition of sucrose stearate. We can correlate these experimental results to the SAXS data, which account for a swelling of the nanochannels as SS % is increased. Several reports in the literature show that the diffusion rate of molecular probes depend on the channel size<sup>8,32,33</sup>.

Therefore, in this second reaction regime the diffusion of the substrate from the nanochannels is the rate determining step.

Taking into account the displayed experimental data, and considering the different sizes of the enzyme and of the substrate also in comparison with the nanochannels diameters, we can conclude that the most probable mechanism for the enzymatic reaction, with the substrate confined in the aqueous channels, is a release of the substrate (first from the surface of the mesophase, then from the aqueous nanochannels) to the aqueous environment, followed by the conversion of the substrate into the reaction product. On the contrary, the enzyme diffusion inside the nanochannels, to convert the substrate, is probably hampered by the larger protein size in comparison to the channel' size.

Finally, if the whole reaction kinetics is considered, it is highlighted that, even if the amount of p-nitrophenyl phosphate released and converted by the enzyme is higher for primitive cubic structure, even after 6 days of reaction the absorbance value is significantly different from the theoretical value expected considering a complete release of substrate (See SI the complete kinetic profile). The origin of this inconsistency could be related to two possible reasons: first, due to the domains of liquid crystals not interconnected to each other and separated by grain boundaries, a complete release of the substrate could be hampered<sup>36</sup>. Secondly, the AP enzymatic

function is inhibited by the presence of high concentrations of the enzymatic product (p-nitrophenol). This latter hypothesis is in agreement with the release profile of the substrate followed for long times at 310 nm: as a matter of fact, it appears that the substrate concentration in solution keeps increasing (due to its continuous release from the cubic phase), without being mirrored by the same trend of the product (monitored at 400 nm). However, for relatively short times the rate-determining step of the reaction kinetic can be attributed to the release of the substrate to the reaction environment, while its conversion is a relatively fast process.

More in general, all the initial velocities of substrate conversion are decreased of 2 orders of magnitude when the substrate is confined into the mesophases with respect to the substrate freely diffusing in buffer solution (See Table 2).

This diffusion rate is controlled, with a good approximation, by the size of the water channels, which is dependent on the SS amount: the Phyt/SS/H<sub>2</sub>O mixed mesophases can be therefore of interest in the biomedical field as drug delivery vehicles to release continuously active molecules in a structurally controlled manner. As an example, while binary mixture Phyt/water present an initial velocity of the product formation of around  $3.78 \times 10^{-4}$  mmol/min, and the maximum absorbance reached after 3 days, in case of the ternary matrix the release can be accelerated to an initial velocity of  $8.56 \times 10^{-4}$  mmol/min and a maximum absorbance reached in 2 days with the higher amount of SS tested.

**Table 2:** Rate of reactions expressed in mmol/min of converted substrate and channels size (nm). Data obtained from the release of substrate converted by the AP enzyme in buffer solution.

<b>Sample</b>	<b>Rate (mmol/min)</b>	<b>Channel Size (nm)</b>
<i>No mesophase</i>	$1.18 \times 10^{-2} (\pm 6 \times 10^{-5})$	/
<i>Phyt</i>	$3.78 \times 10^{-4} (\pm 3 \times 10^{-6})$	2.3
<i>Phyt/5% SS</i>	$5.30 \times 10^{-4} (\pm 1 \times 10^{-5})$	2.8
<i>Phyt/10% SS</i>	$5.5 \times 10^{-4} (\pm 1 \times 10^{-5})$	3.0
<i>Phyt/15% SS</i>	$8.56 \times 10^{-4} (\pm 3 \times 10^{-6})$	3.6

## 2.4 Alkaline Phosphatase inclusion in lipid mesophases

To monitor the effect of enzymatic confinement on the AP enzymatic reaction, we adopted a similar experimental set-up as that described in the previous paragraph, with a different localization of the enzyme and the substrate, i.e., the dry films of Phyt and Phyt/SS were hydrated with an aqueous solution of AP and then they were immersed in a solution of the substrate (see the Experimental section for details). The enzymatic reaction was followed for neat Phyt/H<sub>2</sub>O and swelled (Phyt/H<sub>2</sub>O added with SS) cubic phases in a buffer solution containing  $6 \times 10^{-5}$  M of the substrate. First, we monitored the enzymatic reaction at 400 nm during the first 90 minutes of contact of the mesophase with the substrate containing buffer (Figure 4b). In this way, the release of some non-encapsulated enzyme and/or the enzyme localized quite close to the cubic phase/aqueous environment interface, was monitored.

As a second step, the cubic mesophase was placed in another cuvette, with fresh substrate at the same concentration as the first solution. In this way, we monitored the enzymatic catalysis due to AP encapsulated within the cubic phase (Figure 4c).

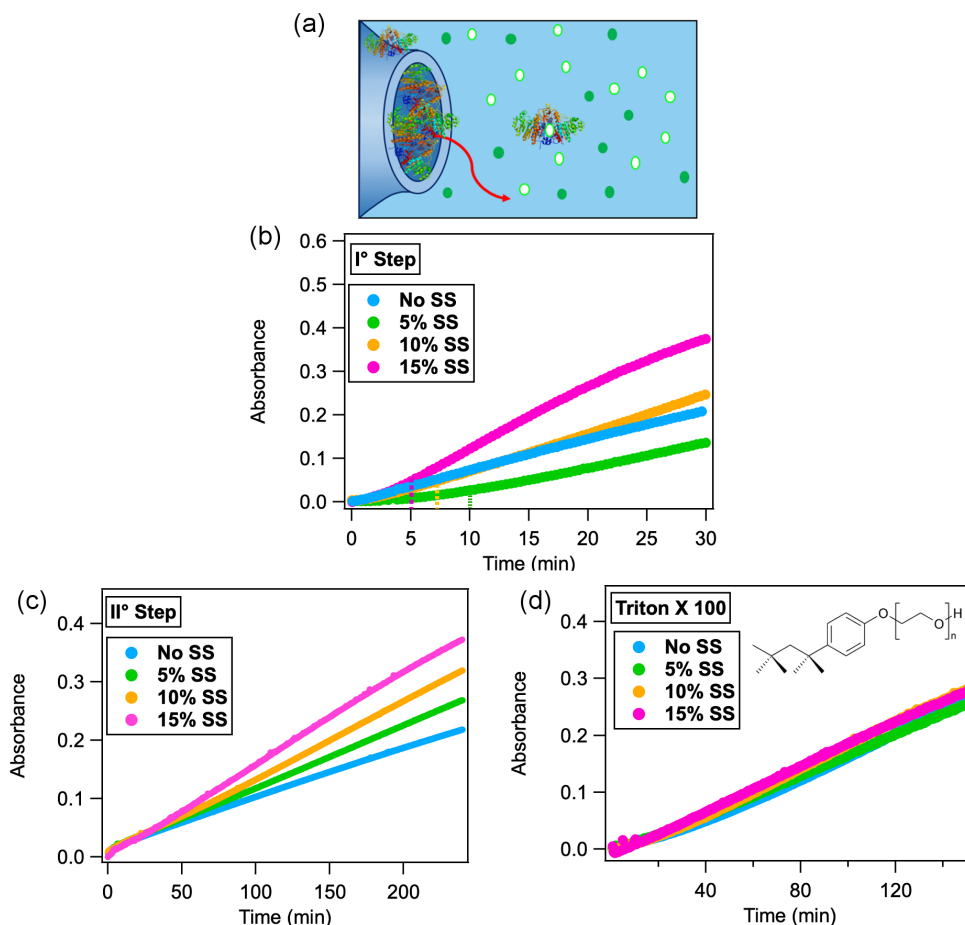


**Figure 4.** Enzymatic kinetics of p-nitrophenyl phosphate in TRIS buffer during the release of AP enzyme encapsulated in cubic phase, schematized in (a). (b) Phyt (cyan markers), Phyt/ 5% w/w SS (green markers), Phyt/10% w/w SS (orange markers) and Phyt/15% w/w SS (purple markers) shows the profile during the first 30 minutes (b) of enzyme released in a buffer solution with substrate, while in (c) it is reported the kinetic profiles in a fresh buffer and substrate solution after the step described in (b). (d) Kinetic profiles from cubic phase with or without SS: during the analogues second step of experiment reported in (c), with the addition of Triton-X-100 which destroy the mesophase.

Similarly to the previous paragraph, where the enzymatic reaction was monitored confining the substrate, the confined AP enzyme in the liquid crystalline mesophase should be discussed in terms of the possible pathways for the enzymatic reaction to proceed. A first possible mechanism to guarantee the close interaction of the enzyme with the substrate is the release of the encapsulated enzyme to the aqueous

environment, while a second possible mechanism is the penetration of the substrate inside the nanochannels of the liquid crystalline mesophase, where it meets the enzyme, and subsequently it is released as a reaction product.

Considering the first experiment, i.e., the cubic phase with the encapsulated enzyme directly immersed in the substrate solution, we notice a different mechanism in the presence of sucrose stearate. In particular, for all mesophases containing SS, two trends can be identified in the kinetic profiles. To interpret this behaviour, in case of Phyt/water sample, we should consider that part of the enzyme can be localized at the liquid crystalline phase/water interface and it is fast released. At this point, the AP in solution is available to convert the substrate molecules, while the remaining AP resides inside the liquid crystalline structure catalyse the substrate conversion more slowly. In line with this hypothesis, samples with varied SS amount exhibit a lag time, between the first and second enzymatic kinetic trend. This is progressively decreased, enhancing the SS concentration: about 10 minutes for 5% w/w SS, 7-8 minutes in the case of 10% w/w SS and 5 minutes with 15% w/w SS (Figure 4b). Considering the swelling of the mesophase induced by the addition of SS, we can relate this variable effect to a variable amount of the enzyme trapped in the mesophases due to the higher water fraction characterizing the mesophase. Indeed, for the binary system, i.e., Phyt/H<sub>2</sub>O in the absence of SS, the trend of the kinetic curve is monotonous (Figure 4b), suggesting that in this case the encapsulation of the enzyme in the liquid crystalline phase is strongly hampered, due to the small size of the nanochannels.

After the first trend, the second part of the curve proceeds with a faster rate for the systems with higher SS percentage, suggesting that the size of nanochannels has a prominent role. This behaviour might be related either to the release of the enzyme from the mesophase (whose rate can increase due to the swelled nanochannels), or

to the penetration rate of the substrate inside the aqueous channels of the mesophase (which, similarly, increases with the nanochannel size).

After this first step, we performed a control experiment to verify that: (i) a significant AP amount was still present inside the mesophases; (ii) the AP amount was comparable for the mesophases, differing by SS amount. (Figure 4d). To this purpose, a set of "control" mesophases was disassembled by immersion in a 24 mg/mL solution of Triton X 100. The non-ionic surfactant, at relatively high concentration<sup>39,40</sup> is able to dissolve the lipid bilayer to yield mixed micelles, with simultaneous quantitative release of AP originally contained in the liquid crystalline mesophase. The AP amount was measured in terms of enzymatic activity (Figure 4d). The substantial overlap of the kinetic profiles confirms that a significant amount of AP, practically identical for all samples, is still present in the mesophases.

Figure 4c reports the kinetic profiles concerning the second step, i.e. the immersion of the mesophases in fresh substrate solutions. Not surprisingly, the conversion rate is strictly dependent on the size of the nanochannels.

The ensemble of experimental data does not allow distinguishing which pathways is occurring whether the substrate diffuses in the mesophase or the enzyme is released. A simple size argument would rule out AP diffusion from the mesophase to the external medium as the prevailing mechanism, but we are not currently able to rule out the simultaneous substrate diffusion in the mesophase. Indeed, the dimension of the enzyme is around 5 nm; considering a partial distribution of AP between the lipid leaflet and the nanochannels of the cubic mesophases, the encapsulation of the protein could be reached. We can probably expect that, in the absence of a chemical potential driving its diffusion from the mesophase to the surrounding medium, the enzyme will be more conveniently localized in the cages of the structure, rather than in the nanochannels.

As mentioned above, the presence of additives results in the swelling of the mesophase, thus for the higher SS amount both the mechanisms are possible, and the results may be a combination of both the pathways. However, with the lower SS concentration, the enzyme release is less feasible, favouring the diffusion of the substrate into the channels.

Besides the mechanism of enzyme-substrate interaction, it is interesting to notice that the enzymatic reaction is in the case of AP confinement in the lipid mesophase, strongly slowed down with respect to the case of substrate confinement (paragraph 2.3) and no confinement (paragraph 2.2) case; in addition, as already discussed, the reaction rate and mechanism depend on the structure of the lipid mesophase, in particular on the size of the aqueous channels, which is finely tuneable by controlling the additive concentration. These systems, Phyt/SS/H<sub>2</sub>O ternary mesophases, characterized by a variable and controlled structure, which is closely related to the loading-release properties of the mesophase, represent a suitable scaffold for the confinement and sustained release of active principles of different sizes.

### **3. Conclusion**

In this contribution, we investigated the structural and diffusive properties of phytantriol cubic liquid crystals at maximum hydration loaded with increased concentration of the additive sucrose stearate. SAXS data show an excellent control on the tunability of phytantriol assemblies both on the arrangement and the diameter of the water nanochannels. The transition occurred after the loading of additives in mesophases, finds reason in the membrane energy curvature: since both hydration level and nanochannel size increase, the sugar ester promotes a structure with a more positive curvature. At the maximum concentration tested in this work (15% w/w of SS) the lipid

matrix shows a transition from diamond to primitive cubic structure with a diameter of the swollen nanochannels 22% larger than the ones of Phyt/H<sub>2</sub>O binary system. The UV-Vis kinetics were performed on pure and swollen mesophases, using an enzymatic reaction catalyzed by Alkaline Phosphatase, converting the substrate p-nitrophenyl phosphate (uncolored solution) in p-nitrophenol (green-yellow product). The substrate and the enzyme confined into the channels, showed a velocity reaction change, dependent on the probe size-nanochannel dimension ratio. The investigation performed on the confinement level of the substrate allows observing an exponential increase of the initial velocity of the reaction with the swelling of the structure. Since the concentration of the substrate, during the initial step of the reaction, is low and quite constant, it can be reasonable to consider the release step as the rate-determining process. However, after that period, additional factor (i.e., the inhibition of the enzyme from the product) becomes significant, modifying the release profiles.

Oppositely, when the protein size is similar to the diameter of the less swollen mesophases, the inclusion of the enzyme is not complete: at increasing SS concentration, protein loaded amount increases in the hybrid systems. The mechanism describing the substrate conversion, in that case, is hard to determine since both the phenomena (released enzyme or converted substrate into the channels and then released) are possible. The experiment made with Triton X confirms the presence of AP enzyme into the structure since the rate of conversion becomes higher; moreover, the presence of a very similar amount of protein encapsulated in each mesophase is detected. This work aims to shed light on the intriguing behaviour of the release from the cubic mesophases, highlighting how the investigated systems are appealing as drug-delivery vehicles for the uptake and release of active molecules.

## 4. Experimental

### ***Instruments:***

**-Small Angle X-ray Scattering:** SAXS measurements were performed on a S3-MICRO SAXS/WAXS instrument (HECUS GmbH, Graz, Austria) which consists of a GeniX microfocus X-ray Sealed Cu K $\alpha$  source (Xenocs, Grenoble, France) with power of 50 W. The source provides a focused X-ray beam with  $k = 0.1542$  nm Cu K $\alpha$  line. The instrument is equipped with two one-dimensional (1D) position sensitive detectors, (HECUS 1D-PSD-50M system) each detector is 50 mm long (spatial resolution 54  $\mu\text{m}/\text{channel}$ , 1024 channels) and covers a  $q$ -range of  $0.003 < q < 0.6 \text{ \AA}^{-1}$  (SAXS) and  $1.2 < q < 1.9 \text{ \AA}^{-1}$  (WAXS). The temperature was controlled by means of a Peltier TCCS-3 Hecus. SAXS curves of bulk cubic phases were recorded at 25-30-35-40-45-50 °C in a kapton solid sample holder. SAXS profiles were then recorded for 15 minutes each temperature waiting 20 minutes of thermal equilibration. SAXS data analysis is detailed in the SI.

**-UV-Vis Spectrophotometer:** UV-Vis measurements were performed on UV-Cary 3500 Agilent Technologies, which allows data collection in the range 190-1100 nm wavelength with different available bandwidths that can be selected between 0.1 and 5.0 nm at 0.01 nm intervals: the light spot on the sample is 1.5 mm. The instrument presents a Xenon flash lamp, double out-of-plane Littrow monochromator for fast data collection. There are eight cuvette position with eight detectors collecting the light signal which arrive on the sample at 1.5 cm from the bottom of the cuvette. It presents a magnetic stirrer able to mix the solution in cuvette with the appropriate stir bar. The temperature is controlled by different Peltier blocks in the range 0-100 °C.

### ***Samples preparation:***

**-SAXS bulk cubic phases** with or without the additive sucrose stearate were prepared according to the following procedure: 30 mg of Phyt were weighted in a 2 mL glass flask in the absence (for pure Phyt systems) or in the presence of appropriate amounts

of sucrose stearate in order to reach a final amount in the final lipid mixture of 5, 10, or 15% wt. About 0.5 mL of chloroform was used to solubilize the mixtures, then the solvent was removed under a gentle nitrogen flux. The lipid films were left under vacuum overnight, then hydrated with 16  $\mu$ L Milli-Q water and left for at least 12 hours to equilibrate before the experiments.

**-UV-Vis bulk cubic phases:** For the UV-Vis experiments, the same protocol described for SAXS was employed for the mesophases preparation, with doubled lipid amount. The cubic phases prepared for the experiment of p-nitrophenyl phosphate encapsulation were prepared by hydrating the lipid films with 31  $\mu$ L of TRIS buffer solution pH 7.5 containing  $5 \times 10^{-3}$  M of the substrate, in order to reach a theoretical final concentration in the cuvette of  $6 \times 10^{-5}$  M.

The cubic phases prepared for the experiment of AP encapsulation were prepared by hydrating the lipid films with TRIS buffer pH 7.5 solution containing 16 U/mL AP enzyme, with a theoretical final value in cuvette after dilution (final volume 2.5 mL) of 0.2 U/mL.

To perform these measurements, we built-up a home-made modified plastic flask where a plastic ring was tied to the top of cuvette leaving the mesophase infusing into the buffer until the reaction was complete. Moreover, in order to homogenize the reaction solution, the buffer was stirred with cuvette stirrer bars during all the time of the experiments.

## Supporting Information

Supporting information text

Supporting Information File

File Name: SI\_Manuscript

File Format: .pdf

Title: Confinement of substrates in nanochannels of liquid crystal lipid mesophases: effects on enzyme kinetics

## Acknowledgements (optional)

Costanza Montis acknowledges the European Union's Horizon 2020 program (evFOUNDRY grant agreement 801367).

## References

- (1) Zhai, J.; Fong, C.; Tran, N.; Drummond, C. J. *ACS Nano* **2019**, *13*, acsnano.8b07961.
- (2) Bulpett, J. M.; Snow, T.; Quignon, B.; Beddoes, C. M.; Tang, T.-Y. D.; Mann, S.; Shebanova, O.; Pizzey, C. L.; Terrill, N. J.; Davis, S. A.; Briscoe, W. H. *Soft Matter* **2015**, *11* (45), 8789.
- (3) Oka, T.; Hasan, M.; Islam, M. Z.; Moniruzzaman, M.; Yamazaki, M. *Langmuir* **2017**, *33* (43), 12487.
- (4) Oka, T.; Tsuboi, T. A.; Saiki, T.; Takahashi, T.; Alam, J. M.; Yamazaki, M. *Langmuir* **2014**, *30* (27), 8131.
- (5) Oka, T.; Saiki, T.; Alam, J. M.; Yamazaki, M. *Langmuir* **2016**, *32* (5), 1327.
- (6) Yaghmur, A.; Laggner, P.; Zhang, S.; Rappolt, M. *PLoS One* **2007**, *2* (5).
- (7) Shearman, G. C.; Ces, O.; Templer, R. H.; Seddon, J. M. *J. Phys. Condens. Matter* **2006**, *18* (28), S1105.
- (8) Negrini, R.; Mezzenga, R. *Langmuir* **2012**, *28* (47), 16455.
- (9) Gustafsson, J.; Ljusberg-Wahren, H.; Almgren, M.; Larsson, K. *Langmuir* **1996**, *12* (20), 4611.
- (10) Van'T Hag, L.; De Campo, L.; Garvey, C. J.; Feast, G. C.; Leung, A. E.; Yepuri,

- N. R.; Knott, R.; Greaves, T. L.; Tran, N.; Gras, S. L.; Drummond, C. J.; Conn, C. E. *J. Phys. Chem. Lett.* **2016**, 7 (14), 2862.
- (11) Liu, Q.; Dong, Y. Da; Boyd, B. J. *Langmuir* **2016**, 32 (20), 5155.
- (12) Speziale, C.; Zabara, A. F.; Drummond, C. J.; Mezzenga, R. *ACS Nano* **2017**, 11 (11), 11687.
- (13) Murgia, S.; Bonacchi, S.; Falchi, A. M.; Lampis, S.; Lippolis, V.; Meli, V.; Monduzzi, M.; Prodi, L.; Schmidt, J.; Talmon, Y.; Caltagirone, C. *Langmuir* **2013**, 29 (22), 6673.
- (14) Murgia, S.; Falchi, A. M.; Meli, V.; Schillén, K.; Lippolis, V.; Monduzzi, M.; Rosa, A.; Schmidt, J.; Talmon, Y.; Bizzarri, R.; Caltagirone, C. *Colloids Surfaces B Biointerfaces* **2015**, 129, 87.
- (15) Caltagirone, C.; Falchi, A. M.; Lampis, S.; Lippolis, V.; Meli, V.; Monduzzi, M.; Prodi, L.; Schmidt, J.; Sgarzi, M.; Talmon, Y.; Bizzarri, R.; Murgia, S. *Langmuir* **2014**, 30 (21), 6228.
- (16) Bazylińska, U.; Kulbacka, J.; Schmidt, J.; Talmon, Y.; Murgia, S. *J. Colloid Interface Sci.* **2018**, 522, 163.
- (17) Van'T Hag, L.; De Campo, L.; Tran, N.; Sokolova, A.; Trenker, R.; Call, M. E.; Call, M. J.; Garvey, C. J.; Leung, A. E.; Darwish, T. A.; Krause-Heuer, A.; Knott, R.; Meikle, T. G.; Drummond, C. J.; Mezzenga, R.; Conn, C. E. *Langmuir* **2019**.
- (18) Vallooran, J. J.; Assenza, S.; Mezzenga, R. *Angew. Chemie - Int. Ed.* **2019**, 58 (22), 7289.
- (19) Montis, C.; Castroflorio, B.; Mendoza, M.; Salvatore, A.; Berti, D.; Baglioni, P. *J. Colloid Interface Sci.* **2015**, 449, 317.
- (20) Mendoza, M.; Montis, C.; Caselli, L.; Wolf, M.; Baglioni, P.; Berti, D. *Nanoscale* **2018**, 10 (7), 3480.

- (21) Tran, N.; Hawley, A. M.; Zhai, J.; Muir, B. W.; Fong, C.; Drummond, C. J.; Mulet, X. *Langmuir* **2016**, *32* (18), 4509.
- (22) Negrini, R.; Mezzenga, R. *Langmuir* **2011**, *27* (9), 5296.
- (23) Tyler, A. I. I.; Barriga, H. M. G.; Parsons, E. S.; McCarthy, N. L. C.; Ces, O.; Law, R. V.; Seddon, J. M.; Brooks, N. J. *Soft Matter* **2015**, *11* (16), 3279.
- (24) Barriga, H. M. G.; Tyler, A. I. I.; McCarthy, N. L. C.; Parsons, E. S.; Ces, O.; Law, R. V.; Seddon, J. M.; Brooks, N. J. *Soft Matter* **2015**, *11* (3), 600.
- (25) Tangso, K. J.; Fong, W. K.; Darwish, T.; Kirby, N.; Boyd, B. J.; Hanley, T. L. *J. Phys. Chem. B* **2013**, *117* (35), 10203.
- (26) Jia, S.; Du, J. D.; Hawley, A.; Fong, W. K.; Graham, B.; Boyd, B. J. *Langmuir* **2017**, *33* (9), 2215.
- (27) Jia, S.; Tan, A.; Hawley, A.; Graham, B.; Boyd, B. J. *J. Colloid Interface Sci.* **2019**, *548*, 151.
- (28) Mendozza, M.; Caselli, L.; Montis, C.; Orazzini, S.; Carretti, E.; Baglioni, P.; Berti, D. *J. Colloid Interface Sci.* **2019**, *541*, 329.
- (29) Fong, W. K.; Hanley, T. L.; Thierry, B.; Tilley, A.; Kirby, N.; Waddington, L. J.; Boyd, B. J. *Phys. Chem. Chem. Phys.* **2014**, *16* (45), 24936.
- (30) Wlodek, M.; Kolasinska-Sojka, M.; Szuwarzynski, M.; Kereiche, S.; Kovacik, L.; Zhou, L.; Islas, L.; Warszynski, P.; Briscoe, W. H. *Nanoscale* **2018**, *10* (37), 17965.
- (31) Das, K.; Roy, B.; Satpathi, S.; Hazra, P. *J. Phys. Chem. B* **2019**, *123* (18), 4118.
- (32) Sun, W.; Vallooran, J. J.; Zabara, A.; Mezzenga, R. *Nanoscale* **2014**, *6* (12), 6853.
- (33) Assenza, S.; Mezzenga, R. *J. Chem. Phys.* **2018**, *148* (5).
- (34) Barauskas, J.; Landh, T. *Langmuir* **2003**, *19* (23), 9562.

- (35) Dean, R. L. *Biochem. Mol. Biol. Educ.* **2002**, *30* (6), 401.
- (36) Vallooran, J. J.; Negrini, R.; Mezzenga, R. *Langmuir* **2013**, *29* (4), 999.
- (37) Ghanbari, R.; Assenza, S.; Saha, A.; Mezzenga, R. *Langmuir* **2017**, *33* (14), 3491.
- (38) de Backer, M.; McSweeney, S.; Rasmussen, H. B.; Riise, B. W.; Lindley, P.; Hough, E. *J. Mol. Biol.* **2002**, *318* (5), 1265.
- (39) Caritá, A. C.; Mattei, B.; Domingues, C. C.; De Paula, E.; Riske, K. A. *Langmuir* **2017**, *33* (29), 7312.
- (40) Pizzirusso, A.; De Nicola, A.; Sevink, G. J. A.; Correa, A.; Cascella, M.; Kawakatsu, T.; Rocco, M.; Zhao, Y.; Celino, M.; Milano, G. *Phys. Chem. Chem. Phys.* **2017**, *19* (44), 29780.

# Lipid Liquid Crystalline Mesophases with tuneable size of aqueous nanochannels: effects on the enzymatic reaction rates.

Debora Berti\*<sup>1</sup>, Marco Mendoza<sup>1</sup>, Costanza Montis<sup>1</sup>, Arianna Balestri<sup>1</sup>

Address: <sup>1</sup>Department of Chemistry “Ugo Schiff” and CSGI, Via della Lastruccia 3-13, Sesto Fiorentino 50019 (FI)

E-mail: Debora Berti – [debora.berti@unifi.it](mailto:debora.berti@unifi.it)

\* Corresponding author

<b>Materials and Methods</b>	<b>Page</b>
S.1 <i>Materials</i>	S2
S.2 <i>SAXS data elaboration</i>	S2
<b>Supplementary Figures</b>	
S.3 <i>Lambert Beer Plot</i>	S3
S.4 <i>Rate of reaction varying the concentration of Sucrose Stearate</i>	S4
S.5 <i>Experiments with Triton X</i>	S5
<b>References</b>	S6

## Materials and Methods

### S.1 Materials:

Phytantriol (Phyt) was a gift of Royal DSM (purity >99%). Sucrose Stearate (SS) (Crodesta F110-PW-(RB)) was a gift of Croda Europe Ltd. Rawcliff Bridge, Goole, United Kingdom. TRIS buffer was prepared with Trizma® hydrochloride purchased by Fluka BioChemika (>99.0% (AT)) and TRIZMA® BASE (>99.9% (titration)) purchased by Sigma Chemical Co. The enzyme Alkaline Phosphatase (AP) (REF 11 097 075 001) 1000 U/mL purchased by Roche Diagnostic (Indianapolis, USA) and the substrate p-nitrophenyl phosphate (>99% purity) purchased by Fluka. Triton X 100 was purchased by Fluka (>99.0% purity).

### S.2 SAXS data elaboration:

Equation (1) was used to calculate lattice parameter (d) of cubic and hexagonal phase:

$$q = \left(\frac{2\pi}{d}\right) \sqrt{h^2 + k^2 + l^2} \quad (1)$$

where (hkl) are Miller index related to the considered structures. In a Pn3m structure are (110), (111), (200), (211), (220)... while in H<sub>II</sub> mesophases are (100), (111), (200)... Eq. (2)<sup>1</sup> was used to calculate water channel radii  $r_w$  in Pn3m cubic phase while Eq. (3)<sup>1</sup> was used to calculate volume water fraction  $\varphi_w$ :

$$r_w = \sqrt{(-A_0/2\pi\chi)d} - l_c \quad (2)$$

$$\varphi_w = 1 - 2A_0 \left(\frac{l_c}{d}\right) - \frac{4}{3}\pi\chi \left(\frac{l_c}{d}\right)^3 \quad (3)$$

where  $A_0$  and  $\chi$  are topological parameters respectively the ratio of the area of the minimal surface in a unit cell to (unit cell volume)<sup>2/3</sup> and the Euler–Poincaré characteristic, that for the diamond cubic mesophase (Pn3m), are  $A_0=1.919$  and  $\chi=-2$ . Equation (4)<sup>2</sup> and (5)<sup>3</sup> describe water channel radii ( $r_w$ ) of hexagonal phase H<sub>II</sub> and water volume fraction ( $\varphi_w$ ) respectively:

$$r_w = \frac{0.5256d - l_c}{0.994} \quad (4)$$

$$\varphi_w = \frac{2\pi r_w^2}{\sqrt{3}d^2} \quad (5)$$

We assumed that chain length  $l_c$  into the range of 25-50 °C, is constant and assume value of about 1.4 nm calculated by the data reported in literature<sup>4</sup>.

## Supplementary Figures

### S.3 Lambert-Beer Plot

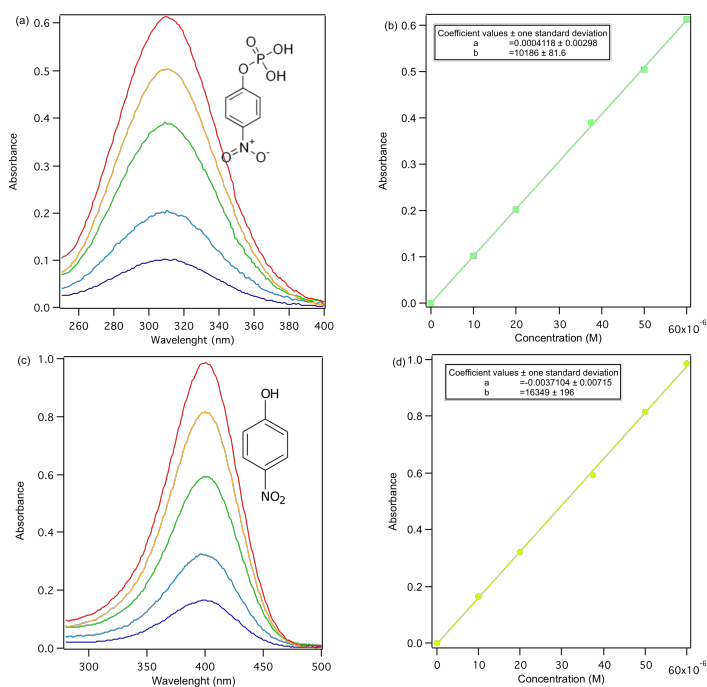


**Figure S.2:** UV-Vis absorbance spectra into the range 250-500 nm of p-nitrophenyl phosphate (a) and p-nitrophenol (c) and the relative Lambert-Beer Plot to calculate the molar extinction coefficient of both compounds respectively reported in (b) and (d).

The molar extinction coefficients calculated from the Lambert-Beer plots of the reaction substrate and product (see SI) are  $\epsilon = 10186 \text{ L mol}^{-1}\text{cm}^{-1}$  and  $\epsilon = 16349 \text{ L mol}^{-1}\text{cm}^{-1}$  at 310 and 400 nm for p-nitrophenyl phosphate and p-nitrophenol, respectively.

### S.4 Rate of reaction varying the concentration of Sucrose Stearate

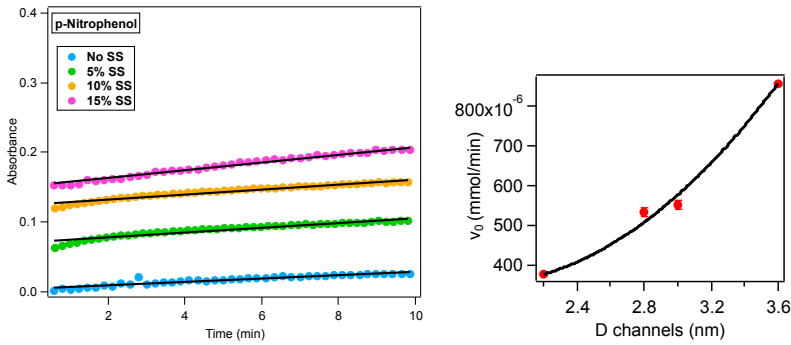


**Figure S3:** Linear fit of kinetic curves (during the first 10 minutes of reaction), encapsulating the substrate p-nitrophenyl phosphate in cubic phase, doped with increased concentration of the additives: No SS (cyan markers), 5% SS (green markers), 10% SS (orange markers) and 15% SS (purple markers), immersed in a buffer solution containing 0.1 U/mL AP enzyme. The curves are off-set to make clearer the image for the readers. Besides the kinetics image, there is a plot of initial velocity as a function of the diameter of water channels.

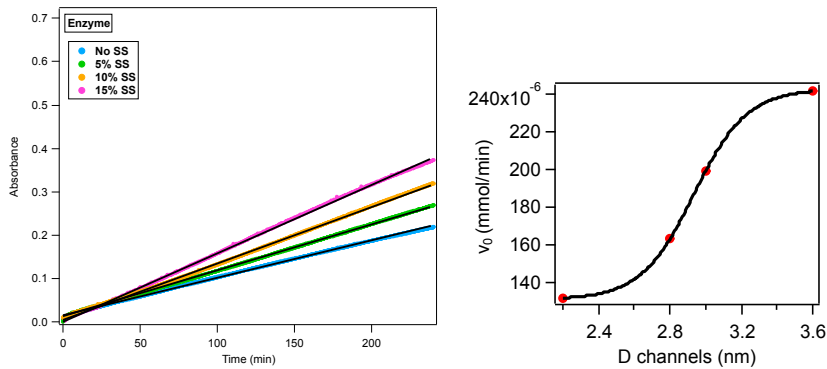


**Figure S4:** The enzymatic reaction profiles of the cubic phase loaded by AP enzyme, during the first 4 h, in a buffer solution containing  $6 \times 10^{-5}$  M of the substrate. No SS (cyan markers), 5% SS (green markers), 10% SS (orange markers), and 15% SS (purple markers) are fitted with a linear equation showed with a black line. Besides the kinetics data, there is a plot of initial velocity as a function of the diameter of water channels. The error bars are smaller than the size of the marker.

The slopes obtained by the linear fitting showed in Figure S4, are converted in mmol/min of substrate considering the molar extinction coefficient of the product and the final volume into the cuvette (2.5 mL). All these data are reported in Table S1.

**Table S1:** Rate of reactions expressed in (mmol/min of converted substrate) and channels size (nm). Data obtained by cubic phase loaded with AP enzyme during the second step of reaction.

Samples	Rate (mmol/min)	Channels Size (nm)
No Cubic Phase	$1.180 \times 10^{-2} (\pm 6 \times 10^{-5})$	/
Phyt	$1.314 \times 10^{-4} (\pm 2 \times 10^{-7})$	2.2
Phyt/5% SS	$1.630 \times 10^{-4} (\pm 1 \times 10^{-7})$	2.8
Phyt/10% SS	$1.990 \times 10^{-4} (\pm 4 \times 10^{-7})$	3.0
Phyt/15% SS	$2.417 \times 10^{-4} (\pm 3 \times 10^{-7})$	3.6

### S.5 Experiments with Triton X 100

With the experimental setup chosen to register the absorbance of the developed product during the reaction, the first step of enzymatic kinetic was performed to eliminate the adsorbed enzyme outside the cubic phase without Triton X 100. Successively, it was added at each sample (with different Sucrose Stearate amount) 60 mg of surfactant dissolved in 2.5 mL of TRIS buffer, where it was added the substrate to reach a concentration around  $6 \times 10^{-5}$  M (the results of this experiments are shown in the main text).

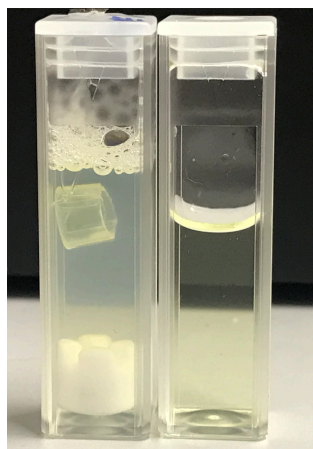


**Figure S5:** The experimental setup used to perform the kinetic experiments from the cubic phase. The cubic phase was placed into the plastic ring, immersed into the buffer solution. A cuvette magnetic stir bar was used to homogenize the system during the reaction (400 rpm). After 2 h, in case of Triton X 100 (cuvette on the left), it appears a yellow milk-like dispersion compared to the kinetics performed without it (cuvette on the right).

## References:

- (1) Negrini, R.; Mezzenga, R. *Langmuir* **2012**, *28* (47), 16455.
- (2) Reese, C. W.; Strango, Z. I.; Dell, Z. R.; Tristram-Nagle, S.; Harper, P. E. *Phys. Chem. Chem. Phys.* **2015**, *17* (14), 9194.
- (3) Marsh, D. *Handbook of lipid bilayers*; 2013.
- (4) Barauskas, J.; Landh, T. *Langmuir* **2003**, *19* (23), 9562.

# Paper VI



# Relationship between structure and diffusive properties of lipid liquid crystals

*Marco Mendoza, Viola Tinti, Costanza Montis, Debora Berti\**

AUTHOR ADDRESS Department of Chemistry “Ugo Schiff” and CSGI, 50016, Via della Lastruccia 3-13, Sesto Fiorentino (FI).

KEYWORDS: Lipids, FCS, liquid-crystals, mesophases, diffusive properties

ABSTRACT (Word Style “BD\_Abstract”).

## 1. Introduction:

Lamellar and Non-lamellar mesophases are ubiquitous in natural systems and connected to different physiological or pathological state of cells<sup>1,2</sup>. Generally, the perturbation of cell membranes with different molecular compounds affects the structural properties and the related physico-chemical membrane features. In particular, cubic mesophases are characterized by two interpenetrated not interconnected water nanochannels, separated by lipid bilayer. These structures are generally recognized as Pn3m (diamond), Im3m (primitive) and Ia3d (gyroid) architectures, which are described by Infinite Periodical Minimal Surfaces (IMPS).

The inclusion of different kind of molecules in 1-monoolein (MO)/water system can be a useful approach to tune the mesophase' structure in order to choose the best conditions for the applicative purpose. Indeed, a better description of the effects promoted by molecular additives on the curvature, and consequently on the structural parameter of the mesophase, requires to treated dividing additives in hydrophobic and amphiphilic. Generally, one of the most important parameters is the additive concentration, where, above a "critical" amount, a phase transition is induced. Hydrophobic molecules are generally recognized to interact mainly with the hydrophobic chain of lipids, increasing the volume of hydrophobic portion; in that way, the curvature increase, becoming more negative, promoting a transition from cubic to inverted hexagonal phases. However, this is true for relatively low concentrations of oils<sup>3-6</sup>: above a certain fraction of hydrophobic additive, the oil-lipid mixture assemble in bicontinuous cubic micelles (Fd3m symmetry), or also inverted micelles<sup>7,8</sup>. In other words, the aqueous channels of the mesophases become progressively smaller until the dispersant oil separates the water domains through a surfactant monolayer. However, the literature reports on these effects also in the case of fatty acids<sup>9-12</sup>, vitamin E<sup>13</sup>; thus, hydrophobic additives are not necessary oils. It is of

relevance to evaluate also the effects of active hydrophobic molecules on the structure of the cubic mesophases as reported by Drummond et al.<sup>14</sup> or also the enzymes modifying the lipid structure and their consequent organization<sup>15</sup>.

Amphiphiles interact with the lipid membrane locating itself spontaneously to the interface; however, the final effects are a combination of the chemical composition of the surfactant and also to the hindrance of hydrophobic chains. Mezzenga et al.<sup>16</sup> have reported the effect of a sugar ester (sucrose stearate) on the structure of the mesophases. Considering a bigger volume of headgroup with respect to the hydrophobic chains, and the affinity of sucrose with water producing hydrogen bond interactions, the diamond cubic structures is swelled in a primitive cubic mesophases where the diameter of nanochannels are bigger in size. However, some other amphiphiles are reported in literature, i.e., caproic acid combined with 1,2-dilauroyl-sn-glycero-3-phosphocholine (DLPC) or 1,2-distearoyl-sn-glycero-3-phosphocholine (DSPC)<sup>17</sup>, 1,2-dioleoyl-sn-glycero-3-phospho-(1'-rac-glycerol) (DOPG)<sup>18,19</sup> which are able to promote a transition in mesophases presenting a less negative curvature, until the lamellar phases.

Where the classification of other molecular additives becomes complicated, it is necessary to consider their effects on the structure. The addition of molecules with responsivity to the pH, UV-Vis light, magnetic field and ionic strength, make the bilayer systems quick to react to the external stimulus promoting structural change. These considerations could be useful to classify the behavior of stimuli-responsive additives included into the bilayer; indeed, azobenzene derivate<sup>20-25</sup>, oleic acid and charged lipids can be used to build up sensitive liquid crystals to the light, changing the molecular conformations, or to the pH<sup>26-31</sup> or ionic strength<sup>32</sup> changing the ratio of the hydrophobic and hydrophilic molecular volumes. Thus, through the external stimuli, the additive acts like hydrophobic/amphiphilic molecules, promoting structural changes. In this

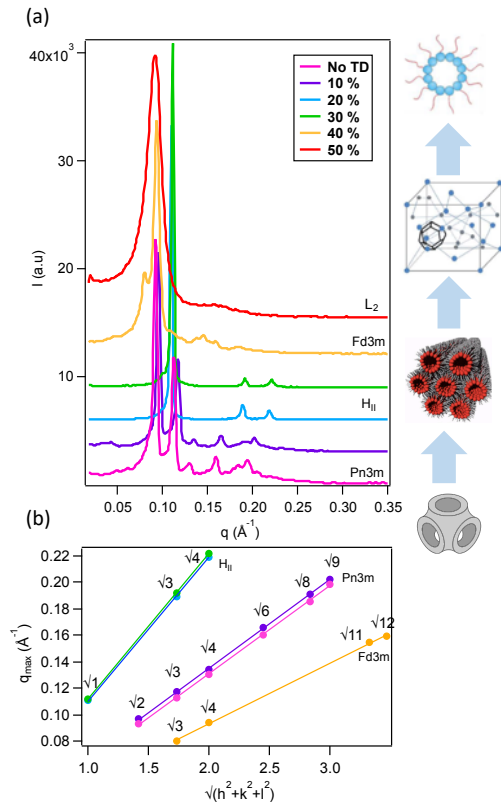
contribution, we built up the phase diagram of a complex quaternary matrix, at the maximum hydration level, composed by MO, DOPG and tetradecane (TD) varying the composition of the components. Small-Angle X-Ray Scattering (SAXS) technique highlight the complex polymorphism of liquid crystals depending on the ability of additives to impose their own curvature to the MO membrane and their relative concentration. With the aim to study the relationship between structure and diffusive properties, Fluorescence Correlation Spectroscopy (FCS) techniques was used to compare systems with the same structure, but with different lattice parameters. Indeed, loading cubic phases with different hydrophilic fluorophore probes (Rhodamine 110 and Rhodamine B Dextran) different in size, it was tested the influence of the channel size on the diffusive properties of the probes.

## **2. Results and Discussion:**

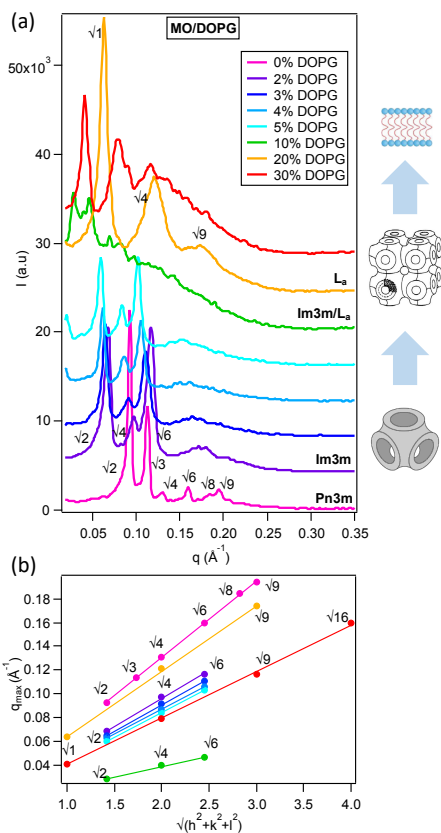
### **2.1. Phase behavior of MO/DOPG/TD/water systems**

Figure 1 shows the SAXS profiles of MO/H<sub>2</sub>O systems loaded with different amount of TD varying the additive amount into the range 0-50% w/w, in water excess at 25 °C. As notable, all the curves with an increased concentration of TD show a shift to higher scattering vectors, suggesting a decrease of a parameter in the direct space, i.e., the channels' size. For the relatively low amount of tetradecane, the diamond cubic structure is preserved. However, above 10% w/w TD, a phase transition from cubic to hexagonal array is observed, analogously to the inclusion of hydrophobic inorganic nanoparticles showed in other works<sup>33-35</sup>. This behavior can be fully explained in terms of frustration packing energy, since the inclusion of a hydrophobic additive produces a decrease of this energetic term, favoring the hexagonal array. However, the additional

higher amount of TD into the MO mesophases, induce a phase transition corresponding to the Fd3m structure, a bicontinuous cubic micelles. The more is the amount of the oil, the more is the the disorder, since the typical Bragg reflexes of Fd3m structure disappear (Figure 29), showing a broad scattering curve positioned around  $0.092 \text{ \AA}^{-1}$ . This value corresponds to a typical dimension around 6.8 nm, which describes the average distance of micelles between each other dispersed in the oil environment. The inverted micelles can be justified considering the significant amount of oil molecules functioning as dispersant medium, while the MO surfactant separates water from oil in a nano-spherical shape micelle. In summary, the inclusion of TD, in agreement with some works reported in literature<sup>7,8</sup>, due to its hydrophobic nature, produce a shrinking of water nanochannels, promoting transition to structure with an increased (in absolute value) membrane curvature.



**Figure 1:** Small angle X-ray scattering curves reordered at 25 °C at the maximum hydration level in MO assemblies added by increased amount of tetradecane additive: 0 % TD (purple curve), 10% w/w (violet curve), 20% w/w (cyan curve), 30% w/w (green curve), 40% (orange curve) and 50% w/w (red curve). (b) Linear fit to calculate the lattice parameter of mesophases; the sample containing 50% TD it is not shown since it is an inverted micelles structure.



**Figure 2:** (a) Small Angle X-ray Scattering curves at 25 °C at the maximum hydration level in MO assemblies added by increased amount of DOPG additive: 0% w/w (purple curve), 2% w/w (violet curve), 3% w/w (blue curve), 4% w/w (cyan curve), 5% w/w (light cyan curve), 10% w/w (green curve), 20% w/w (orange curve) and 30% w/w (red curve). (b) Linear Fit to calculate the lattice parameter of mesophases.

Analogously to TD effect, DOPG amphiphilic lipid was tested on the MO bilayer, enhancing the additive amount in MO/DOPG/water systems. While the TD molecules interact mainly with the hydrophobic chains of the bilayer, DOPG locates spontaneously to the interface. Its huge polar headgroup produces an uptake of water into the channels, analogously to the SS behavior described in other works<sup>16</sup>.

The inclusion of DOPG on the lipid bilayer is shown in Figure 2, where – increasing the concentration of the amphiphilic additive – a shift to lower scattering vectors is recorded. Oppositely to the TD effect, DOPG swells the lipid bilayer; indeed, the relatively low DOPG amount (2-5% w/w) produces an overall swell effect on the Pn3m structure, promoting a transition from diamond to primitive cubic assemblies. In agreement with the literature, the lamellar phases are observed starting from 10% w/w DOPG, where both lamellar and Im3m mesophases can be observed. The SAXS profiles, relative to the samples with 10% DOPG, show an intensity increase in the low q-region: since a water excess hydrate the dry lipid film, the broad contribution to the scattering intensity describe a partial dispersion of MO/DOPG lipids in liposomes. Moreover, for the samples with more than 10%, the lamellar Bragg reflex can be detected, overlapped to the liposome's contribution, indicating the coexistence of liposomes and bulk multilayers.

Some considerations should be made, concerning the MO/DOPG and MO/TD systems. All concentrations in this paragraph are expressed as % w/w; from Figure 2, a relatively low DOPG concentration produces a dramatical effect on the bilayer morphology compared to the TD additive. The molecular weight ratio between TD and DOPG is around 1:4; thus, the small DOPG concentration corresponds to an exiguous number of molecules assembled with MO. Therefore, DOPG imposes its curvature more than TD; tetradecane does not assemble to the water-lipid interface, due to its non-surfactant nature.

After an initial evaluation of TD and DOPG effects, a mixture of MO with both the additives allows to explore the ternary phase diagram, taking into account that the system presents four components, considering water added in excess. The investigated additives show an opposite effect on the MO bilayer, since combining them both with the 1-monoolein, the main contribution involved to temper the structure of the mesophase is evident.

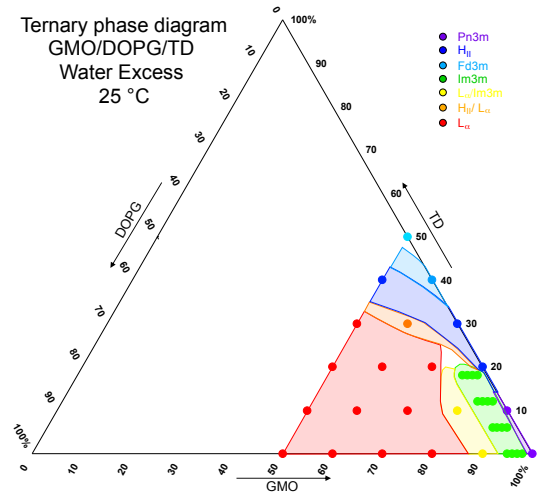


**Figure 3:** Ternary phase diagram of MO/DOPG/TD system shows the Pn3m structure (violet region), Im3m (green region), Lamellar (red region), H<sub>II</sub> (blue region), Fd3m (cyan region). The orange and yellow regions describe the coexistence of Lamellar/H<sub>II</sub> and Lamellar/Im3m structure.

All the results are reported in the ternary phase diagram and shown in Figure 3. The L<sub>α</sub> region is the most extended for the investigated concentration of the additives. The Im3m structure is observed in a small region of the phase diagram, analogously for the Pn3m. Thus, it seems that the bicontinuous mesophases are stable in case of not significant perturbation of the bilayer. It is evident that the possibility to control both the thickness and the water channel size of bicontinuous phases is limited by the thermodynamical stability of the structures, and these features of the mesophases cannot be modified in an infinite range of possibilities in any case.

## **2.2 Fluorescence Correlation Spectroscopy to test diffusive properties.**

Based on the results showed in the previous section, the introduction of molecules with different features allows us to extend the LCs structure range compared to the neat MO systems. As highlighted before, the inclusion of DOPG and TD to MO assemblies shows a complex phase behavior depending on the relative concentration of the additives and their ability to impose their curvature in MO bilayer. However, even if their contribution can be perfectly counterbalanced (since they have opposite effects), it is reasonable to think that the *in-meso* diffusive properties of molecular probes confined into the channels are dependent on the variation of the water channels size. Indeed, the inclusion of DOPG and TD in MO systems allows for swelling or shrinking the nanochannels, producing a different lattice parameter for the same structure; for this reason, the diffusive properties of fluorophore through FCS experiments can be tested to verify a relationship between structure and diffusive properties.

The molecular probes involved in this investigation are Rhodamine 110 and Rhodamine B Dextran, two hydrophilic fluorophores spontaneously encapsulated in the hydrophilic domains of liquid crystals. The molecular structure and FCS curves of the probes freely diffusing in water at 25 °C, are reported in Figure 4.

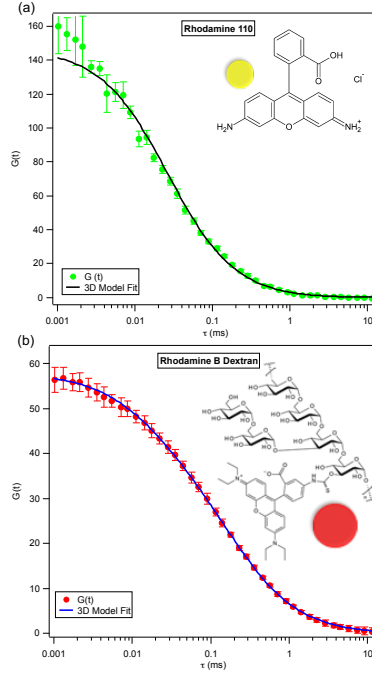


**Figure 4:** FCS curves of (a) Rhodamine 110 and (b) Rhodamine B Dextran in water at 25 °C and their fit curves obtained by a 3D model with (a) single component and (b) two component.

The mathematical model to extract information on the diffusion coefficients of the probes is reported in Eq. 1:

$$G(\tau) = \frac{1}{\langle c \rangle \pi^2 w_0^2 z_0} \left( 1 + \frac{4D\tau}{w_0^2} \right)^{-1} \left( 1 + \frac{4D\tau}{z_0^2} \right)^{-\frac{1}{2}} \quad (1)$$

Where  $\langle c \rangle$  is the average concentration of the probe in the confocal volume,  $w_0$  and  $z_0$  are respectively the lateral ( $z_0$ ) and axial ( $w_0$ ) defining parameters of detection volume with a 3D ellipsoidal Gaussian shape, and  $D$  the diffusion coefficient of the probe. This model provides information on one fluorescent probe diffusing in a 3D space. While Rhodamine 110 shows an excellent fit result with the equation 3.10, the Rhodamine B Dextran, due probably to the

synthesis procedure and work-up, does not show a single component: this is also confirmed by a separation of a concentrated fluorophore solution with a Vivaspin® provided with a membrane cut-off 5000 M<sub>w</sub>. The best-fitting result can be obtained with a 3D model of two different components, and the mathematical equation reported in Eq. 2:

$$G(\tau) = \frac{1}{\langle c \rangle \pi^2 w_0^2 z_0} \left[ f_1 \left( 1 + \frac{4D_1\tau}{w_0^2} \right)^{-1} \left( 1 + \frac{4D_1\tau}{z_0^2} \right)^{-\frac{1}{2}} + f_2 \left( 1 + \frac{4D_2\tau}{w_0^2} \right)^{-1} \left( 1 + \frac{4D_2\tau}{z_0^2} \right)^{-\frac{1}{2}} \right] \quad (2)$$

Where  $f_1$  and  $f_2$  are the fractions parameters describing the abundance of a fluorescent component with respect to the other.

The diffusion coefficient of the Rhodamine 110 probe is 430  $\mu\text{m}^2/\text{s}$ <sup>36</sup>, while there are two diffusion coefficients for Rhodamine B-Dextran: 420  $\mu\text{m}^2/\text{s}$ <sup>36</sup> for the free Rhodamine B and 41  $\mu\text{m}^2/\text{s}$  for Rhodamine B labeling Dextran polysaccharide. In order to be clearer in the discussion, the diffusion coefficient of Rhodamine B Dextran will be expressed in an average value based on the relative abundance of the fluorophores. For this reason, the diffusion coefficient  $D_{\text{RBdex}}=166$   $\mu\text{m}^2/\text{s}$ <sup>37</sup>.

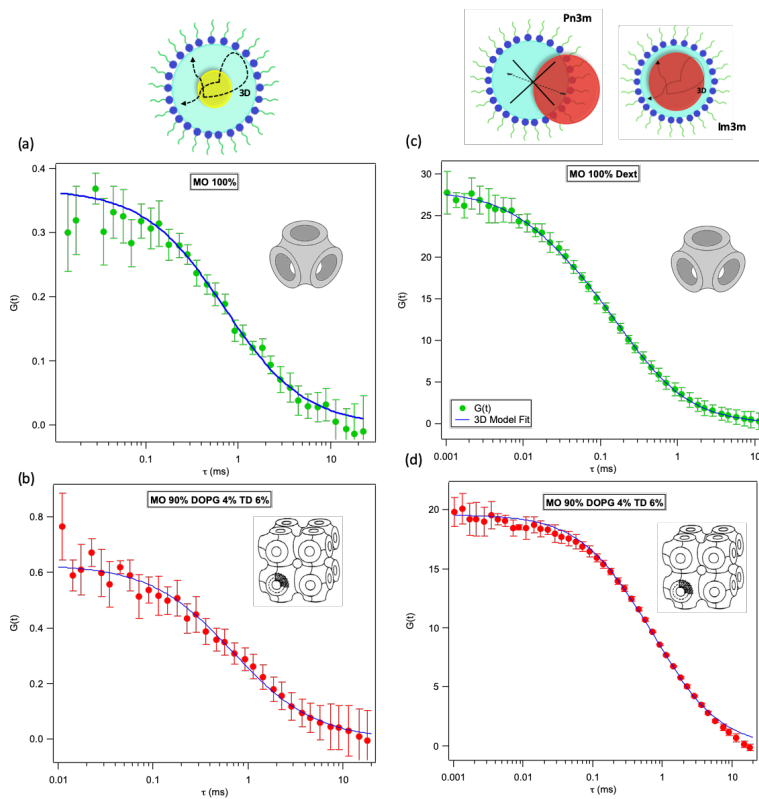


**Figure 5** FCS curves of Rhodamine 110 (a-b) and Rhodamine B Dextran (c-d) in Pn3m structure (a-c) and Im3m (b-d) structures. On top, a representative sketch of the probe Rhodamine 110 (yellow dot) in a water nanochannels of both Pn3m and Im3 mesophases, while the Rhodamine B Dextran (represented as red dot double in size of yellow dot), match the dimension of Im3m nanochannels, while it locates spontaneously out of the channels in a Pn3m mesophases.

In agreement with the literature<sup>37</sup>, the dimensions of probes are around 1 nm and 2.6 nm for Rhodamine 110 e Rhodamine B Dextran respectively, so that it can be evaluated the encapsulation in liquid crystals, based on the size of the probe. First, using the same equation 1

and 2, the fitting models were used to treat the FCS results recorded on Pn3m liquid crystals (100% MO composition) and Im3m (90% MO, 4% DOPG and 6% TD). In those cases, the 3D motion of the probes is allowed by the 3D tortuosity of cubic mesophases nanochannels, since the model used was the same for a “free” fluorophore. The results showed in Figure 5 suggest that, in the case of Rhodamine 110, a confinement effect can be seen in both the prepared samples; indeed, the diffusion coefficient, compared to the D value of the freely diffusing probe in water, is at least one order of magnitude lower. This phenomenon is related to the confinement of water in nanochannels.<sup>38,39</sup> The Rhodamine B Dextran shows a different behavior: while the average diffusion coefficient is around  $30 \mu\text{m}^2/\text{s}$  in Im3m mesophases, showing a confinement effect, in the case of Pn3m is quite close to the  $166 \mu\text{m}^2/\text{s}$  value. Thus, considering the dimension of the diamond cubic structure comparable to the probe size, the hindered fluorophore cannot be entrapped, producing a “free” diffusion of the probe in the surrounding medium.

At this point, to control the relationship between structure and diffusive properties, the FCS experiments were performed on lamellar and hexagonal mesophases comparing samples showing the same phase behavior but characterized by a different lattice parameter. In those cases, the equation describing the diffusion of the probes is slightly different from the 3D model reported in Eq. 1-2: the spatial probes diffusion, is allowed in a 2D direction in case of a lamellar structure (a thick layer of water separate two bilayer and probes move parallel or perpendicular to the lipid membrane), and 1D direction of hexagonal mesophases (where the movement of the probes is possible along the direction of the cylindrical structure). The mathematical equations are reported in Eq. 3 and 4, for two components for a 2D and 1D diffusion respectively<sup>40</sup>. However, it should be taken into account that in case of Rhodamine 110,  $f_1=1$  and  $f_2=0$  in both of these equations.

$$G(t) = \frac{1}{N} \left[ f_1 \left( 1 + \frac{4D_1\tau}{w_0^2} \right)^{-1} + f_2 \left( 1 + \frac{4D_2\tau}{w_0^2} \right)^{-1} \right] \quad (3)$$

$$G(t) = \frac{1}{N} \left[ f_1 \left( 1 + \frac{4D_1\tau}{z_0^2} \right)^{-1/2} + f_2 \left( 1 + \frac{4D_2\tau}{z_0^2} \right)^{-1/2} \right] \quad (4)$$

The lamellar samples compared in that analysis present a lattice parameter of 115 Å (80% MO and 20% DOPG) and 216 Å (50% MO, 20% DOPG and 30% TD). Thus, a swelled lamellar phase can be reached in that conditions, since the water amount added to the dry lipid film is the same in both case. The FCS experiments performed with the fluorophores are showed in Figure 6.

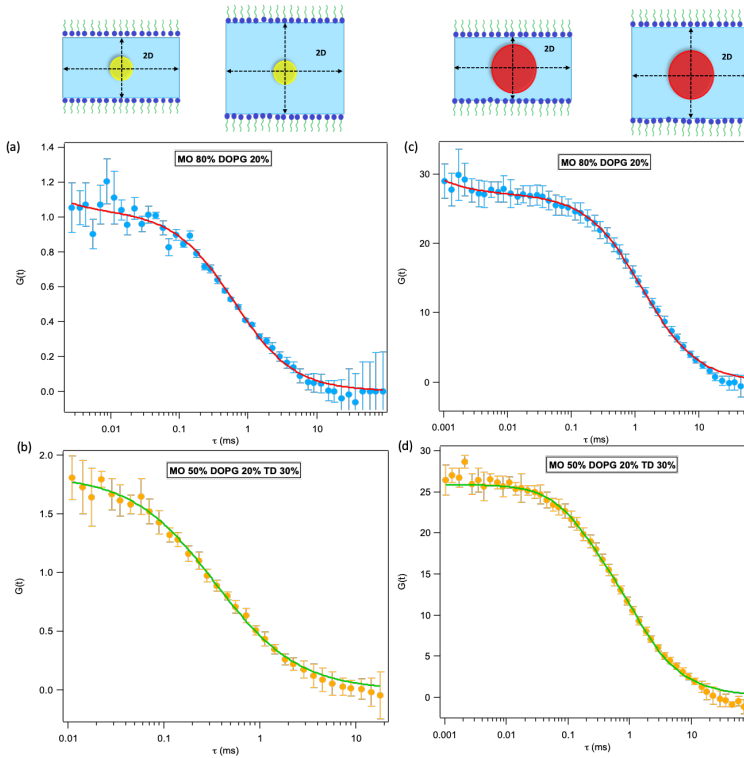


**Figure 6** FCS curves of Rhodamine 110 (a-b) and Rhodamine B Dextran (c-d) in lamellar structure with different lattice parameters; (a-c) are relative to the sample MO 80% and DOPG 20% with a lattice parameter 115 Å, while (b-d) represent the FCS curves relative to the sample swelled (MO 50%, DOPG 20% and TD 30%) with a lattice parameter 216 Å. On top, a representative sketch of the probe Rhodamine 110 (yellow dot) and Rhodamine B Dextran (represented as red dot double in size of yellow dot), located in water.

From the fitting results, the Rhodamine 110 diffusion coefficients in both the lamellar samples is smaller than the probes in aqueous solution, thus in agreement to the results reported before about cubic mesophases, it is reasonable to think a confinement of the fluorophore between two leaflets of different lipid bilayer separated by a thin layer of water. In particular, the results highlight that the swelled samples present a less confinement level of the probe in the case of Rhodamine 110: indeed, the diffusion coefficients are 13  $\mu\text{m}^2/\text{s}$  and 24  $\mu\text{m}^2/\text{s}$  for MO 80%-DOPG 20% and MO 50%-20% DOPG-30% TD respectively. The analysis of Rhodamine B Dextran curves shows a peculiar behavior: the dimension of the probe is similar to the water layer separating the leaflet of the membrane; thus the probe is locked between the bilayer confirmed by the very low diffusion coefficient (the average value is around 1  $\mu\text{m}^2/\text{s}$  and 1.2  $\mu\text{m}^2/\text{s}$  for the un-swelled and swelled sample respectively). In those conditions, the Rhodamine B labeling the polysaccharide moiety shows a locked situation suggesting a no-diffusional property of the fluorophore.

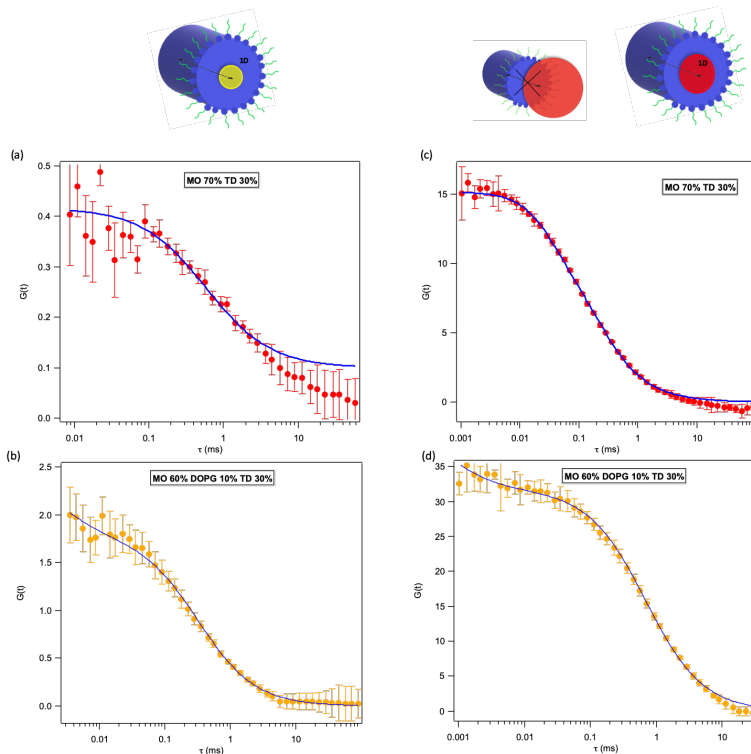


**Figure 7** FCS curves of Rhodamine 110 (a-b) and Rhodamine B Dextran (c-d) in hexagonal structure with different lattice parameters; (a-c) are relative to the sample MO 70% and TD 30% with a lattice parameter 57 Å, while (b-d) represent the FCS curves relative to the sample swelled (MO 60% DOPG 10% TD 30%) with a lattice parameter 76 Å. On top, a representative sketch of the probe Rhodamine 110 (yellow dot) and Rhodamine B Dextran (represented as red dot double in size of yellow one), located in water channels.

Figure 7 shows the best fitting result modeling the FCS curves as the Eq. 4. About the hexagonal mesophases, the probe's motion is allowed along with the directionality imposed by the cylinders assembled in an  $H_{II}$  array. Thus, accordingly to the 1D model, the diffusion

coefficient was extracted. In that experiments, comparing the hexagonal sample composed by a mixture of MO (70%) and TD (30%) with the swelled sample containing 60% MO, 10% DOPG and 30%TD swelling the system of around 2 nm (from 57 Å to 76 Å of lattice parameter). Rhodamine 110 shows in both samples a diffusion coefficient smaller, showing a confinement level of the fluorophore, more than the other mesophases. This is consistent with the dimension of the hydrophilic domains, where the probes are encapsulated since water nanochannels in  $H_{II}$ . Moreover, the Rhodamine B Dextran size is more prominent than water channels; thus, the encapsulation is not possible within the sample 70% MO 30% TD while it is almost locked in case of swelled  $H_{II}$ . In order to summarize the results, all the diffusion coefficients are reported in Table 4 as a function of water nanochannels size or thickness of the water layer.

<b>Table 4: Comparison of the diffusion coefficients derived by FCS curve for swelled and de-swelled cubic, hexagonal and lamellar phases. Rhodamine 110 and Rhodamine B Dextran were used for the experiments.</b>				
<b>Samples</b>	<b>Rhodamine 110</b>		<b>Rhodamine B Dextran</b>	
	$D_{No-Swelled}$	$D_{Swelled}$	$D_{No-Swelled}$	$D_{Swelled}$
<b>Cubic</b>	11±1	12±1	140±18	17±1
<b>Lamellar</b>	13±1	24±2	15±5	10±3
<b>Hexagonal</b>	14±2	5±1	158±15	8±2

## AUTHOR INFORMATION

### Corresponding Author

\*[deboraberti@unifi.it](mailto:deboraberti@unifi.it)

## Author Contributions

The manuscript was written through contributions of all authors. All authors have given approval to the final version of the manuscript.

## Funding Sources

Any funds used to support the research of the manuscript should be placed here (per journal style).

## ACKNOWLEDGMENT

(Word Style “TD\_Acknowledgments”).

## REFERENCES

- (1) Almsherqi, Z. A.; Kohlwein, S. D.; Deng, Y. Cubic Membranes: A Legend beyond the Flatland\* of Cell Membrane Organization. *J. Cell Biol.* **2006**, *173* (6), 839–844. <https://doi.org/10.1083/jcb.200603055>.
- (2) Almsherqi, Z. A.; Landh, T.; Kohlwein, S. D.; Deng, Y. Chapter 6 Cubic Membranes. In *International Review of Cell and Molecular Biology*; Elsevier Inc., 2009; Vol. 274, pp 275–342. [https://doi.org/10.1016/S1937-6448\(08\)02006-6](https://doi.org/10.1016/S1937-6448(08)02006-6).
- (3) Rappolt, M.; Cacho-Nerin, F.; Morello, C.; Yagmur, A. How the Chain Configuration Governs the Packing of Inverted Micelles in the Cubic Fd3m-Phase. *Soft Matter* **2013**, *9* (27), 6291. <https://doi.org/10.1039/c3sm50308a>.
- (4) Templer, R. H.; Seddon, J. M.; Duesing, P. M.; Winter, R.; Erbes, J. Modeling the Phase Behavior of the Inverse Hexagonal and Inverse Bicontinuous Cubic Phases in 2:1 Fatty

Acid/Phosphatidylcholine Mixtures. *J. Phys. Chem. B* **1998**, *102* (37), 7262–7271.  
<https://doi.org/10.1021/jp972837v>.

(5) Mionić Ebersold, M.; Petrović, M.; Fong, W.-K.; Bonvin, D.; Hofmann, H.; Milošević, I. Hexosomes with Undecylenic Acid Efficient against *Candida Albicans*. *Nanomaterials* **2018**, *8* (2), 91. <https://doi.org/10.3390/nano8020091>.

(6) Guillot, S.; Salentinig, S.; Chemelli, A.; Sagalowicz, L.; Leser, M. E.; Glatter, O. Influence of the Stabilizer Concentration on the Internal Liquid Crystalline Order and the Size of Oil-Loaded Monolinolein-Based Dispersions. *Langmuir* **2010**, *26* (9), 6222–6229.  
<https://doi.org/10.1021/la903927w>.

(7) Pouzot, M.; Mezzenga, R.; Leser, M.; Sagalowicz, L.; Guillote, S.; Glatter, O. Structural and Rheological Investigation of Fd3m Inverse Micellar Cubic Phases. *Langmuir* **2007**, *23* (19), 9618–9628. <https://doi.org/10.1021/la701206a>.

(8) Yagmur, A.; de Campo, L.; Salentinig, S.; Sagalowicz, L.; Leser, M. E.; Glatter, O. Oil-Loaded Monolinolein-Based Particles with Confined Inverse Discontinuous Cubic Structure (Fd 3 M). *Langmuir* **2006**, *22* (2), 517–521. <https://doi.org/10.1021/la052109w>.

(9) Tran, N.; Hawley, A. M.; Zhai, J.; Muir, B. W.; Fong, C.; Drummond, C. J.; Mulet, X. High-Throughput Screening of Saturated Fatty Acid Influence on Nanostructure of Lyotropic Liquid Crystalline Lipid Nanoparticles. *Langmuir* **2016**, *32* (18), 4509–4520.  
<https://doi.org/10.1021/acs.langmuir.5b03769>.

(10) Tran, N.; Mulet, X.; Hawley, A. M.; Fong, C.; Zhai, J.; Le, T. C.; Ratcliffe, J.; Drummond, C. J. Manipulating the Ordered Nanostructure of Self-Assembled Monoolein and

Phytantriol Nanoparticles with Unsaturated Fatty Acids. *Langmuir* **2018**, *34* (8), 2764–2773. <https://doi.org/10.1021/acs.langmuir.7b03541>.

(11) Yaghmur, A.; Al-Hosayni, S.; Amenitsch, H.; Salentinig, S. Structural Investigation of Bulk and Dispersed Inverse Lyotropic Hexagonal Liquid Crystalline Phases of Eicosapentaenoic Acid Monoglyceride. *Langmuir* **2017**, *33* (49), 14045–14057. <https://doi.org/10.1021/acs.langmuir.7b03078>.

(12) Shao, X.; Bor, G.; Al-Hosayni, S.; Salentinig, S.; Yaghmur, A. Structural Characterization of Self-Assemblies of New Omega-3 Lipids: Docosahexaenoic Acid and Docosapentaenoic Acid Monoglycerides. *Phys. Chem. Chem. Phys.* **2018**, *20* (37), 23928–23941. <https://doi.org/10.1039/C8CP04256J>.

(13) Dong, Y. Da; Larson, I.; Hanley, T.; Boyd, B. J. Bulk and Dispersed Aqueous Phase Behavior of Phytantriol: Effect of Vitamin E Acetate and F127 Polymer on Liquid Crystal Nanostructure. *Langmuir* **2006**, *22* (23), 9512–9518. <https://doi.org/10.1021/la061706v>.

(14) Zhai, J.; Luwor, R. B.; Ahmed, N.; Escalona, R.; Tan, F. H.; Fong, C.; Ratcliffe, J.; Scoble, J. A.; Drummond, C. J.; Tran, N. Paclitaxel-Loaded Self-Assembled Lipid Nanoparticles as Targeted Drug Delivery Systems for the Treatment of Aggressive Ovarian Cancer. *ACS Appl. Mater. Interfaces* **2018**, *10* (30), 25174–25185. <https://doi.org/10.1021/acsami.8b08125>.

(15) Fong, W.; Sanchez-Ferrer, A.; Rappolt, M.; Boyd, B. J.; Mezzenga, R. Structural Transformation in Vesicles upon Hydrolysis of Phosphatidylethanolamine and Phosphatidylcholine with Phospholipase C. *Langmuir* **2019**, *acs.langmuir.9b02288*. <https://doi.org/10.1021/acs.langmuir.9b02288>.

(16) Negrini, R.; Mezzenga, R. Diffusion, Molecular Separation, and Drug Delivery from Lipid Mesophases with Tunable Water Channels. *Langmuir* **2012**, *28* (47), 16455–16462. <https://doi.org/10.1021/la303833s>.

(17) Zhai, J.; Tran, N.; Sarkar, S.; Fong, C.; Mulet, X.; Drummond, C. J. Self-Assembled Lyotropic Liquid Crystalline Phase Behavior of Monoolein–Capric Acid–Phospholipid Nanoparticulate Systems. *Langmuir* **2017**, *33* (10), 2571–2580. <https://doi.org/10.1021/acs.langmuir.6b04045>.

(18) Tyler, A. I. I.; Barriga, H. M. G.; Parsons, E. S.; McCarthy, N. L. C.; Ces, O.; Law, R. V.; Seddon, J. M.; Brooks, N. J. Electrostatic Swelling of Bicontinuous Cubic Lipid Phases. *Soft Matter* **2015**, *11* (16), 3279–3286. <https://doi.org/10.1039/c5sm00311c>.

(19) Barriga, H. M. G.; Tyler, A. I. I.; McCarthy, N. L. C.; Parsons, E. S.; Ces, O.; Law, R. V.; Seddon, J. M.; Brooks, N. J. Temperature and Pressure Tuneable Swollen Bicontinuous Cubic Phases Approaching Nature’s Length Scales. *Soft Matter* **2015**, *11* (3), 600–607. <https://doi.org/10.1039/c4sm02343a>.

(20) Jia, S.; Tan, A.; Hawley, A.; Graham, B.; Boyd, B. J. Visible Light-Triggered Cargo Release from Donor Acceptor Stenhouse Adduct (DASA)-Doped Lyotropic Liquid Crystalline Nanoparticles. *J. Colloid Interface Sci.* **2019**, *548*, 151–159. <https://doi.org/10.1016/j.jcis.2019.04.032>.

(21) Tangso, K. J.; Fong, W. K.; Darwish, T.; Kirby, N.; Boyd, B. J.; Hanley, T. L. Novel Spiropyran Amphiphiles and Their Application as Light-Responsive Liquid Crystalline Components. *J. Phys. Chem. B* **2013**, *117* (35), 10203–10210. <https://doi.org/10.1021/jp403840m>.

- (22) Fong, W.; Negrini, R.; Vallooran, J. J.; Mezzenga, R.; Boyd, B. J. Responsive Self-Assembled Nanostructured Lipid Systems for Drug Delivery and Diagnostics. *J. Colloid Interface Sci.* **2016**, *484*, 320–339. <https://doi.org/10.1016/j.jcis.2016.08.077>.
- (23) Fong, W.-K.; Malic, N.; Evans, R. A.; Hawley, A.; Boyd, B. J.; Hanley, T. L. Alkylation of Spiropyran Moiety Provides Reversible Photo-Control over Nanostructured Soft Materials. *Biointerphases* **2012**, *7* (1), 3. <https://doi.org/10.1007/s13758-011-0003-9>.
- (24) Jia, S.; Fong, W.-K.; Graham, B.; Boyd, B. J. Photoswitchable Molecules in Long-Wavelength Light-Responsive Drug Delivery: From Molecular Design to Applications. *Chem. Mater.* **2018**, *30* (9), 2873–2887. <https://doi.org/10.1021/acs.chemmater.8b00357>.
- (25) Du, J. D.; Fong, W.-K.; Salentinig, S.; Caliph, S. M.; Hawley, A.; Boyd, B. J. Phospholipid-Based Self-Assembled Mesophase Systems for Light-Activated Drug Delivery. *Phys. Chem. Chem. Phys.* **2015**, *17* (21), 14021–14027. <https://doi.org/10.1039/C5CP01229E>.
- (26) Negrini, R.; Fong, W.-K.; Boyd, B. J.; Mezzenga, R. PH-Responsive Lyotropic Liquid Crystals and Their Potential Therapeutic Role in Cancer Treatment. *Chem. Commun.* **2015**, *51* (30), 6671–6674. <https://doi.org/10.1039/C4CC10274F>.
- (27) Salentinig, S.; Sagalowicz, L.; Glatter, O. Self-Assembled Structures and p K a Value of Oleic Acid in Systems of Biological Relevance. *Langmuir* **2010**, *26* (14), 11670–11679. <https://doi.org/10.1021/la101012a>.
- (28) Gontsarik, M.; Mohammadtaheri, M.; Yaghmur, A.; Salentinig, S. PH-Triggered Nanostructural Transformations in Antimicrobial Peptide/Oleic Acid Self-Assemblies. *Biomater. Sci.* **2018**, *6* (4), 803–812. <https://doi.org/10.1039/C7BM00929A>.

- (29) Prajapati, R.; Gontsarik, M.; Yaghmur, A.; Salentinig, S. PH-Responsive Nano-Self-Assemblies of the Anticancer Drug 2-Hydroxyoleic Acid. *Langmuir* **2019**, *35* (24), 7954–7961. <https://doi.org/10.1021/acs.langmuir.9b00838>.
- (30) Gontsarik, M.; Yaghmur, A.; Ren, Q.; Maniura-Weber, K.; Salentinig, S. From Structure to Function: PH-Switchable Antimicrobial Nano-Self-Assemblies. *ACS Appl. Mater. Interfaces* **2019**, *11* (3), 2821–2829. <https://doi.org/10.1021/acsami.8b18618>.
- (31) Li, Y.; Angelova, A.; Hu, F.; Garamus, V. M.; Peng, C.; LI, N.; Liu, J.; Liu, D.; Zou, A. PH-Responsiveness of Hexosomes and Cubosomes for Combined Delivery of Brucea Javanica Oil and Doxorubicin. *Langmuir* **2019**, *acs.langmuir.9b02257*. <https://doi.org/10.1021/acs.langmuir.9b02257>.
- (32) Oka, T.; Hasan, M.; Islam, M. Z.; Moniruzzaman, M.; Yamazaki, M. Low-PH-Induced Lamellar to Bicontinuous Primitive Cubic Phase Transition in Dioleoylphosphatidylserine/Monoolein Membranes. *Langmuir* **2017**, *33* (43), 12487–12496. <https://doi.org/10.1021/acs.langmuir.7b02512>.
- (33) Mendoza, M.; Montis, C.; Caselli, L.; Wolf, M.; Baglioni, P.; Berti, D. On the Thermotropic and Magnetotropic Phase Behavior of Lipid Liquid Crystals Containing Magnetic Nanoparticles. *Nanoscale* **2018**, *10* (7), 3480–3488. <https://doi.org/10.1039/C7NR08478A>.
- (34) Mendoza, M.; Caselli, L.; Salvatore, A.; Montis, C.; Berti, D. Nanoparticles and Organized Lipid Assemblies: From Interaction to Design of Hybrid Soft Devices. *Soft Matter* **2019**, No. August. <https://doi.org/10.1039/C9SM01601E>.

(35) Mendoza, M.; Caselli, L.; Montis, C.; Orazzini, S.; Carretti, E.; Baglioni, P.; Berti, D. Inorganic Nanoparticles Modify the Phase Behavior and Viscoelastic Properties of Non-Lamellar Lipid Mesophases. *J. Colloid Interface Sci.* **2019**, *541*, 329–338. <https://doi.org/10.1016/j.jcis.2019.01.091>.

(36) Gendron, P.-O.; Avaltroni, F.; Wilkinson, K. J. Diffusion Coefficients of Several Rhodamine Derivatives as Determined by Pulsed Field Gradient–Nuclear Magnetic Resonance and Fluorescence Correlation Spectroscopy. *J. Fluoresc.* **2008**, *18* (6), 1093–1101. <https://doi.org/10.1007/s10895-008-0357-7>.

(37) Peulen, T.; Wilkinson, K. J. Diffusion of Nanoparticles in a Biofilm. *Environ. Sci. Technol.* **2011**, *45* (8), 3367–3373. <https://doi.org/10.1021/es103450g>.

(38) Montis, C.; Castroflorio, B.; Mendoza, M.; Salvatore, A.; Berti, D.; Baglioni, P. Magnetocubosomes for the Delivery and Controlled Release of Therapeutics. *J. Colloid Interface Sci.* **2015**, *449*, 317–326. <https://doi.org/10.1016/j.jcis.2014.11.056>.

(39) Salvati Manni, L.; Assenza, S.; Duss, M.; Vallooran, J. J.; Juranyi, F.; Jurt, S.; Zerbe, O.; Landau, E. M.; Mezzenga, R. Soft Biomimetic Nanoconfinement Promotes Amorphous Water over Ice. *Nat. Nanotechnol.* **2019**, *14* (6), 609–615. <https://doi.org/10.1038/s41565-019-0415-0>.

(40) Montis, C.; Baglioni, P.; Berti, D. Monitoring the Interaction of Nucleolipoplexes with Model Membranes. *Soft Matter* **2014**, *10* (1), 39–43. <https://doi.org/10.1039/C3SM52254G>.